The University of Nottingham

UNITED KINGDOM · CHINA · MALAYSIA

Department of Chemical and Environmental

Engineering

INVESTIGATING THE EFFECT OF LIQUID VISCOSITY ON TWO-PHASE GAS-LIQUID FLOWS

ABOLORE ABDULAHI, B.Sc., M.Sc.

Thesis submitted to the University of Nottingham for the degree of Doctor of Philosophy

DECEMBER 2013

Abstract

Simultaneous flow of gas-liquid in pipes presents considerable challenges and difficulties due to the complexity of the two-flow mixture. Oil-gas industries need to handle highly viscous liquids, hence studying the effect of changing the fluid viscosity becomes imperative as this is typically encountered in deeper offshore exploration. This work looks at the effect of liquid viscosity on gas-liquid flows. The work was carried out using two different pipes of 67mm and 127mm internal diameter.

For the experiments carried out on the 67mm diameter pipe, air and three different liquids were used with viscosities 1, 42 and 152cp. With these experiments, the effect of viscosity on the entrainment process from the Taylor bubble in a vertical tube was investigated with the Taylor bubble being held stationary in a downward liquid flow with the use of three different gas injection methods. Taylor bubble length, the gas flow rate and the liquid flow rate approaching the stationary bubble were varied. In addition, the wake length below the stationary bubble was measured at different conditions of gas and liquid superficial velocities and comparison was made with the work by previous authors. Videos were taken with high speed camera to validate the measurement taken on wake lengths. A Wire Mesh Sensor system was placed at two different positions below the air injection point on the 67mm diameter pipe of the stationary bubble facility whose data acquisition provided time and cross-sectionally resolved information about spatial distribution. This information was used to generate time averaged void fraction, bubble size distribution and contour plots of the two-phase flow structure. A Probability Density Function (PDF) of void fraction can be obtained from the former, with PDFs of the wake section of the stationary bubbles showing that the flows are in the bubbly region while the PDF for the entire slug unit assumed that for a typical

Abolore Abdulahi

twin-peaked slug flow. The interpretation of this is that holding a bubble stationary can simulate real slug flow. Results on the bubble length measurement and gas loss into a bubble wake have shown good agreement with existing work by other authors.

Experiments on the 127 mm diameter pipe were carried out because most published work on gas/liquid flow were on smaller diameter pipes with air and water, yet many of the industrial applications of such flows in vertical pipes are in larger diameter pipes and with liquids which are much more viscous than water. Another important parameter considered in the study is pressure because of its effect on gas density. This part of the research goes some way to rectify this lack and presents void fraction and pressure gradient data for sulphur hexafluoride with gas densities of 28 and 45 kg/m^3 and oil (viscosity 35 times water). The gas and liquid superficial velocities were varied in the ranges 0.1-3 and 0.1-1 m/s respectively. The void fraction was also measured with a Wire Mesh Sensor system. Flow patterns were identified from the signatures of the Probability Density Function of cross-sectionally averaged void fraction. These showed the single peak shapes associated with bubbly and churn flow but not the twin-peaked shape usually seen in slug flow. This confirms previous work in larger diameter pipes but with less viscous liquids. For the bubble to churn flows investigated, the pressure gradients decreased with increasing superficial gas velocity. The change in pressure ultimately affects the density of gas in the two-phase flow mixture. Though there was little effect of pressure on void fraction below certain transitional flow rates, the effect became significant beyond these values. Different statistical analysis techniques such as power spectral density, probability density function, mean, standard deviation and time series of the acquired data have been used which also show the significant effect of pressure on void fraction at high gas density which have not been measured previously.

Abolore Abdulahi

List of Publications

Abdulahi, A., Eastwick, C.N. and Azzopardi, B.J., *"Experiments on a Stationary Taylor Bubble in a Downward Two-Phase Flow"*, (Paper under review for submission into International Journal of Multiphase Flow).

Abdulahi, A., Eastwick, C.N. and Azzopardi, B.J., *"Gas entrainment from a stationary Taylor bubble"*, (In preparation for submission into Journal).

Hernandez-Perez, V., Abdulkadir, M., Abdulkareem, L., **Abdulahi, A.** and Azzopardi, B.J., *"The effect of the liquid physical properties on inclined gas-liquid flow"* Journal of Fluids Engineering (Under review)

Abdulahi, A., Eastwick, C.N., Azzopardi, B.J., Smith, I.E. and Unander, T.E. (2013) *"Effect of pressure on a vertical two-phase flow with a high viscosity liquid"*, 8th International Conference on Multiphase Flows, ICMF 2013, Jeju, South Korea, May 26-31.

Abdulahi, A., Abdulkareem, L.A., Sharaf, S., Abdulkadir, M, Hernandez-Perez, V. and Azzopardi, B.J. (2011), *"Investigating the Effect of Pipe Inclination on Two-Phase Gas-Liquid Flows using Advanced Instrumentation"* Proceedings of the ASME/JSME 2011, 8th Thermal Engineering Joint Conference (AJTEC2011), March 13-17, Honolulu, Hawaii, USA.

Abdulahi, A. and Azzopardi, B.J., *"Two-phase Upward Flow in a Slightly Deviated Pipe"*, Journal of Fluids Engineering (Accepted Manuscript)

Abolore Abdulahi

Abdulahi, A. and Azzopardi, B.J., "*Slug Flows in inclined pipes*", (Paper under review for publication)

Abdulahi, A., Eastwick, C.N. and Azzopardi, B.J., 2011. "*Gas entrainment from a stationary Taylor Bubble*", A paper presented at Midlands Energy Graduate School (MEGS), Loughborough University. 11 December.

Acknowledgement

Abolore Abdulahi

My sincere appreciation to my friends: Ugochukwu Anyanwu, Chijioke Nwankwor, Malgorzata Wiatros, Sylvia Kokonya, Ekundayo Olusegun, Disu Ismoila and family, Sola Fatokun, Kehinde Famoriyo, Jimoh Muritala, Raji Uthman/Saheed , Lookman Omodudu, Gani Apena, Musa Taiwo/Kehinde and family, Funmilola Olowookere, Chidi Nwonyi, Ismaila Rasaq, The Muslim community at Nottingham and other loved ones who have supported me and frequently asked about the progress of my work.

Finally, I would like to thank my wife for her support and my children for their endless patience. We hope to share the rewards that may emanate from this work together. My mum's strength of character and hard work has been a quality inculcated in me which has always propelled me to seek ultimate success wherever it could be found. My late dad's philanthropic nature as well as his rare combination of brilliance and moral uprightness has been qualities I work hard every day to emulate. Many thanks to my brothers and sisters for the unflinching support they gave me during the period of this work.

This work is dedicated to Almighty God and to the memories of my late father (M.B. Abdulahi Logun) as well as my late brother (Muftau Abdulahi).

To God be the glory

Table of Contents

Abolore Abdulahi

Abolore Abdulahi

Abolore Abdulahi

List of Figures

Abolore Abdulahi

Abolore Abdulahi

Abolore Abdulahi

Abolore Abdulahi

Abolore Abdulahi

Abolore Abdulahi

Abolore Abdulahi

List of Tables

Abolore Abdulahi

Chapter One
Introduction

1.1   Background

A phase has been described by Modell and Reid (1983) as a region of thermodynamic system, throughout which all physical properties of a material are essentially uniform. A phase can either be gas, liquid or solid. In contrast to single phase flow, multiphase flow is a complex mixture of multiple fluids in the same geometry. Multiphase flow found application in many industrial fields, which include nuclear plants, heat exchangers, steam generators, boilers, reboilers, chemical reactors, pipelines and risers for hydrocarbon production. For instance, in petroleum industries, oil, natural gas and/or sand flows may emerge up the well tubing which can later be separated into different phases (solid, liquid and gas) and then processed for domestic use. The stages involved in processing are very complex due to the interaction between phases.

In modelling gas-liquid flows for liquids with viscosities considerably higher than water, industries are hampered in not knowing how the important phenomena characterising the flow will change with increasing liquid viscosity. For instance, when oil is produced during petroleum exploration, the reservoir pressure decreases and the oil flow rate decreases in proportion to the decreasing pressure difference between the reservoir and the processing facility. At low oil flow rates, a well becomes unstable and this leads to reduced production and processing problems. The formation of slug flow in pipelines is a manifestation of such flow instability.

The literature is awash with two-phase studies addressing mainly the flow behaviour for low viscosity liquids and gases (typically water which has a viscosity of around 0.001 Pa s, 1 cP). Very few studies have addressed high-viscosity multiphase flow behaviour. However, the oil industry has to handle liquids which have much higher viscosities; ranging up to 200cp.

Research in two-phase gas-liquid flows has been carried out since the mid twentieth century (Bennett et al. (1965), Turner et al. (1969), Alves (1954), Belkin et al. (1959), Nishikawa et al. (1969)) with motivation initially based on the needs of nuclear power and chemical industries. Since the later part of the twentieth century, there has been more focus on the subject area by oil and gas industries. With the increase in demand for oil globally and a decrease in oil and gas discovery in conventional offshore regions, oil exploration in deeper water has become prevalent. Risers employed for deeper water are now commonly made of larger diameters pipework (greater than 100mm) than the conventional ones to convey more fluid and to reduce pressure losses during fluid transport. Previous researchers have shown that the structure of the gas-liquid flow in large diameter pipes is different from that seen in small diameter pipes. An example is the absence of the classical bullet-shaped Taylor bubbles in slug flow which have been observed in small diameter pipes.

1.2   Aims and Objectives

1.2.1   Aims

The aim of the research described in this thesis is to investigate high viscosity liquid-gas flows in vertical pipes at conditions relevant to the oil and gas industries, based on the needs described in the previous section.

The work was supported by TMF5 and was undertaken at the SINTEF Multiphase Laboratory in Norway and within the Faculty of Engineering Laboratories at the University of Nottingham

The work reported in this Thesis can be divided into two: The first part looks at gas-liquid flows in a 127mm diameter pipe over a range of gas and liquid superficial velocities using a high viscosity liquid at two different pressure conditions, giving a high and low density gas and allowing the impact of both viscosity and pressure in larger diameter pipes to be investigated. The second part deals with gas-liquid flow in 67mm pipe with the gas phase kept stationary while the liquid phase is allowed to move downward with liquids with three different viscosities. The configuration is known as a stationary Taylor bubble.

1.2.2   Objectives

The objectives for the experiments carried out at SINTEF will focus on:

- Vertical SF_6-oil flows at two different pressures (4.5 to 7.5 bara).

- Void fraction measurements performed with calibrated Wire Mesh Sensor (WMS).

- Differential pressure measurements using calibrated differential pressure transducers

- Statistical methods for data gathering from the information extracted.

- Gathering and implementing information necessary for improvement of current two-phase flow models.

The objectives for the experiments carried out in Nottingham on the 67mm diameter pipe are:

- Compare water-air flows to previous research based on small diameter pipes to validate experimental design and methodology.

- Investigate the impact of bubble cap geometry on formation of stationary bubble including wake behaviour.

- Investigate the impact of a range of gas and liquid superficial velocities (0.008-0.08 and 0.25-0.33 m/s respectively) on void fraction in wake and bubble geometry.

- Repeat experiments for two oils of high viscosity in direct replacement for water, recording void fraction, bubble geometry and wake characteristics.

- Draw conclusions regarding the impact of viscosity on bubble behaviour.

1.3   Rationale for use of Stationary Taylor Bubble

In the oil industry, the challenge is in predicting the risk of moving slugs in pipelines, with an experimental setting the unsteadiness of slug flow makes accurate and detailed measurement of flow a major challenge.

The front of a slug could be regarded as a propagating, continuously breaking wave, which continuously entrains gas. Since slug flow has two major parts: the Taylor bubble section and the liquid slug section, making one of the parts (Taylor bubble section) stationary is an ideal way of adequately studying a slug flow. Such a study enhances insight into the physical mechanisms of gas entrainment and re-coalescence in a slug flow which will lead to a better prediction of a gas-liquid two-phase flow related to these processes. However, there are some differences between this flow situation and that of an upward slug flow. For instance, in an upward flow, the tube wall is running downwards relative to the slug. Hence, the film velocity relative to the slug in an upward slug flow will be much higher than in this experimental case. Moreover, the turbulence level in a moving slug flow will be different from this experimental work. Riiser et al. (1992) have emphasized that even if this type of situation is not exactly like that

of a slug flow, the advantage of having a standing tail allows accurate measurement of the entrained rate which is always difficult to realize with an advancing slug. Riiser et al. (1992) have a view that the entrainment mechanisms, together with the drift of small bubbles in the slug, control the void fraction. Brauner and Ullmann (2004b) noted that the underlying physical mechanism for the gas entrainment either from a stationary elongated bubble, or from a Taylor bubble in slug flow, are essentially the same. Hence, they concluded that the rate of gas entrainment from the bubble tail is sometimes determined by the rate of turbulent kinetic energy available at the bubble wake from recurrent generation of the surface energy of the entrained bubbles. With all these considerations put together, it is expected that the data obtained from the entrainment measuring part of this work will be close to those obtained from a real slug flow.

A slug flow is commonly classified into two sections: the Taylor bubble section and the liquid slug section (shown in Figure 1.1 (a)). In a typical slug flow for a vertical two-phase flow, the gas in the liquid slug rises through the liquid, coalescing with other gas bubbles within the liquid slug as it rises and then with the Taylor bubble. The liquid passes over the Taylor bubble in the form of a film and runs down the side of the bubble. A wake region forms at the base of the Taylor bubble through liquid film impinging on the Taylor bubble tail. As a result of the impinging film, gas is swept from the Taylor bubble into the slug to form small bubbles; this is known as entrainment. These small bubbles can be seen in Figure 1.1 (a) being part of the liquid slug. Part of these bubbles may re-coalesce at the wake of the Taylor bubble while others disperse into the liquid slug below it. A Taylor bubble can be divided into the nose section and the falling film

part shown in Figure 1.1 (b), with the lower end of the Taylor bubble forming the bubble wake.
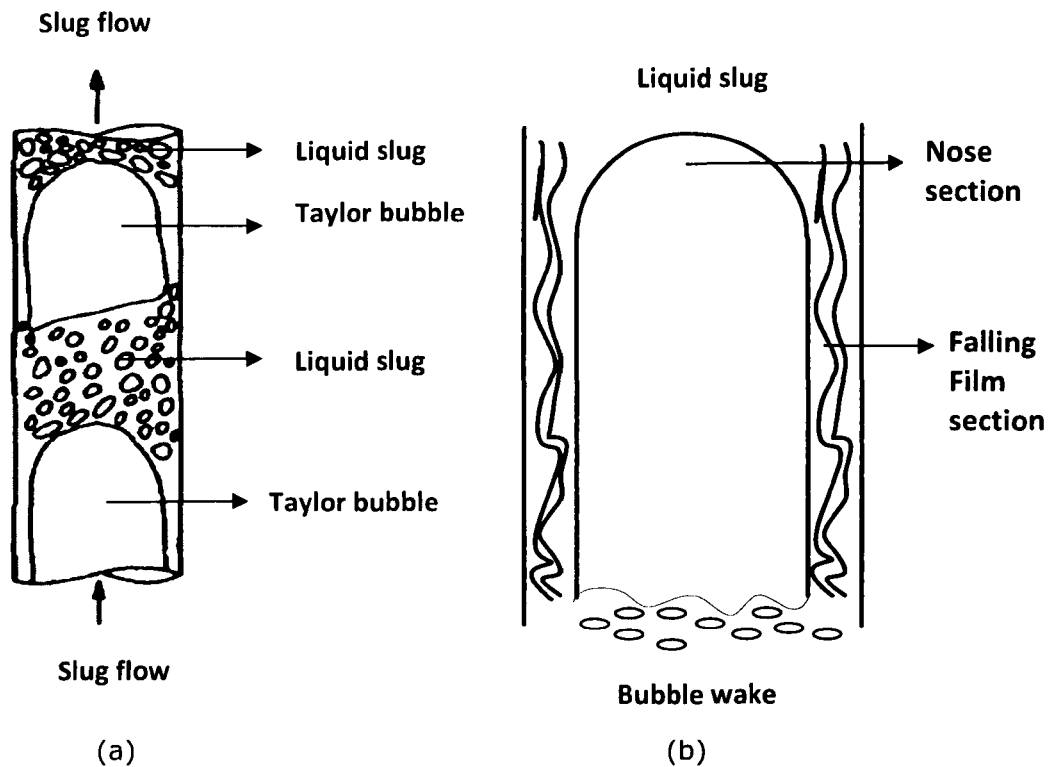
Figure 1.1: A cross section of (a) a typical slug flow (Taitel et al. (1980)) (b) a Taylor bubble showing the nose and the falling film sections

1.4   Structure of Thesis

This thesis is divided into 9 chapters which are described below:

Chapter one gives an introduction to the thesis, with some description of the problems, aims and objectives of the work as well as the structure of the thesis.

Chapter two contains a review of published work on two-phase flows in vertical pipes. In addition, industrial models available for predicting the void fraction and pressure drop are described, with a survey of viscosity effect, film thickness, gas entrainment and recoalescence.

Chapter three describes the experimental apparatus for the research work at SINTEF, Norway; the 127mm diameter rig design, the properties of

fluids used and the technique for measurements of void fraction and differential pressure gradient. This chapter also gives a brief description of the data acquisition software and instrumentation.

Chapter four presents the experimental results obtained on the 127mm diameter pipe carried out at SINTEF using SF_6-oil, providing a thorough analysis of the results especially comparison of results from the two pressure conditions investigated.

Chapter five describes the experimental facility for the research work at the Nottingham laboratory with the rig design, properties of the fluid used and method of data acquisition. The results are reported in Chapters 6 and 7.

Chapter six gives the detail of the results and analysis of the on air-water experiment.

Chapter seven presents the experimental results using the Laser Focal Displacement Meter (LFDM) for liquid film thickness measurements. Results are also compared with published work.

Chapter eight presents the experimental results and analysis of air-oil data using two oils of different viscosities. The analysis includes comparison with the air-water experiments from chapter 6 hence providing analysis of the impact of viscosity.

Chapter nine brings together all the key conclusions from this work. Recommendations for further work are also provided.

Chapter Two
Literature Survey

2.1   Introduction

The work within this thesis describes investigations of two-phase gas-liquid flow for liquids of high viscosity in both small and large diameter pipes. The need for this research is driven by practical needs and fills a gap in knowledge, as identified within this chapter. This review also draws out existing knowledge which was used to establish methodology and provide validation with the limited data that exists within the open literature. This literature survey first presents an overview of flow patterns occurring in vertical gas-liquid flows which also includes flow pattern maps. Later, it identifies efforts by previous researchers on proposing prediction models for void fraction as well as models for transition from one flow regime to another. This is then followed by an overview of entrainment and recoalescence as well as a brief literature on effect of viscosity. Lastly, the survey ends with falling film thickness measurement

2.2   Gas-Liquid flow patterns

Two-phase flows through vertical, horizontal or inclined pipes adopt flow patterns that vary depending on pipe geometry and orientation. Although most of the flow regime studies on gas–liquid two-phase flow have dealt with either horizontal or vertical tubes using low viscosity liquids in vertical flows, there are limited results that have been reported for high viscosity liquids in vertical flows especially as it affects entrainment of gas (for instance, Su and Metcalfe (1997)). Before the work on high viscosity liquid that

exists is described, there is need to briefly summarize the types of flows seen within two phase vertical flow.

2.2.1   Vertical gas-liquid flows

Azzopardi (2006) identified the major flow patterns in a vertical gas-liquid flows as bubbly, slug, churn and annular flows as can be seen in Figure 2.1. The change of flow patterns occur when the conditions of flow are altered. For instance, if a system starts with a single phase liquid flow through pumping of the liquid into a vertical pipe and then gas is injected into the lower end of the pipe, bubble flow occurs. When the gas flow rate is further increased while the liquid flow rate remains constant, the flow pattern changes, which results into a slug flow. This is attributed to the coalescence of the small bubbles in the previously formed bubbly flow. Again, when the flow rate of the gas is increased further, the flow pattern changes again to what is called churn flow. This results from the deformation of the agglomerated bubbles because of instability in the flow. If the gas flow rate is increased further, annular flow is formed. A brief description of each flow pattern will be discussed further.

Other authors like Dziubinski et al. (2004) have proposed different flow patterns as shown in Figure 2.2. The major addition to the flow pattern proposed by Dziubinski et al. (2004) is the presence of froth flow (F) and dispersed flow (D). In some cases, slug and churn flow regions are classified as intermittent flows with the flow pattern map shown in Figure 2.3 as described by Ali (2009)
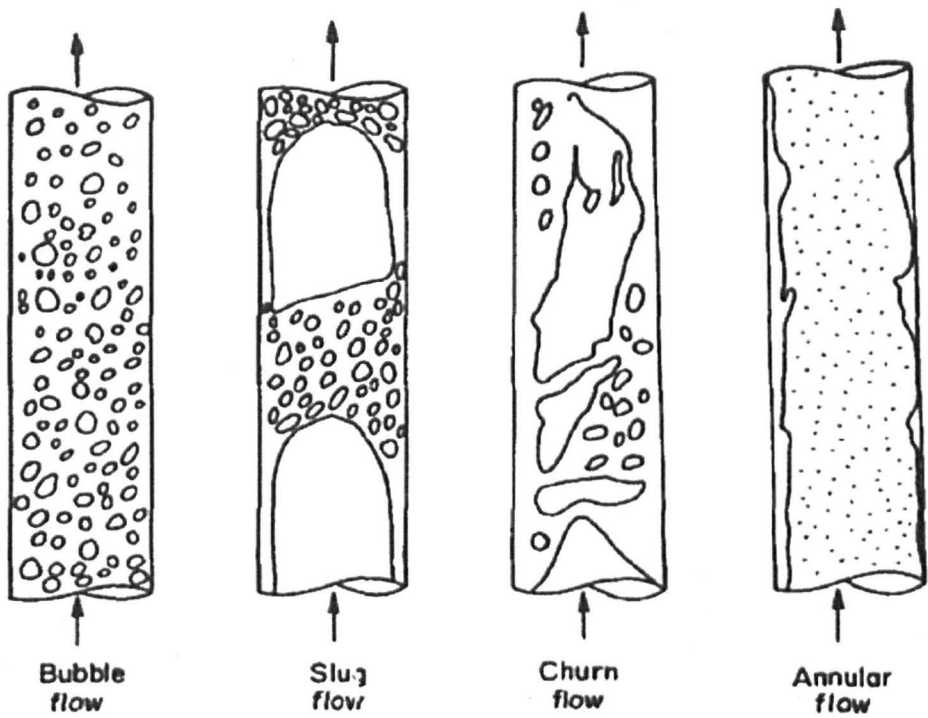
Figure 2.1: Flow patterns in vertical flow (Taitel et al. (1980))

B   S   F   A   D
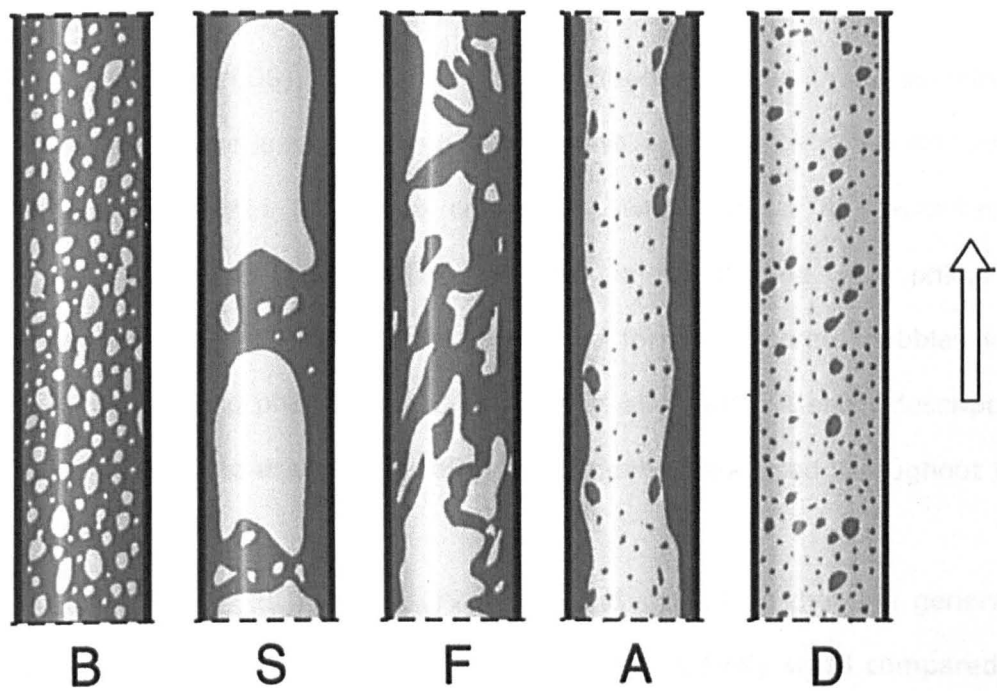
Figure 2.2: Basic flow structures in vertical upward flow: B–bubble flow,

S–slug flow, F–froth flow, A–annular flow, D–dispersed flow Dziubinski et al.

(2004)
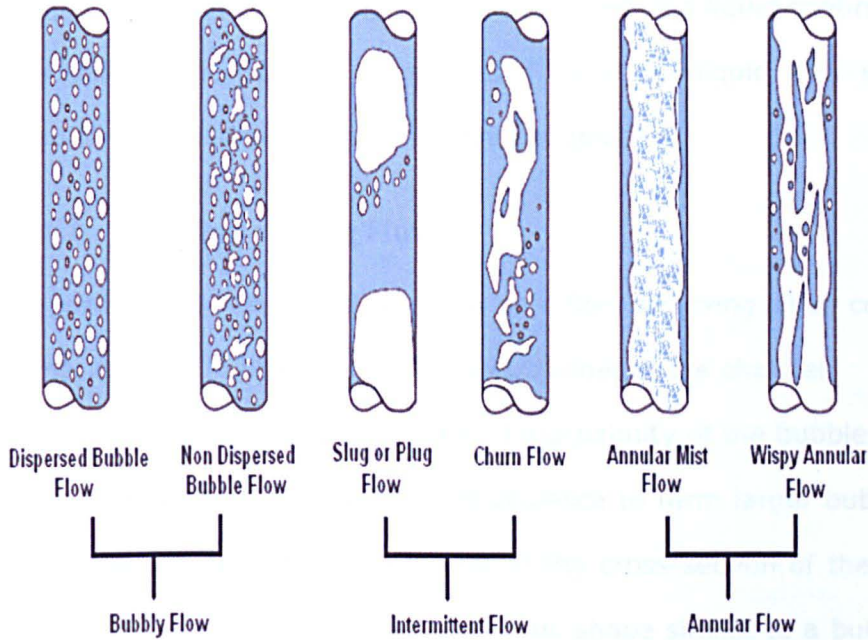
Figure 2.3: Flow pattern shown in Ali (2009)

2.2.1.1   Bubbly Flow

In Azzopardi (2006), bubbly flow is described as a two-phase system of flow where there is a continuous liquid phase with the gas phase dispersed as bubbles within the liquid continuum, while Hewitt and Hall-Taylor (1970) describes bubbly flow as one in which the gas phase is approximately uniformly distributed in the form of discrete bubbles in a continuous liquid phase as cited in Taitel et al. (1980). A short description is given below to establish a definition of bubbly flow used throughout the thesis.

In bubbly flow, gas bubbles vary in size and shape and they are generally non-uniform (Figure 2.1). However, they are relatively small compared to the diameter of the tube in which they are formed. These bubbles rise within the liquid due to buoyancy. They gather together at the centre of the pipe in some instances while they are distributed near the wall of the pipe in other instances. Two sub-regimes are derived from bubbly flows which are termed as "discrete bubble" and "dispersed bubble". Discrete

bubbles are small bubbles which are suspended in a liquid continuum while dispersed bubble flow is characterised by a gas-liquid flow where one phase is dispersed in the other continuous phase.

2.2.1.2   Slug or Plug Flow

Azzopardi (2006) described slug flow as a flow occurring when coalescence begins, and the bubble size tends towards that of the channel.

With an increasing gas void fraction, the proximity of the bubbles becomes closer such that bubbles collide and coalesce to form larger bubbles; with the bubble size tending towards that of the cross-section of the pipe. The front of these bubbles has a characteristic shape similar to a bullet, with a hemispherical nose and a blunt tail end. These bubbles are commonly referred to as "Taylor bubbles" or in some cases, "Dumitrescu bubbles" as can be seen in Figure 2.4.

Hemispheral bubble nose
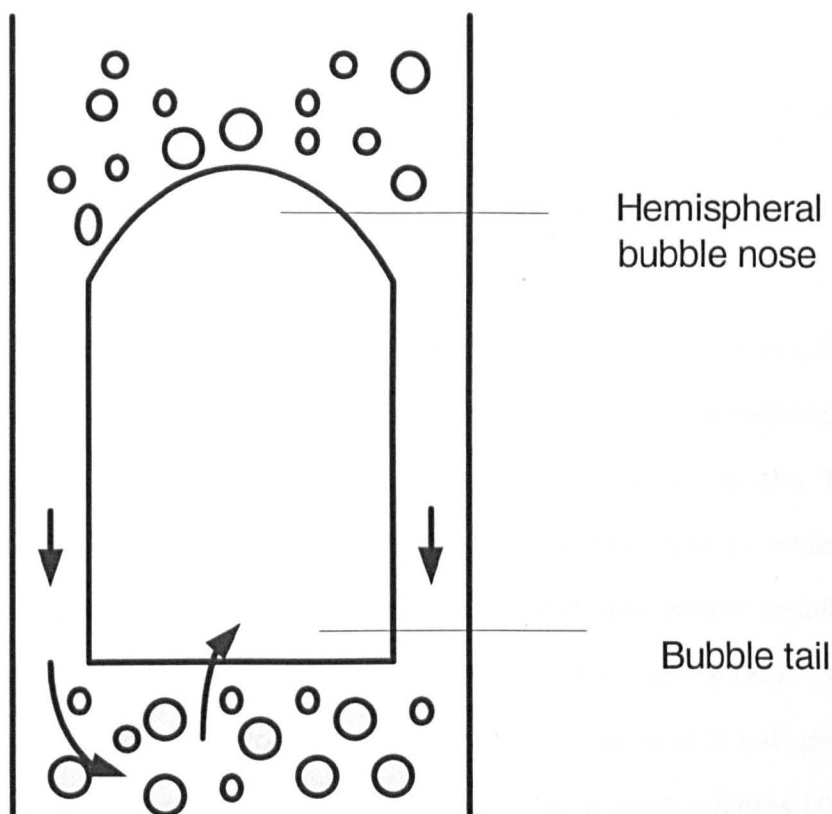
Bubble tail

Figure 2.4: A typical Taylor bubble showing the nose and the tail section

The Taylor bubbles are separated from one another by "slugs"` of liquid which have small bubbles present within them. The behaviour of the entrained gas travelling in-between the Taylor bubbles is not well understood. Taylor bubbles are surrounded by a thin liquid film which forms between the gas bubble and the wall of the pipe. These films may flow downward due to the force of gravity even though the net flow of fluid is upward. Therefore, slug flow displays *intermittency* in the flow direction, which results in a significant change in the shear stress/frictional pressure gradient, resulting in negative values that are not consistent with some correlations. Further details on these films will be discussed in the later part of this Chapter (section 2.13).

Slug flow patterns have been argued to be absent in large diameter pipes. (for instance Omebere-Iyari (2006), Sharaf (2011), Ali and Yeung (2013)) although Pioli et al. (2012) showed its presence in very large diameter pipes using very high viscosity liquids (with μ=200Pa.s). Part of this research will demonstrate this argument as will be illustrated in Chapters 3 and 4.

2.2.1.3   Churn flow

For churn flow, Azzopardi (2006) reported that the Taylor bubbles in slug flow at higher velocities break down into an unstable pattern in which there is a churning or oscillatory motion of liquid in the tube. The procedure involves increasing the superficial gas velocity which enables the structure of the flow to become unstable which results in the breakdown of the Taylor bubbles. The gas-liquid flow mixture travels up and down in an oscillatory or churning motion, but with a net upward flow. This type of flow is characterised by irregular shaped bubbles (Figure 2.1) which results from the instability of the Taylor bubbles. This flow pattern is

in fact an intermediate flow pattern between the slug and annular flow regimes.

Churn flow is an important pattern, which often covers a fairly wider range of gas flow rates than other flow regimes. At the lower end of the range (i.e. at low gas flow rates of churn flow), the flow may be regarded as a broken-up form of slug flow, with occasional bridging of the tube by the liquid phase. At the higher end of the range, churn flow may be considered as a degenerate form of annular flow, with variation in the direction of the film flow and very large waves being formed on the interface. In this higher range which has close proximity to annular flow, the term "semi-annular flow" has sometimes been used to describe this. Previous studies have shown that a mechanistic description of the gas-liquid interaction in the churn flow regime is very difficult, hence the flow remains the least understood, as reported by Van Der MeuLen (2012).

2.2.1.4   Annular Flow

For annular flow, Azzopardi (2006) described this configuration as being characterised by liquid travelling as a film on the channel walls whereas Hewitt and Hall-Taylor (1970) described annular flow as a flow which is characterized by the continuity of the gas phase along the pipe in the core. As soon as the interfacial shear of a high gas velocity on the liquid film interface becomes dominant over the gravitational force, the liquid is expelled from the centre of the tube and flows as a thin film on the wall of the pipe which forms an annular ring of liquid thereby "wetting" the wall. The gas flows concurrently with the liquid as a continuous phase up the centre of the tube. The interface between the gas and the liquid is disturbed by high frequency waves and ripples (in Figures 2.1 and 2.2). Waves are formed on the surface of the liquid film and the amplitude of the waves increases as the gas velocity increases. Liquid may also be

entrained in the gas core in the form of small droplets, and the fraction of liquid that is entrained may be balanced by the re-deposition of droplets from the gas core onto the liquid film. The liquid phase is always moving upwards, whether as droplets or as a film, which is the main difference between annular flow and churn flow, although there is a continuous gas core in both flow patterns.

2.2.1.5   Wispy-Annular Flow

Bennett et al. (1965) were the first authors to first identify this unusual flow pattern. A further increase in the flow rate for annular flow will result in the formation of large liquid objects within the gas core which are referred to as "wisps". Hewitt and Roberts (1969) have classified this as a separate flow pattern while other flow maps rarely mention it. For instance, Hawkes et al. (2000) suggested that the observed wisps may have arisen from agglomeration of the drops that are present in large concentrations within the gas core. Under some circumstances, bubbles of gas may be entrained in the liquid film.

2.3   Flow pattern maps

The range of conditions that particular flow structures present are illustrated in diagrams often called the flow maps. Authors including Hewitt and Roberts (1969) identified flow pattern from visual observation at the initial stages of research into two-phase flows. Hewitt and Roberts (1969) came up with a flow pattern map plotted on the liquid momentum flux against gas momentum flux as shown in Figure 2.5. Since this map is based on visual observation, it is assumed to provide subjective information.

Taitel et al. (1980) developed a flow pattern map which appears to be the most commonly used flow pattern map with coordinates of liquid superficial velocity and gas superficial velocity. This is shown in Figure 2.6 for a map for air/water mixture in a 50mm diameter tube. Many other flow pattern maps nevertheless exist such as the mechanistic map by Shoham (2006) which is able to illustrate the flow pattern for all pipe orientations. The map also takes into consideration the fluid properties. This is depicted in Chapter 3 for the high viscosity liquid and high gas density used.
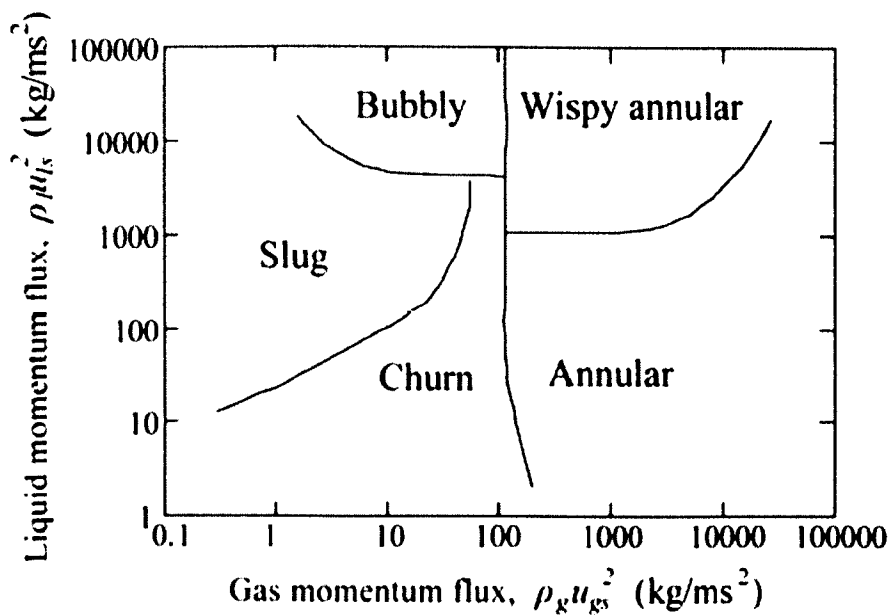
Figure 2.5: Flow pattern map of Hewitt and Robert (1969)
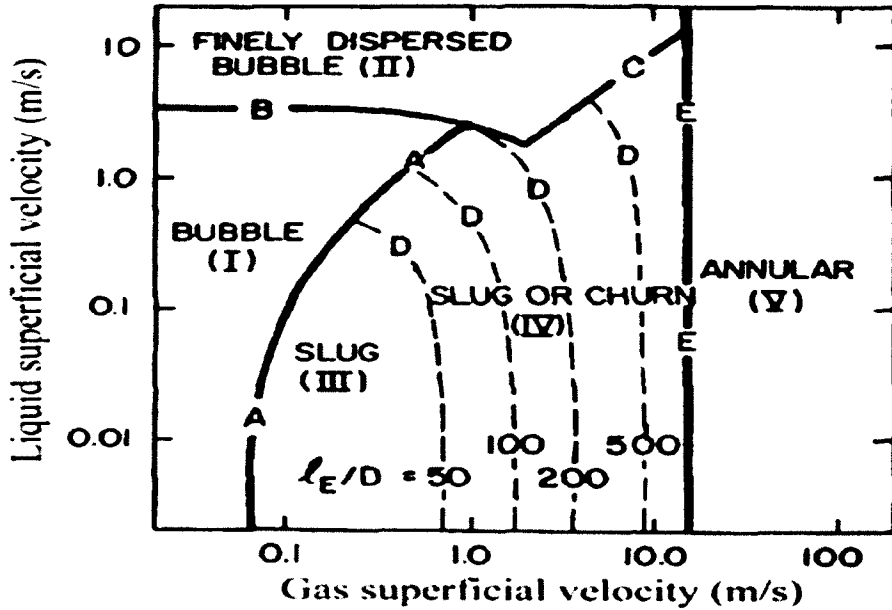
Figure 2.6: Flow pattern map of Taitel et al. (1980)

2.4 Flow pattern identification: void fraction

measurements

Costigan and Whalley (1997) identified six flow patterns by examination of void fraction traces and PDFs as shown in Fig 2.7. This method of using PDF has proved to be very vital in establishing flow regimes. This is also applied in analysing results in the current study.

Furthermore, based on their identification of flow regimes from Figure 2.8, the same methodology was employed for data in the current study which show the data points plotted using Shoham mechanistic map illustrated in Chapter 3.
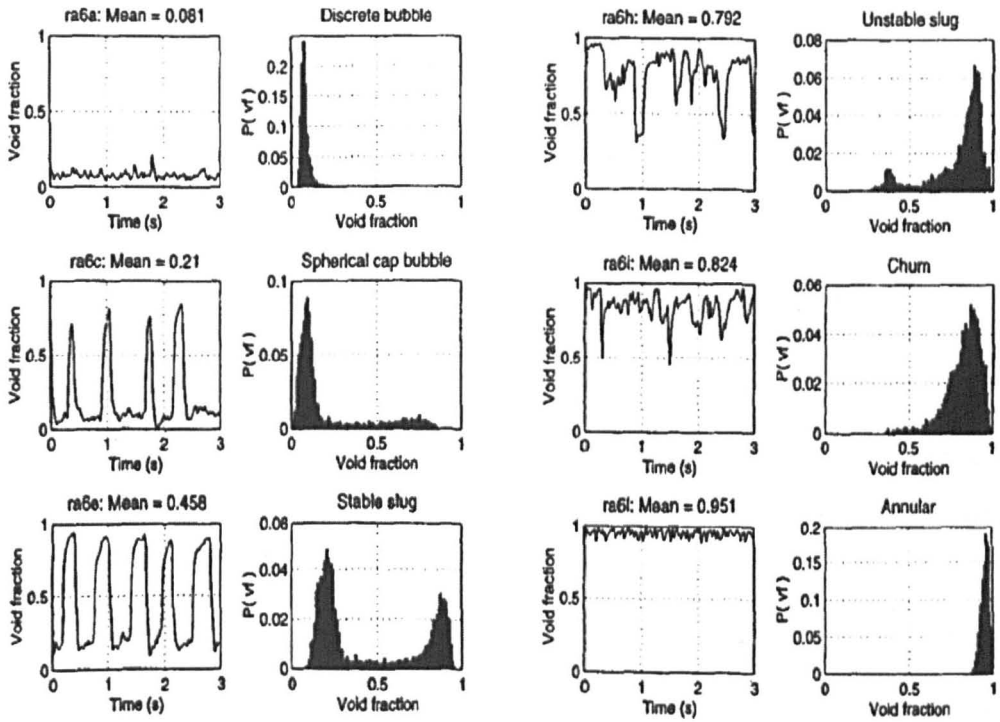
Figure 2.7: Typical void fraction traces and their PDFs Costigan and Whalley (1997)
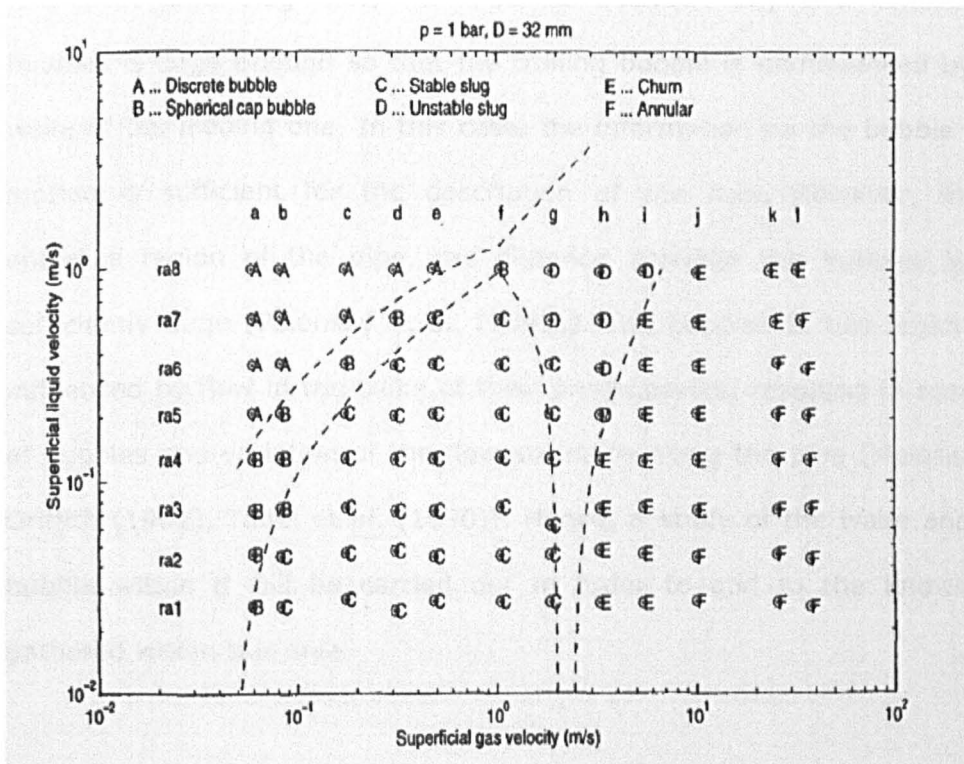
Figure 2.8: Data points on flow map Costigan and Whalley (1997).

Having established definitions for all of the flow types, slug flow will now be reviewed in more depth as this is the critical flow regime for the current study.

2.5   Slug flow and its Characteristics

Slug flow exists over a broad range of gas and liquid flow rates and is encountered in a wide variety of industrial applications like oil and gas wells, process vaporizers and gas-liquid pipeline reactors (Nigmatulin and Bonetto (1997)).

In developed slug flow, the Taylor bubbles occupy most of the pipe cross-section and move upward with a constant velocity. The liquid around the elongated bubbles moves downward as a thin falling film. The liquid velocity in the film is usually several times larger than the mean velocity of the liquid in the slug. Each slug sheds liquid in its tail to the subsequent film, which accelerates as it moves downward (Talvy et al. (2000)). For a fully developed slug flow, the distance between any two consecutive bubbles is large enough so that the trailing bubble is uninfluenced by the wake of the leading one. In this case, the information on the bubble nose motion is sufficient for the description of the flow. However, in the entrance region of the pipe, the distance between the bubbles is not sufficiently large (Polonsky et al. (1999)). The bubbles in this region are influenced by flow in the wake of their predecessors, resulting in merging of bubbles and variation of the flow structure along the pipe (Moissis and Griffith (1962), Taitel et al. (1990)). Hence, a study of the wake and the bubble within it will be carried out in order to add to the knowledge gathered within this area.
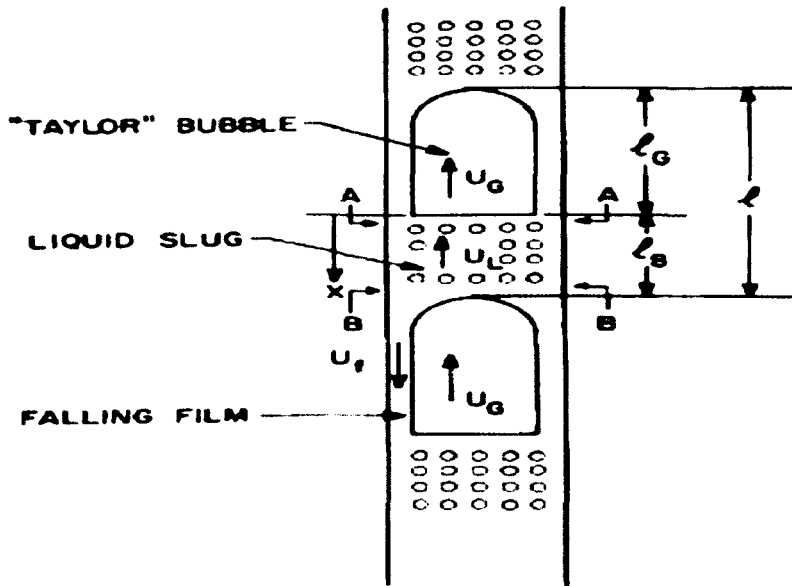
Figure 2.9: Schematic description of slug flow geometry (Taitel et al. (1980))

Considering two consecutive Taylor bubbles, as can be seen in Fig 2.9, the first (top) bubble will move at a velocity given by Nicklin et al. (1962) relation:

$$u_g = 1.2u_l + 0.35\sqrt{gD} \tag{2.1}$$

According to Taitel et al. (1980), the second (lower) bubble will move at the same speed when the slug length, *ls*, (in Figure 2.9) is long enough so that the velocity profile in the liquid at the front of the second bubble will be the same as that at the front of the first bubble, namely, the average velocity is u_l and the centreline velocity is $1.2u_l$

Moissis and Griffith (1962) measured the velocity profiles in the wake of a stationary plastic 'bubble'. This simulation has some shortcomings. The rigid boundary of the plastic model does not represent the free-surface boundary of the gas bubble. In addition, the flow conditions in their experiments are different from those in a real slug flow where the gas bubble moves relative to the pipe walls.

The rise of a single bubble in stagnant and moving liquid in a vertical pipe has been studied by numerous researchers, both theoretically Dumitrescu (1943); Davies and Taylor (1949); Goldsmith and Mason (1962); Collins et al. (1978) Zukoski (1966), Mao and Dukler (1990) and experimentally White and Beardmore (1962). Most of the data are related to the flow around the nose of the bubble. The interest in gas entrainment from stationary large bubbles attached to spargers emerges from two diverse routes. One is related to the design and performance of circulating bubble columns while the other is to get insight into the gas entrainment process from the Taylor bubbles in a gas–liquid slug flow. In real slug flow, measurements of the gas entrainment into the liquid slug are complicated due to the fast movement of the Taylor bubbles and the intermittency in the flow as reported by Brauner and Ullmann (2004b).

In slug flow, gas is often entrained from the large elongated gas bubble into the liquid slug and this is thought (if not taken for granted) to have a significant effect on the slug behaviour. It is hence desirable to understand and model this phenomenon in order to understand its impact as well as to improve the accuracy of the prediction of slug characteristics (Bonizzi and Issa (2003)). In achieving this, it is imperative to understand the principle of gas exchange between the Taylor bubble and its liquid slug and this is therefore the subject of chapters 5 and 6 for water-air and 8 for oil-air, introducing the impact of viscosity into this study.

2.6   Models for transition between flow

regimes

Since a flow pattern map may be constructed either experimentally or theoretically, many researchers have proposed theoretical models for the

transition from a flow regime to another by considering the inter-phase characteristics between these regimes. The common flow regime inter-phases are bubble to slug, slug to churn, churn to annular and bubble-slug-churn to dispersed bubble transitions.

The combined flow pattern boundary is shown in Figure 2.10 which includes the boundaries by various workers for pipe diameters less than 100mm.
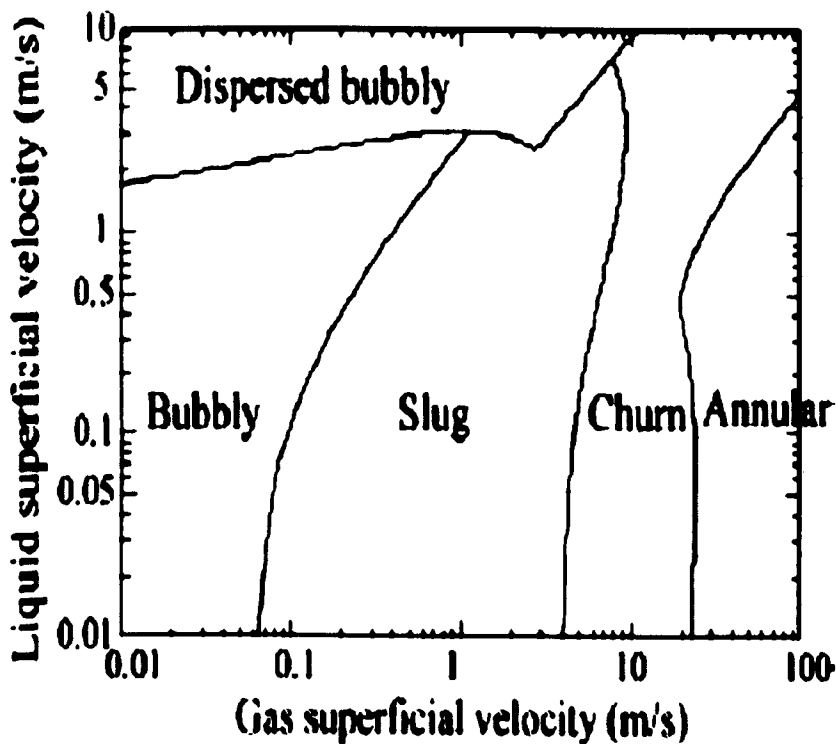
Figure 2.10: Combined flow pattern map for pipes with diameter less than 100mm (Bubble-to-slug: Taitel et al. (1980), Slug to churn: Jayanti and Hewitt (1992), Churn to annular: Barnea (1986), intermittent to dispersed bubble: Taitel et al. (1980), Barnea (1982))

2.6.1   Bubble to slug flow transition

The relationship between bubble coalescence caused by agglomeration and break-up by turbulence is key to the transition from bubbly-slug flow.

Radovcich and Moissis (1962) investigated the frequency of bubble collision and found out that a rapid increase occurs at a void fraction of ε_g > 0.2. Taitel et al. (1980) employed the critical void fraction, which they suggested at ε_{gc} = 0.25, for transition from bubble to slug flow regime. The transition equation is given by using the terminal velocity of a large bubble, U_0,

$$u_{ls} = \frac{1 - \varepsilon_{gc}}{\varepsilon_{gc}} u_{gs} - (1 - \varepsilon_{gc})U_0 \qquad (2.2)$$

In a correlation by Harmathy (1960), U_o is given by

$$U_o = 1.53 \left[\frac{(\rho_l - \rho_g) g \sigma}{\rho_l^2} \right]^{0.25} \qquad (2.3)$$

Song et al. (1995) used a 25mm diameter pipe to propose the following correlation for bubble flow,

$$\varepsilon_{gc} = 0.55 - 2.37(\frac{D_b}{D_t}) \qquad (2.4)$$

An extension to this work for a larger diameter pipe was done by Azzopardi (2006) through assessing the data from Cheng et al. (2002) in a 29 mm pipe and Guet et al. (2002) in a 72 mm pipe.

2.6.2   Slug to churn flow transition

A review of the slug to churn transition was done by Jayanti and Hewitt (1992) which assessed models based on four different mechanisms: Dukler and Taitel (1986)'s entrance effect; McQuillan and Whalley (1985)'s flooding; Kaichiro and Ishii (1984)'s wake effect and Brauner and Barnea (1986)'s bubble coalescence. In effect, Jayanti and Hewitt (1992) presumed that the flooding mechanism is the most closely related to the slug-churn transition. They made two major improvements to the model

by McQuillan and Whalley (1985). First, the correlation by Broz (1954) was employed in place of Nusselt (1916) relationship for the film flow rate surrounding Taylor bubbles, due to its wide range of applicability (Fulford (1964)). Secondly, the effect of Taylor bubble length on flooding velocity was additionally considered. The model gives relatively good prediction for a pressurised system that was assessed by Watson and Hewitt (1999) up to 5 bara.

2.6.3   Bubble-slug-churn   to   dispersed   bubble   flow transition

At a high liquid flow rate, there is an increase in the rate of bubble break-up. This is due to turbulence and the transition to the slug flow is suspended leading to a dispersed bubble regime as shown in Figure 2.9. Taitel et al. (1980) derived the correlation for transition to dispersed bubble flow by using the maximum stable bubble diameter proposed by Hinze (1955).

Taitel et al. (1980) suggested a maximum volumetric packing at $\varepsilon_g = 0.52$ which can be the transition to the dispersed bubbly flow.

$$u_{ls} = \left(\frac{1 - \varepsilon_g}{\varepsilon_g} \right) u_{gs} = 0.923 u_{gs} \qquad (2.5)$$

2.6.4   Churn to annular flow transition

The critical condition of a sufficiently high gas velocity to keep the entrained droplets suspended was suggested by Taitel et al. (1980). From the force balance for a droplet, the following result could be inferred:

$$\frac{1}{2} C_D \frac{\pi D_d^2}{4} \rho_g u_g^2 = \frac{\pi D_d^3}{6} g \Delta \rho \qquad (2.6)$$

A correlation by Hinze (1955) was used to predict the maximum stable drop size:

$$D_d = \frac{We_c \sigma}{\rho_g u_g^2}$$
(2.7)

The churn to annular transition is expressed from the combination of equations (2.6) and (2.7) by using critical Weber number, $We_c = 30$ and Drag coefficient, $C_D = 0.4$ as suggested by Turner et al. (1969) in the Kutateladze number which is given in equation (2.19):

$$Ku = \frac{u_{gs}\sqrt{\rho_g}}{\left[\sigma g (\rho_l - \rho_g)\right]^{0.25}} = 3.1$$
(2.8)

Barnea (1986) suggested a churn-to-annular transition for all ranges of pipe inclinations with two mechanisms considered to cause the transition. These mechanisms are the instability of liquid film and the blockage at wave crest due to large water accumulation.

2.7   Models for void fraction

Void fraction models are currently being used in oil and gas industries to predict void fraction especially when the results may be needed to ensure continuous flow of gas and liquid from the reservoir. Some of these models perform well for predicting void fraction. These models have been compared with data from experimental campaigns described in Chapter 4 (section 4.2.3)

2.7.1   Homogeneous and Separated flow model

The homogeneous model is based on the assumption that one phase is dispersed with the other phase continuous and that both phases flow move with the same velocity, whereas a separated model considers the slip

velocity U_R (defined by $\dfrac{u_g}{u_l}$) between the phases. From the mass balance of

each phase of the fluid, void fraction can be expressed as:

$$\varepsilon_g = \frac{1}{1 + U_R \dfrac{\rho_g\left(1 - x_g\right)}{\rho_l x_g}} \tag{2.9}$$

Several correlations have been reported for U_R, (for instance Chisholm

(1972), Premoli et al. (1970)). The simple correlation given by Chisholm

(1972) gives a relatively good prediction as follows:

$$U_R = \left[1 - x_g\left(1 - \frac{\rho_l}{\rho_g}\right)\right]^{0.5} \tag{2.10}$$

While Premoli et al. (1970) at CISE suggested the following equation:

$$U_R = 1 + E_1\left(\frac{j}{1 + E_2 j}\right)^{0.5} \quad \text{for} \quad \frac{j}{1 + E_2 j} > E_2$$

$U_R = 1$ for other conditions, $\tag{2.11}$

where $j = \dfrac{\varepsilon_{gH}}{1 - \varepsilon_{gH}} \quad j = \dfrac{\varepsilon_{gH}}{1 - \varepsilon_{gH}}$ $\tag{2.12}$

$$E_1 = 1.578 \, Re^{-0.19}\left(\frac{\rho_l}{\rho_g}\right)^{0.22} \quad \text{and} \tag{2.13}$$

$$E_2 = 0.0273 We. \, Re^{-0.51}\left(\frac{\rho_l}{\rho_g}\right)^{-0.08} \tag{2.14}$$

Here, Reynold, Re and Weber, We numbers used are defined as

$$Re = \frac{\left(\dot{m}_g + \dot{m}_l\right) D_t}{\eta_l} \quad \text{and} \tag{2.15}$$

$$We = \frac{\left(\dot{m}_g + \dot{m}_l\right)^2 D_t}{\sigma \rho_l} \tag{2.16}$$

2.7.2   Drift-flux model

Zuber and Findlay (1965) proposed the following correlation for the mean gas velocity using mixture velocity and drift velocity v_{gd} as follows:

$$\frac{u_{gs}}{\varepsilon_g} = C_o u_m + v_{gd} \tag{2.17}$$

C_o and v_{gd} can be identified by plotting the results on the $\dfrac{u_{gs}}{\varepsilon_g}$ versus u_m.

2.7.3   Direct correlations

Beggs and Brill (1973) proposed a correlation based on the air/water experimental data obtained from their 25 to 38mm diameter pipes at several inclination angles. The correlation depends on the flow pattern, input liquid content, $\lambda = (1 - \varepsilon_{gH})$ and inclination angle, β:

$$\varepsilon_g = 1 - \varepsilon_1(0)\left[1 - C_{B4}\left(\sin 1.8\beta - 0.333\sin^3 1.8\beta\right)\right] \tag{2.18}$$

$$\varepsilon_1(0) = \frac{C_{B1}\left(1 - \varepsilon_{gH}\right)^{C_{B2}}}{Fr^{C_{B3}}} \tag{2.19}$$

$$Fr = \frac{\left(u_{gs} + u_{ls}\right)^2}{gD_i} \tag{2.20}$$

Table 2.1: Constants for Beggs and Brill correlation

Constants	Fr<L$_1$ (Segregated)	L$_1$<Fr<L$_2$ (Intermittent)	Fr>L$_1$,L$_2$ (Distributed)
C$_{B1}$	0.98	0.845	1.065
C$_{B2}$	0.4846	0.5351	0.5824
C$_{B3}$	0.0868	0.0173	0.0609
C$_{B4}$ (upflow)	Eq (2.32)	Eq (2.34)	0
C$_{B4}$ (downflow)	Eq (2.33)	Eq (2.33)	Eq (2.33)

$$C_{B4} = \varepsilon_{gH} \ln \left[\frac{0.011 N_{lv}^{3.539}}{\left(1 - \varepsilon_{gH}\right)^{3.768} Fr^{1.614}} \right] \qquad (2.21)$$

$$C_{B4} = \varepsilon_{gH} \ln \left[\frac{4.7 N_{lv}^{0.1244}}{\left(1 - \varepsilon_{gH}\right)^{0.3692} Fr^{0.5056}} \right] \qquad (2.22)$$

$$C_{B4} = \varepsilon_{gH} \ln \left[\frac{2.96 \left(1 - \varepsilon_{gH}\right)^{0.305} N_{lv}^{0.0978}}{Fr^{0.4473}} \right] \qquad (2.23)$$

$$N_{lv} = u_{ls} \left(\frac{\rho_l}{g\sigma} \right)^{0.25} \qquad (2.24)$$

$$L_1 = \exp\left(-4.62 - 3.757 X_b - 0.481 X_b^2 - 0.0207 X_b^3\right) \qquad (2.25)$$

$$L_2 = \exp(1.061 - 4.602 X_b - 1.609 X_b^2 - 0.179 X_b^3 + 0.000635 X_b^5) \qquad (2.26)$$

$$X_b = \ln\left(1 - \varepsilon_{gH}\right) \qquad (2.27)$$

2.8   Models for pressure gradient

2.8.1   Lockhart-Martinelli parameter

Two-phase frictional pressure gradient was predicted by Lockhart and Martinelli (1949) using two-phase multiplier,

$$\phi_l^2 = \frac{(\Delta p / \Delta z)_{TP}}{(\Delta p / \Delta z)_l} \qquad \phi_g^2 = \frac{(\Delta p / \Delta z)_{TP}}{(\Delta p / \Delta z)_g} \qquad (2.28)$$

These parameters were correlated with a dimensionless parameter X (shown in Figure 2.10),

$$X = \sqrt{\left(\frac{\Delta p}{\Delta z} \right)_l \bigg/ \left(\frac{\Delta p}{\Delta z} \right)_g} \qquad (2.29)$$

In Figure 2.11, the subscripts tt, vt, tv and vv represents viscous and turbulent flow for liquid and gas phase respectively.

Chisholm and Laird (1958) suggested the equations for this relationship given by

$$\phi_l^2 = 1 + \frac{C}{X} + \frac{1}{X^2}$$ (2.30)

For the turbulent-turbulent case, which can be applied to most cases, Chisholm and Laird (1958) suggested $C = 21$.

Overall models give good prediction for the first step; however there still exists significant error. Hence, an understanding of the detailed flow structure is necessary to develop the physically-based model for a specific flow pattern.
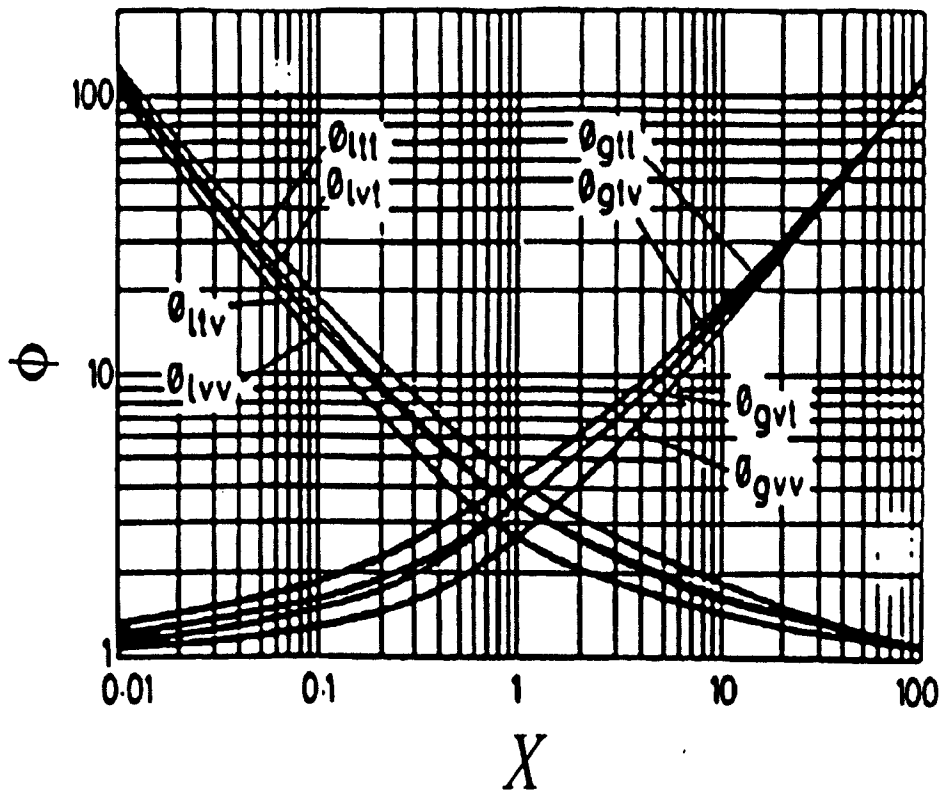
Figure 2.11: Two-phase multiplier versus Lockhart- Martinelli parameter

2.8.2   Slug flow models

Models for slug flow were proposed by Fernandes et al. (1983), Sylvester (1987) and de Cachard and Delhaye (1996). Recent work on slug flow modelling by researchers include Benítez-Centeno et al. (2012), Sarica et al. (2011). Brauner and Ullmann (2004a) have developed the idea of considering the entrainment to the liquid slug and investigated the effect of the fluids, flow rates, physical properties, pipe diameters, inclination and Taylor bubble/liquid slug lengths, which they called the Taylor bubble wake model.

A schematic diagram of the Taylor bubble wake model is depicted in Figure 2.12. Superscripts 'w' and 's' in the liquid indicate slug wake and far wake regions, respectively. Void fraction in the wake region ε_{ls}^{w} is higher than that in the far wake region ε_{ls}^{s}. Since Taylor bubbles move faster than liquid slugs, liquid is shed to the film surrounded by Taylor bubbles.
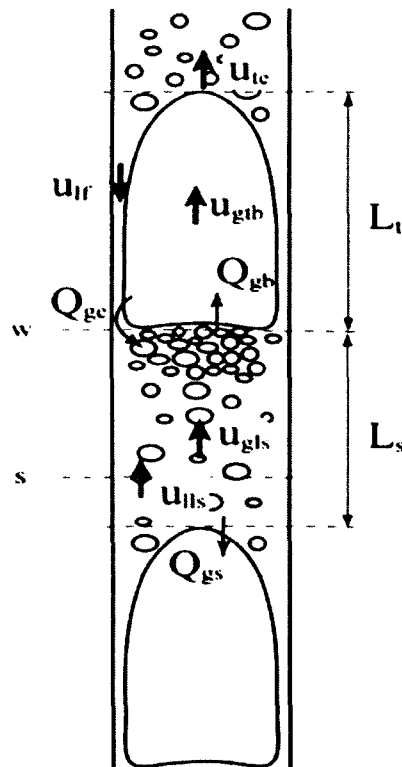
Figure 2.12:   Schematic diagram of the Taylor bubble wake model (Brauner and Ullmann (2004a))

Abolore Abdulahi

When the volumetric flow rate of bubble entrainment from a Taylor bubble Q_{ge} and re-coalescence Q_{gh} to the successive Taylor bubble nose is given, the net gas flow rate $Q_{gs} = Q_{ge} - Q_{gh}$ is released from the Taylor bubble and absorbed into the successive Taylor bubble. This causes Taylor bubble translation velocity, u_{te}, to be higher than the velocity of Taylor bubble u_{gtb}

2.8.3. Churn flow models

One of the difficulties found in churn flow is that its definition is ambiguous. Hewitt and Jayanti (1993) and Barbosa Jr et al. (2001) pointed out the difference on the characteristics of flow structure between churn and slug/annular flow:

• A steep increase of pressure gradient due to the gas/liquid interaction occurs after the breakdown of slug flow. The pressure gradient decreases with the gas superficial velocity. The pressure recovery can be observed in annular flow region (Figure 2.13).

• Periodic reversals of huge waves and liquid film are observed in churn flow, whilst unidirectional film flows in annular flow. The work by Govan et al. (1991) shows the link between the transition from churn flow and capability of creating flooding waves.

• A large amount of entrainment is observed in churn flow due to the huge waves. The entrained fraction decreases with increasing gas flow rate and increases again in annular flow. The difference of entrainment mechanism was found by Azzopardi (1983).
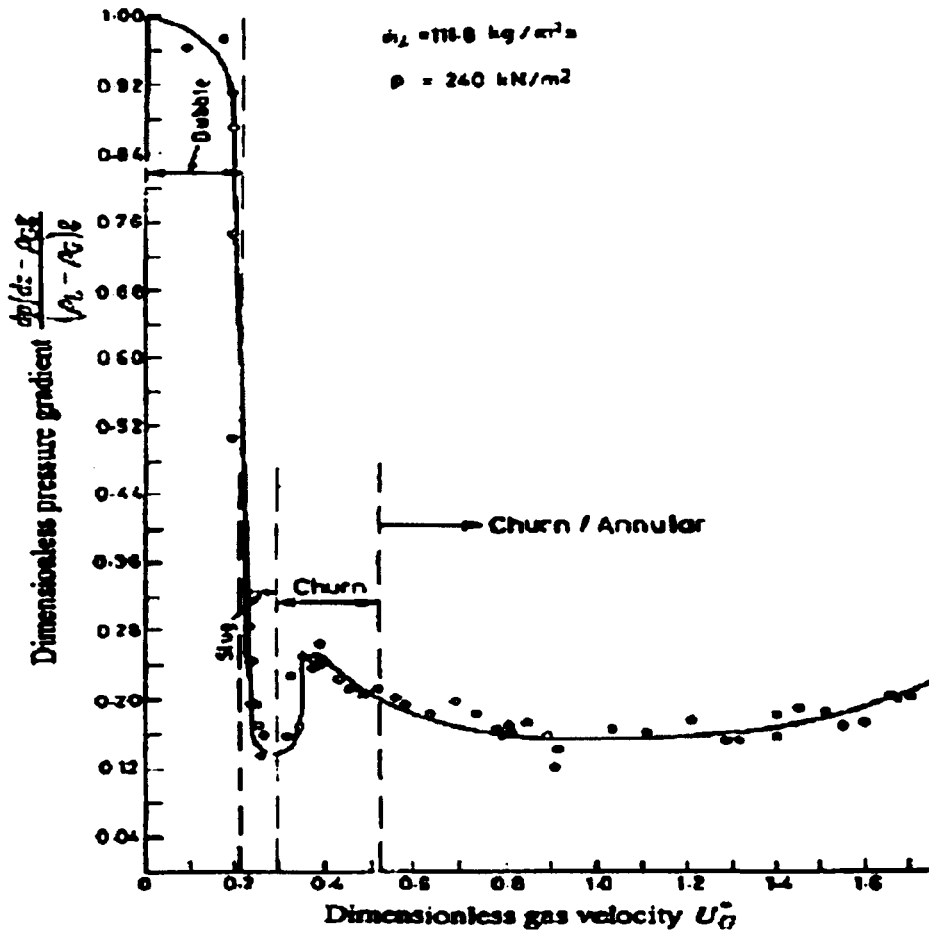
Figure 2.13: Dimensionless pressure gradient against dimensionless gas velocity by Owen (1986)

The plot shown by Owen (1986), described in Figure 2.13, shows a decreasing $\frac{dp}{dz}$ in the bubble to slug region, while the slug to churn region shows an increasing pressure gradient. However, this plot does not show an increasing pressure gradient for large diameter pipes, since slug flows do not occur in such pipes. This is shown in Chapter 4 (section 4.3)

2.9   Entrainment in Taylor bubbles' wakes

Entrainment is the process of gas loss from the rear of a Taylor bubble, which results in small gas bubbles in the liquid slug. According to Kockx et al. (2005), the first step in the entrainment process is a transition from a

smooth to a rough free surface of the falling liquid film along the Taylor bubble. Kockx et al. (2005) observed that only after this roughness or waves appeared on the free surface, gas entrainment increased perceptibly. Hence they concluded that entrainment is assumed to be caused by the fact that the free surface of the liquid pool is not capable of responding to the (transverse) oscillations of the incoming film as schematically shown in Figure 2.14.
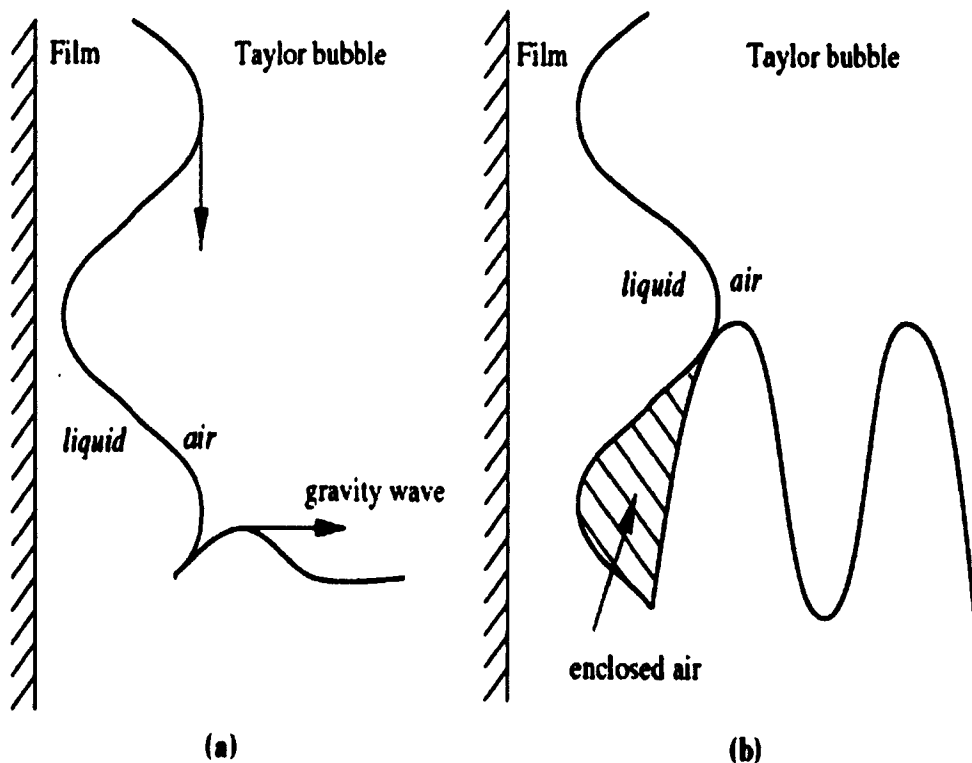
Figure 2.14: Entrainment mechanism at the bottom of the Taylor bubble due to distortions on the falling liquid film Kockx et al. (2005)

The aspects of the entrainment in Fig 2.14 above have been described by Kockx et al. (2005) as follows: When a wave on the film surface approaches the pool it generates a gravity wave, which propagates on the pool surface as shown in Fig 2.14 (a). When the slope of the induced gravity wave is large enough and the waves on the film surface travel fast enough, the crest of the gravity will contact the next wave on the film surface and air will be enclosed as can be seen in Fig 2.14 (b).

Delfos et al. (2001b) suggested that entrainment could only occur when the intensity of the turbulent velocity fluctuations in the film is sufficiently strong to provoke it. Hence they affirmed that the entrainment rate is proportional to both the velocity with which the film flow enters the Taylor bubble wake, and the intensity of the turbulent velocity fluctuations in the film. In their concept, for short Taylor bubble length, L_{TB}, the entrainment process is governed by the turbulence present in the flow upstream of the bubble; whereas for large L_{TB}, it is governed by the wall shear-generated turbulence.

The first model for the entrainment flux was proposed by Fernandes et al. (1983). They proposed that the gas flux out of the rear of the Taylor bubble is connected to a thin boundary layer in the Taylor bubble, which develops as a result of the liquid film flowing downward. Experiments on a stationary Taylor bubble in a vertical pipe with internal diameter, D_i = 51mm by Su (1995) resulted in the creation of a bubble by injecting gas through a small pipe, with outer diameter D_u = 19mm, in the centre of the vertical pipe and a downward liquid flow. The author observed that the vortices in the wake of the Taylor bubble play an important role in the entrainment process. These vortices tear the gas off the fixed bubble and entrain it into the liquid slug in the form of a swarm of small bubbles.

Several attempts have been made to propose theoretical models for the prediction of the shape and rise velocity of Taylor bubbles in gas-liquid cases. However, due to the complex hydrodynamics, the development of a generalized solution taking care of all the physical and geometrical parameters is formidable. Therefore, several researchers have proposed solutions on the basis of different simplifying assumptions. The assumption of inviscid flow past the nose of the bubble has provided the first and probably the simplest analysis of the problem (Mandal et al. (2007)).

Recent work on gas entrainment model was carried out by Skartlien et al. (2012) but the authors' work was based on horizontal pipes.

2.10   Re-coalescence

Re-coalescence is the process by which a part of the entrained gas bubbles in the liquid slug coalesce with the bottom of the Taylor bubble. In literature, the re-coalescence flux is often neglected and thus only the net gas flux out of the rear of the Taylor bubble is usually considered. Direct re-coalescent measurements can give us information whether the flux is negligible or not. Measurements have only been performed by Kockx (1999) and Delfos et al. (2001a) by means of helium-injection method based on the basic idea of injecting small helium bubbles, which approximately behave similar to the air bubbles, into the wake of the Taylor bubble. By measuring the helium concentration in the Taylor bubble, entrainment and re-coalescent fluxes were derived. However, the work only considered water as liquid which has low viscosity compared to higher viscosity oils in the current study.

The Taylor bubble velocity is understood in vertical co-current flow. For the downward flow, the velocity measurement has been briefly reported by Nicklin (1962) and Griffith and Wallis (1961); and has been investigated more extensively by Martin (1976).

The general form of expressing the rise velocity of the elongated bubbles, U_{TB} in upward (co-current) flow is given by the equation below:

$$u_{TB} = c_1\sqrt{gD} + c_2 u_L \qquad (2.31)$$

On the right hand side, the first term of the equation represents the absolute transitional velocity of the Taylor bubble in stagnant liquid ($U_L=0$), g is the acceleration due to gravity, D is the diameter and U_L is the

mean downward liquid velocity whereas the coefficient C_1 is a function of the physical properties of the liquid and the duct diameter

Three meaningful dimensionless parameters were introduced by White and Beardmore (1962) which are:

Froude number, $Fr = \dfrac{U_{TB}}{\sqrt{gD}}$ (2.32)

which represents the inertial effects (negligible if Fr < 0.0025).

In some of the analysis in this Thesis, a modified Froude number is used based on gas superficial velocity which is given as:

$$Fr_g = \frac{\rho_g U_{gs}^2}{\left(\rho_l - \rho_g\right)gD}$$ (2.33)

This was achieved by squaring both sides of equation (2.32), then multiplying both the numerator and the denominator by density. i.e.

$$\left(Fr\right)^2 = \left(\frac{U_{TB}}{\sqrt{gD}}\right)^2 \times \left(\frac{\rho_g}{\rho_l - \rho_g}\right)$$ (2.34)

Eötvos Number, $E_o = \dfrac{\rho g D^2}{\sigma}$ (2.35)

which represents the surface tension effects (neglected if E_o > 70)

Morton Number, $M_o = \dfrac{g\mu^4}{\rho\sigma^3}$ (2.36)

which represents the viscous effects (negligible if $M_o < 10^{-8}$)

The values of $C_1 = 0.35$ eqn 2.31, is accepted provided that viscous and surface tension effects are negligible.

Since the value of C_1 plays a great role in flow analysis and it is affected by viscous effects, it is necessary to look into the influence of viscosity change on the flow during experimentation.

Lastly, Ohnesorge number (Oh) relates to the ratio of the viscous forces to the inertial and the surface tension forces which is expressed as follows:

$$Oh = \frac{\mu}{\sqrt{\rho \sigma D}} \tag{2.37}$$

This implies that large Oh indicates a significant influence of viscosity. Although, the Ohnesorge number (Oh) takes into account the effect of viscosity, density and surface tension, it does not account for the velocity of flow for the two-phase gas-liquid flows. Hence a dimensionless number which account for this parameter may be used. The Kapitza number (Ka) is defined as the ratio of Froude number (Fr) to the square root of Ohnesorge number (Oh).

$$Ka = \frac{Fr}{\sqrt{Oh}} \tag{2.38}$$

$$\text{Hence Ka} = \frac{\rho_g u_{gs}^2 \sigma^{0.25}}{\left(\left(\rho_l - \rho_g \right)^{0.75} D^{0.75} g \mu_l^{0.5} \right)} \tag{2.39}$$

This equation will play a major role in identifying the effect of viscosity as it relates to gas entrainment especially in Chapter 8.

2.11   Effect of Liquid Viscosity

2.11.1   Survey on effect of Liquid viscosity

Since the most common type of flow regime observed in oil production pipelines is slug flow, the knowledge of the liquid distribution, and hence the void fraction within the liquid slug, is important for the design of slug catchers for pipelines. There are other investigations which have been carried out using air as the gas phase and oil as the liquid phase. However, only a few investigations have been made showing the effect of liquid viscosity on the characteristics and hence the phase distribution in gas-liquid slug flows. Investigations of the influence of liquid viscosity on slug characteristics in horizontal, slightly inclined pipes have been carried out

by Crowley et al. (1984) and Sam and Crowley (1986). According to the results of these investigations, increasing the liquid viscosity is expected to result in increasing slug velocities, increasing liquid film heights and increasing flow averaged liquid holdups. Zukoski (1966) experimentally investigated the influence of viscosity and surface tension on bubble velocity for different tube inclination angles. In particular the combined effects of surface tension and inclination angle are superbly demonstrated. It was observed that for all inclinations, the effect of surface tension is to reduce the bubble velocity more than $(gD)^{1/2}$ when the diameter is reduced, and to finally bring the bubble to rest, altogether. The classical problem is rather well understood for all inclinations, although solution is only available for purely inertial or viscous flow in vertical tubes (Bendiksen (1984)). However, these investigations have not involved vertical pipes as well as gas entrainment rate.

Highly viscous single-phase flow of Newtonian fluids in pipes is probably one of the most understood areas of fluid mechanics. However, its two-phase counterpart is an area that has received little attention, although some studies have been done. Furukawa and Fukano (2001) used glycerine solutions with viscosities of up to 15 mPa s to investigate the effects of liquid viscosity on flow pattern. Fukano and Furukawa (1998) used glycerine solutions with viscosities of up to 10 mPa s to investigate the effect of liquid viscosity on interfacial shear stress and frictional pressure drop. Mori et al. (2007) used glycerine solutions with viscosities of up to 70 mPa s to investigate the inception of disturbance waves and droplets in two-phase flow, while Mori et al. (1999) used viscosities of up to 20 mPa s to investigate the effect of liquid viscosity on interfacial waves. The effects of a highly viscous liquid phase on vertically upward two-phase flow in a pipe was also investigated McNeil and Stuart (2003) as well as in McNeil and Stuart (2004). The former was based on two

approaches (flow pattern independent and flow pattern dependent approaches). A new correlation for the interfacial friction factor was proposed for the highly viscous experimental dataset investigated by the authors. The latter work looked into highly viscous liquid-phase in a nozzle and orifice plate with a vertically upward two-phase flow. The authors concluded from the study that a substantial increase in liquid viscosity has a significant effect on nozzle and orifice plate flows. However, all the work mentioned above could not address the effect of viscosity of gas entrainment below Taylor bubbles in a slug flow. Only the work by Su and Metcalfe (1997) used viscous liquid for entrainment studies. However, the viscosity of the liquid used (6mPa.s) was still far below the viscosities of oils used (42mPa.s and 152mPa.s) for the current study.

2.12   Falling film

Several publications have evolved plunging jets which results from falling film and the associate gas entrainment especially in open pools. However, most of these studies have focused on co-current flows rather than stationary flows which are easily used for predicting the hydrodynamics of plunging jets and the associated gas entrainment which may further be used to generate correlations. In this section, the literature is reviewed and presented regarding falling film and the gas entrainment due to plunging jets.

2.12.1   Falling Film reviewed

Falling and plunging jets commonly studied in open channels have been carried out for several years using different measurement techniques. The studies previously published on falling films and plunging jet in pipes are either in terms of experimental and modelling studies or computational and numerical simulations. These would be itemised as follows:

2.12.1.1   Experimental and modelling studies of falling film

Previous work on plunging jet characteristics were reported for low liquid velocities and for low viscosity liquid such as water as the working fluid. Nusselt (1916) has been reported as one of the early researchers in film thickness measurement. A model was developed which is very useful for the laminar flow region. Another researcher carried out an extensive literature survey on the hydrodynamics of liquid jets and how they affect gas entrainment is Biń (1993). An equation for low velocity jets based on energy balance, for calculating impact jet diameter, which is a function of the jet length, gravity, liquid flow rate and relaxation diameter, was proposed by the author. However, the proposed equation does not take into consideration the effect of the interfacial shear at the liquid-gas interface. Since the work by Biń (1993) was based on low jet velocity, Van De Sande and Smith (1976) worked on high jet velocity thereby proposing a correlation which was based on the Weber number, Reynolds number as well as nozzle design parameters. However, this correlation is valid only for specific combinations of Weber and Reynolds numbers, for some nozzle lengths and nozzle diameters.

McKeogh and Ervine (1981) measured the jet turbulent intensity using a turbulent probe consisting basically of a pitot tube connected to a pressure transducer. The authors proposed a power law relationship which correlated the jet surface roughness, jet radius, jet length, and the jet breakup length. The power index and constant in the correlation depended mainly on the jet turbulence level. Kusabiraki et al. (1992) also carried out experimental studies considering different liquid properties, such as density, viscosity and surface tension, with different nozzle designs and different jet velocities, to determine the effect of jet shape on the gas entrainment. A pitot tube was used to measure the liquid jet velocity near the plunging point while the shape of the jet was determined by analysing

a series of jet photographs. The studies by the authors deduced that correlating jet undulations with different physical properties show the same trend of the measured gas entrainment.

An investigation of falling film entrance region was carried out by Hikita et al. (1987) both theoretically and experimentally in a rectangular inclined channel. The investigation by the authors was on angles of inclination from 10° to 90° using three different fluids which include water and two other different concentrations of aqueous sucrose solution. The authors used a micrometre attached to a pointer to measure film thickness while applying a finite element method to acquire the falling film velocity. The authors used a model which is based on boundary layer approximation that also involves the Galileo number, Ga, (which is a function of the discharge coefficient, inclination angle and the Reynolds number).

The liquid film around a standing bubble was experimentally investigated by Kockx et al. (2005) and Kockx et al. (1998) in a 100mm diameter pipe through continuous injection of air into a narrow tube. The stationary Taylor bubble generated had a length of 150cm. A Laser Induced Fluorescence (LIF) technique was used by the authors and the results obtained show that the liquid film thickness decreases as the distance from the nose of the Taylor bubble increases until an axial distance of 8-9 pipe diameters and film thickness of 2.6 mm are reached. Beyond these points, the liquid film thickness slightly increases to a value of 2.8 mm, thus remaining constant for axial distances larger than 12 pipe diameters. The experimental results obtained by the authors agree well with the prediction of the model proposed by Karapantsios and Karabelas (1995) as well as with measurements results obtained by Su (1995). Unlike Kockx et al. (2005), these authors (Karapantsios and Karabelas (1995) as well as Su (1995)) use a conductance technique to measure falling film thickness. Karapantsios and Karabelas (1995) investigated falling film characteristics

in a vertical pipe of 50 mm I.D. and 2.66 m long over a Reynolds number range of 370 to 11020. The authors took measurements at different lengths from the air injection points (34.4D, 36.4D, 37.8D, 39.8D, 43.8D, and 49.2D) through the use of parallel wire conductance probes located 180° apart in the circumferential location. Karapantsios and Karabelas (1995) proposed a correlation for film thickness, which was a modified version of the correlation proposed by Takahama and Kato (1980), the difference being that the correlation by Karapantsios and Karabelas (1995) is capable of predicting the film thicknesses in flows with higher Reynolds numbers than those of Takahama and Kato (1980). Karapantsios et al. (1989) also employed a conductance technique to measure falling liquid film thickness for Reynolds numbers in the range of 509 and 13090. The authors were able to show extensive statistical analysis of the wave dynamics on the liquid film surface. Other authors that use conductance technique to measure film thickness include Geraci et al. (2007).

Portalski and Clegg (1972) measured falling liquid film thickness utilizing the light absorption technique. Also, the roughness of jet was measured by Davoust et al. (2002) using the same light absorption technique as Portalski and Clegg (1972). However, the suitability of such technique to capture inertia is in doubt.

Some other film thickness measurement techniques have been employed by other researchers including Liu et al. (1993), Liu et al. (1995) Karimi and Kawaji (1998), Karimi and Kawaji (1999), Chu and Dukler (1974), Cummings and Chanson (1997), Chanson and Jaw-Fang (1997), Cummings and Chanson (1999) and Conte and Azzopardi (2003).

Lastly, jet and falling film thickness and waviness measurements, were investigated by researchers including Zhou et al. (2009) who measured film thickness with a confocal chromatic sensor technique. The measurement method adopted by Schagen et al. (2006) was based on

luminescence indicators to determine the local film thickness of a falling film and the temperature distribution over a heated plate.

2.12.1.2   Numerical and Computational Simulation of falling film: the review

It is quite difficult to directly simulate the hydrodynamics of a falling film, as noted by Kostoglou et al. (2010) who reported the reconstruction of film thickness time traces for wavy turbulent free falling films. Hence, simplifications and assumptions based on experimental data are required to simulate such phenomena. Taha and Cui (2006) used the FLUENT code to run CFD simulations on slug flow. The authors' results showed that the film thickness around a Taylor bubble decreased as the surface tension increased.

Haeri and Hashemabadi (2008) developed a CFD simulation for falling film on inclined plates utilizing a finite volume code. Lahey Jr. (2008) presented a direct numerical simulation (DNS) of various incompressible and compressible single and two-phase flows including jets. He provided detailed information on the jet flow structure utilizing a suitable adaptive grid 3D solver. Oron et al. (2009a) and Oron et al. (2009b) derived and analyzed the spatiotemporal dynamics of thin liquid films falling on an oscillating vertical plane via the time-modulated weighted-residual boundary-layer (TMB) equations. Other previous work on numerical modelling of film thickness have been carried out by researchers such as Oron et al. (2009) and Xu et al. (2008).

However, all the above studies do not statistically analyse the development of film thickness in a practical way. The key characteristic of a free falling liquid film is that its thickness changes continuously with the axial distance. In the current work, statistical analysis of the film thickness

as it travels down the pipe while covering a stationary Taylor bubble will

be provided.

Chapter Three
Two-phase flow in a 127mm diameter vertical pipe at elevated pressure

3.0   Introduction

In chapter two, it was emphasized that very little work has been done on viscous liquids. Hence, it is imperative to work with fluid of high viscosity, since oil and gas industries will need to handle highly viscous fluids. This chapter introduces the two-phase flow experiments conducted at SINTEF Multiphase flow laboratory using high viscous liquid. It begins with a description of the medium flow loop, which was designed at the University of Nottingham and then connected to the facilities at SINTEF to give a closed loop. The design methods, as well as the rig components, are also described herein. Finally, experimental results are presented. In this chapter, the experimental results discussed are those carried out at 7.5barg pressure. In this case, differential pressure transducers were used which were connected to (i) the test section and (ii) a reference pressure line. Further discussion of this will be made later in this chapter.

3.1   Overview of the flow facilities

3.1.1   Brief description of the rig

The medium closed loop flow facility at SINTEF Petroleum Research, Multiphase Flow Laboratory was designed to accommodate both vertical and horizontal flow lines as described in Eskerud Smith et al. (2011). A schematic diagram of this loop is given in Figure 3.1. The pipework for the

127mm diameter 9m riser section of the vertical flow facility was designed and constructed at the University of Nottingham. This consists of the gas/liquid mixer at the lower end of the riser as well as a bend at the topside of the riser. The riser was pressure tested at Nottingham before the components were shipped to the SINTEF laboratory at Tiller near Trondheim, where it was incorporated into their Multiphase flow medium scale closed loop for the duration of the tests to allow measurements using a wire mesh sensor and differential pressure transducers to acquire void fraction and pressure gradient data respectively.
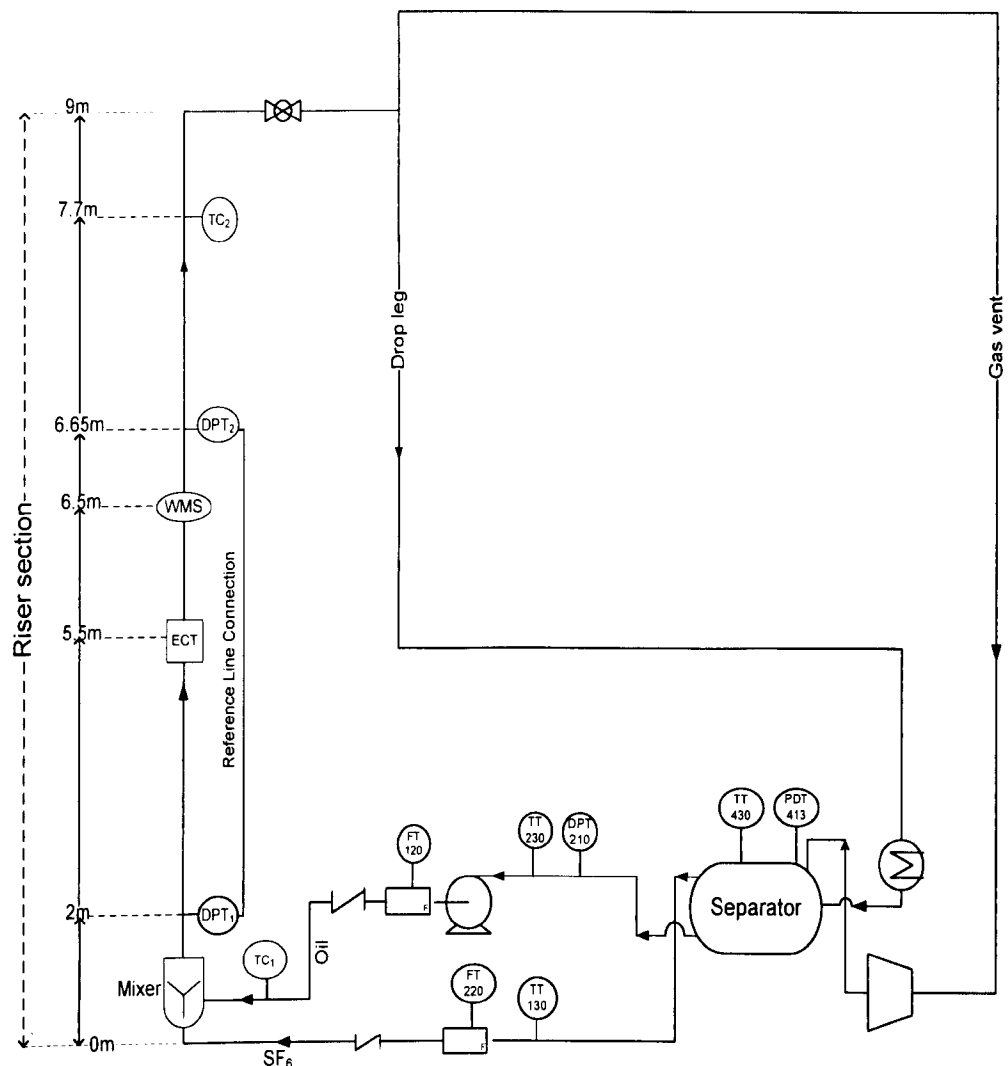
Figure 3.1: The experimental rig with the riser section as labelled

3.1.2   System test fluid: properties and reason for their choice

In this facility, the gas used was Sulphur Hexafluoride (SF_6). The gas was initially compressed to a liquefied form at 80bar in a cylindrical tank. This was sent into the separator (Figure 3.1) which already contained a high viscosity oil mixture (mixture of Nexbase 3080 oil with viscosity of 89mPa.s and Exssol D80 oil with viscosity of 1.76mPa.s). The properties of the fluids are presented in Table 3.1. It is worth noting that the oil samples were chosen because they are non-flammable, transparent and non-toxic. Exssol D80 is de-aromatized aliphatic hydrocarbon oil commonly used in flow loop experiments while Nexbase 3080 is catalytically hydro-isomerised and dewaxed base oil comprising of hydrogenated, highly iso-paraffinic hydrocarbons. The two oils were combined to achieve a mixture with a viscosity of 35mPa.s which was instantaneously monitored using a coriolis flowmeter with model number CMFS400.

Table 3.1: Fluid properties for the experimental campaign

Type of Fluid	Typical Density (kg/m^3)	Viscosity (mPa.s)	Temperature Range, TC_2 (^{0}C)
SF_6 Gas (at 7.9bara)	45	0.0151	
SF_6 Gas (at 4.5bara)	28	0.0151	
Liquid Mixture (Exxsol D80 + Nexbase 3080)	840	35	21.05-25.52

3.1.3   Components of the flow facility

The compressor on this facility has a volumetric capacity of 180 m^3/h and can compress up to 20 bara. The maximum operating speed is 2900 r.p.m. The compressor is driven by an electric motor and most of the heat generated during the compression process is absorbed by the circulating oil in the system. This is removed in the heat exchanger to which water

from the mains was provided at a constant rate as provided in Fig. 3.1. Gas enters the compressor, which has impellers that rotate eccentrically in relation to the centreline of the compressor ring. This results in the change of volume and creates a vacuum and compression process. Compressed gas is directed to the storage tank where the two phases were separated.

The heat exchanger helps to ensure that the system fluid properties are maintained as drop or increase in temperature affects fluid properties which may alter actual data acquired. The oil is circulated by the centrifugal pump via the heat exchanger; hence the oil conditions are regulated by the heat exchanger. The oil temperature was constantly monitored and recorded.

Flow lines and Riser: The riser was made of 316-stainless steel in order to withstand the high pressure to which it was subjected. It was 9 meters tall from the baseline. There was a 90 degrees bend at the end of the riser which connects to the drop-leg as can be seen in Figure 3.1.

Separator: The separator tank had a nominal volume of 10m^3. Gas and oil from the downcomer are separated here before being injected separately back into the riser base.

3.1.4   Gas-liquid mixing section

In the mixer employed here (Figure 3.2c) which is similar to that used by Hernandez Perez (2008), Hernandez Perez et al. (2010), Szalinski et al. (2010) and Azzopardi et al. (2010a), the liquid was introduced into a short annulus from the bottom. Gas was then mixed through 4mm diameter holes at the inner wall of the annulus. The mixture then flows into the main pipe. This design was chosen to: (i) produce small bubble sizes and (ii) to minimize the flow of liquid back into the gas supply line. To avoid liquid from entering the gas injection holes, the shutdown process involves stopping the liquid flow while the gas flow was continuously circulated for a

few more minutes in order to expel all liquid in the test section. The gas flow was then stopped. The holes were positioned in rings up the pipe with an axial spacing of 20mm and a circumferential spacing of 16mm. Alternate holes are staggered to give a triangular array as can be seen in Figure 3.2(b).

(a)

(c)

(b)
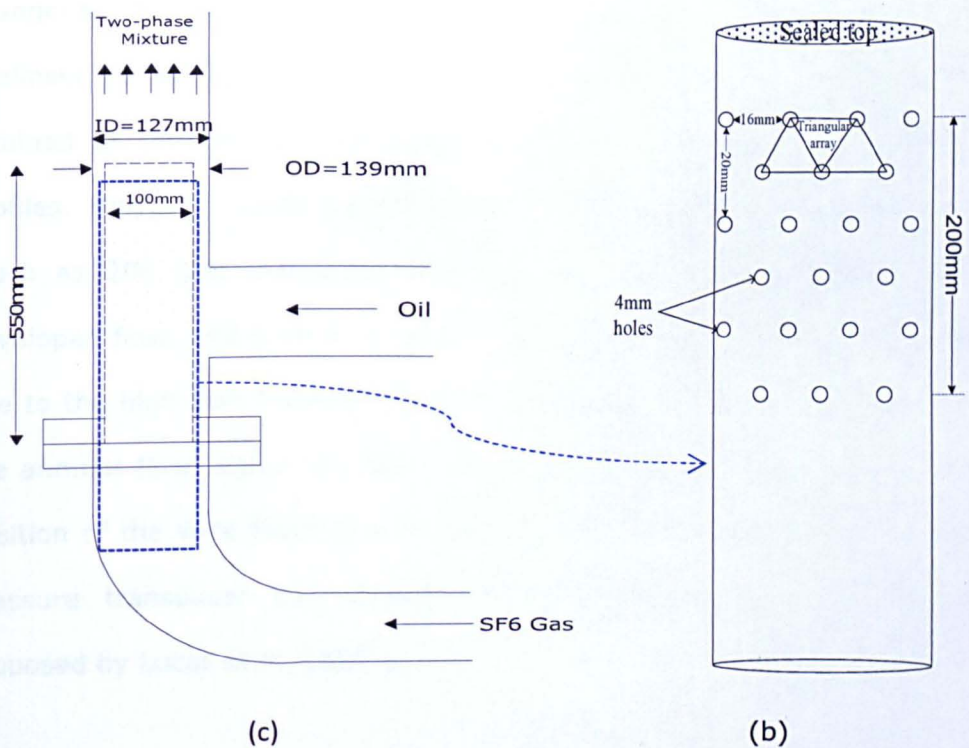
Figure 3.2: Mixing configuration showing (a) gas injection tube (b) layout of the gas injection unit (c) Two-phase flow mixing point

Abolore Abdulahi

3.1.5   Flow measurement section

The flow measurement section contained the measuring instrument for the experiment. The Differential pressure transducers (DPT_1 and DPT_2 shown in Figure 3.3) were placed at two different positions along the riser with a constant pressure reference line positioned in-between the two transducers. One transducer (DPT_1) was placed 2m from the mixing section while the other transducer (DPT_2) was placed 6.65m from the mixing zone, as can be seen in Figure 3.3. The wire mesh sensor was positioned 6.5m from the mixing zone in order to allow measurements to be made on a fully developed flow. It was assumed in this work that steady state conditions have been attained at this axial position and instabilities were ignored. In principle, a two-phase flow is assumed to be fully developed if all the measured properties such as average void fraction, radial void fraction and other measurable parameters do not change as the ratio L to D is increased. Lucas et al. (2005) as well as Szalinski et al. (2010), reported that developed flow conditions are attained at L/D=40 for average void fraction and radial void fraction profiles. However, some experiments on vertical pipes indicate that as much as 200 pipe diameters or more are needed to establish a fully developed flow, and such a length is seldom possible in experimental rigs due to the high cost involved. Besides, such experiments are in mainly in the annular flow region. In the current study, the ratio L/D=51.2 at the position of the Wire Mesh Sensor while it was 52.4 at the position of the pressure transducer downstream. This position is well beyond that proposed by Lucas et al. (2005).
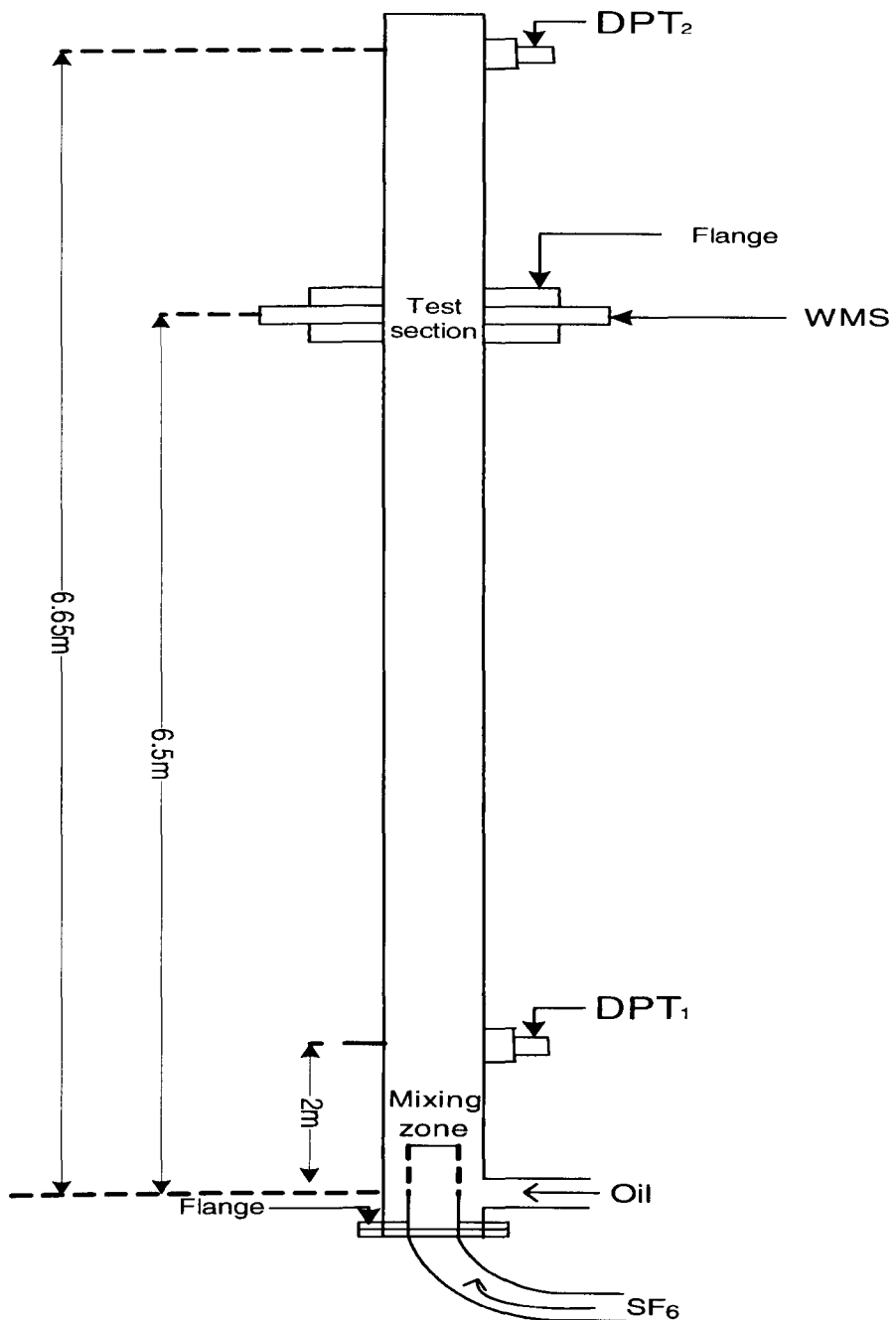
Figure 3.3: Positions of the measuring instruments

3.1.5.1   Differential Pressure Transducers (DPTs)

The differential pressure transducers used in this work had a range between 0-2.5bar with a nominal pressure of 16bar, an accuracy of +/- 0.25% and were made by Impress sensor and systems. The model number was 730-E-2501-1-5-100-J00-1-000. Just like any other measurement technique, calibration is an essential preparation step before using the

transducers. One of the advantages of DP Transmitters is that they have a zero span feature that makes them easy to calibrate. Both DPTs located on the test section in Figure 3.3 (DPT_1 and DPT_2) were calibrated using exactly the same procedure. Although the differential pressure transducers used in the experiment were Supply Company calibrated with a calibration certificate provided to the user, a second calibration was conducted on the transducers to confirm the accuracy of the supplied calibration. The tube for calibration was made of polycarbonate material. The tube was filled with water from one end and the other end was sealed. Each transducer was connected in-between the two ends of the tube via a saddle (one at a time).

The transducer was connected to a 32 channels DAQ card (from National Instruments) which converted the electrical signals from the sensors to the numerical values using LABVIEW 8.6 software (also from National Instruments). The rate of data acquisition was controlled using built-in functions in the software. The data sampling rate for the present study was 1000Hz for duration of 1-3minutes. The signals from the sensors were obtained simultaneously and saved on a PC as EXCEL files. The equation from the calibration plot (shown in Appendix Figure B1) was programmed into Labview to acquire field measurements during experimentation. The program developed by the author using Labview software consists of routines corresponding to each pressure transducer signal, in which the time-varying voltage is converted into pressure.

3.1.5.2   Thermocouples

Two T-type thermocouples, TC1 and TC2, were inserted into both the liquid inlet and the two-phase flow outlet of the riser in Figure 3.1 to ensure that temperature data were logged to monitor and control the temperature as changes to this parameter will have an effect on viscosity.

The calibration of these thermocouples was done using ice, hot and boiling water. A thermometer was inserted into each system (ice cubes, hot and boiling water) to measure the temperature. This temperature measurement with the aid of a mercury thermometer which has an accuracy of $\pm 1^{\circ}C$ was simultaneously taken alongside the voltage readings using a digital multimeter. These data from thermocouple calibration were used to produce a calibration equation that was included in the Labview programme. The plot for this calibration equation is shown in Appendix Figure B2.

3.1.5.3   Wire Mesh Sensor

Capacitance wire mesh sensor which was manufactured by HZDR, Germany was used to acquire void fraction data. Further information on this instrument can be found in Chapter 5. Wire mesh sensor was placed at 6.5m above the mixing section in the riser. The data acquired by the instrument were analysed and the results can be found in section 3.4.2.

3.2   Experimental

The gas and oil flow rates, as well as the oil density, were measured by two coriolis meters. Measurement of the gas density was made through manually weighing a gas sample obtained from the flow loop. The medium flow loop is located inside a building at the SINTEF Multiphase Flow Laboratory at Tiller, Trondheim. The pressure in the test section was initially at 7.9bar, this was later lowered to 4.5bar. For the purpose of this Chapter, data for experiments at 7.9bara are reported. Comparison of the results from both pressure conditions will be discussed in Chapter 4. The velocity of the oil ranged from 0.1-1m/s while that of the gas ranged between 0.1-3m/s.

3.3   Experimental conditions

The experimental conditions at which data were taken have been represented in two different flow pattern maps (Hewitt and Roberts (1969) and Shoham (2006) mechanistic model) with dot and diamond representing discrete experimental points of the current work. A third flow pattern map based on Bennett et al. (1965) is not appropriate because of the assumption of a slip ratio of 1 is invalid for these flows. The Hewitt and Roberts flow map (shown in Figure 3.4) indicate that slug flows existed. However, slugs were not identified during experimentation. The Shoham mechanistic model flow map is identified as a more appropriate flow map which delineates the flow conditions into their respective pattern, as can be seen in Figure 3.5. This is because it does not show existence of slug flows as was observed during experimentation. The results from the observed flow pattern are shown in Table 3.2. The regimes where data appear on Shoham map are also similar to those shown in Table 3.2.
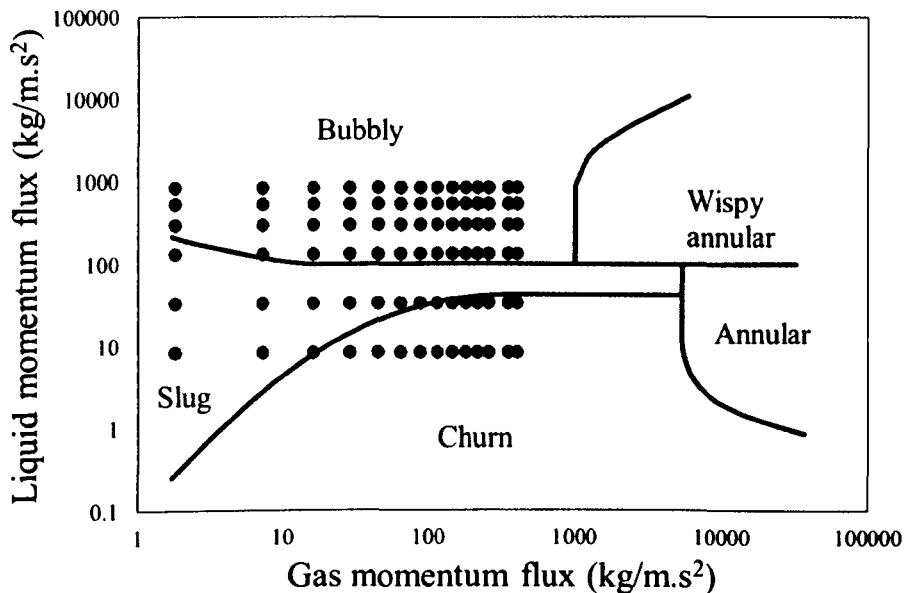
Figure 3.4: Flow pattern identification using the method proposed by Hewitt and Roberts (1969)

Abolore Abdulahi
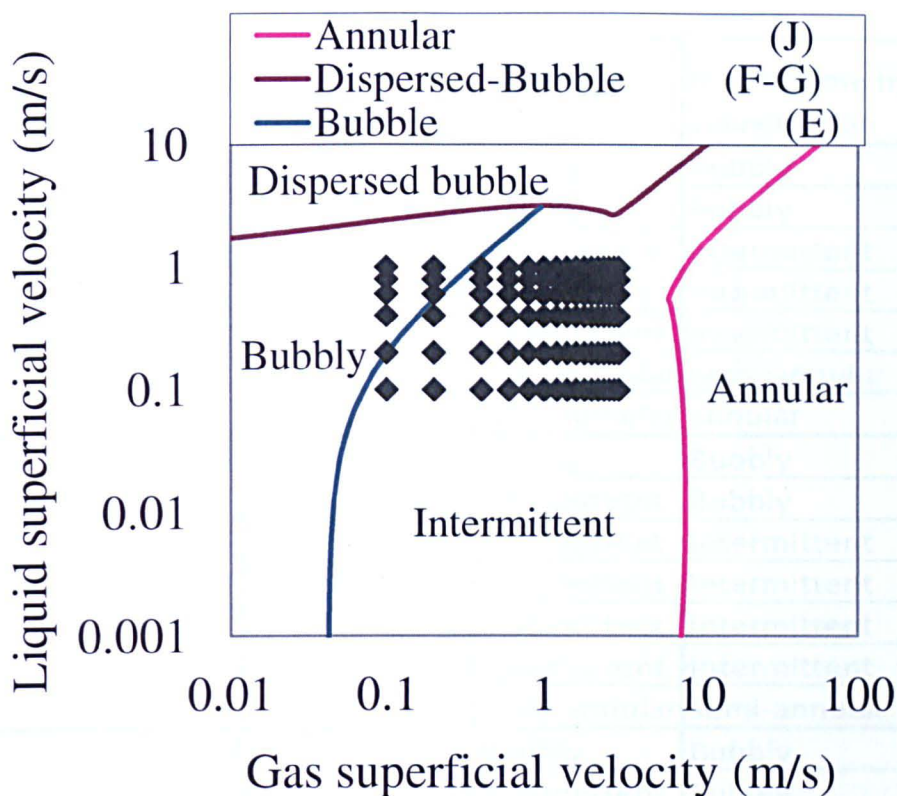
Figure 3.5: Flow pattern showing the positions of experimental points of consideration based on Shoham mechanistic model (Shoham (2006))

3.3.1   Visualisation method of identification

The pipe used for the work was made of steel (hence non-transparent) which made it difficult to see what was happening within the pipe conduit. However, there was a transparent section in the Wire Mesh Sensor which allowed visibility. Through this section, individual flow regimes could be observed although this only revealed what happened around the pipe wall and not the pipe core. Hence, this judgement may not be regarded as a very effective way of identifying regimes but it does give an opinion on what was observed. Bullet-shaped Taylor bubbles were missing in all the flows that were observed. The summary of the flow regimes observed is given in Table 3.2

Table 3.2: Flow regimes during experimentation

Liquid superficial velocity (m/s)	Gas superficial velocity (m/s)	flow regime by PDF	flow regime by visualisation
0.1-0.2	0.1	Bubbly	Bubbly
	0.6	Bubbly	Bubbly
	1	Intermittent	Intermittent
	1.4	Intermittent	Intermittent
	2	Intermittent	Intermittent
	2.4	semi-annular	semi-annular
	3	semi-annular	annular
0.4-0.6	0.1	Bubbly	Bubbly
	0.6	Intermittent	Bubbly
	1	Intermittent	Intermittent
	1.4	Intermittent	Intermittent
	2	Intermittent	Intermittent
	2.4	Intermittent	Intermittent
	3	semi-annular	semi-annular
0.8	0.1	Bubbly	Bubbly
	0.6	Intermittent	Bubbly
	1	Intermittent	Intermittent
	1.4	Intermittent	Intermittent
	2	Intermittent	Intermittent
	2.4	Intermittent	Intermittent
	3	semi-annular	Intermittent
1	0.1	Bubbly	Bubbly
	0.6	Intermittent	Bubbly
	1	Intermittent	Intermittent
	1.4	Intermittent	Intermittent
	2	Intermittent	Intermittent
	2.4	Intermittent	Intermittent
	3	semi-annular	Intermittent

These regimes identified in Table 3.2 have been corroborated by the flow pattern maps previously described in this chapter.

3.4   Results

3.4.1   Pressure Measurement

Pressure is the driving force for flow in pipes. Hence, it is an important design parameter in flow assurance and transient multiphase flows. In all the two-phase experimental campaigns presented in this chapter, time-varying, averaged total pressure drops, as well as pressure gradients, have been measured simultaneously with the other parameters such as gas volume fraction. The local pressures in the riser test section are measured by a pair of differential pressure transmitters (DP_{1-2}) and a reference line. Hence two groups of pressure gradient data are available, named as dP_1 and dP_2. They correspond to the pressure gradient between DP_1/Ref and DP_2/Ref pressure transmitters, respectively. The total pressure gradient consists of three components, gravitational, frictional and accelerational pressure gradients. In these tests, the accelerational pressure gradient was close to zero and has been neglected. The gravitational pressure gradient was estimated from the void fraction data. The time series of the pressure data close to the position of the Wire Mesh Sensor (DP_2) are shown in Figure 3.6

Abolore Abdulahi

(a)   (b)

(c)   (d)
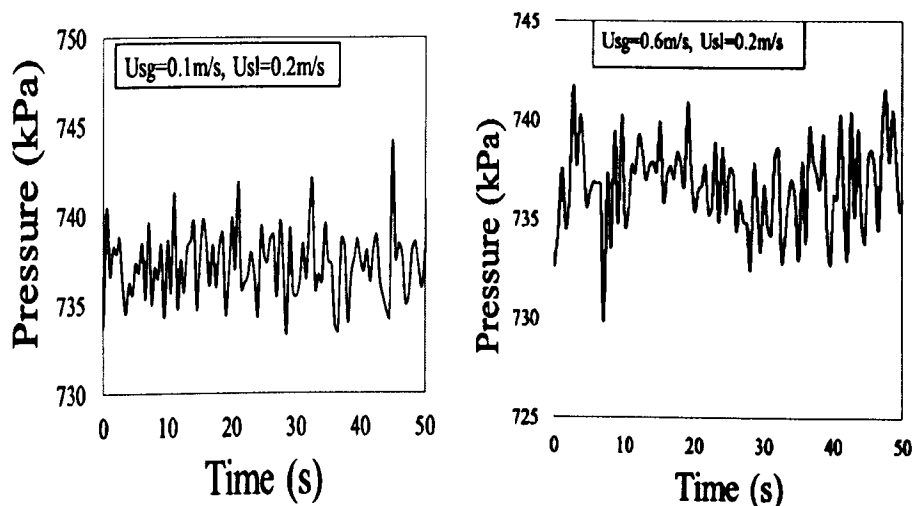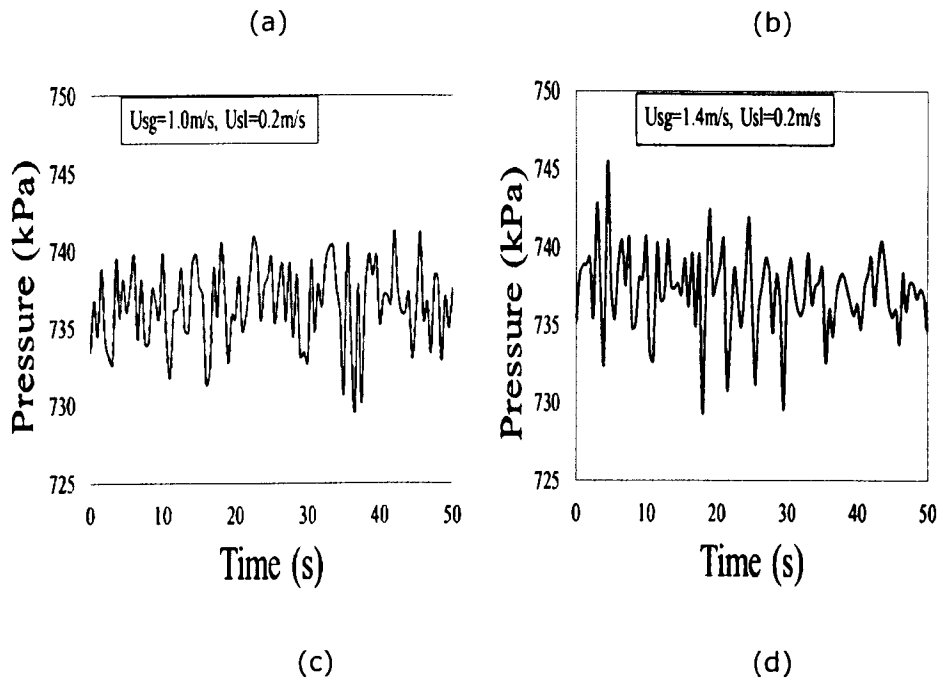
Figure 3.6: Time series of the pressure data at different flow conditions

The maximum and minimum values of the pressure time series can be seen as shown in Figure 3.6. These values are between 730-745kPa. The time series in Fig. 3.6 are able to reveal the fluctuations in the data as the gas-liquid flows through the pipe. The difference between the maximum and the minimum values in the plots do not show a huge pressure fluctuation (more than 50kPa) which are associated with the presence of bridging gas in slug flows. Hence, slug flows were completely missing as evidenced by this description. Hence the minimal pressure fluctuation identified can be attributed to this absence. Plots of the ratio of the standard deviation/mean of the pressure against superficial gas velocity show the extent of the pressure fluctuation as Figure 3.7 shows that the ratio is in the range of +/-0.35%.
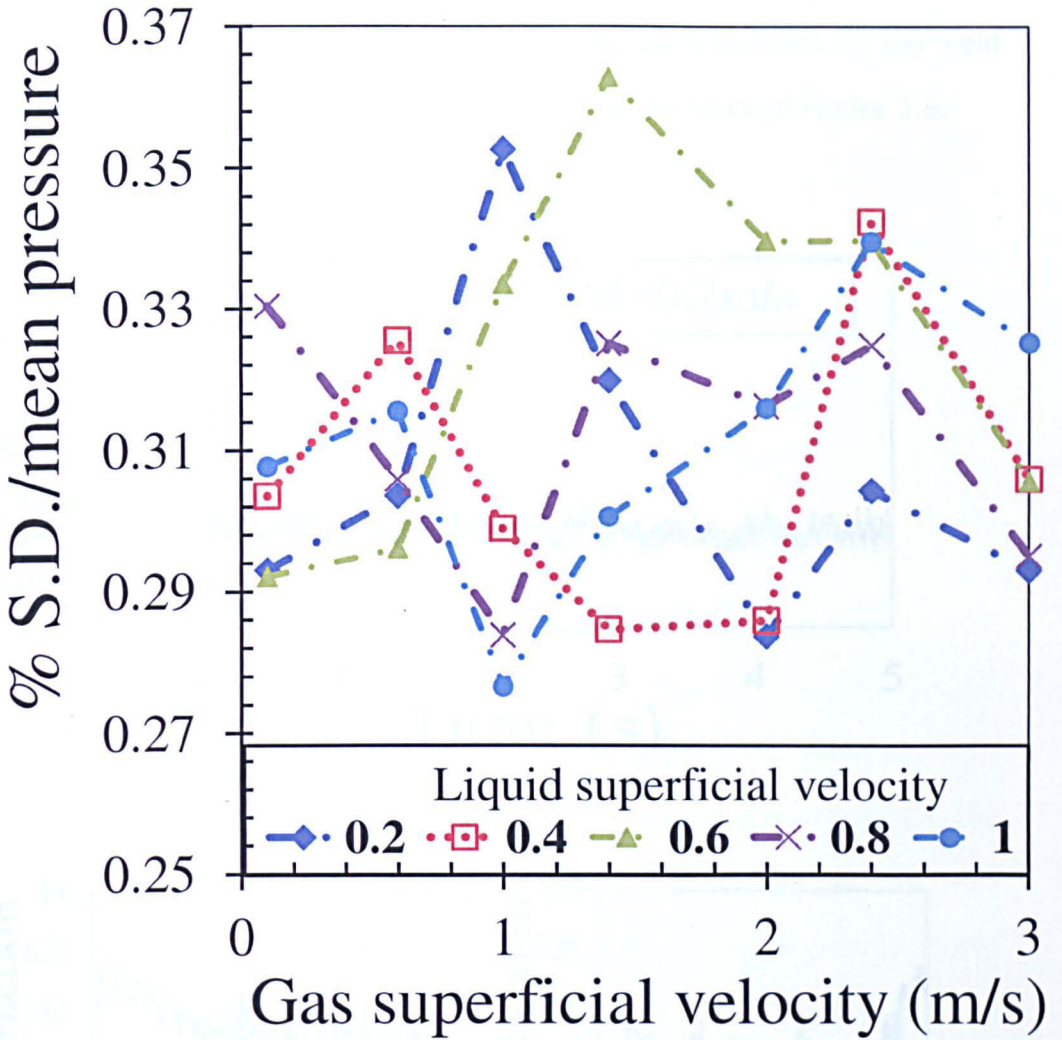
Figure 3.7: Percentage Standard Deviation/Mean Pressure versus superficial gas velocity

3.4.2　　Void fraction

The cross sectional averaged void fractions were acquired with the use of a wire mesh sensor and these results have been used to express flow regimes in terms of time series, probability density function of void fraction and power spectral density. Some of the analyses of the time series are shown in Figure 3.8. Figure 3.8 (a) covers a long time span which may be difficult to make out the detail. Hence, if emphasis is placed on the highlighted section, more information about the time series is

revealed as can be seen in Figure 3.8 (b). This is similar for all other conditions. An interesting feature is that the perturbations in the void fractions in Figure 3.8 are replicated in the pressure plots of Figure 3.6.

(a)

(b)

(c)

(d)   (e)

Time (s)   Time (s)

(f)   (g)
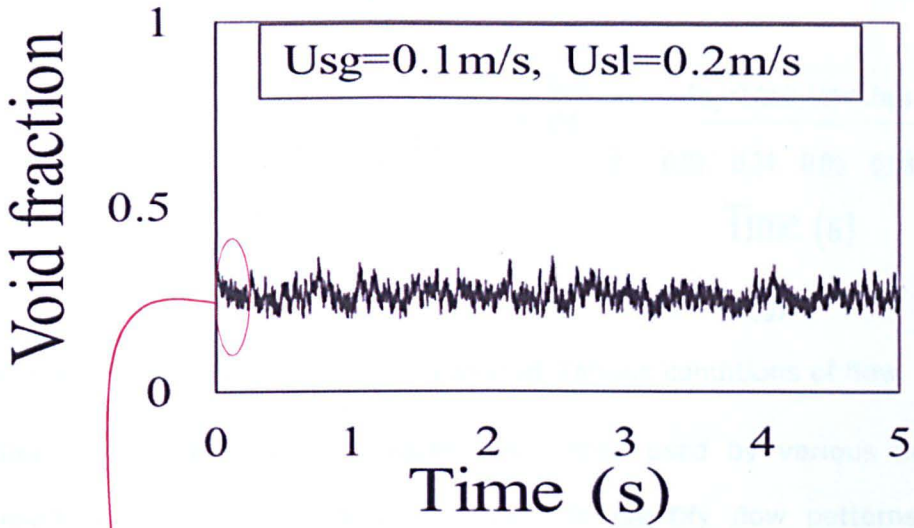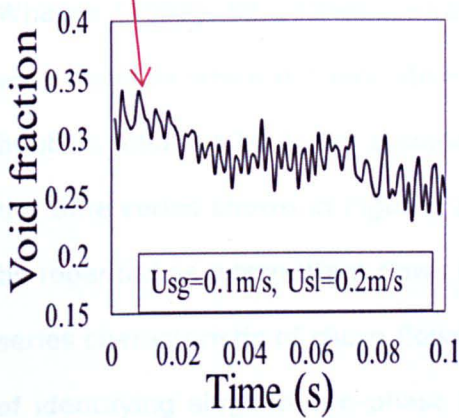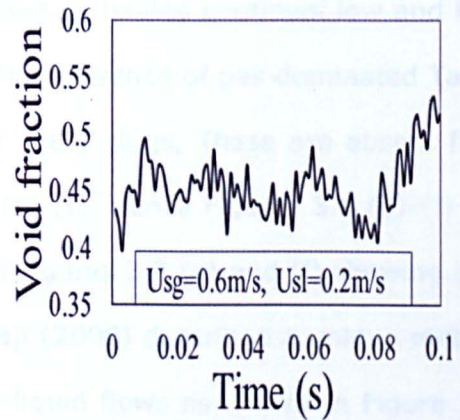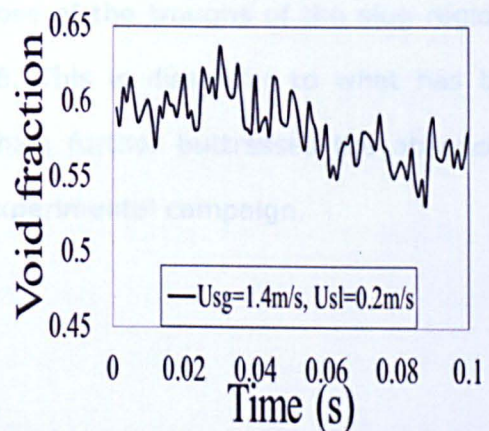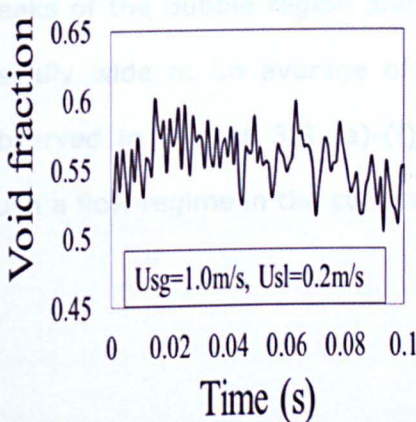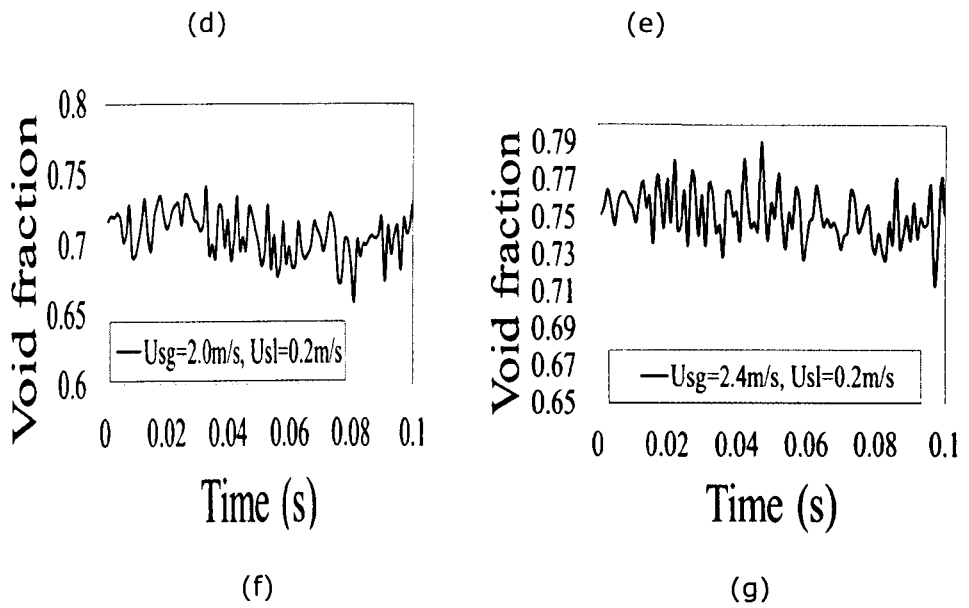
Figure 3.8: Time series of void fraction at various conditions of flow

Time varying void fraction traces have been used by various authors, including Costigan and Whalley (1997) to identify flow patterns. Void fractions below 0.25 are categorised as bubbly flow by Costigan and Whalley (1997). Slug flows are regarded as having continual low and high void fractions which are indicative of the presence of gas dominated Taylor bubbles followed by liquid dominated liquid slugs, These are absent from the time series shown in Figures 3.8 (a)-(f). Hence Figures 3.8 (b)-(f) can be regarded as intermittent flows with Figures 3.8 (e) and (f) showing time series characteristic of churn flows. Kaji (2008) described a unique method of identifying slugs in two-phase gas-liquid flows as shown in Figure 3.9. From this description, the range of magnitude between the values for the peaks of the bubble region and those of the troughs of the slug region is usually wide at an average of 0.6. This is dissimilar to what has been observed in Figures 3.8 (a)-(f) which further buttresses the absence of such a flow regime in the current experimental campaign.
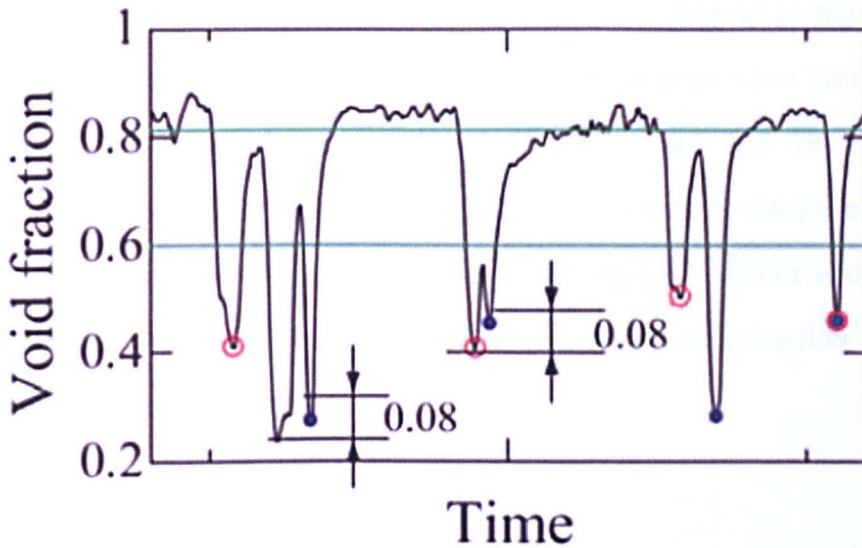
Figure 3.9: Criteria for the detection of slug (Kaji (2008))

Nevertheless, other flow pattern delineating signatures can be used to identify positions of the two-phase flows as observed during experimentation which will be discussed later in this chapter.

3.4.3   Probability density function of void fraction

Probability density function is a function of a continuous random variable, whose integral across an interval gives the probability that the value of the variable lies within the same interval. In this chapter, the variable used is void fraction. Costigan and Whalley (1997) used the probability density functions (PDF) to identify flow regimes. In their work, they used two meters to examine the dynamic variation of void fraction in air-water flows in a vertical 32mm diameter tube. The research led to the identification of six flow regimes through examination of the void fraction traces and their probability distribution functions. The regimes identified were: bubble flow, spherical cap bubble flow, stable slug flow, unstable slug flow, churn flow and annular flow. Using PDF in the current study, the narrow single peaks which occur at void fractions between 0.06 and 0.4, as defined by Costigan and Whalley for discreet bubbly flows can be seen in Figures 3.10 (a) and (b). Spherical cap bubble flows (have a PDF trace that has a single

Abolore Abdulahi

peak like bubble flow but with a broadening tail extending at higher void fraction). Stable slug flows and unstable slug flow both have twin peaks. However, they are all absent in Figure 3.10 (a) and (b). This is understandable as the pipe diameter in Costigan and Whalley's case was 32mm. Churn flow which has a void fraction close to 0.8 but with erratic liquid film thickness that has large disturbances with void fraction down to less than 0.6 was present.

(a)   (b)
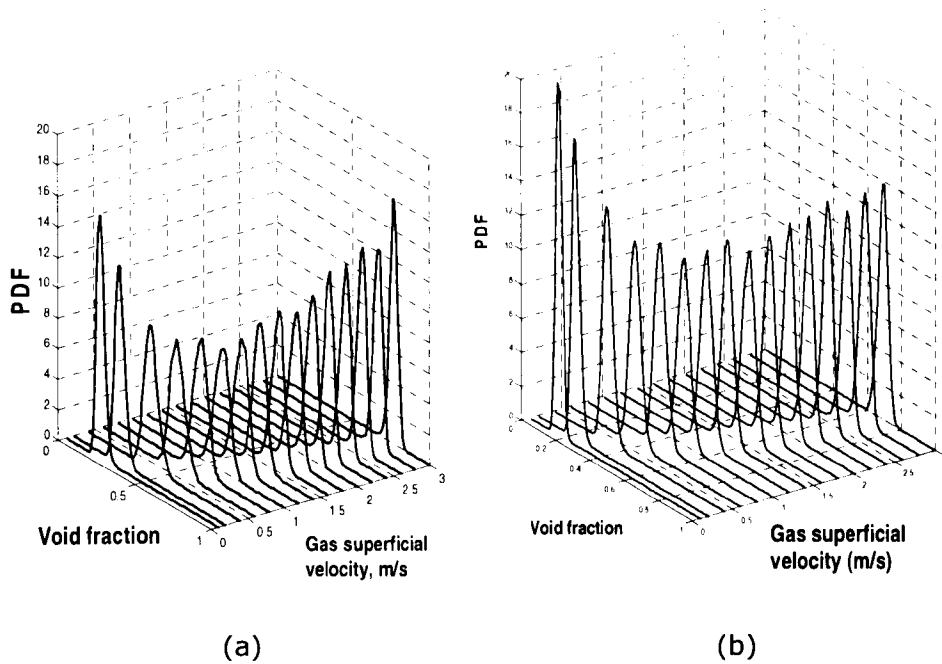
Figure 3.10: Probability Density Function plots for liquid superficial velocities at (a) 0.4m/s, (b) 0.8m/s

Radial profiles can also be extracted from the data of the wire mesh sensor as can be seen in Figures 3.11 (a) and (b). They are time and azimuth averaged gas fraction. The x-axis displays the distance in mm of the respective ring from the centre of the pipe. Unlike previous work with other instruments, the radial profiles are obtained relatively easily from the WMS data because the WMS intrusively scans the full cross-section of the pipe. Radial void fraction for bubble flows show that small bubbles tend to move to the pipe wall which results in increasing the effect of wall drag

as well as increasing the wall shear stress. This was also reported by Olerni et al. (2013). As the gas superficial velocities are increased, the bubbles increase in momentum and they tend to coalesce, which results in their movement towards the pipe core. At low gas volume fraction and low gas superficial velocity (for bubbly flows), the concentration are high towards the wall periphery as can be seen in Figure 3.11
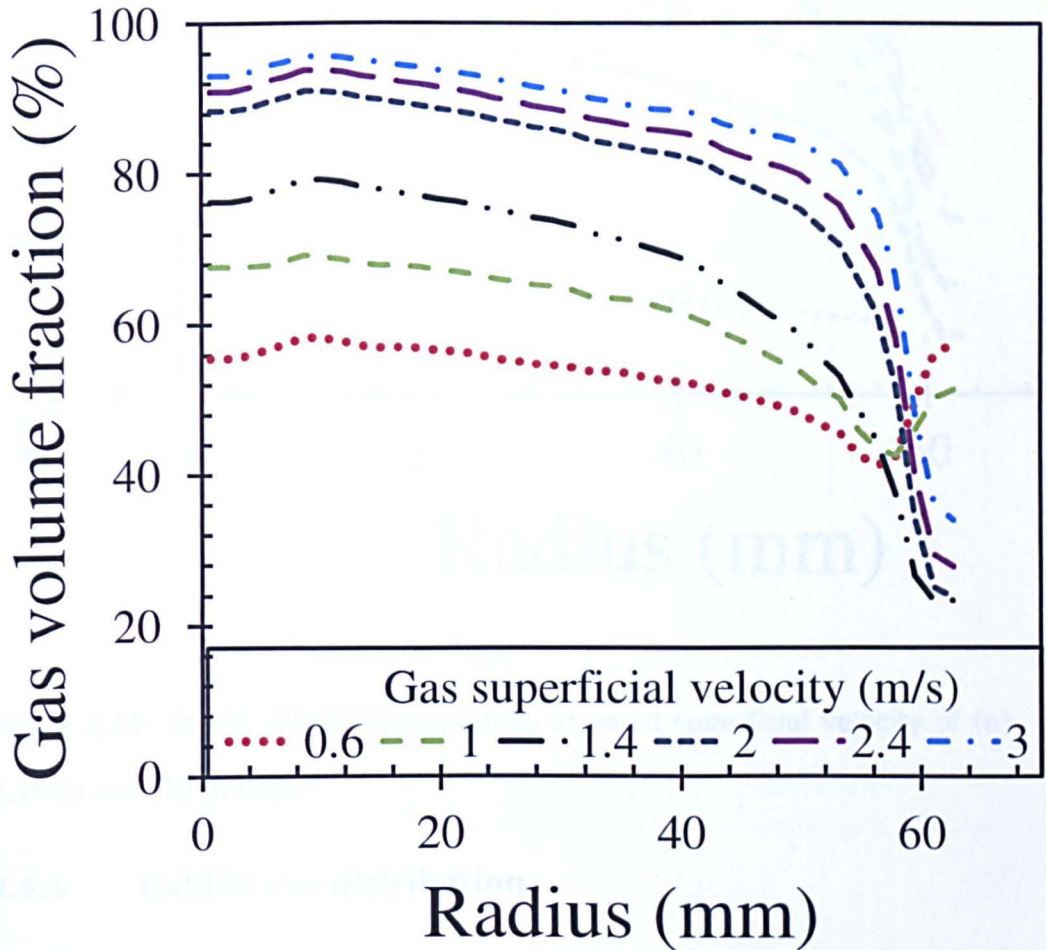
(a)
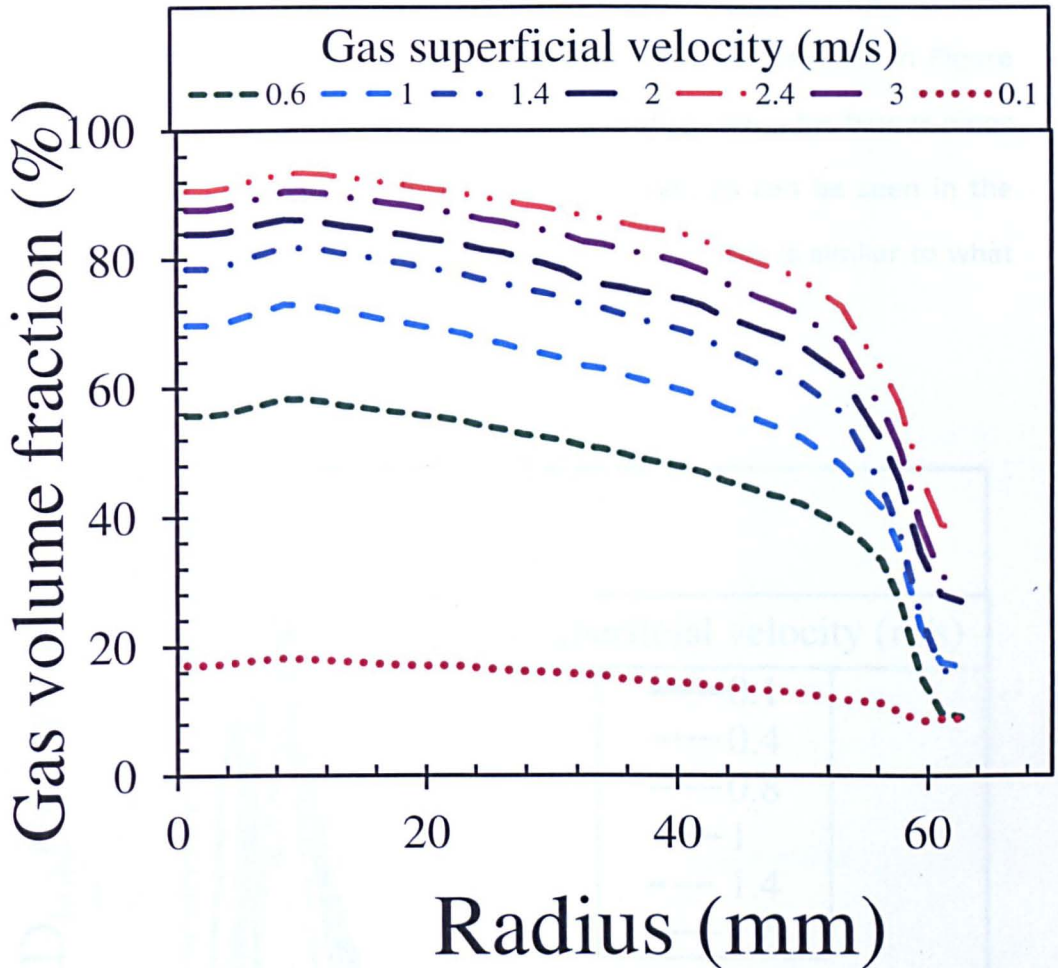
(b)

Figure 3.11: Radial void fraction profiles at liquid superficial velocity of (a) 0.2m/s and (b) 0.4m/s

3.4.4   Bubble size distribution

Details on the methodology for extracting bubbles size information from Wire mesh sensor data can be found in Prasser et al. (2001). They are constructed by summing the contribution of the bubbles of a given range of diameters to the integral volumetric gas fraction. The partial gas fraction ($d\epsilon/dD_{Bub}$ in %/mm) is plotted against the equivalent bubble diameter (D_{Bub}). When integration is carried out over the entire bubble size distribution, the result is the volumetric gas fraction averaged over time and cross-section. There is a general shift in the peak from left to

right as the superficial gas velocity is increased. This indicates that bubbles grow bigger as they gather more momentum. This can be seen in Figure 3.12 for liquid superficial velocity of 0.1m/s. Bubble sizes for bigger pipes cover a broader range than those in smaller pipes, as can be seen in the work by Prasser et al. (2004) shown in Figure 3.13. This is similar to what is shown in Figure 3.12.
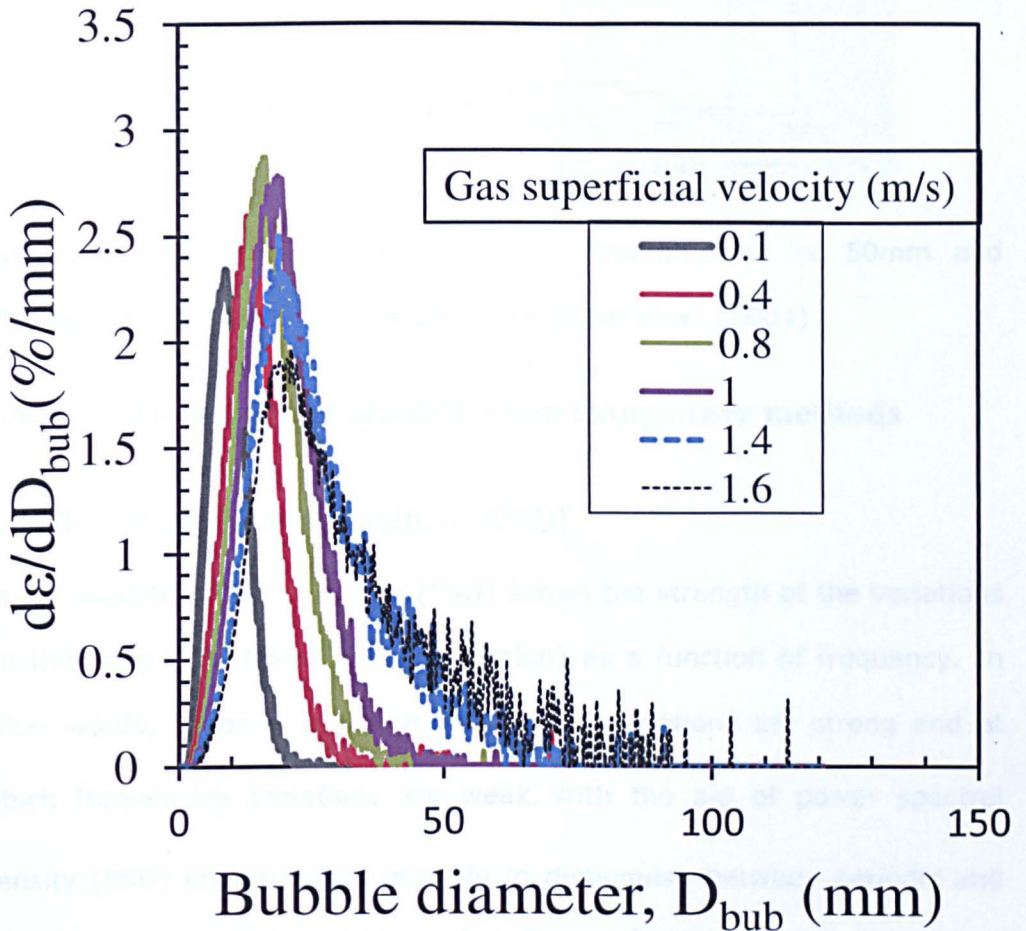
Figure 3.12: Bubble size distribution plot at Usl=0.1m/s
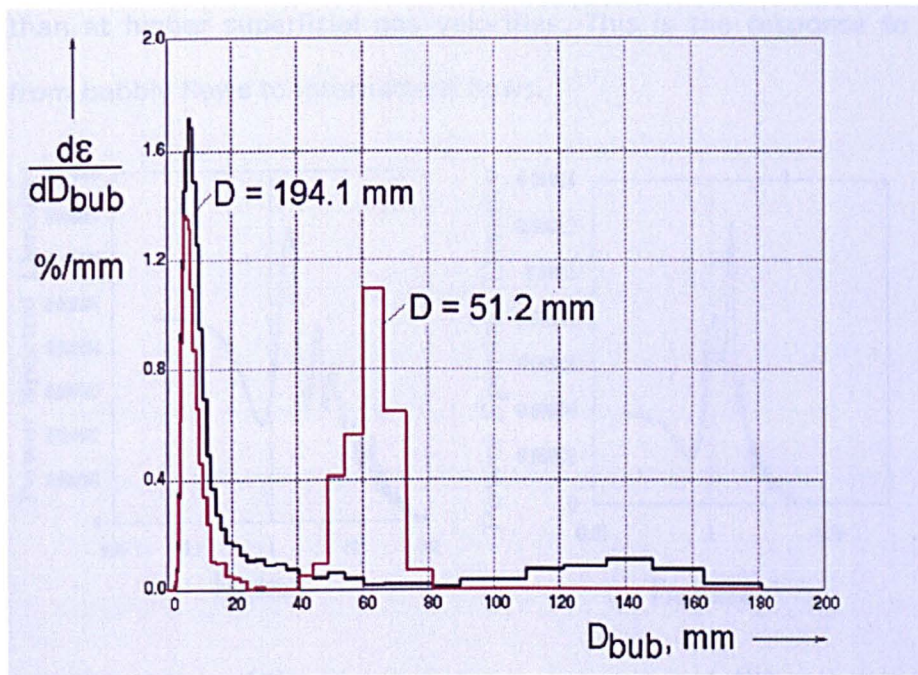
Figure 3.13: Comparison of bubble size distributions for 50mm and 200mm diameter pipes as measured by Prasser et al. (2004)

3.4.5   Flow pattern identification using other methods

3.4.5.1   Power Spectral Density (PSD)

Power spectral density function (PSD) shows the strength of the variations (in this case, it is taken for void fraction) as a function of frequency. In other words, it shows at which frequencies variations are strong and at which frequencies variations are weak. With the aid of power spectral density (PSD) analysis, it is possible to distinguish between periodic and chaotic responses. It is known that for a chaotic motion, the power spectrum is a continuous function. Since intermittent region of two-phase flow is regarded as chaotic, PSD analysis is a useful tool in identifying flow regimes. The transition from smooth flows to chaotic flows can be identified through the PSD signatures. In Figures 3.14(a)-(d) at low superficial gas velocities, the harmonic signal response is more chaotic

Abolore Abdulahi

than at higher superficial gas velocities. This is the response to changes from bubbly flows to intermittent flows.

(a)

(b)

(c)

(d)
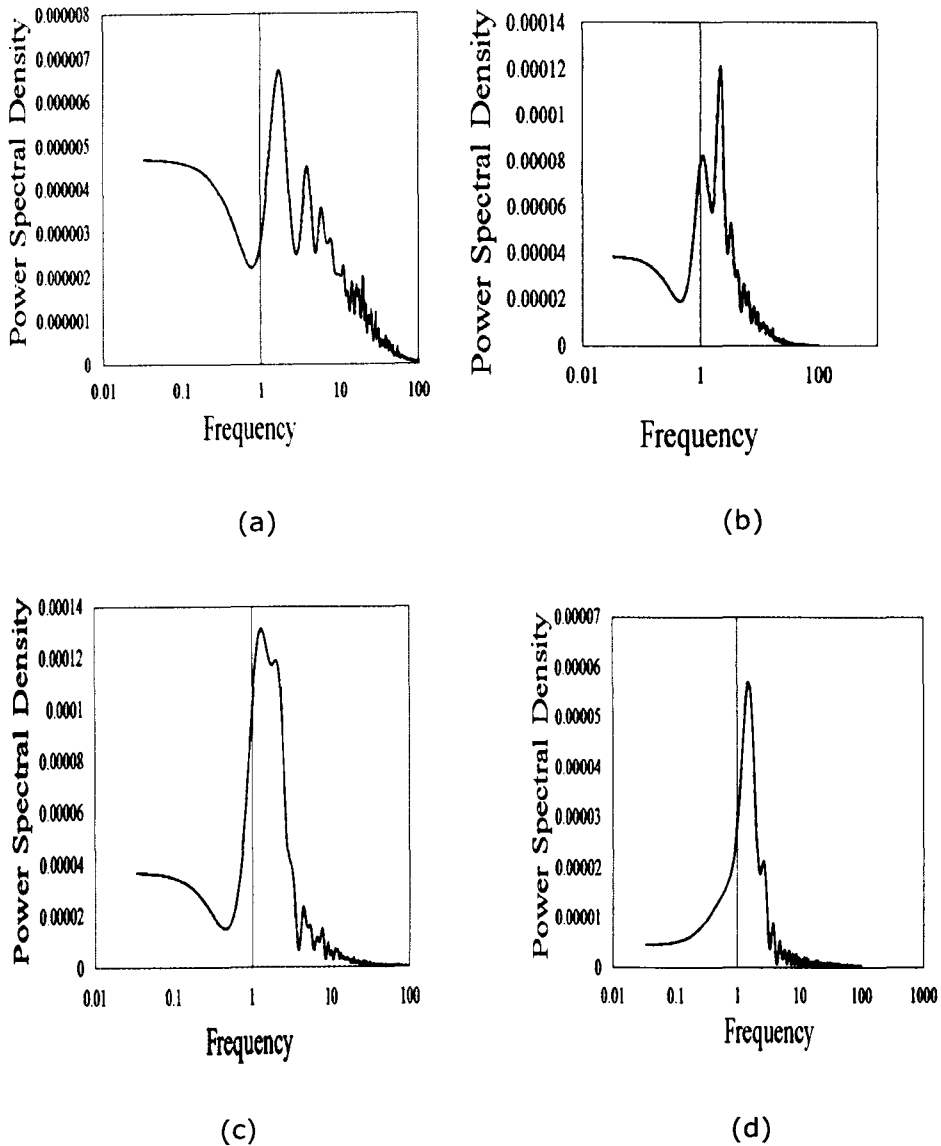
Figure 3.14: PSD and frequency plots at liquid superficial velocity of 0.4 m/s and gas superficial velocities (m/s): (a) 0.1, (b) 0.6, (c) 1.0, (d) 2.0

3.5   Summary

A set of data have been obtained on a large diameter pipe at high pressure with high viscosity liquid and high density gas. The following summary could be drawn from this chapter:

- The mechanistic flow pattern of Shoham (2006) performed well for the set of experimental conditions under review.

- The time series of void fraction revealed the absence of bridging gas troughs that is characteristic of slug flows.

- The characteristic twin peaked PDFs that indicates the presence of slug flows did not feature in any of the PDFs for the current study which highlights the absence of slug flows in big diameter pipes

- Radial distribution of void fraction show that for bubbly flows the bubbles tend to move away from the pipe core towards the pipe wall while they move towards the centre of the pipe for other flow regimes as a result of bubble coalescence. Hence for bubbly flows, the plot is nearly flat while for other flows the plots are almost parabolic.

- By using the frequencies from power spectral density, the change from one regime of flow to another can be identified as the harmonic signals smooth out as the flows move from bubbly to intermittent flows.

- Bubble size distribution plots reveal that the bubbles increased in diameter as the superficial gas velocities are increased. However, the two characteristic division of bubble layers observed by Prasser et al. (2004) in small diameter pipes was absent, while a similar shape for big pipe in Prasser's work has been observed in the current study.

- Pipe diameter, viscosity of the oil as well as the gas density have probably played a major role in shifting the flow regimes, hence, the usual flow pattern maps which have mainly been obtained from air-water experiments may not be relevant for handling such fluids. Although some of the flow maps do consider these fluid properties, they are unable to fit-in well for good flow delineation. New maps has however been suggested.

Chapter Four
Effect of pressure on a two-phase gas-viscous liquid flow

4.1   Introduction

Most work in two-phase flow has focused on pressures close to atmospheric. However, the conditions in oil and gas wells can be at very high pressures. Some recently discovered fields have pressures >300bar. Therefore, the effect of pressure on gas/liquid flows needs to be understood. When gas and liquid are forced to flow together inside a pipe, there are different geometrical configurations, or flow regimes, that occur. The regimes depend on the fluid properties, the size of the conduit and the flow rates of each of the phases. The flow regime can also depend on the configuration of the inlet; the flow regime may take some distance to develop and it can change with distance as (perhaps) the pressure, which affects the gas density changes. For fixed fluid properties and pipe configuration, the flow rates are the independent variables that when adjusted, will often lead to changes in the flow regime.

Studies on the effect of pressure on two-phase gas-liquid flows which have been carried out in the past have focused on water or other liquids with similar viscosities. Hence most of the available industrial models and correlations have been validated with experimental results from air-water data. In this chapter, an investigation into the effect of pressure on a two-phase flow of gas using a high viscosity liquid will be reported. This was carried out on a large diameter pipe (127mm). As earlier noted in chapter 3, the experiments were conducted at two different pressures: 7.9 and 4.5 bar. This chapter will compare the results for both pressures as well as

with other published data. For clarity, in this chapter low and high pressure refer to 4.5 and 7.9 bar respectively

4.2　Mean void fraction

4.2.1　Comparison of mean void fraction at low and high pressure

As a first step, mean void fraction acquired using a WMS for both pressure conditions are compared. These are shown in Figures 4.1 (a)-(d). At low superficial liquid velocities, the effect of pressure was insignificant because almost all the data fall on the same line as can be seen in Figures 4.1(a) and slightly apart in Figure 4.1(b) between gas superficial velocities of 0.5-2.5m/s. This may still be regarded to be within the uncertainty region for WMS (which has been reported by Da Silva et al. (2007) to have a confidence interval of 95%) However, in Figure 4.1 (c) as the liquid velocities increases the effect of pressure begins to show at a gas superficial velocity of 0.8m/s at a liquid velocity of 0.6m/s (Figure 4.1c. Beyond this velocity, the mean void fraction at high pressure were seen to be higher than those at low pressure, Figure 4.1d

(a)

(b)

(c)

(d)
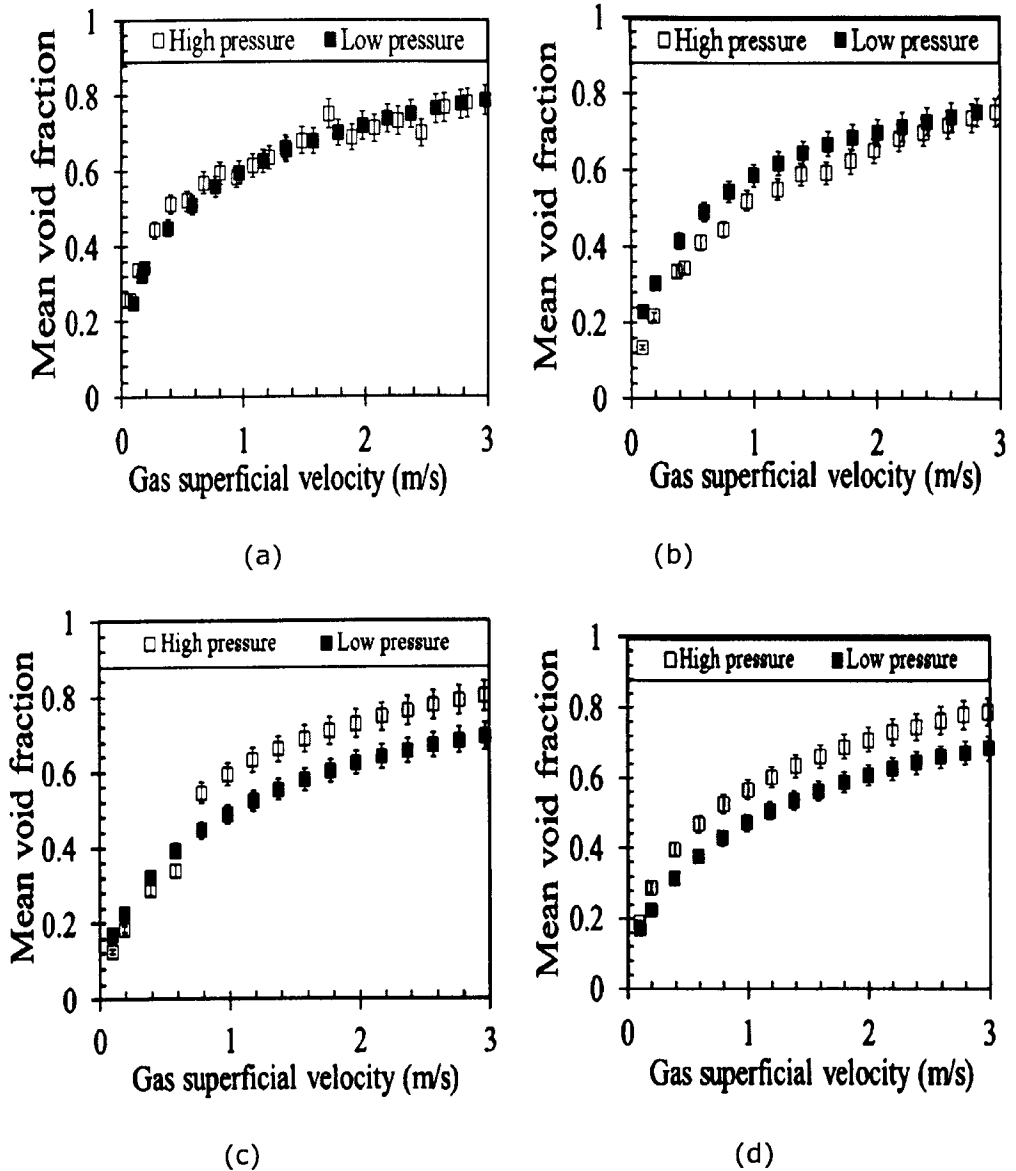
Figure 4.1: Effect of pressure on void fraction at superficial liquid velocities (m/s) (a) 0.2, (b) 0.4, (c) 0.6, (d) 0.8

4.2.2   Comparison between calculated void fraction and measured void fraction

Effect of pressure can be further evaluated by comparing the void fraction values of both low and high pressure experiments obtained from WMS with those calculated using data acquired from differential pressure transducers over a range of superficial liquid velocities. In Figure 4.2, the void fraction

calculated from equation 4.1 as well as the measured void fraction were almost the same at low pressure.

$$\left(\frac{\left(\frac{dp}{dz} \Big/ g \right) - \rho_l}{\left(\rho_g - \rho_l \right)} \right) \qquad\qquad (4.1)$$

However when the pressure was elevated, the difference becomes significant, especially at low superficial gas velocities. The calculated void fraction was derived from the relationship between total pressure gradient, gravitational pressure gradient (assuming frictional pressure gradient is zero and a steady state flow with acceleration pressure gradient equals zero). Abduvayt et al. (2003) show that the transition between flow regimes occurs as a result of changes in the pressure in the pipe, pipe diameter and the inclination angle even with the same superficial gas velocity and liquid velocities as can be seen in Figures 4.2 (a)-(e) at different pressures. However comparing measured void fraction with calculated void fraction may not necessarily reveal this transition as evidenced in Figures 4.2 (a)-(e).

(a)   (b)

(c)   (d)
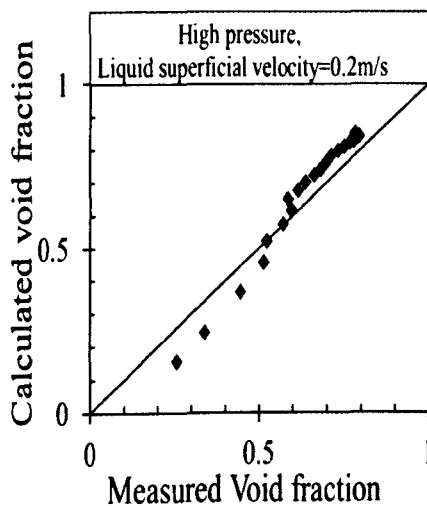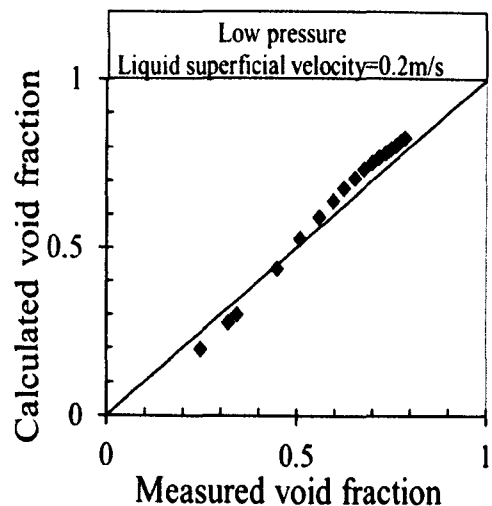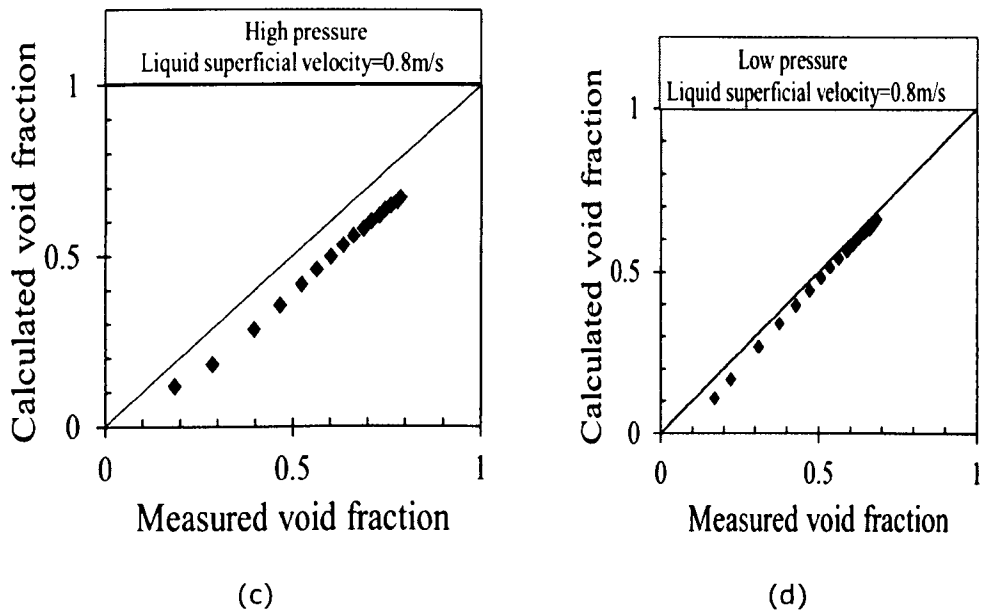
Figure 4.2: Comparison between Measured void fraction from Wire Mesh Sensor and calculated void fraction from Differential Pressure Transducers at different velocities

4.2.3   Comparison of measured void fraction with other void fraction prediction models

The oil industry has a great number of void fraction prediction models. Many of these models have been modified to fit into transient flows to effectively predict flow assurance and multiphase flows. For instance, OLGA for flow assurance as well as 1D LedaFlow and Maximus use some of these models in flow assurance predictions. Hence, it is imperative to carry out analysis based on these models in order to suggest ways of improving on the performance of the existing models since some of these models have been observed to either under-predict or over-predict void fraction. In this section, comparisons will be made with the models at the conditions set for the experimental campaign.

Figures 4.3-4.5 show some of the comparisons between experimental work and predictions from various models. In Figure 4.3, the liquid momentum

was too low and the predicted void fraction deviates significantly from those obtained from experiments. However, the Beggs and Brill model at a superficial liquid velocity of 0.1m/s and the CISE/Friedel model at a superficial liquid velocity of 0.2m/s have predictions closer to those obtained from the experimental work. The liquid momentum for the flow conditions shown in Figure 4.4 is greater. The CISE/Friedel and homogenous models over-predict the void fraction at low liquid (0.4m/s) and high gas superficial velocities while Beggs and Brills under-predicts at superficial liquid velocity of 0.6m/s. In Figure 4.5, Uls=0.8m/s both the homogenous and CISE/Friedel models perform well while the Beggs and Brill model over-predicts the void fraction.

(a)   (b)
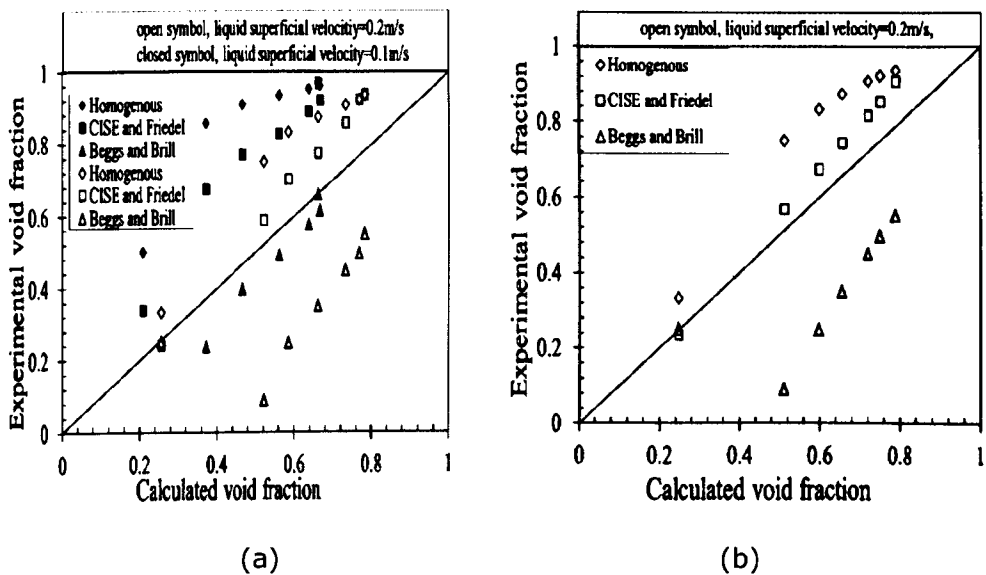
Figure 4.3: Comparison of models with experimental data at superficial velocities of 0.1m/s and 0.2m/s (a) High pressure (b) Low pressure
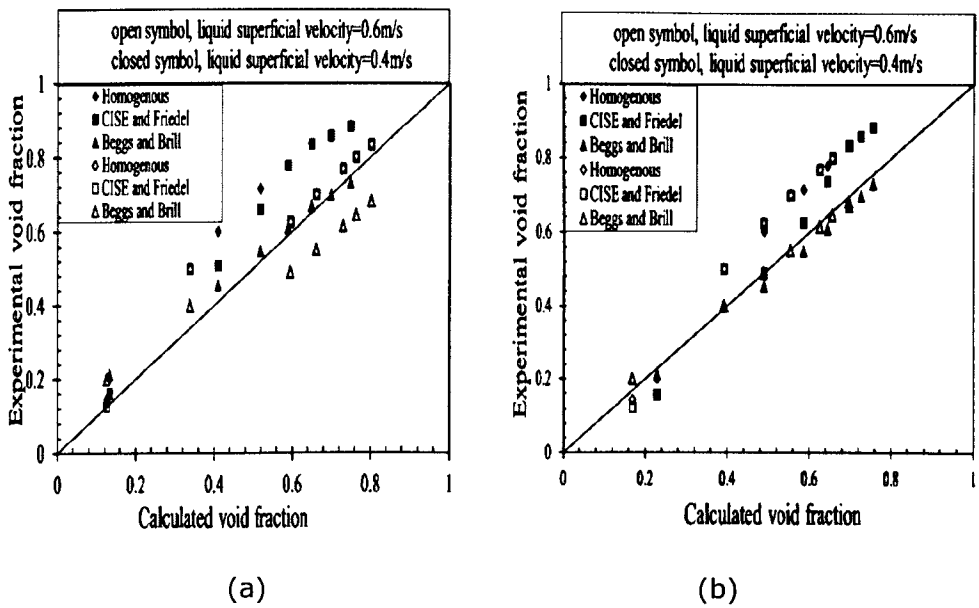
Figure 4.4: Comparison of models with experimental data at superficial velocities of 0.4m/s and 0.6m/s (a) High pressure (b) Low pressure
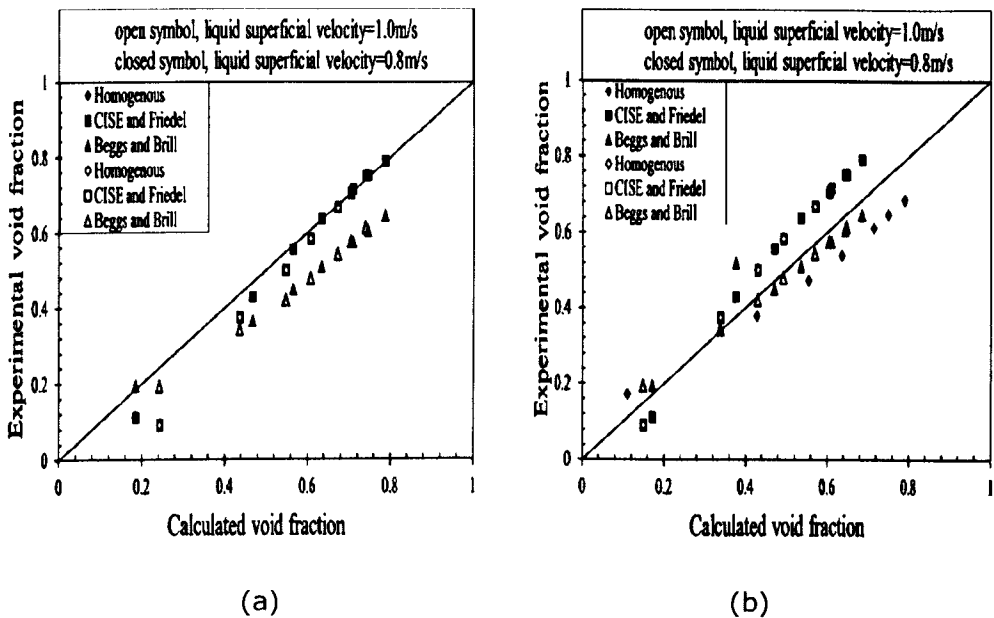
Figure 4.5: Comparison of models with experimental data at superficial velocities of 0.8m/s and 1.0m/s (a) High pressure (b) Low pressure

In summary, the models are quite effective at higher liquid velocities. These liquid velocities are the points at which the liquid momentum is high enough to avoid reverse flows, which may occur at low liquid superficial

velocities. In addition, the results show that the models perform better at lower pressure than at high pressure as can be seen in Figure 4.5. Beggs and Brill model appears to be the best option as it is the closest to experimental results in overall. As reported by Szalinski et al. (2010), these correlation perform well with oil at low viscosity although poorly with water at a lower viscosity. However, their performance with highly viscous liquid is not well understood.

4.3   Pressure gradient

The pressure gradient relationship with superficial gas velocity was found to be linear for both low and high pressure experiments as can be seen in Figure 4.6 at low superficial liquid velocity. However, this changed as the liquid velocity increased further. In this case, the slope is in a decreasing direction because at this stage of the co-current flow, the gravitational portion of the pressure gradient dominates over the frictional pressure gradient which is in agreement with Owen (1986), as reported by Hewitt (2012). However, the minima and maxima in the plot shown by Owen (see Figure 2.13) are absent in this case. Since this was used to delineate flow pattern, it is perhaps a result of the pipe diameter involved in the current study preventing the formation of slug flow. This observation was also reported by Zangana (2011).

Abolore Abdulahi
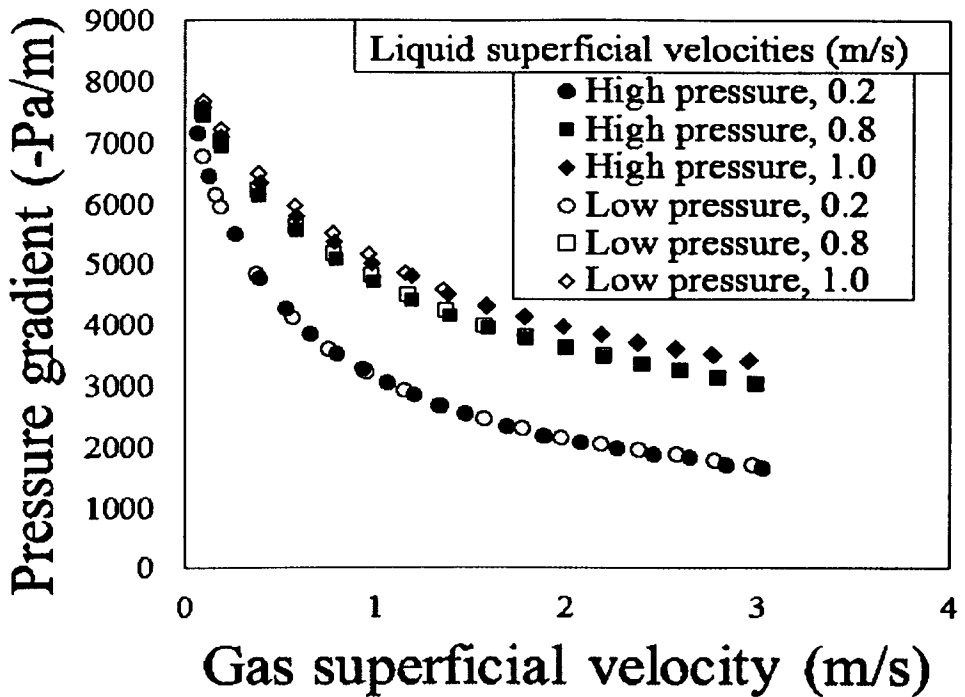
Figure 4.6: Pressure gradient relationship with superficial gas velocities

The axes of Figure 4.6 are dimensional with units. It might be more appropriate to examine the data in terms of equivalent dimensionless groups. Pressure drop can be written as a ratio to the gravity head based on the density difference between gas and liquid in a manner similar to that used by Owen (1984). The gas superficial velocity was replaced by a

Kutateladze number, $\dfrac{u_{gs}\rho_g^{0.5}}{\left(\left[\rho_l-\rho_g\right]g\sigma\right)^{0.25}}$, rather than the Froude number,

expressed as $V_G{}^*$ in Owen (1986) as this was more appropriate for larger diameter pipes. As can be seen in Figure 4.7, the effect of pressure becomes more visible using these axes. However, the effect is still small.
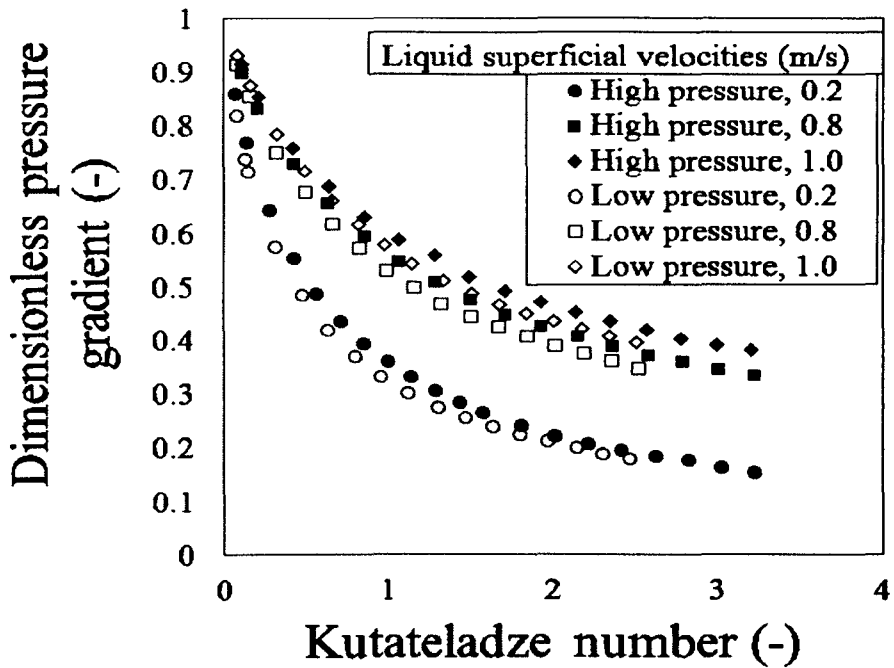
Figure 4.7: Dimensionless pressure gradient relationship with Kutateladze number

The clear difference between Figures 4.6 and 4.7 is as a result of the changes in gas density. For Figure 4.6, the changing function was gas superficial velocity but for Figure 4.7, gas densities changed as well as the gas superficial velocities.

4.4   Flow structures comparison

The gas-liquid flow structures, as revealed by the wire mesh sensor are illustrated in Figures 4.8-4.9 at high and low pressures. At low superficial gas velocities, there are no significant changes in the bubble distribution between the high and low pressures. However, at higher velocities, wisps are easily noticed when the pressure was elevated, as can be observed in Figure 4.9. (Note, blue region represents liquid/oil while the red region represents gas, SF_6). Wisps are large liquid objects which are observed within the gas core at both high liquid and gas flow rates. Their appearance has been compared to ectoplasm. Hence to identify a wisp,

there must be merging together of liquid droplets which leads to the formation of large lumps of liquid in the gas core. As can be seen in Figure 4.9 (a), large lumps of liquid which are represented with blue colour break up the continuous gas core (shown in red colour).

Hawkes et al. (2000) have suggested that the wisps arise from agglomeration of the drops that must be present in large concentrations within the gas core. Azzopardi et al. (2008) have shown the existence of these wisps in the region usually identified as churn flow region.

A   B

(0.1)   (0.6)   (1.0) (1.4) (2.0)   (2.4)   (3.0)   (0.1)   (0.6)   (1.0) (1.4) (2.0)   (2.4)   (3.0)
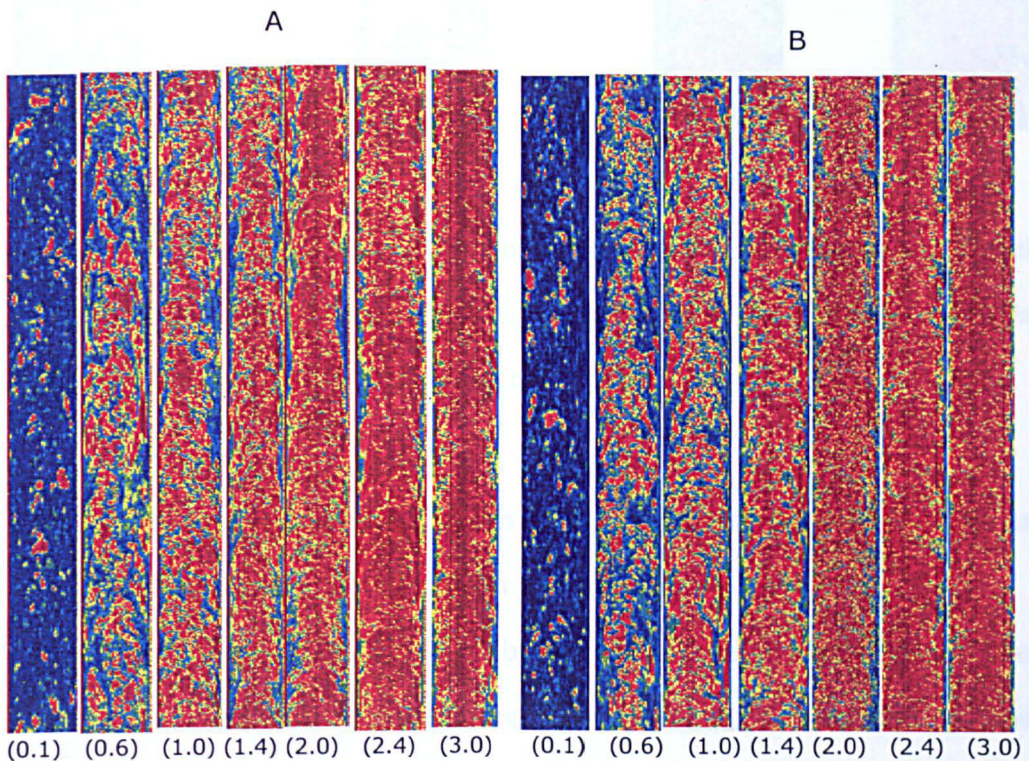
Figure 4.8: Visualisation of wire mesh sensor data with superficial liquid velocity at 0.4 m/s and gas superficial velocity as indicated below each structure (A and B at high and low pressures respectively)

Wisps

(a)   (b)   (c)   (d)

Figure 4.9: Visualisation of wire-mesh sensor data at liquid superficial velocity of 0.2 m/s and gas superficial velocities of (a) 1.0, (b) 1.4 m/s High pressure; (c) 1.0, (d) 1.4 m/s Low pressure

Wisps also exist at low pressures but this highlights that wisps exist at high pressure, as may be the case in subsea systems.

Interestingly, wisps were observed by Hernandez Perez et al. (2010) and Sharaf et al. (2013) at the same superficial liquid velocities. Wisps frequencies with these published works are compared in section 4.7.

4.5   Bubble size distribution

Details on the methodology for extracting bubbles size information from Wire mesh sensor data can be found in Prasser et al. (2001). Bubble size distributions for selected gas superficial velocities and at liquid superficial velocities of 0.2, 0.4, 0.6, 0.8 and 1.0 m/s are shown in Figure 4.10. They are constructed by summing the contribution of the bubbles of a given

range of diameters to the integral volumetric gas fraction. The partial gas

fraction ($d\epsilon/dD_{Bub}$) is plotted against the equivalent bubble diameter (D_{Bub}).

When integration is carried out over the entire bubble size distribution, the

result is the volumetric gas fraction averaged over time and cross-section.

At the lowest liquid velocity of 0.2m/s, high pressure causes formation of

bubbles greater than 100mm in diameter while lower pressure causes

bubbles with diameters less than 100mm to be formed as shown in Figure

4.10 (a)-(b). However, as the liquid velocity is increased the bubble sizes

for low pressure conditions become larger as shown in Figure 4.10 (c)-(d).

(a)

(b)

(c)

(d)

Abolore Abdulahi

(e)   (f)
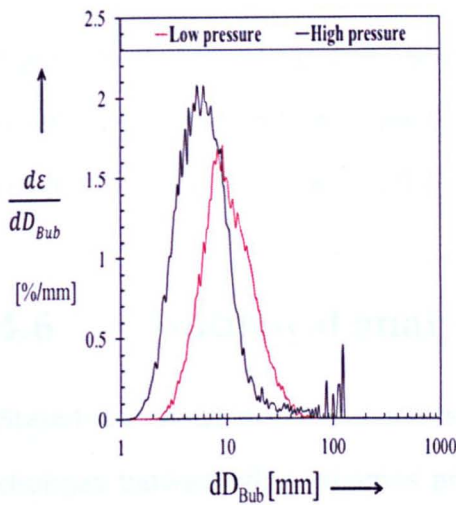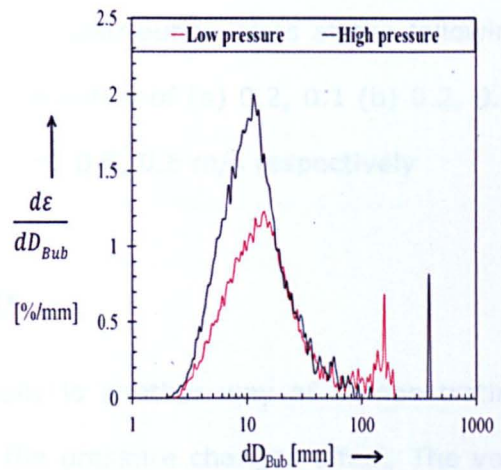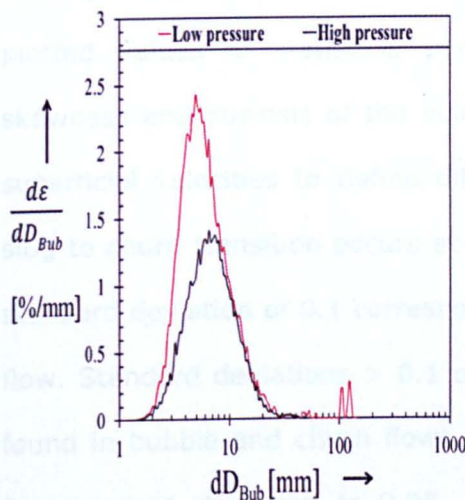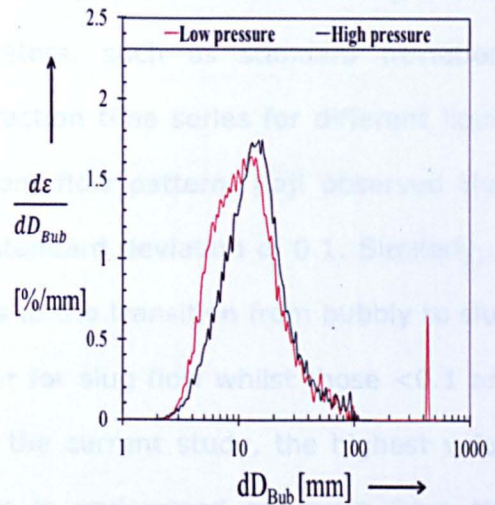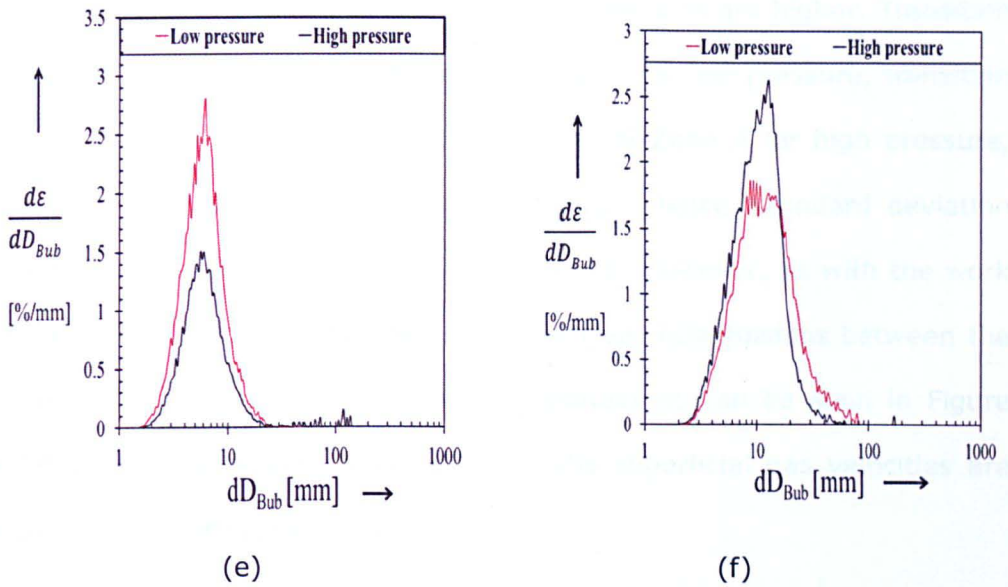
Figure 4.10: Some selected bubble size distribution plots at the following conditions: liquid and gas superficial velocities of (a) 0.2, 0.1 (b) 0.2, 0.6, (c) 0.4, 0.1, (d) 0.4, 0.6, (e) 0.6, 0.1, (f) 0.6, 0.6 m/s respectively

4.6   Statistical analysis

Statistical analysis of data statistically is another way of demonstrating changes between flow regimes and the pressure changes effect. The void fraction data considered in the current work have been examined to identify a more objective method of flow pattern delineation. Kaji (2008) plotted values of statistical parameters, such as standard deviation, skewness and kurtosis of the void fraction time series for different liquid superficial velocities to define different flow pattern. Kaji observed that slug to churn transition occurs at a standard deviation of 0.1. Similarly, a standard deviation of 0.1 corresponds to the transition from bubbly to slug flow. Standard deviations > 0.1 occur for slug flow whilst those <0.1 are found in bubble and churn flows. In the current study, the highest value for standard deviation is 0.05. This is understood to result from the absence of slug flow. The peak of standard deviation could be a transition from bubbly flow to intermittent flow, as can be seen in Figure 4.11. The

standard deviation values of the lower pressure data are higher. Transition occurs at different positions for each pressure (for low pressure, transition occurs in zone B while the transition occurs in Zone A for high pressure, especially for low superficial liquid velocities). Hence, standard deviation could be a useful tool to identify flow regimes. However, as with the work of Kaji (2008), Figure 4.12 does not show clear relationships between the values of Kurtosis and flow pattern. Skewness as can be seen in Figure 4.13 show a decreasing relationship as the superficial gas velocities are increased for both pressure variation.
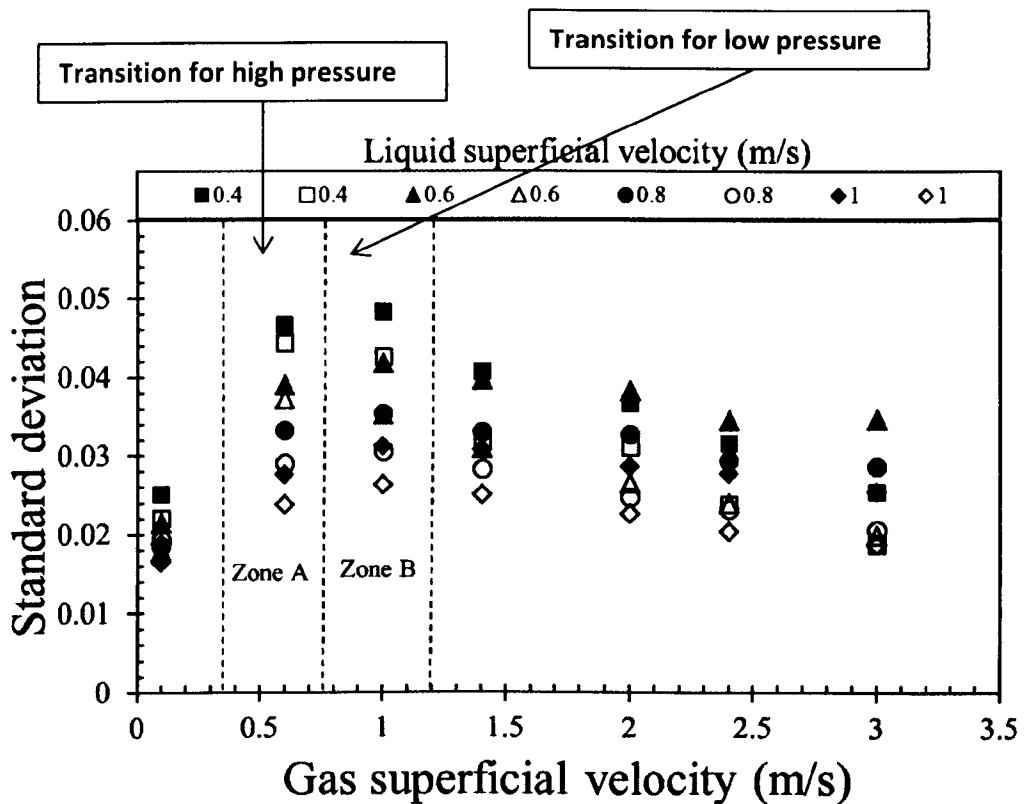
Figure 4.11:   Standard deviation of void fraction versus superficial gas velocity (open symbol-high pressure, closed symbol-low pressure)
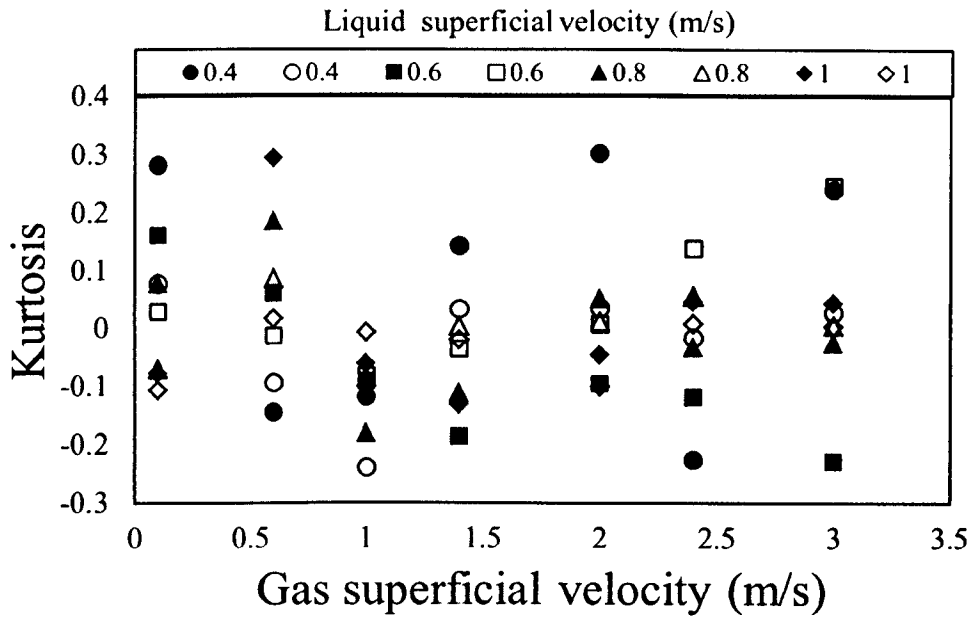
Figure 4.12: Kurtosis versus superficial gas velocity (open symbol-high pressure, closed symbol-low pressure)
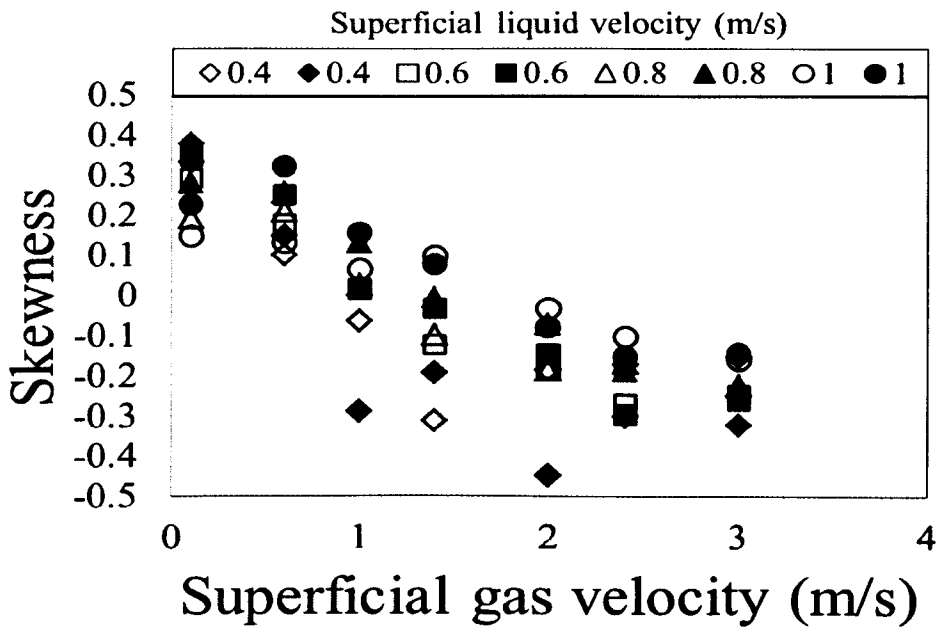
Figure 4.13: Skewness versus superficial gas velocity (open symbol-high pressure, closed symbol-low pressure)

Abolore Abdulahi

4.7   Effect on frequency

A different approach from what was used by Hubbard (1965) and Nydal (1991) has been used to obtain the frequency. This is referred to as the Power Spectral Density (PSD) method. Hubbard and Duckler (1966) used PSD of pressure fluctuation to identify flows such as separated, dispersed and intermittent flows for horizontal pipes. Dominant frequencies were obtained using the Power Spectrum Density functions (PSD). This was estimated by using Fourier transform of the Auto Covariance function of the void fraction time series. Further details on this analytical method have been reported by Kaji (2008).

When the dominant frequencies are acquired using this method, they are plotted against their respective gas superficial velocities, as shown in Figure 4.14. In most cases, the frequencies increase as the pressure is increased (Figure 4.14). They are also higher as the liquid superficial velocities increase. However, the trends are quite irregular at low gas velocities. These can be attributed to changes in flow pattern, perhaps from bubbly flow to intermittent regime. This is similar to what was reported by Szalinski et al. (2010)
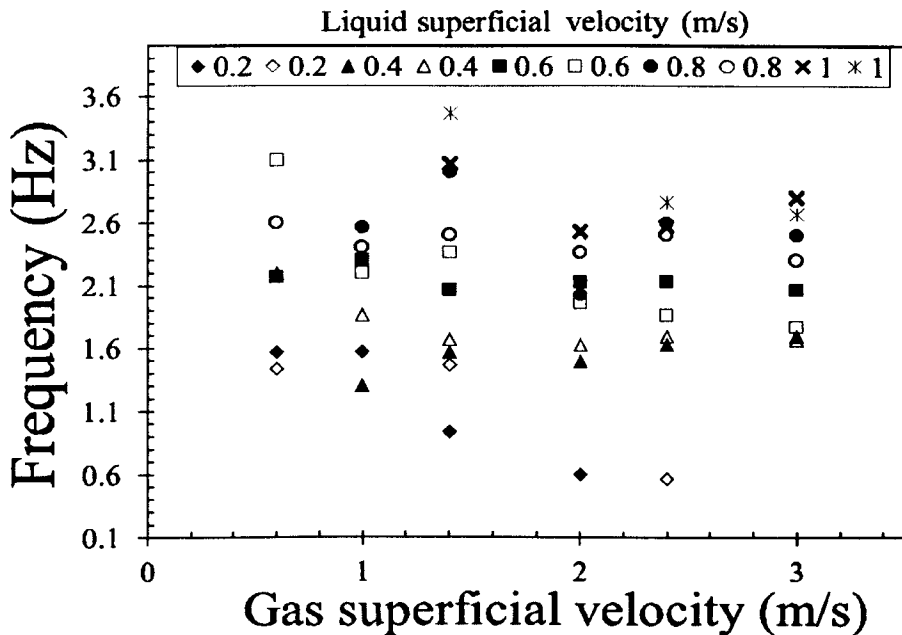
Figure 4.14: Frequency of periodic structures as derived from power spectral density analysis: closed symbols and x =High pressure, open symbols and ✶=Low pressure

A good way to describe the frequency of periodic structures is in terms of the Strouhal number (fD_t/u). As could be seen in Figure 4.15, the data for gas based Strouhal number versus the Lockhart-Martinelli parameter for low and high pressures lie on a line parallel with the data of Azzopardi et al. (2010a), Legius et al. (1997) and others. This is expected as Gokcal et al. (2009) reported that there was a distinct effect of viscosity in their data, which was for horizontal pipes. In fact, the higher the viscosity in this plot the higher the movement to the left of the plot for all cases compared. In other words, data for low viscosity liquid (for instance, water) lie to the far right while those for higher viscosity (for instance, Oil with viscosity of 35cp in the current study) lie to the far left of the plot.

Abolore Abdulahi
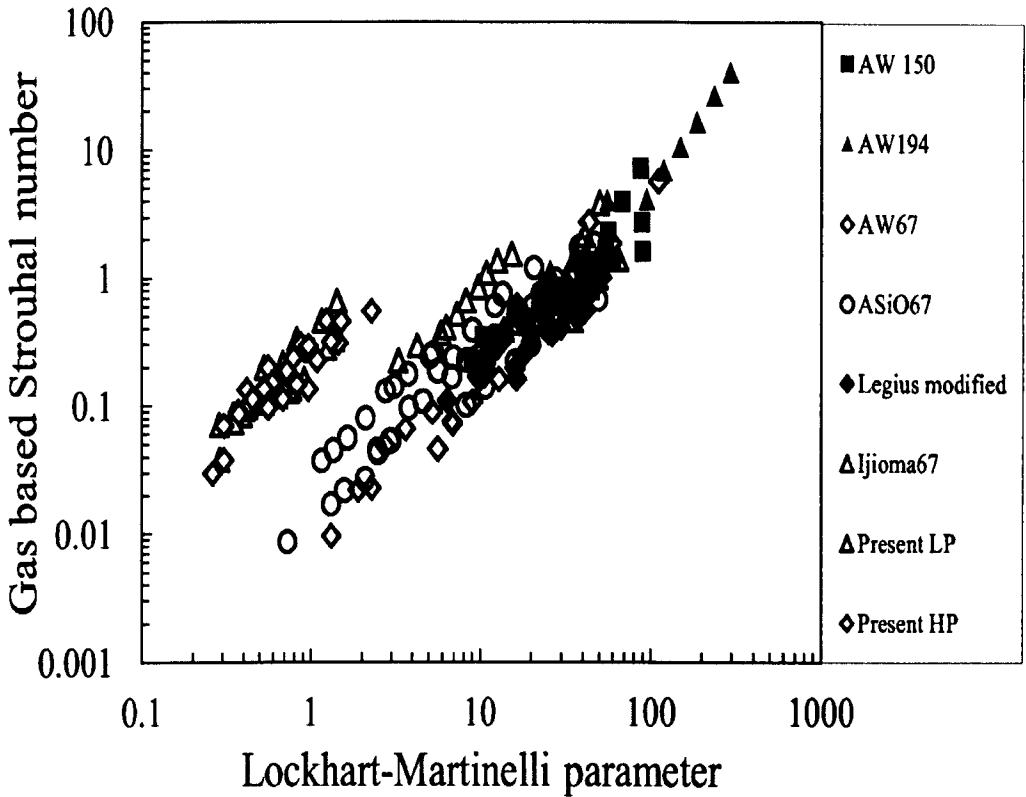
Figure 4.15: Gas based Strouhal number versus Lockhart-Martinelli parameter (Note AW=Air-water,ASiO=Air-Silicone Oil while 150,194 and 67 mean corresponding pipe diameters)

In Figure 4.15, the Silicone Oil used by Azzopardi et al. (2010a) denoted as Ijioma67 had a viscosity of 5mPa.s and water experiments had viscosity of 1mPa.s while Legius et al. (1997) work was based on experiments using water with a viscosity of 1mPa.s. By plotting gas based Strouhal number against the product of the dimensionless inverse viscosity number and velocity ratio as proposed by Gokcal et al. (2009) to account for viscosity effect (see Figure 4.16), the data in the present study is compared with data of Szalinski et al. (2010) who used oil with a viscosity of 5cp in a 67mm diameter pipe. Similar trend is shown between the compared data. Hence, the effect of viscosity is imperative in proposing a good design.
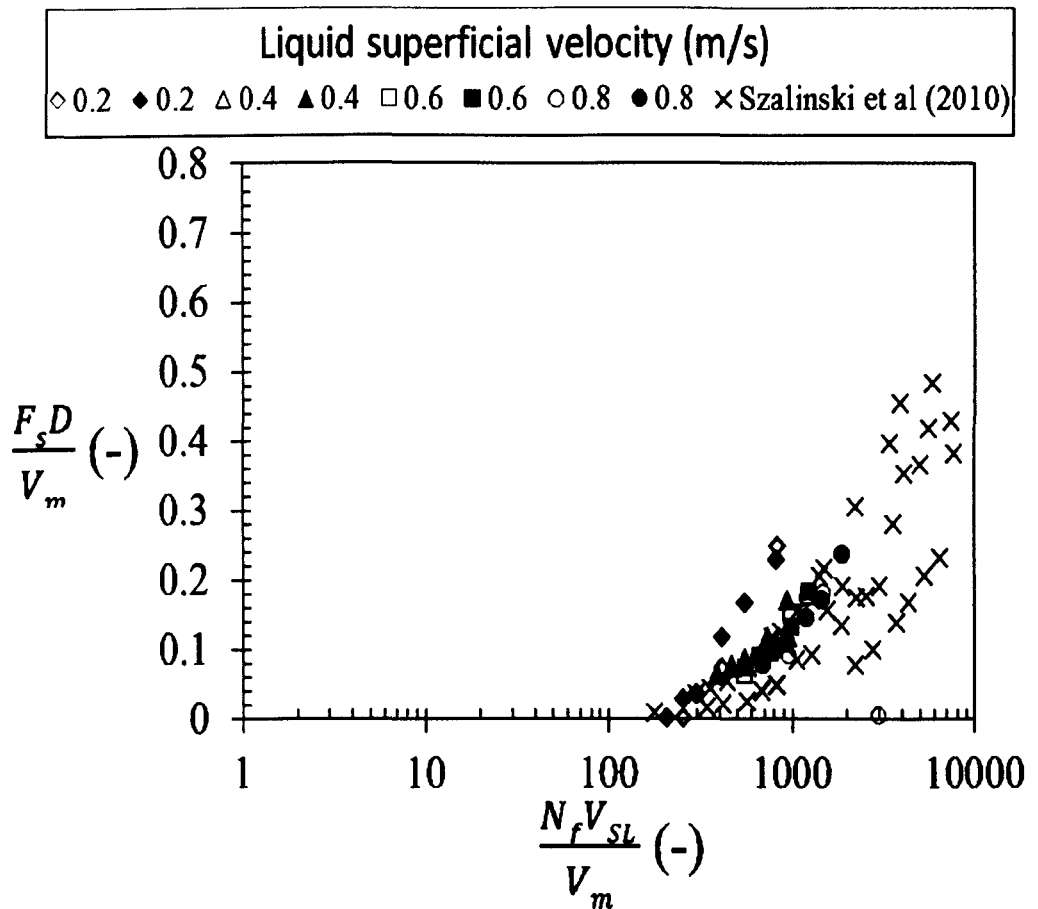
Figure 4.16: Gas based Strouhal number versus Inverse viscosity number

and velocity ratio (where $N_f = \dfrac{D^{1.5}\sqrt{\rho_l\left(\rho_l - \rho_g\right)g}}{\mu_l}$)

Since wisps were observed in the current work as earlier reported in section 4.4, it is worth plotting the frequencies of these wisps to compare with published data in Figure 4.17. These wisps are seen to increase with increase gas superficial velocity, which is in agreement with those observed by Sharaf et al. (2013) but the trend vary from those observed by Hernandez Perez et al. (2010).

Abolore Abdulahi
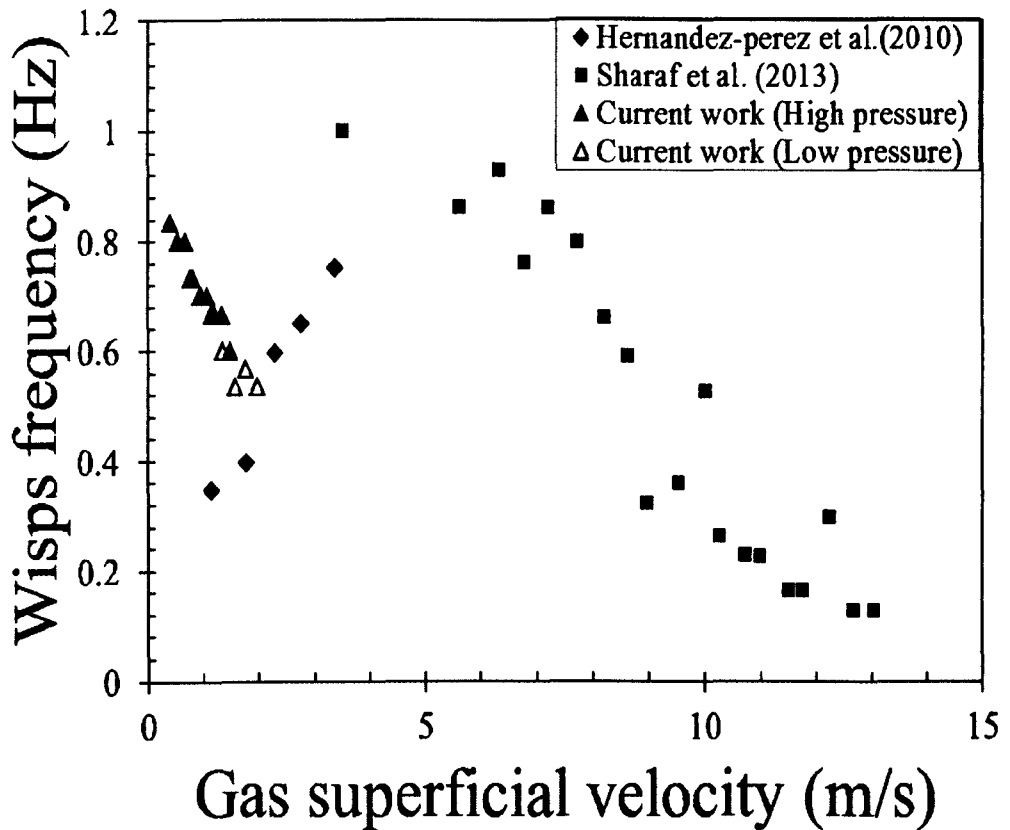
Figure 4.17: Wisps frequency versus gas superficial velocity compared with data from Sharaf et al. (2013) and Hernandez Perez et al. (2010)

Since the viscosities of the fluids for all cases compared in Figure 4.17 are different, it is more logical to make comparison based on the viscosity change. Figure 4.18 expresses Wisps frequencies in terms of dimensionless numbers, with consideration given to viscosity changes. On a general note, the trends shown in this plot are seen to be the same especially comparing the work of Sharaf et al. (2013) and the current work.
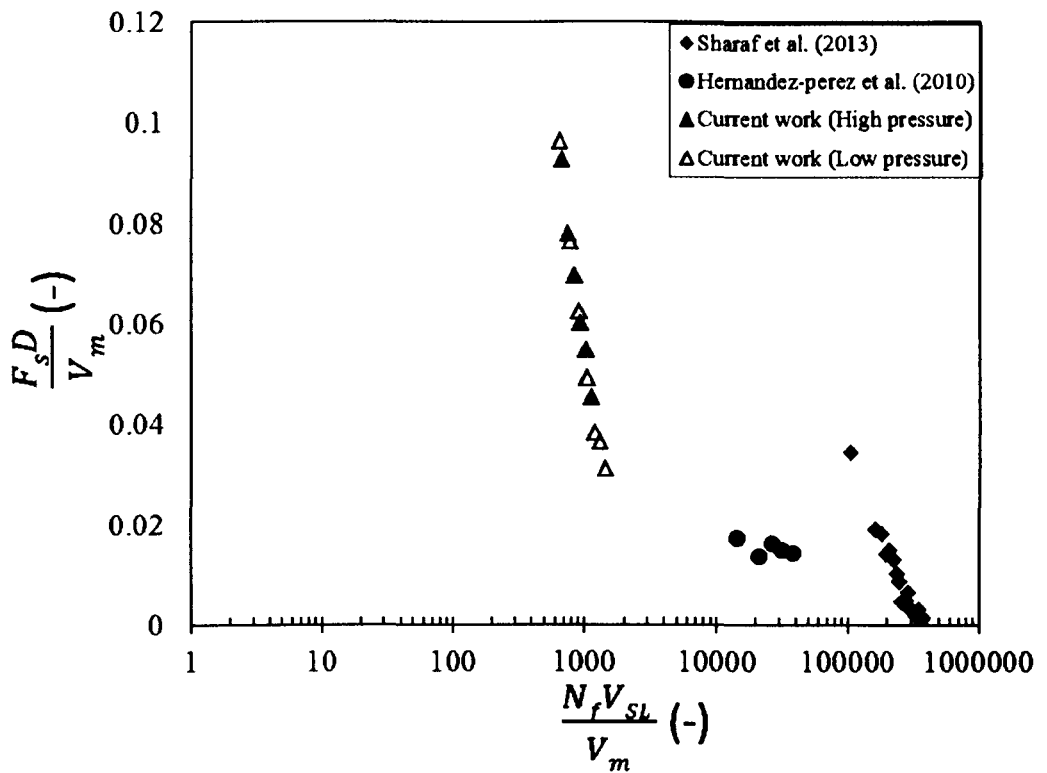
Figure 4.18: Strouhal number versus product of viscosity number and velocity ratio plotted and compared with data from Sharaf et al. (2013) and Hernandez Perez et al. (2010)

When the differences in gas superficial velocities are analysed in terms of Weber number, the resulting plots show similar trend with the work by Sharaf et al. (2013), as can be seen in Figure 4.19. The ratio of wisps frequency (f_w) to the overall frequency (f) is plotted against the Weber number in Figure 4.19. This is high at low Weber number in the work by Sharaf et al. (2013) compared to the current study. This may be attributed to the viscous effect of the liquid on the bubble coalescence process.
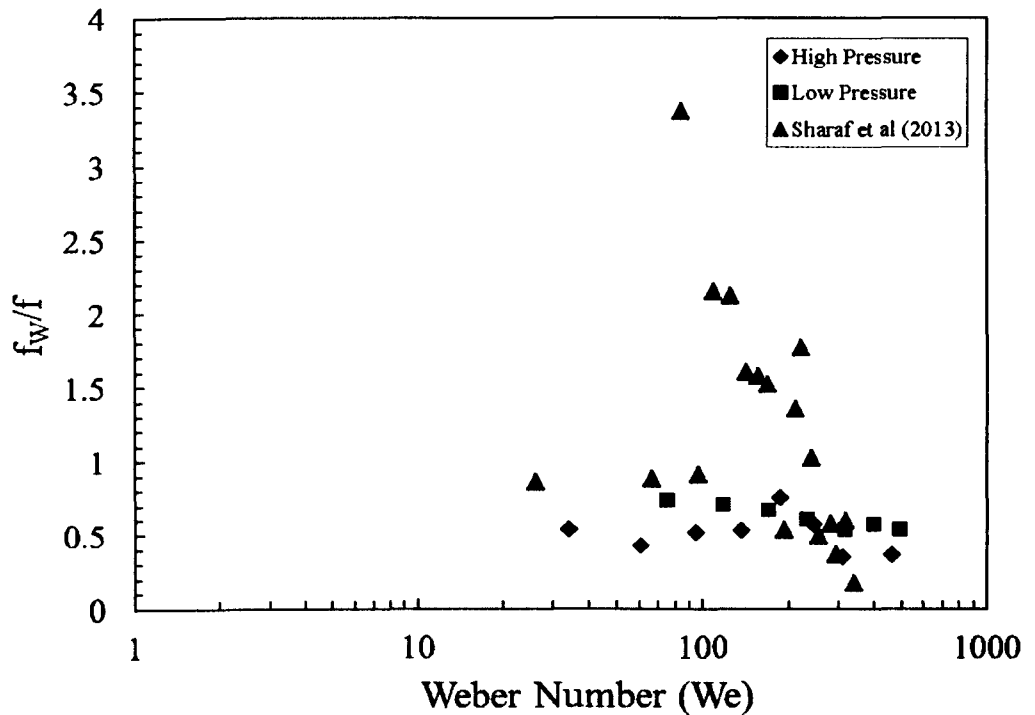
Figure 4.19: Ratio of wisps frequency to overall frequency against Weber number for both low and high pressure compared with data from Sharaf et al. (2013)

4.8   Summary

Two-phase flow data at two different pressure conditions have been analysed and the results have been compared to see the effect of pressure as well as the performance of predictive models. The following can be summarised for this chapter:

• With the flow structures, wisps are observed at higher pressure and at lower pressure using the Wire Mesh Sensor

• Pressure has more effect on mean void fraction at higher liquid superficial velocity than at low liquid velocities as shown in the text.

• As the liquid velocity goes up, the calculated void fraction shows some disparity from measured void fraction.

- Correlations of CISE/Friedel, homogeneous and Beggs and Brills perform well at higher liquid superficial velocities when compared with those measured from experiment for void fraction. This could be attributed to higher momentum at higher liquid velocity. Better agreement was observed for higher pressure than for lower pressure.

- The pressure gradient relationship observed by Owen (1984) is absent in the current study due to the non-appearance of slugs in large diameter pipes.

- Viscosity effect can be moderated using dimensionless numbers

- Standard deviation is a promising tool for flow regime delineation although skewness and kurtosis do not reveal any significant flow pattern.

Chapter Five
Experimental Arrangement for Downflow with 67mm vertical pipe

5.1   Introduction

The previous chapters provided an insight into two-phase flow in vertical pipes. However, classical slug flow was completely absent in such a pipe diameter. Since the most common type of flow regime observed in gas-liquid flows in well risers is slug flow, the knowledge of the liquid distribution, and hence the void fraction within the liquid slug, is important for the design of slug catchers for pipelines. As discussed in Chapter Two, a typical slug unit has two sections: the Taylor bubble and the liquid slug section. Gas from the Taylor bubble is entrained in the liquid slug below it for a flow in pipes. However, the entrained gas is difficult to measure in a two-phase concurrent flow. Hence, a method was devised to hold the slug unit stationary. The first authors to utilise this method were Davidson and Kirk (1969). In a subsequent work by Davidson et al. (1979), the method was further developed. Other authors, such as Riiser et al. (1992), Su and Metcalfe (1997), Delfos (1996) and Bacon et al. (1995), have also used methods similar to the one proposed by Davidson and Kirk (1969). In this chapter, a combination of the previous methods and an entirely different approach for a stationary Taylor bubble will be discussed and evaluated. The different approach which involves holding a bubble stationary using spherical and conical caps will be discussed further in section 5.2.3

Abolore Abdulahi

5.2   Overview of the flow facilities

To generate a stationary Taylor bubble, the closed liquid circuit, shown schematically in Figure 5.1, with a working section of 67mm internal diameter pipe and length 3m, and an open gas circuit was employed. The experimental system allowed investigations of liquid flow rates ranging from 10-150 litres/minute and for gas flow rates from 0-10 litres/minute. In the work reported in this and the subsequent two Chapters, tap water was used as the liquid. It was maintained at 22±0.5°C. While the work reported in Chapter 8 used oil. The gas used was air taken from the laboratory compressed air supply.

A full description of the experimental rig can be found in section 5.2.1, with the experimental procedures summarised in section 5.2.2. Three different physical cases were investigated across a range of conditions. Different gas injection geometry configurations were used to generate different stationary bubble shapes. This is described in more details in section 5.2.3. High speed video imaging was utilised to capture details of the flow which is described in section 5.4.1. Information relating to the measurement methodologies regarding void fraction acquisition with the use of wire mesh sensor can be found in section 5.4.2

5.2.1   Experimental Apparatus

Figure 5.1 provides a schematic of the experimental rig, highlighting features of the working section in the enlarged view within the box to the right of the overall schematic. The liquid flow is driven by an adjustable progressive cavity pump whose rotation speed can be controlled manually to achieve a desired flow rate. To select the liquid flow rate, a series of valves are used in conjunction with the pump controls with a bypass circuit incorporated into the system to provide finer control on flow rate adjustment. Flow measurement was via a turbine flowmeter, model MG025

manufactured by Trimec Industries, which can measure liquid flow rate in the range 10-150 litres/min up to a temperature of $80^\circ C$ and a pressure of 20bar. It has an accuracy of $\pm 0.5\%$ of reading and a repeatability of 0.033%.

The pipe section immediately after the pump before the riser is well-jacketed with both inner and outer pipes to prevent increase in temperature. The inner pipe conveys the working fluid while the outer pipe has a counter-current flow of cold water which ran round the pipe containing the working fluid to ensure the temperature is maintained. A thermocouple is connected to this end which ensured that temperature is monitored periodically. The pipework outside of the working section was constructed with copper pipe 50.8mm in inner diameter, with a transition to the 67mm internal diameter perspex pipe. The copper pipe is joined to the perspex pipe on the test section by a flange. The working section is made of perspex pipe, primarily to allow visibility of fluid flow, and had an internal diameter of 67mm, a thickness of 5mm and a length of approximately 2m.
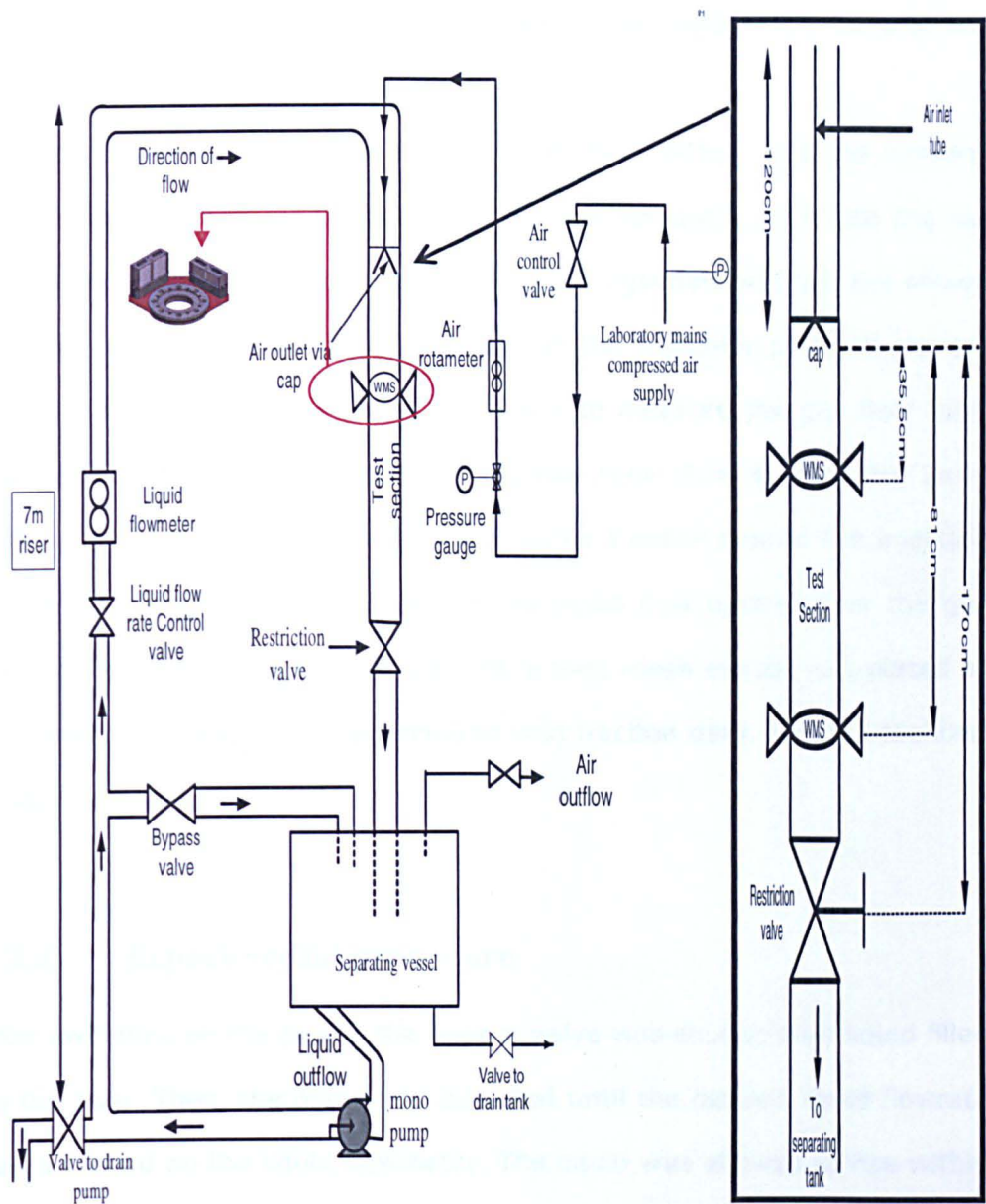
Figure 5.1: Bubble Hold down facility: (left) test facility (right) test section with the two positions of WMS

At the bottom of the working section there is a valve to provide a facility to prime the equipment to a fully flooded condition. After passing through the test section, the two-phase mixture was fed to a large separator vessel. The separation of gas from the liquid was enhanced through the presence of baffles, as well as fine and coarse meshes in the tank. The latter also helped in sieving from the liquid any impurity that may be present in the

flow loop. The total capacity of the liquid in the system was 10% of the liquid held within the separator vessel.

The gas system was an open system with the injection into the working section as shown in Figure 5.2. The gas was released back into the lab from a vent in the separator vessel. The gas injection systems are shown in more detail in Figure 5.3. Upstream of the injection point, there are pressure regulation points and a rotameter to measure the gas flow rate. The gas injection was delivered by a narrow tube of inner diameter 7mm and outer diameter of 10mm, which includes a collar around the injection pipe to provide flow straightening of the liquid flow upstream of the gas entry point. Within the working section, a wire mesh sensor was placed at two positions to capture time averaged void fraction data. This is described in section 5.4.2

5.2.2   Experimental procedure

After switching on the pump, the bypass valve was shut so that liquid filled up the riser. Then, the pump was adjusted until the desired liquid flowrate was achieved on the liquid flowmeter. The liquid was allowed to rise within the test section up to where the nose of the bubble was formed. This was made possible through a valve located at about 2.9m below the downcomer which helped to cause a restriction to flow. With this restriction, liquid built up to a level above the cap or the injection points shown in Figure 5.2, which formed a liquid column. Air was then introduced at this point. It took several minutes for the bubble to become stabilised, after which timed measurements such as bubble length, wake length and void fraction were taken. The liquid film falling down along the bubble ran into the bubble wake and eventually entrains gas.

5.2.3   The injection methods

Three injection methods were used in this experiment: a conical cap, a spherical cap and a nozzle jet geometry which had no cap. These are shown in Figure 5.2. The geometries of the two caps are also shown in Figure 5.3. With the nozzle jet geometry, the 7mm ID tube was reduced to 3.4mm toward the tip of the tube so that the gas exited in a form of jet as adopted by Bacon et al. (1995).
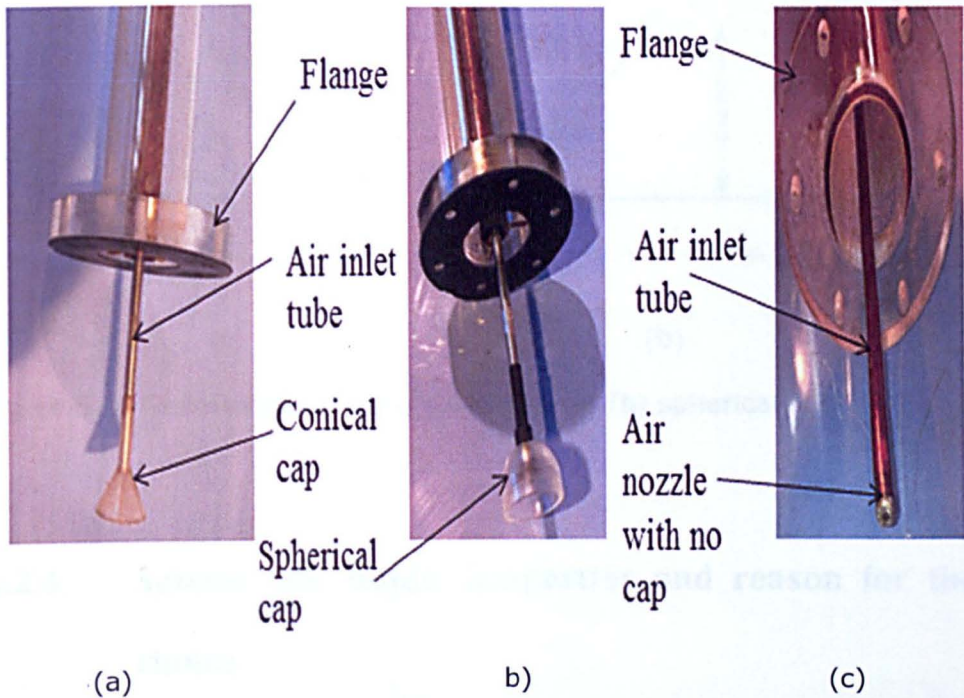
Figure 5.2: The three air inlet geometries used (a) conical (b) spherical (c) no cap

The conical cap was made from a plastic laboratory funnel of wall thickness 3mm and base diameter 44mm (Figure 5.3a). The point at which the air tube was connected to this cap was 30mm from the base of the cap. The spherical cap was machined from Perspex material with a base diameter of 47mm and a wall thickness of 5mm, as shown in Figure 5.3(b). This was shaped in order to simulate the nose of a theoretical Taylor bubble, as defined by Dumitrescu (1943), which had a radius of curvature expressed

Abolore Abdulahi

as Rn=0.375D. According to Kockx (1999), the purpose of the caps is to enhance the stability of the bubble in the centre of the main vertical pipe and to simulate the shape of a real Taylor bubble as accurately as possible. In effect, without the cap, the bubble had a tendency to become unstable, which could result in the deformation into a non-symmetric bubble.
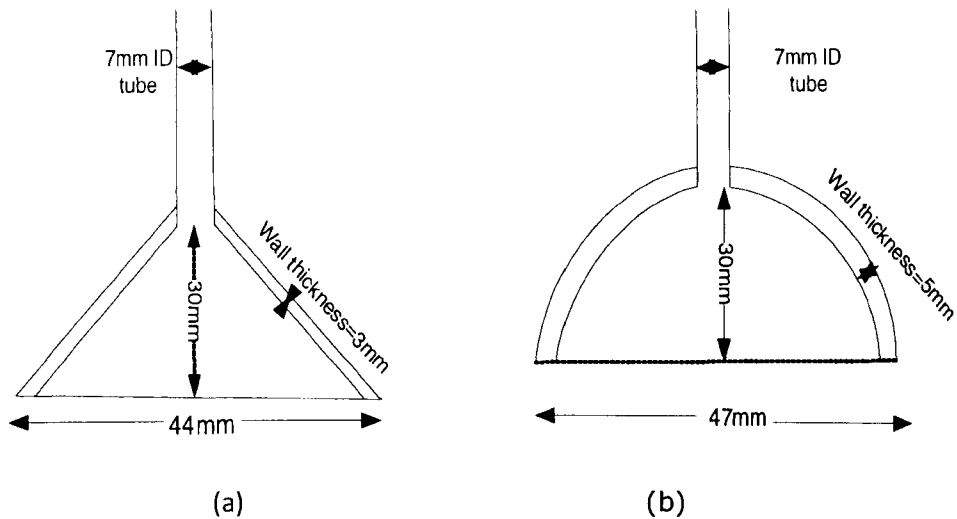
Figure 5.3: Geometry of the caps: (a) conical (b) spherical

5.2.4   System test fluids: properties and reason for their choice

Fluids of different viscosities were used for the tests in order to investigate the effect of viscosity. Air was chosen as the test gas for both economic and environmental reasons. For low viscosity fluid, water was chosen for the same reasons as air. While for high viscosity fluid, Shell Tellus oils 22 and 68 were chosen over other viscous fluids for the following reasons:

✓ Thermal stability: They have been tested and shown to withstand extreme conditions of load and temperature. In addition, they are highly resistant to degradation and sludge formation.

✓ Oxidation resistance: They resist oxidation in the presence of air, water and copper.

Abolore Abdulahi

✓ Hydrolytic stability: Shell Tellus Oils are chemically stable in the presence of moisture hence reducing the risk of corrosion and rusting.

✓ Excellent air release and anti-foam properties: One beauty of the oils is that they are quick at releasing air without excessive foaming. Since air is involved in the experiment, it would easily be released from the mixture thereby avoiding its recirculation in the oil. This is particularly important for a gas entrainment study

✓ Low friction: Shell Tellus Oils have high lubrication properties and excellent low friction features in hydraulic systems operating at both low and high speeds.

✓ Compatibility property: Shell Tellus Oils are compatible with most pumps

Table 5.1: Properties of the Fluid used during experimentation

Fluid properties				
Shell Tellus Oil at 22°C	Tellus 22	Tellus 68	Water	Air
Density (kg/m^3)	866	875	1000	1.204
Dynamic viscosity (kg/m.s)	0.042	0.152	0.00102	0.00000102
Dynamic viscosity (cP)	42	152	1.02	0.00102
Surface Tension in Air	0.027		0.072	

The fluid properties in Table 5.1 were obtained in the laboratory using measuring instruments. For the viscosity of the fluids, a DV-I Prime Viscometer made by Brookfield Engineering Laboratories was used to measure accurate viscosities while a densitometer was used to measure the density of the fluids. The results from the densitometer were compared with measurement using mass per unit volume method and they are within 2%.

Abolore Abdulahi

5.3   Data acquisition methods

5.3.1   High speed video system

An Ametek v675 phantom camera http://www.visionresearch.com/Home/) was used for capturing images during experimentation. Ten grams of Sodium Fluorescein was added to the water as a form of dye to provide colouration of the liquid in order to ensure visibility when using the high speed video camera. The CCD camera produced digital images of 1280 x 800 pixels with a maximum frame rate of 1000 frames/sec.

The lens of the camera has a maximum focal length of 300mm. This was used to acquire images at both the bubble and the wake section, post-experimental analysis to be carried out by interrogating each frame. This was critical in analysing the wake length, which is very difficult to measure visually during experimentation, especially when in a turbulent flow region. The set up for the image acquisition is shown in Figure 5.4

Abolore Abdulahi
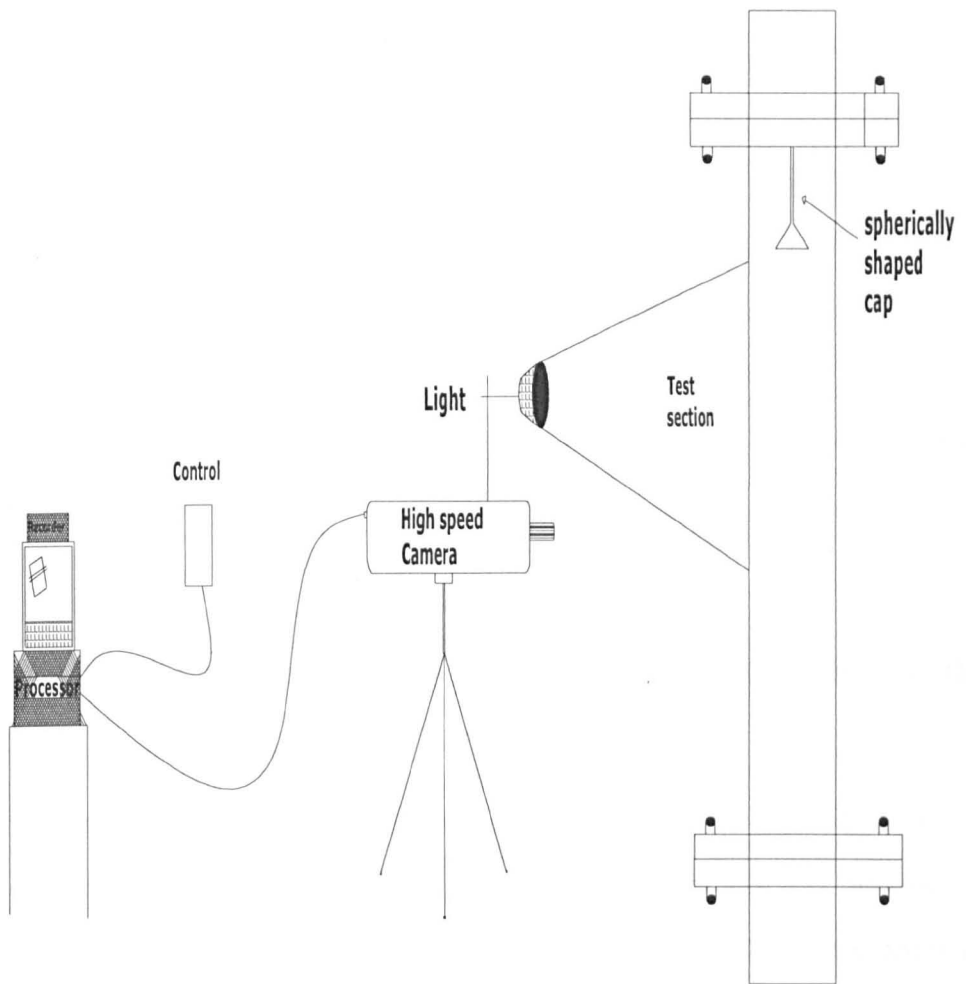
Figure 5.4: Set-up for image acquisition

5.3.2   Wire Mesh Sensor (WMS)

5.3.2.1   Void fraction

Several techniques have been used to measure void fraction, with a review of the subject published by Hewitt (1978). This generally classifies the techniques by the extent of the volume being investigated. Average methods average the result of the measurement along a considerable length of pipe. Localised methods usually give information over the tube cross-section. Point methods give information of the void fraction at a specific point) A common technique consists of measuring the quantity of

Abolore Abdulahi

liquid present instantaneously in a pipe section with two-quick closing valves. Hewitt (1978) concluded that the two quick closing valves technique gave the best result. In addition, the technique was also easy to implement while also being economically advantageous and suitable for all liquids. The main disadvantage if compared to a localised method, such as Capacitance probes (WMS), is that the void fraction measured is averaged across the test section. In addition, its fluctuations cannot be detected. Hence, the need to choose better instrumentation for void fraction acquisition

5.3.2.2   Measurement of Void Fraction using Capacitance Wire Mesh Sensor

In order to get more insight into the distribution of the small bubbles below the Taylor bubble, a good measurement method was desired. The technique adopted here was the measurement of the time-averaged void fraction distribution. The output of this was used to extract spatial information on the time-average of the local presence of bubbles via a Wire Mesh Sensor (WMS). The Wire Mesh Sensor is shown in Figures 5.5 and 5.6. The WMS used in the current study acquired data for an entire cross section every millisecond. An acquisition time of 8 seconds was employed for each experimental run. It is assumed that 8 seconds was enough to allow gas-liquid flows through the WMS since a frequency of 1000Hz is chosen. Large amounts of data were acquired for each experimental case. Analysing the results from the sensor provided the cross sectionally averaged void fraction. The results obtained are presented and discussed in Chapter 6. The Probability Density Function (PDF) gives the frequency of occurrence of each void fraction while the time series shows the variation of the void fraction data at different time

intervals. The WMS was also used to generate bubble size distributions. Various authors, such as Azzopardi et al. (2010b), Pietruske and Prasser (2007), Richter et al. (2002), Wangjiraniran et al. (2005), Prasser et al. (2005b) and Thiele et al. (2008)) have used the Wire Mesh Sensor to carry out research in two-phase flow.
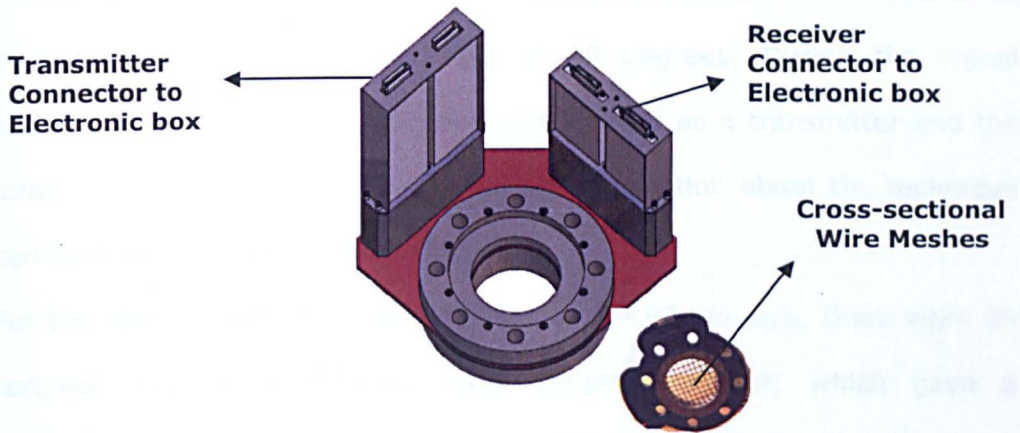
Figure 5.5.: Capacitance Wire Mesh Sensor (Inset shows a WMS with crossing wires)
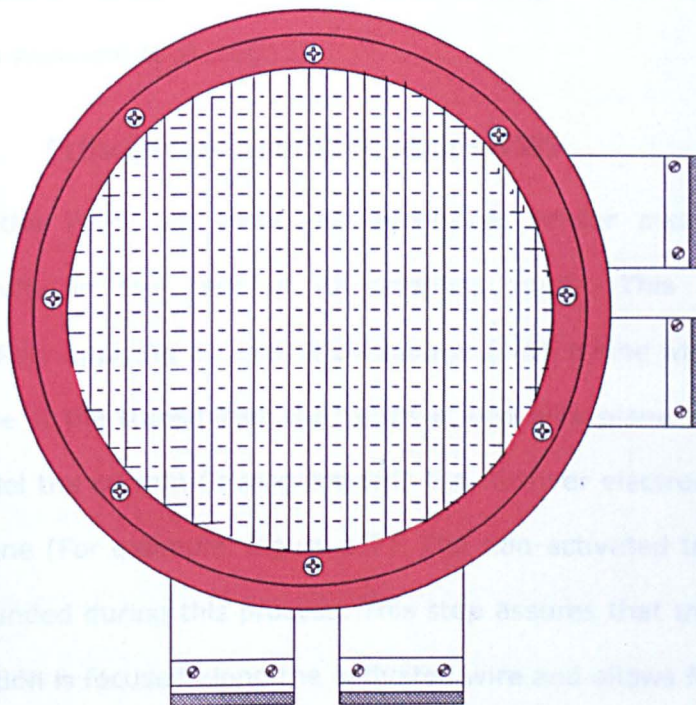
Figure 5.6.: 24x24 Capacitance Wire Mesh Sensor

Abolore Abdulahi

Wire Mesh Sensors are sensitive to the capacitance of the fluid. In the case of a two-phase flow, the water phase is slightly conducting, while the gas phase is practically an ideal insulator. The mode of operation and theory behind the tomographic instrument has been discussed in detail by Prasser et al. (1998) and Prasser et al. (2004). The sensor consists of two grids of parallel wires which span over the measurement cross-section. The wires of both planes cross at an angle of 90 degrees. During the signal acquisition, one plane of electrode wires is used as a transmitter and the other as a receiver (Figure 5.5). Further information about the technique can be found in Da Silva et al. (2010).

For the specific Wire Mesh Sensor used in the 67mm pipe, there were 24 receiver and 24 transmitter wires 250µm diameter, which gave a measuring matrix with 24x24 elements. The distance between the wires is 3mm and the inner diameter of the sensor was equivalent to that of the test section. Further information about the specific sensor used can be found in Abdulahi et al. (2011).

5.3.2.3   Principles of operation of the WMS

Within the WMS, an associated electronic sensor measures the local permittivity in the gaps of all crossing points. This is achieved by successfully applying an excitation voltage (with a sine wave of 5 MHz) to each one of the transmitter electrodes at one wire plane whilst measuring in parallel the current flowing towards the receiver electrodes at the other wire plane (For example, Figure 5.7). The non-activated transmitter wires are grounded during this process. This step assures that the electrical field distribution is focused along the activated wire and allows for a sampling of only a defined region within the pipe. In this way, the measured currents are unambiguously related to the corresponding crossing point. For the permittivity measurements, a sinusoidal alternating voltage is applied and

then a demodulation scheme is subsequently applied. The measured data are sent to a computer where they are processed and displayed after digitizing. This processing method is able to generate up to 7,000 images per second. Further details of the electronic circuits used may be found in Da Silva et al. (2010)
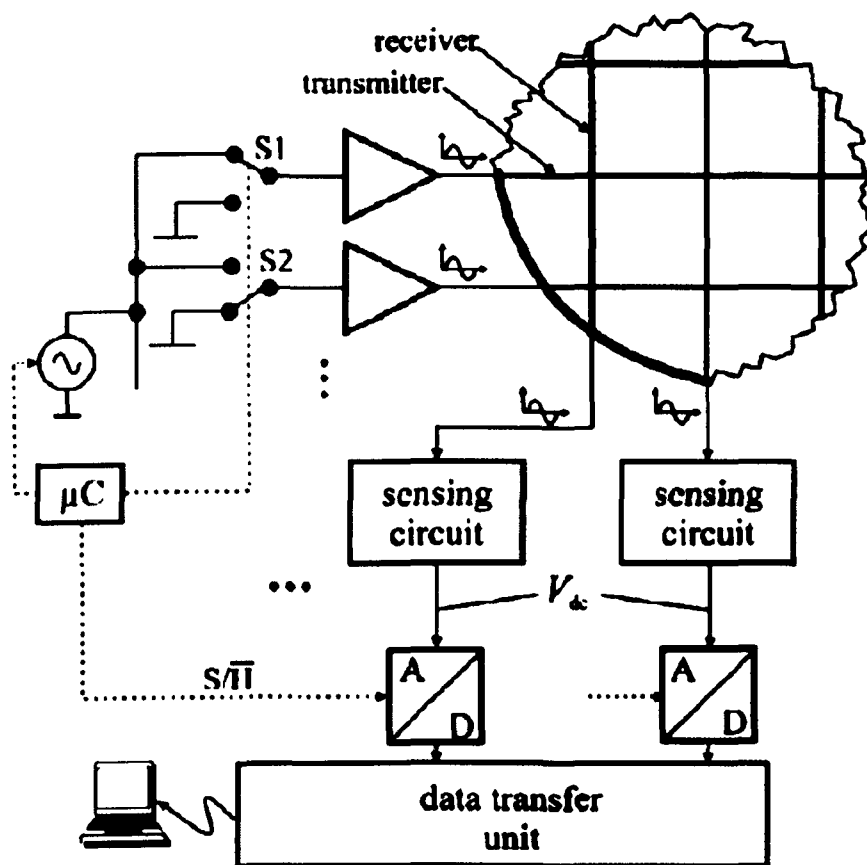
Figure 5.7: Block diagram of the measurement electronics for a 2 x 2 wire section of the wire-mesh sensor (adapted from Da Silva et al. (2010))

The principle of operation of the wire mesh sensor is that the high speed imaging of the flow is based on the capacitance measurements made at each crossing point of the wire. The wire mesh subdivides the flow channel cross-section into a number of independent sub regions, with each crossing point representing one region.

The output from a wire mesh sensor is in the form of a data matrix V $(i, j,$ $k)$, which represent the voltage measured at each (i, j) crossing point with $i \in (1,...,0.24)$ and $j \in (1,...,0.24)$ and at a given time step, k. These voltage readings are proportional to the relative permittivity of the two-phase mixture ε_m, as reported by da Siva $et\ al.$ (2010)

$$V = a \ln \left(\varepsilon_m \right) + b \tag{5.1}$$

where a and b are constants which represent the specific parameters of the electronics. The constants a and b in equation 5.1 require reference measurements for their determination. This in turn allows calculating the mixture permittivity at every crossing point of the wire to be found. First, the sensor measures the empty pipe, i.e., gas which has low permittivity ($\varepsilon_{r,G} = 1$), which yields a reference data matrix V^G (i, j). This data is normally an average of the raw data over a sufficient temporal range to suppress noise. This procedure is then repeated with the entire cross-section covered with the liquid phase, with a high permittivity value of $\varepsilon_{r,L}$ which gives another reference data matrix denoted by V^L (i, j). On the basis of equation (5.1) for the two conditions described, the measured mixture permittivity is calculated by

$$V(i, j, k) = a \ln \varepsilon_m (i, j, k) + b \tag{5.2}$$

subject to the boundary conditions given by:

$$\varepsilon_m \left(i, j, k \right) = \varepsilon_{r,G} = 1; V \left(i, j, k \right) = V^G \left(i, j \right)$$

$$\varepsilon_m \left(i, j, k \right) = \varepsilon_{r,L}; V \left(i, j, k \right) = V^L \left(i, j \right)$$

The values of the boundary conditions are then substituted into equation (5.2) which is then solved simultaneously with equation (5.1) to obtain the values of the constants, a and b.

$$\varepsilon_m \left(i, j, k \right) = \varepsilon_{r,G} = 1; \ V \left(i, j, k \right) = V^G \left(i, j \right)$$

Abolore Abdulahi

Hence equation (5.2) becomes

$$V^G(i,j) = a \ln 1 + b \quad \text{since} \quad \varepsilon_m(i,j,k) = 1$$

But ln1=0,

therefore $V^G(i,j) = b$ (5.3)

Also, substituting the boundary condition for the liquid phase,

$\varepsilon_m(i,j,k) = \varepsilon_{r,L}; V(i,j,k) = V^L(i,j)$ directly into equation (3.2), this gives

$$V^L(i,j) = a \ln \varepsilon_{r,L} + b \tag{5.4}$$

Substituting equation (5.3) into equation (5.4) yields,

$$V^L(i,j) = a \ln \varepsilon_{r,L} + V^G(i,j) \tag{5.5}$$

Hence, $a = \dfrac{V^L(i,j) - V^G(i,j)}{\ln \varepsilon_{r,L}}$ (5.6)

By substituting equations (5.6) and (5.3) into (5.2), this becomes

$$V(i,j,k) = \frac{V^L(i,j) - V^G(i,j)}{\ln \varepsilon_{r,L}} \ln \varepsilon_m(i,j,k) + V^G(i,j) \tag{5.7}$$

When rearranged in order to obtain $\varepsilon_m(i,j,k)$, equation (5.7) becomes

$$V(i,j,k) - V^G(i,j) = \frac{V^L(i,j) - V^G(i,j)}{\ln \varepsilon_{r,L}} \ln \varepsilon_m(i,j,k) \tag{5.8}$$

$$\ln \varepsilon_m(i,j,k) = \frac{V(i,j,k) - V^G(i,j)}{V^L(i,j) - V^G(i,j)} \ln \varepsilon_{r,L} \tag{5.9}$$

$$\varepsilon_m(i,j,k) = \exp\left[\frac{V(i,j,k) - V^G(i,j)}{V^L(i,j) - V^G(i,j)} \ln \varepsilon_{r,L}\right] \tag{5.10}$$

McKeen and Pugsley (2003) reported different models for the description of the effective permittivity of a mixture based on different assumptions of how the phases are geometrically distributed. The parallel model is most commonly used for gas-liquid flows. This defines the effective permittivity as being linearly dependent on the phase fraction. The void fraction is

Abolore Abdulahi

obtained from the measured permittivity ε_m using the Wire mesh as follows:

$$\alpha(i,j,k) = \frac{\varepsilon_{T.L} - \varepsilon_m(i,j,k)}{\varepsilon_{T.L} - \varepsilon_{T.G}}$$

(5.11)

where $\varepsilon_{T.G}$ is the gas permittivity which is 1 while $\varepsilon_{T.L}$ is the liquid permittivity.

Different levels of complexity may be used to analyse the resulting 3D matrix of the void fraction data $\alpha(i,j,k)$. Image sequences of the flow, as well as cross-sectional images from the pipe, can be generated, to mention but a few. Three-dimensional contour images of the gas-liquid interface may be generated, showing for example the shape of bubbles. By averaging the measured void fraction in space and/or in time, quantitative insights of the flow are obtained which yield a time series of void fraction or mean void fraction over the entire measurement.

5.3.2.4 Method involved in Processing of Void fraction from WMS

In order to obtain quantitative information on the two-phase flow, both timed and cross-sectional averaging of the void fraction data were used similar to the description in Prasser et al. (2002). The averaging was based on weight coefficients which defined the contribution of each crossing point of wires (i, j) in the sensor matrix to the size of the domain, over which the averaging was done. The weight coefficients ($a_{i,j}$) needed to obtain a cross-sectional averaged void fraction is defined as shown in Figure 5.8. The averaging was done by individually calculating each sampling period as indicated below in equation 5.12:

$$\bar{\varepsilon} = \varepsilon(t_k) = \sum_i \sum_j a_{i,j} . \varepsilon_{i,j,k}$$

(5.12)

Abolore Abdulahi

In calculating the radial time averaged void fraction, the average of the local instantaneous void fractions over the measurement period and over a number of ring-shaped domains (m) was performed using the following equation:

$$\bar{\varepsilon} = \frac{1}{k_{\max}} = \sum_{k}\sum_{i}\sum_{j} a_{i,j,m}.\varepsilon_{i,j,k} \tag{5.13}$$

Where $a_{i,j,m}$ are the weight coefficients which indicate the contribution of each measurement point with the indexes i, j to a ring with the number m while $k_{\max}$ is the maximum time interval. The ring-shaped averaging domains covered a given radial distance from the centre of the sensor as can be seen in Figure 5.9.
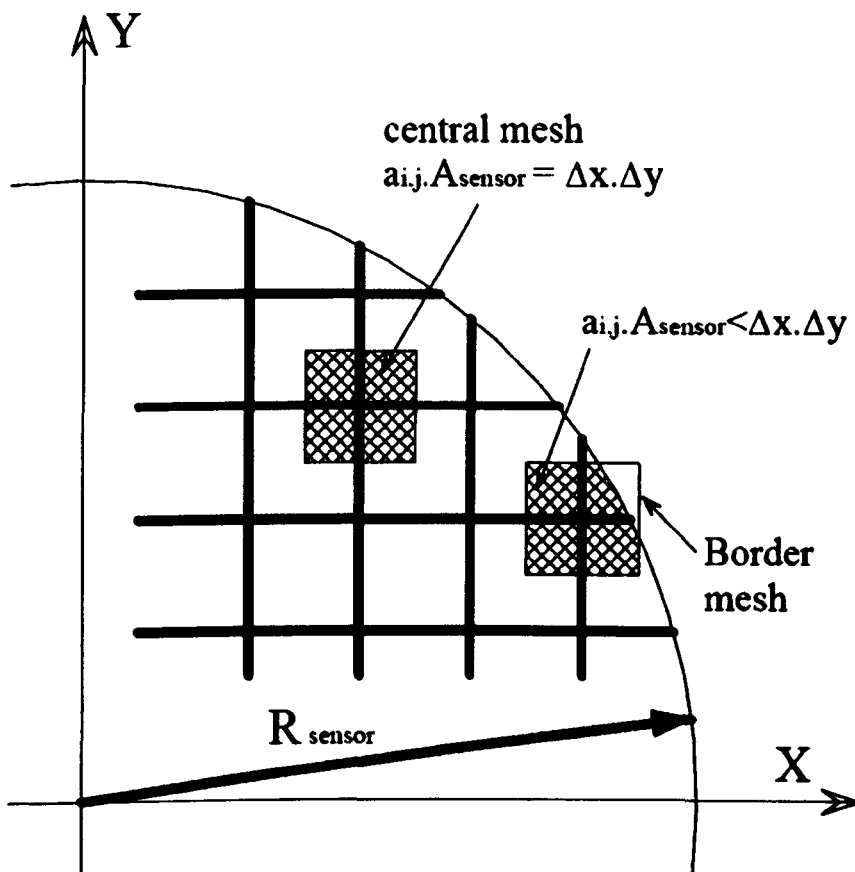
Figure 5.8: Weight coefficients for the cross-section averaging of local void fractions measured by the WMS (Prasser et al. (2002))
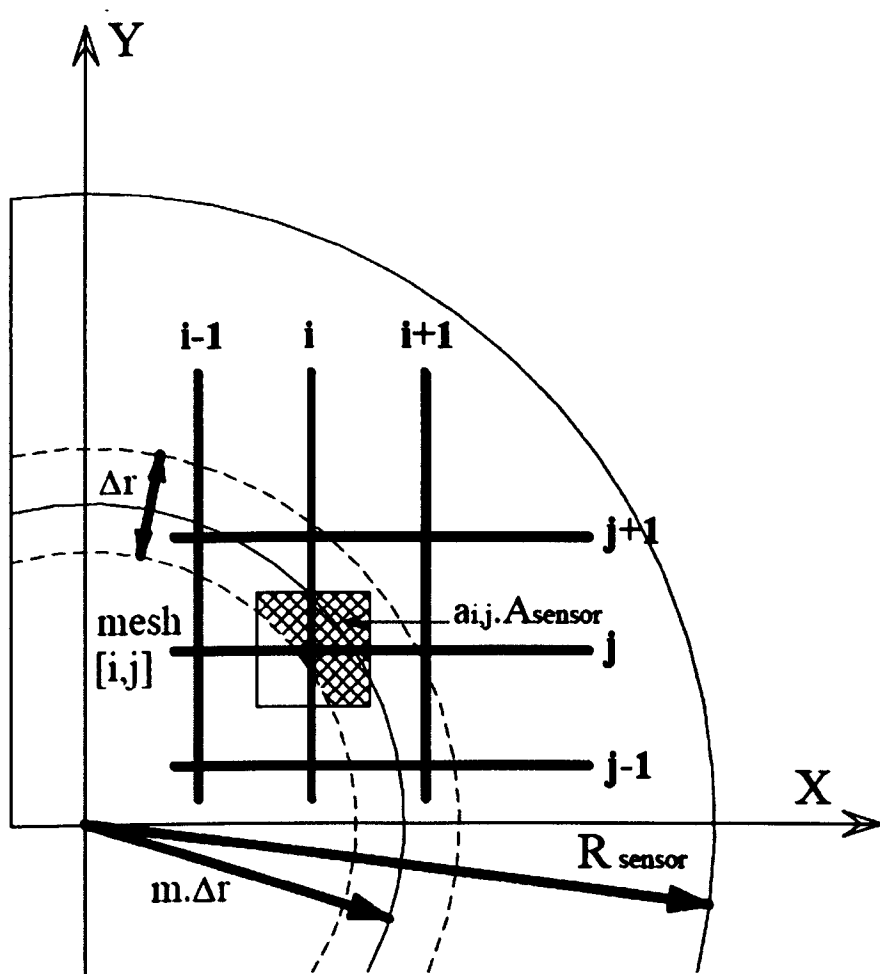
Figure 5.9: Weights coefficients for the cross-section averaging of local void fractions over a number of ring-shaped domains (Prasser *et al.* (2002))

It is worth mentioning that the same methods described above were applied to the Wire Mesh Sensor measurements in Chapters 4 and 5. The only difference being the number of crossing wires in the sensor. Since a larger diameter pipe was used for the experiments carried out in those Chapters, more crossing wires were necessary in order to maintain the high resolution of the instrument. Hence a 32x32 Wire Mesh Sensor was applied in that case. For a smaller diameter pipe (say 38mm diameter pipe), a 16x16 Wire Mesh Sensor is the common type. These wires are so designed to capture bubbles of very small diameters. Although the distance between each crossing wires may vary depending on the number

Abolore Abdulahi

of crossing wire involved, they are usually in the range 2.8-3mm. For instance, it is 2.8mm for 16x16 Wire Mesh Sensor but it is 3mm for 32x32 Wire Mesh Sensor.

5.4   Velocity Measurement based on rise velocity

The downward liquid velocity in the current study could be varied over a wide range of values; however, only under a limited range of conditions could a stable stationary bubble be created. This range was related to the relative velocity of the stagnant bubble and the liquid. In a typical bubble column experiment, gas is bubbled through a stationary/still liquid. In this case, the rise velocity can be calculated using the correlation by Nicklin (1962) for a slug flow which is given in eqn 5.1

$$U_{TB}=1.2U_m +0.35\sqrt{gD} \tag{5.1}$$

Where $U_m=U_{gs}+U_{ls}$

According to Zukoski (1966), the first contribution in the equation 5.1 is the transportation by the mean flow which is zero. However, in the case of a stationary bubble, the bubble velocity is zero (because it is stationary) and the mean liquid velocity to maintain the bubble at a stationary position can be measured. This mean velocity is equivalent to $0.35\sqrt{gD}$. Su and Metcalfe (1997) have identified that when the liquid mean velocity is close to the drift velocity of Taylor bubbles in a stagnant liquid, the long bubbles simulate real stationary Taylor bubbles very well. This velocity has been calculated from the parameters identified above in order to keep the bubble stationary. In the work by Delfos et al. (2001b), this velocity was 0.35m/s whereas in the current work, this velocity was 0.29m/s

Hence, the liquid velocities for this work have been set at 0.25m/s, 0.29m/s and 0.33m/s for the investigations, to ensure that Taylor bubbles can be created for the gas flow rates and geometries employed. The accuracy of the liquid velocities is within $\pm 5\%$.

Chapter Six
Experiments on a stationary downward flow with air-water in a 67mm diameter pipe

6.1   Introduction

This chapter introduces the results from the experiments on a stationary bubble for air-water. As discussed in Chapter 5, the held-down bubble is designed to simulate a real slug flow. Also recall that a slug unit has a Taylor bubble and a liquid slug with the wake bridging the front of one Taylor bubble and the tail of the next one. Details of these have previously been explained in Chapter 2.

6.2   Breakdown of Results

At the initial stage, bubble lengths as well as wake lengths were measured with the aid of a meter rule placed by the test section. The results were measured visually and the average values were taken since the bubble tail tended to oscillate. These results were validated with measurements made using the high speed camera. The results from bubble length measurements are discussed in section 6.2.1, while the effect of gas loss from the measured stationary bubble is discussed in section 6.2.2. The gas loss from the stationary bubble results from falling liquid film impinging on the lower end of the stationary bubble. This impingement causes entrainment at the wake, which is discussed in section 6.2.3. Section 6.2.4 describes the wake length measurements. Lastly, sections 6.3 and 6.4 explain the statistical analysis of results from Wire Mesh Sensor, especially in terms of void fraction measurements.

6.2.1   Effect of Bubble Length

A simple held down bubble is shown in Figure 6.1. This was achieved with spherically and conically shaped caps, which helped its stability. As the gas injected through the cap was increased, the length of the bubble grew. Figures 6.2(a) and (b) indicate how the bubble lengths changed with increased superficial liquid velocities. It is clear from the results in Figure 6.2 that the bubble length increases with increasing superficial gas velocity but decrease with increasing superficial liquid velocity. The plots also show the error bars obtained through statistical analysis of the mean and standard deviation of the bubble lengths which revealed the repeatability of the work. The plots show that the bubble tends to be unstable at higher superficial gas velocities, as the standard deviation at these velocities are in the maximum range of ±2.6m/s. The same trend was observed for all of the three geometries used. When the Taylor bubble length increased, the void fraction in the wake also increased. This is because the liquid film impinging on the bubble wake acquires more momentum, thereby causing more small bubbles to tear off the Taylor bubble. The small air bubbles entrained from the large bubble are not simply swept away from the entrance with the average flow but concentrate in the wake of the bubble (Figure 6.1). The void fractions in this wake are shown in the time series of Figure 6.10b.

Abolore Abdulahi
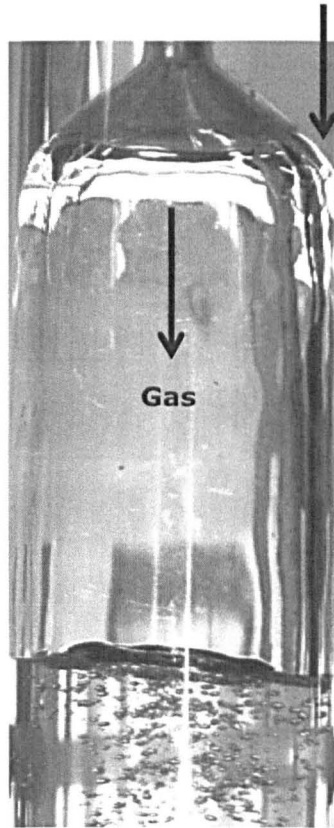
Figure 6.1: A simple held down bubble as observed during experimentation with a conical cap

The voidage in the wake is usually much higher than further downstream. This is in part due to some bubbles going upwards to merge with the tail of the Taylor bubble and others travelling down with the liquid. Also, the wall jets carrying the air with them into the liquid slug are expected to penetrate deep into the liquid slug. According to Mao and Dukler (1985), the length needed to redistribute the momentum of the wall jets is about 8-16 tube diameters. This length could be regarded as the first vortex below the standing Taylor bubble, which was obtained in the current work. More of this will be discussed in a later section.

(i)   (ii)
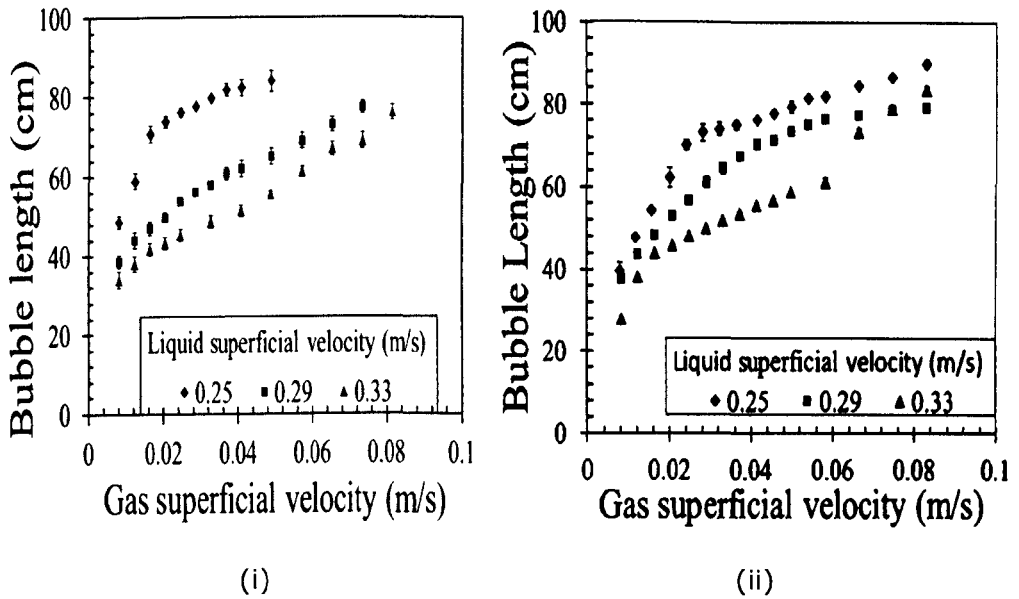
Figure 6.2 (a): Length of simulated Taylor bubble against superficial gas velocity at different superficial liquid velocities with error bars (i) conical cap (ii) spherical cap
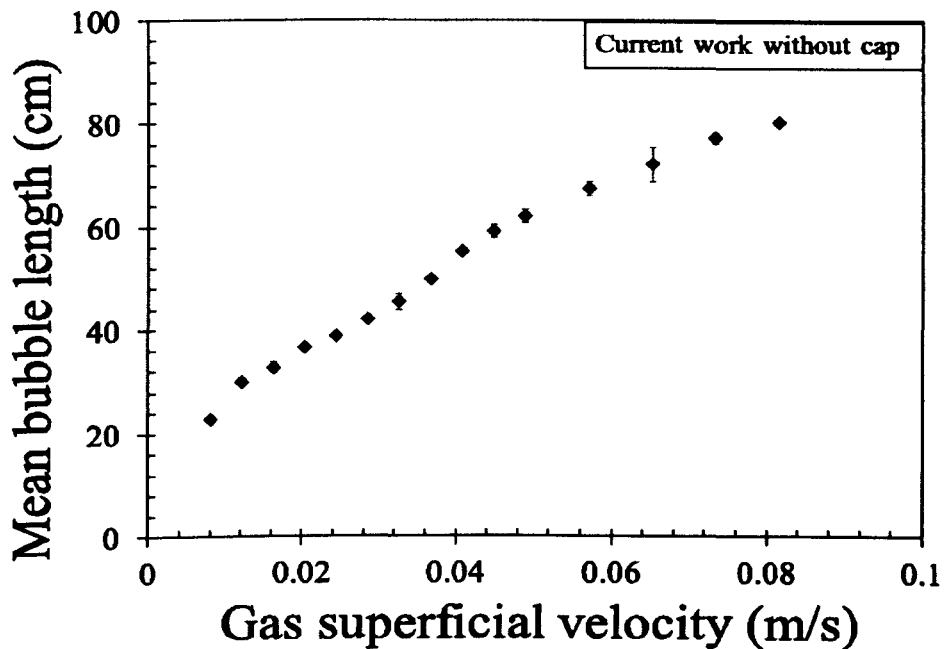
Figure 6.2 (b): Length of bubble against superficial gas velocity at 0.52m/s liquid velocity

6.2.2   Gas loss from the Taylor bubble

A stationary Taylor bubble reaches a steady state when the bubble length

Abolore Abdulahi

does not change and the rate of gas inflow is equal to the rate of gas outflow. Hence, the superficial gas velocity can be assumed to be equal to the gas loss since the flow is through the same cross sectional area. This method has been adopted by Delfos et al. (2001b), Bacon et al. (1995), Su and Metcalfe (1997) and Riiser et al. (1992). Although this method does not take into account the process of re-coalescence, it enables a comparison of the present study with work by the various authors mentioned above. This comparison can be seen in Figure 6.3, which shows similar trend. The Froude number in the current study is a modified one which is described in equation 2.33 of Chapter 2. For instance, at a Fr_G below 25×10^{-7}, the work by Delfos et al. (2001b) shows good agreement with the present study. However as the Froude number is increased beyond this point, the differences become significant. This could be taken as meaning that at low superficial gas velocity, the bubble lengths generated are almost the same but as the gas velocity becomes higher, the effect of pipe diameter becomes more pronounced and the length increases rapidly. Comparing the present work with the work of Su and Metcalfe (1997) shows better agreement at high Froude number, Fr_G especially above 30, which translates to high superficial gas velocities. Su and Metcalfe (1997) used 50-50 wt% water-glycerin mixture with a viscosity of $6 \times 10^{-3} kg/m.s$ and a density of $1125 kg/m^3$. This has been compared with the current study in Figure 6.4 but for Figure 6.3, the work on water by Su and Metcalfe (1997) was used for comparison. As can be observed there is a strong effect of viscosity on bubble length. This effect will be evaluated with other viscous liquids in Chapter 8. With the work of Riiser et al. (1992), the data is fairly comparable with the current work as can be seen in Figure 6.3, although the results do not go above a Fr_G of 18×10^{-7}. However, the work of Bacon et al. (1995) shows little agreement with the current study. Bacon et al. (1995) observed that the bubble grew

with increasing gas flow rate and decreasing liquid flow rate which has been observed in the present work. The differences with the current study may be attributed to the fact that an open ended downcomer was used. This restricted the liquid flow rate because of the tendency of their apparatus to de-flood. In addition, entrainment was created by a plunging film jet in the present study, while it was created directly from gas spargers d in the work by Bacon et al. (1995).
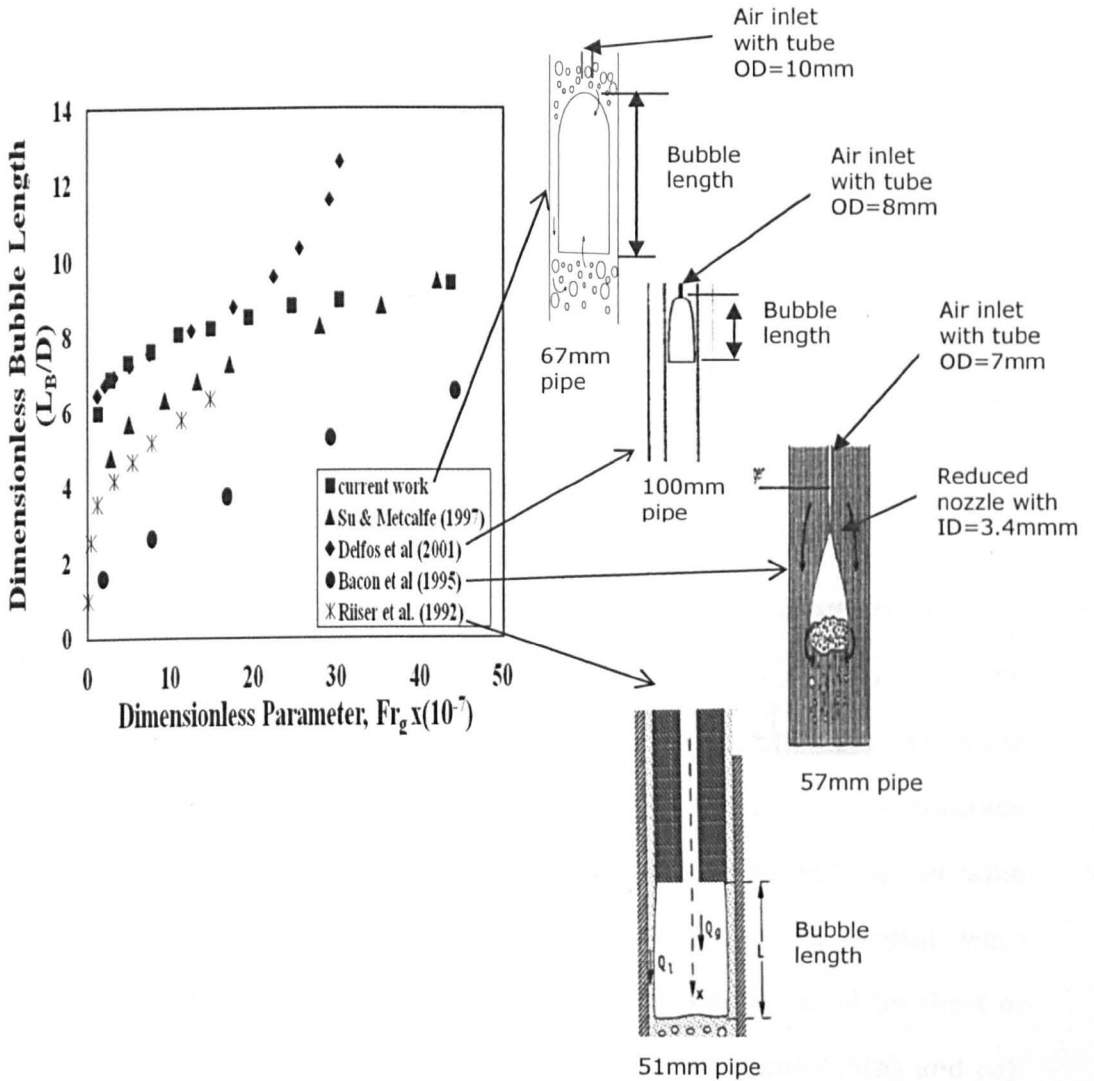
Figure 6.3: Bubble length as a function of Dimensionless Froude number based on results from conical cap
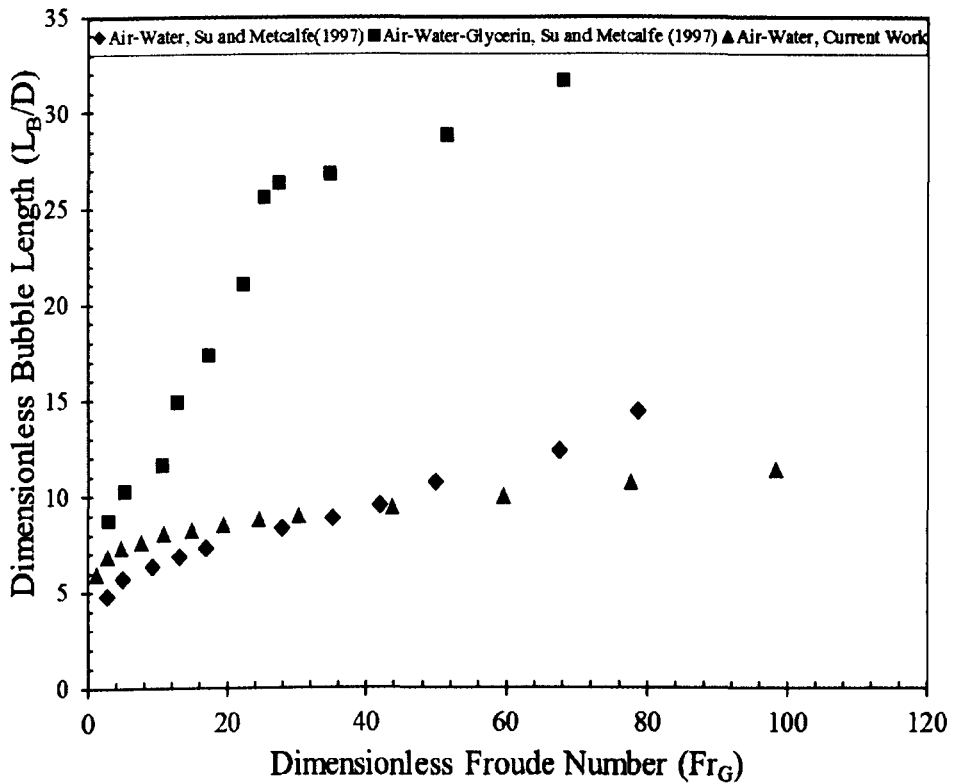
Figure 6.4: Dimensionless bubble length versus Froude number using different viscosity liquids

Since the conical cap geometry results did not agree well with the work by Bacon et al. (1995), which was one of the gas injection methods used by these authors for experimentation, the "no cap" geometry tests were done with air-water. This involved placing the gas injection tube centrally without a cap, as described in Chapter 5. When the bubbles became stable, images were taken and measurements of bubble lengths were made at various superficial gas velocities. These images could be short or long depending on the flow dynamics, as shown in Figures 6.5(a) and (b). The results show very good agreement, as can be seen in Figure 6.6. It is worth mentioning that stability of bubbles was only achieved at high superficial liquid velocities (0.52m/s) in this case.
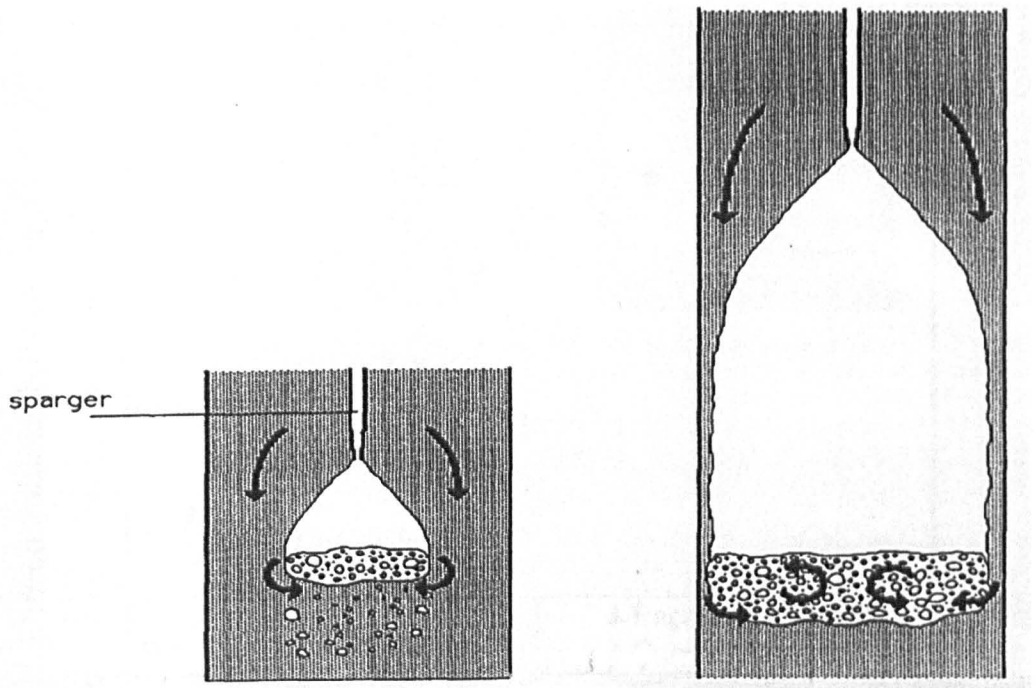
Figure 6.5 (a): Images of bubbles as observed by Bacon et al. (1995); (i) bubble at low gas rate (ii) at high gas rate

(i)   (ii)
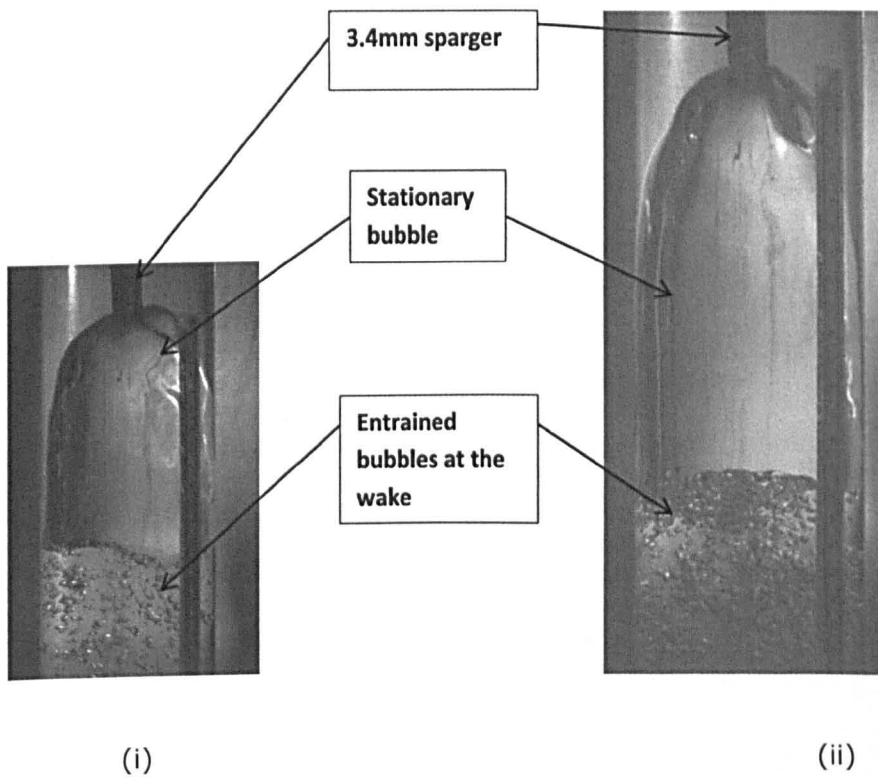
Figure 6.5 (b): Images of bubbles as observed in the current study; (i) bubble at low gas rate (ii) at high gas rate
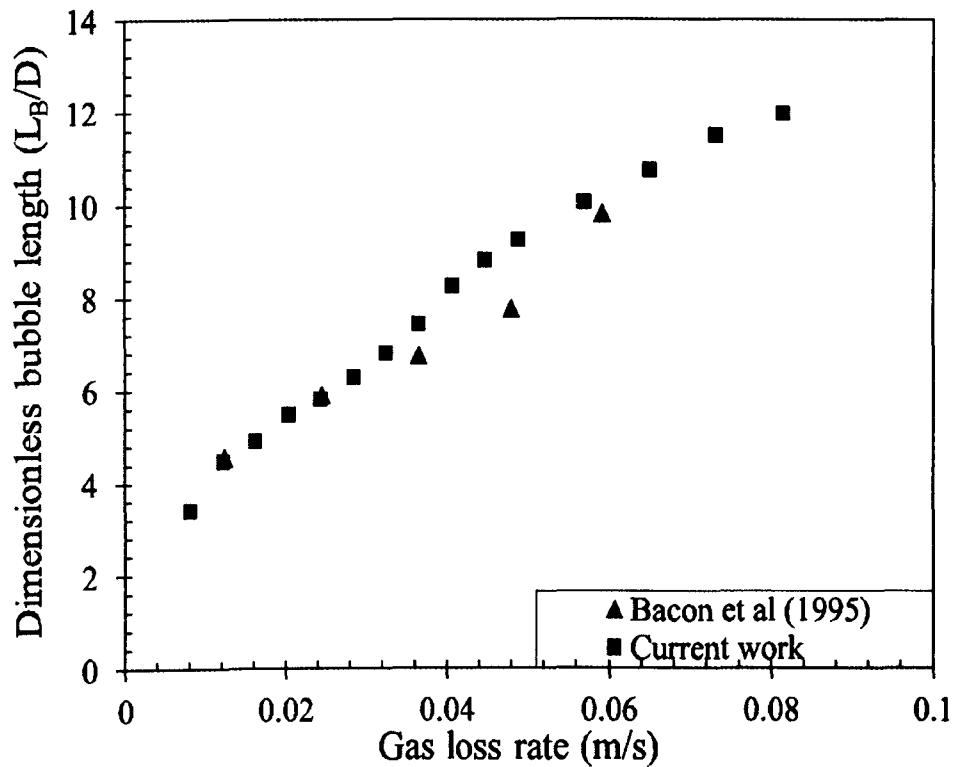
Figure 6.6: Comparison of bubble length measurement with work by Bacon et al. (1995)

6.2.3   Entrainment from the tail of the Taylor bubble tail

The flow rate of the entrained air is very low for the small bubbles in these experiments. This can be observed directly from the low void fractions measured.

The entrainment at the wake of the bubble was captured with the help of the high speed video camera. This helped to detect in more detail the process involved in the distribution of small bubbles in the region below the Taylor bubble. The tail position can clearly be seen in Figure 6.7, while the nose of the bubble is as shown in Figure 6.1.
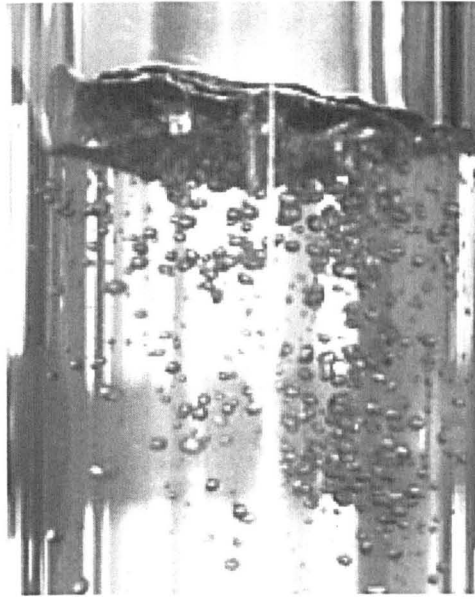
Figure 6.7: Entrained bubbles at the wake of the Taylor bubble

With the aid of high speed video recordings, Riiser et al. (1992) were able to observe waves travelling downward on the interface of the falling film which are not visible without using such a time stretching device. They observed that the perturbation of the tail appeared simultaneously with the waves and led to the formation of very thin fingers of gas at the perimeter of the bubble tail. This was elongated by shear and then broke up to be entrained in the wake. It can be seen in Figure 6.7 that, in line with the work by Riiser et al. (1992), the entrained gas is more concentrated towards the tail end of the standing bubble. Some bubbles were entrained downwards by the liquid jet entering the front of the liquid slug, but these bubbles were just a few millimetres in size, compared to those directly behind the stationary bubble. This is further analysed with a bubble size distribution parameter and is discussed later in section 6.4.

6.2.4   About the Wake of Taylor bubble

Coalescence with the Taylor bubble takes place at the bottom surface of the Taylor bubble. Therefore, it must depend on the details of the flow

below the bottom of the Taylor bubble, which is called the wake of the Taylor bubble (Delfos et al. (2001a)). This is very unsteady; although it moves vigorously, the wake surface is nearly flat. Lee et al. (1999), Sotiriadis et al. (2005) and Sotiriadis and Thorpe (2005) have described the wake, or re-circulation region, of a ventilated cavity (a name given to a simulated Taylor bubble) as shown in Figure 6.8. This description is used in the present work.
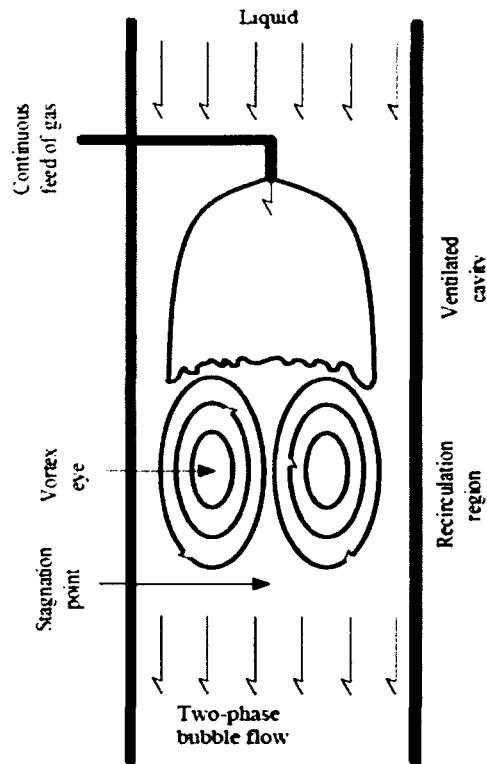
Figure 6.8: Flow geometry for ventilated cavity and recirculation region (Sotiriadis and Thorpe (2005))

Van Hout et al. (1992) reported that the wake length is $L_w= (2\pm0.5)$ D. Similarly Pinto and Campos (1996) have defined the length of the wake as a vertical distance between the lower surface of the bubble and the lower stagnation point in the wake, L_w is considered to be constant and equal to 2.35D whilst Delfos et al. (2001b) proposed $L_w=1-1.5$ D. These were compared with the wake lengths measured in the current study with the

Abolore Abdulahi

results shown in Table 6.1. The wake lengths were measured by studying the images acquired through video recordings.

Table 6.1: Comparison of wake length values

Author	Wake Length, L_W	Pipe diameter considered by author (mm)	Maximum wake length at D=0.067m	Minimum wake length at D=0.067m	Maximum value (cm)	Minimum value (cm)	geometry
Van Hout et al (1992)	(2±0.5)D	50	0.1675	0.1005	16.75	10.05	rising bubble
Pinto and Campos (1996)	2.35D	52	0.15745		15.745		rising bubble
Delfos 1996 & Delfos et al (2001)	1-1.5D	100	0.1005	0.067	10.05	6.7	stationary bubble
current work	(1.5-2.2)D	67	0.1474	0.1005	14.7	10.05	stationary bubble

As well as the results of observations of wake length, particle image velocimetry (PIV) techniques were used to study the flow in the wake and near wake regions of individual Taylor bubbles rising through stagnant and co-current columns of Newtonian liquids by Nogueira et al. (2006). The wake was classified into three types: Laminar, Transition and Turbulent. These authors concluded that the wake flow pattern depends on a dimensionless number, N_f (define as $N_f = \dfrac{\left(gD^3\right)^{\frac{1}{2}}}{\nu}$) which was originally proposed by Campos and Carvalho (1988).

When all the conditions mentioned above are taken into consideration, bearing in mind that the wake length in a turbulent flow is very difficult to determine visually, wake lengths in the current work were determined from high speed camera videos due to the underlying fact about the difficulty in observing turbulent wake length. This measurement was done by first making a video recording of the wake lengths which were later

studied by replaying the videos to note down the lengths. This shows that the lengths are within the range of 10-15cm which is equivalent to (1.5-2.2) pipe diameters. This relationship is shown in Figure 6.9 at different superficial gas velocities. Bearing in mind that Delfos et al. (2001b) have also used photographs to determine the length of the recirculating wake, the conclusion from this is that wake length generally depends on pipe diameter and the wake flow classification.
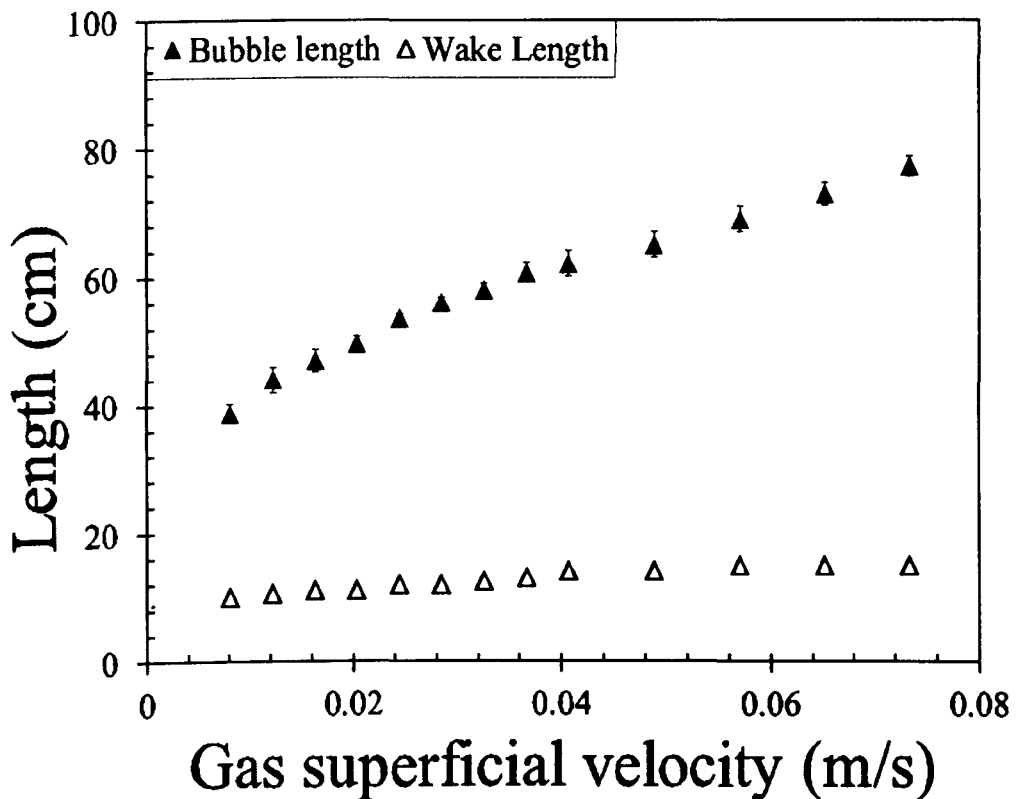
Figure 6.9: Simultaneous bubble length and wake length measurement at liquid superficial velocity of 0.29m/s

6.3   Probability Density Function and Time Series

In gas-liquid flow, the fraction of the cross section occupied by the gas/vapour phase is defined as the void fraction. Knowledge of the void fraction is imperative for determining the acceleration and gravity

components of pressure drop, from which the friction component can be obtained (see Azzopardi (2006)). Probability density functions and the power spectral density obtained from void fraction time series data are useful for flow pattern characterization. The term 'Probability Density Function' (PDF) is used in the current study to describe the function which represents the relative distribution of frequency of occurrence of void fraction within a stipulated region. Since it is difficult to plot all the data on a single chart, it is important to group the void fraction data to enhance easy visualisation. This is achieved through statistical means using the Probability Density Function. These Probability Density Functions (PDFs) of the time series from experiment using water and air have been plotted in Figures 6.12-6.14.

Averaged-time series indicate the sequence of void fractions, measured typically at successive times spaced at uniform time intervals. The time series in Figures 6.10-6.11 show that the maximum void fraction was around 0.85 and the minimum was around 0.71 when the instrument was placed at about 35.5cm below the bubble nose while the maximum was about 0.115 and the minimum was about 0.07 when the instrument was placed at about 81cm below the bubble nose for a conical cap gas injection geometry. This highlights the importance of void fraction time series in determining the flow regime and the spread of bubbles in a two-phase flow.

Abolore Abdulahi

(a)

(b)
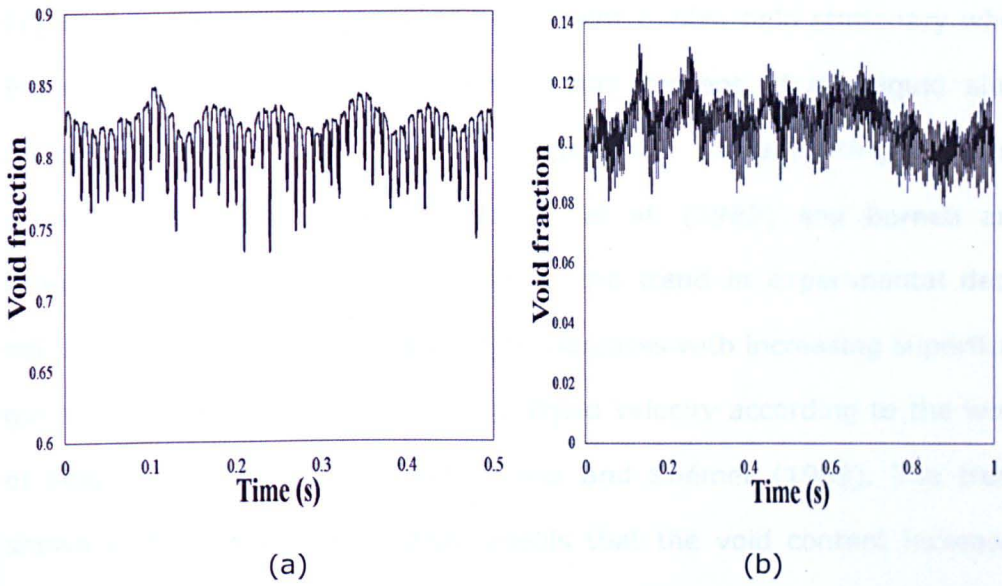
Figure 6.10: Time series of data when instrument was place at (a) 35.5cm

and (b) 81cm below the bubble nose.
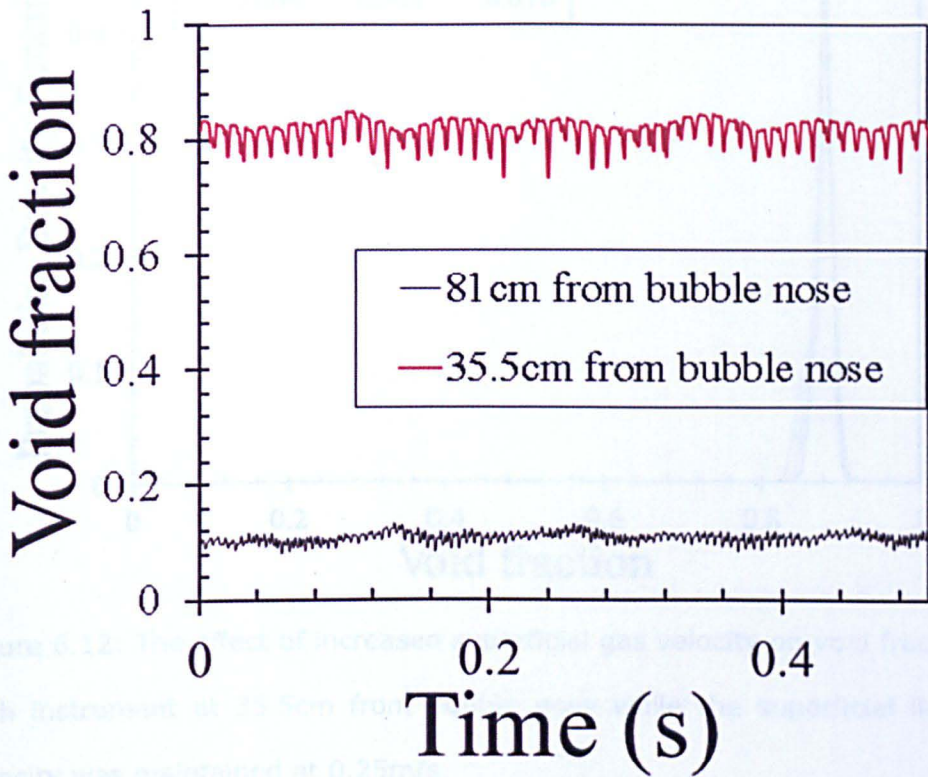
Figure 6.11: Combined time series of data for both cases shown in Figure

6.10

Figure 6.10 (a) depicts the trend in a Taylor bubble held stationary while Figure 6.10 (b) depicts the trend in void content of the liquid slug. Although several models have been proposed for predicting the void content of the liquid slugs, Fernandes et al. (1983) and Barnea and Brauner (1985), none of them predicts the trend in experimental data, which has shown that the void fraction increases with increasing superficial gas velocity, whatever the superficial liquid velocity according to the work of Mao and Dukler (1985) and Barnea and Shémer (1989). The trend shown in the current study also reveals that the void content increases with superficial gas velocity, as can be seen in Figure 6.12.
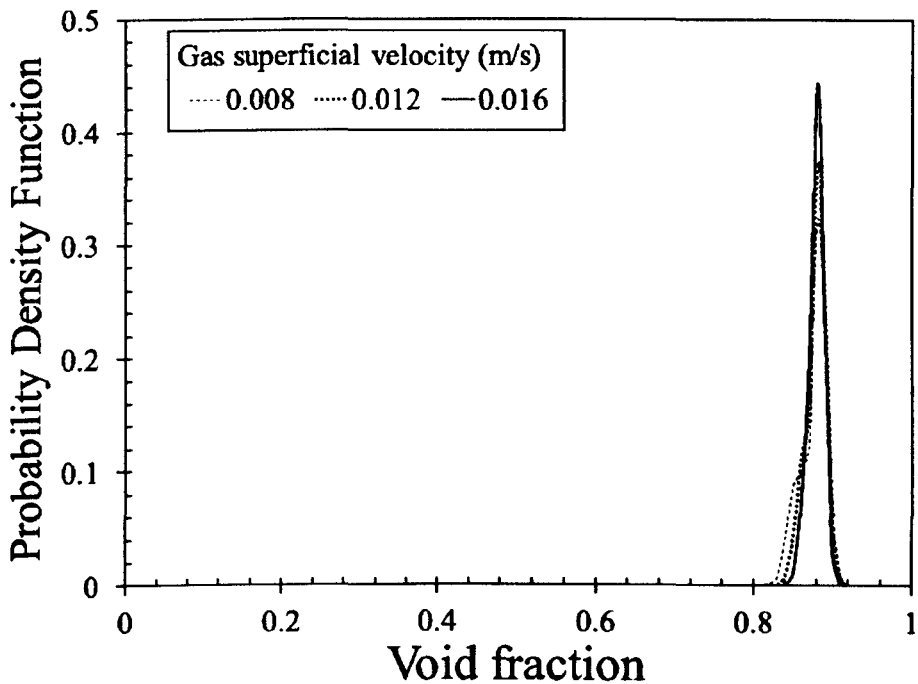
Figure 6.12: The effect of increased superficial gas velocity on void fraction with instrument at 35.5cm from bubble nose while the superficial liquid velocity was maintained at 0.25m/s

The results obtained from experiments at different flow conditions were assessed for the presence of bubbles in the wake region of the Taylor bubble using the Probability Density Function. Plots of the fluid flow at

Abolore Abdulahi

conditions when the superficial liquid velocity was sufficient to keep the bubble stationary (i.e. 0.29m/s) were compared with other superficial liquid velocities at different superficial gas velocities. Other velocities would have been considered but at a liquid velocity higher than 0.33m/s, the stationary bubble was observed to be too short (below 5cm) and the onset of entrainment was much delayed, while at a very low liquid velocity, less than 0.25m/s, the bubble was so long that it could not be captured within the test section, even when a small volume of gas was introduced.
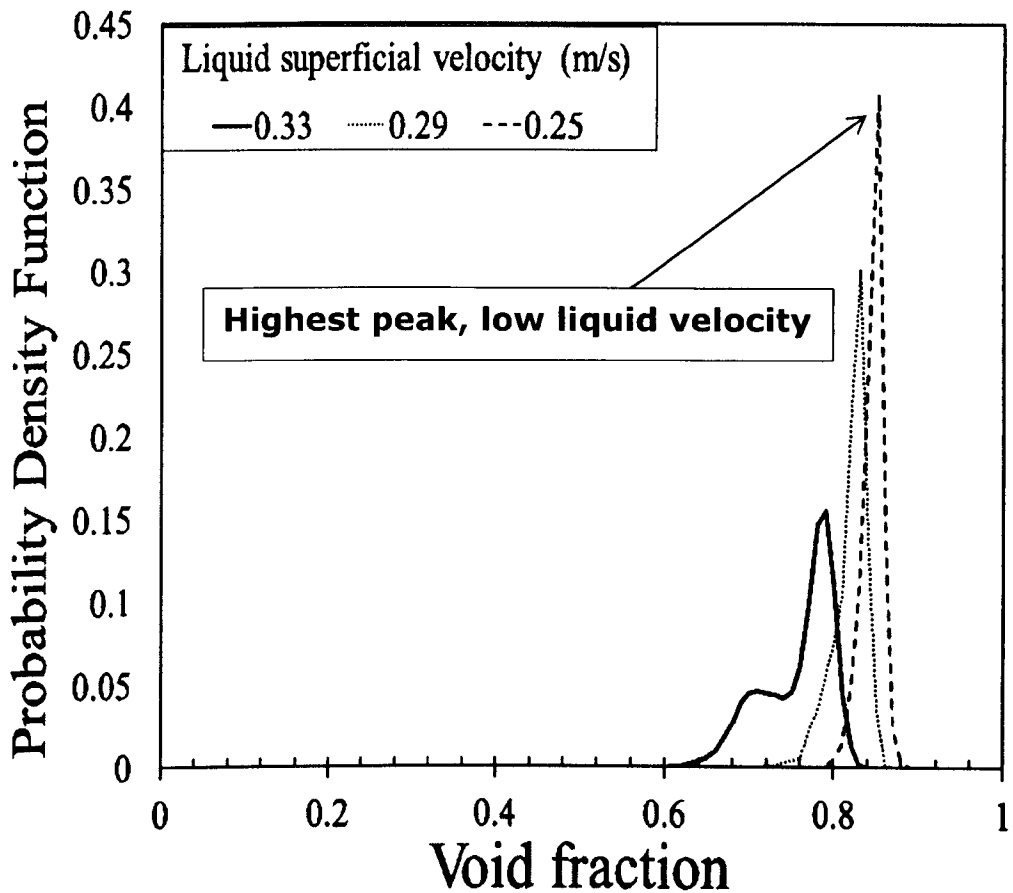
Figure 6.13: The effect of increased superficial liquid velocity on void fraction with instrument at 35.5cm from bubble nose

From Figure 6.13, it can be observed that at a superficial liquid velocity of 0.33m/s, the peak of the PDF was lower than those for superficial liquid

velocities of 0.29m/s and 0.25m/s (the superficial gas velocity being maintained at 0.016m/s). This peak occurred at volume fraction of 0.8. At a void fraction of 0.88, the PDF was highest when the superficial liquid velocity was at 0.25m/s. A similar observation is seen in Figure 6.14 for the wake section. Void fraction is highest at the lowest superficial liquid velocity of 0.25m/s. The lowest void fraction occurs at the highest superficial liquid velocity of 0.33m/s, both at a constant superficial gas velocity of 0.016m/s. This is an indication that the volume fraction of gas present in the wake increased as superficial liquid velocity increased, for the same superficial velocity of gas. The effect of liquid film on bubbles could not be ruled out. Besides, the lengths of the Taylor bubble in all cases are quite different.
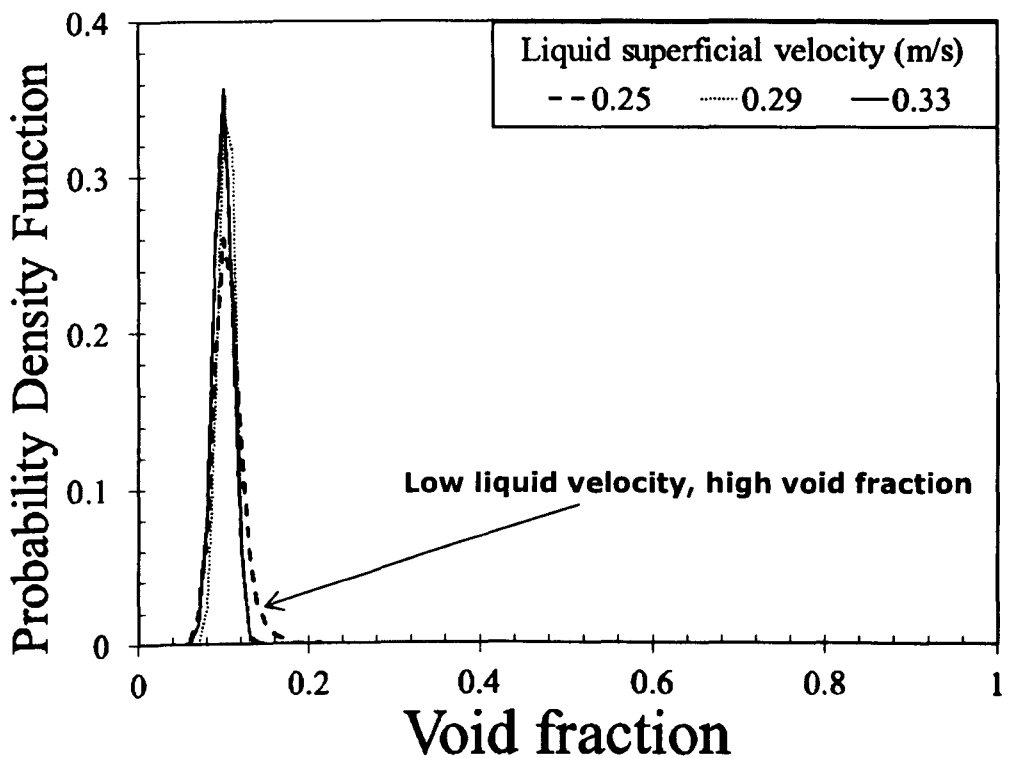
Figure 6.14: The effect of increased superficial liquid velocity on void fraction with instrument at 81cm from bubble nose

Considering the work by other authors, for instance Azzopardi (2006) and Costigan and Whalley (1997), and combining the two PDFs from the two positions of the instrument, a typical slug flow pattern which has twin peaks as shown in Figure 6.15(a) is obtained. This is a clear indication that WMS has effectively been able to capture both the stationary Taylor bubble section (where gas volume fraction is high) and the wake section (where there is low gas volume fraction) when placed at two different locations. Therefore the stationary Taylor bubbles in the current study replicates a slug flow. Hence the methodology is hereby proven to be valid.
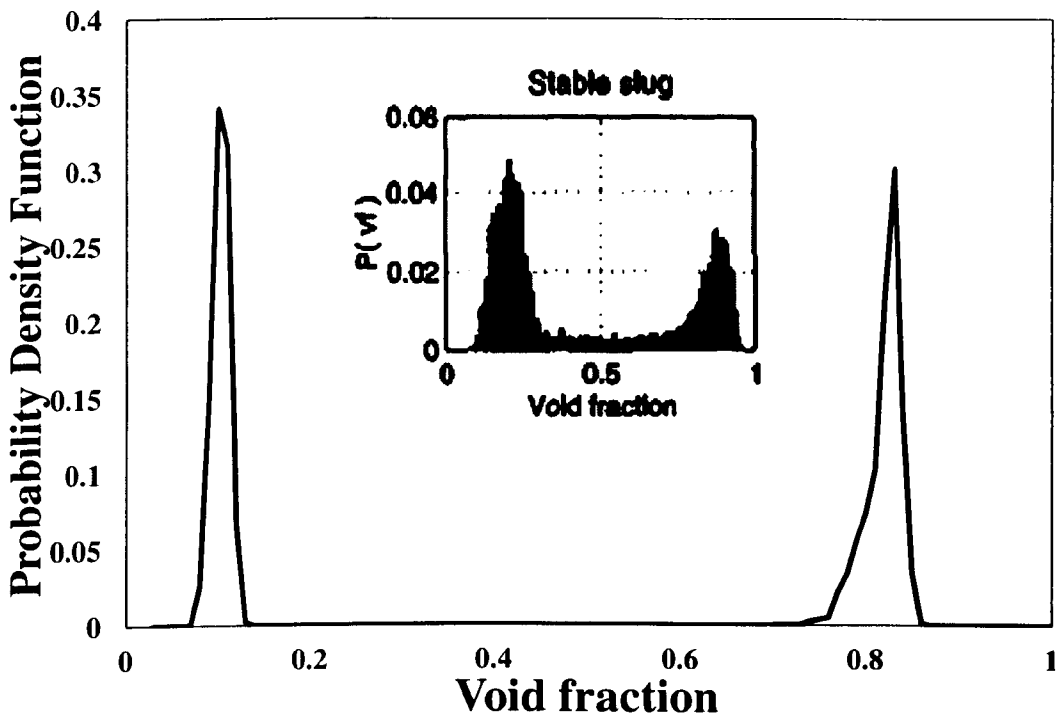
Figure 6.15 (a): A typical PDF of a slug flow at Usg=0.016m/s and Usl=0.29m/s (Inset, PDF of a slug flow by Costigan and Whalley (1997)

A comparison of a typical slug flow from the current work shown in Figure 6.15 (a) with the data of Hernandez Perez et al. (2010) can be seen in Figure 6.15 (b). The twin peaks of the low void fraction section (the liquid slug part) and the high void fraction section (the Taylor bubble section) can clearly be noticed in the plot. Though the data from Hernandez Perez

Abolore Abdulahi

et al. (2010) show higher PDF peaks, both work show similar trends as the peaks for low void fraction liquid slug and high void fraction Taylor bubble appear at almost the same void fraction values. The difference in the PDF values may be attributed to the length of the experimental time for data acquisition in both cases.
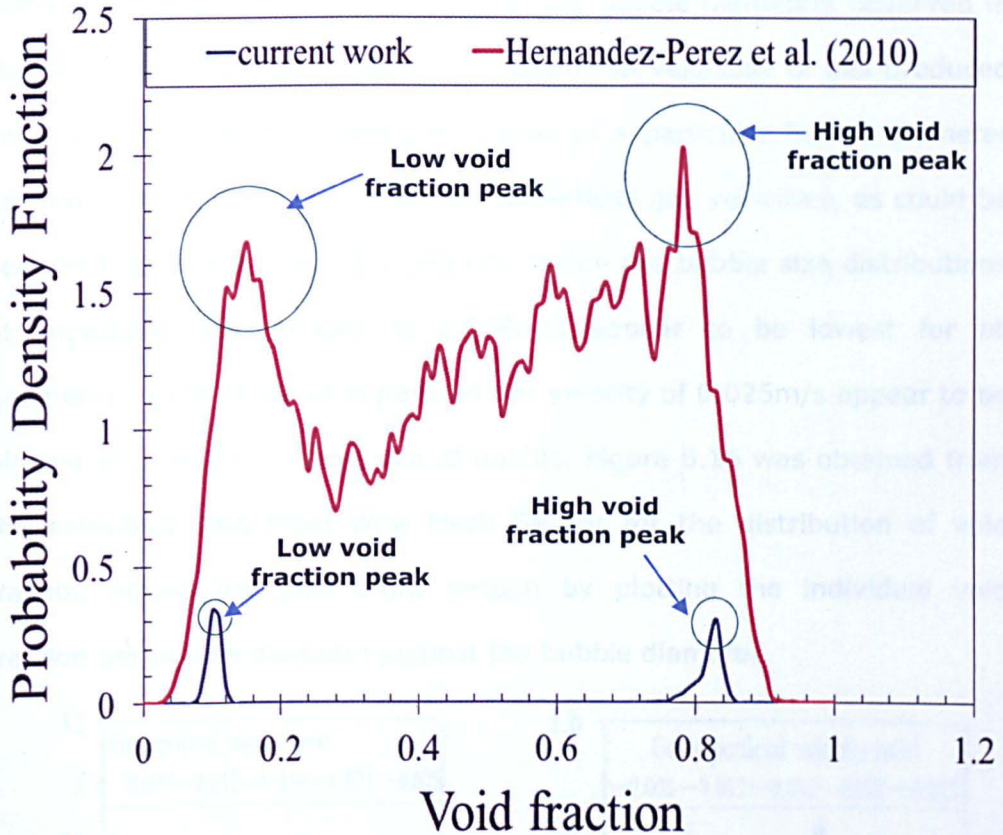
Figure 6.15 (b): Comparison of the PDF of a slug flow in the current work with Hernandez Perez et al. (2010) slug flow data.

6.4 Bubble Size Distribution in Slug

A Wire Mesh Sensor has been used by various authors (Da Silva et al. (2010); Prasser et al. (2001)) to obtain the bubble size distribution. Bubble size distributions are constructed by summarizing the contribution of the bubbles of a given range of diameters to the integral volumetric gas fraction. In Prasser et al. (2001), the partial gas fractions $d\epsilon/dD_{Bub}$ was

　　　　　　　　　　　　　　　　　　　Abolore Abdulahi

plotted against the equivalent bubble diameter dD$_{Bub}$. They observed that the resulting curves were uneven at large diameters because there were only a few large bubbles which carry most of the gas volume. A similar observation was noticed in this work as can be seen in Figure 6.16. Da Silva et al. (2010) observed that a bubbly flow occurred at bubble diameters lower than 20mm, similar to the bubble diameters observed in this work. In the present study, low superficial velocities of gas produced small bubbles such that their distribution at a particular bubble diameter are low compared with those at high superficial gas velocities, as could be seen in Figures 6.16 (a), (b), and (c). Hence the bubble size distributions at superficial gas velocity of 0.008m/s appear to be lowest for all geometries while those at superficial gas velocity of 0.025m/s appear to be highest at almost the same size of bubble. Figure 6.16 was obtained from the extracted data from Wire Mesh Sensor for the distribution of void fraction across the pipe cross section by plotting the individual void fraction per bubble diameter against the bubble diameter.

(a)

(b)
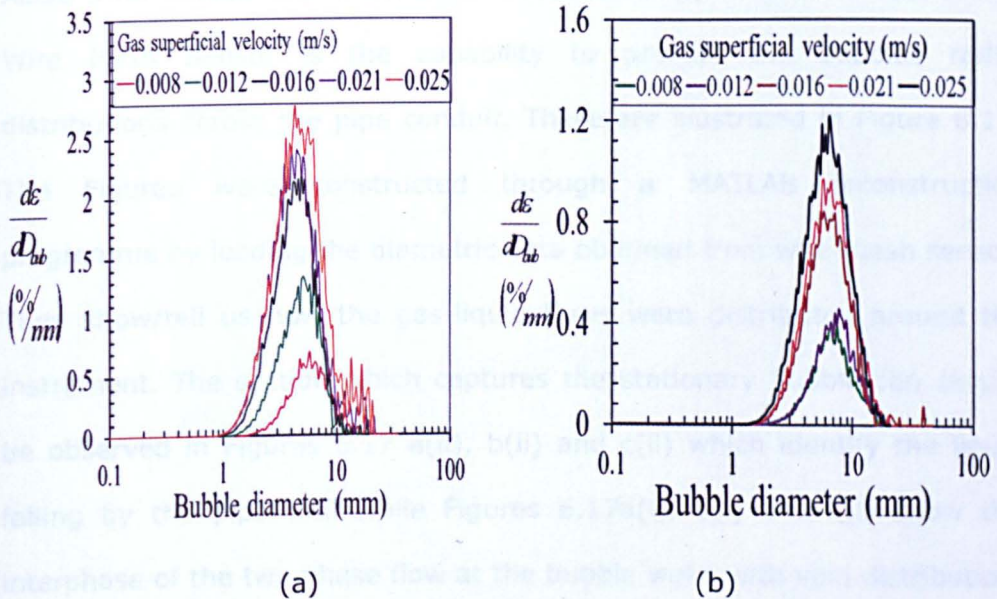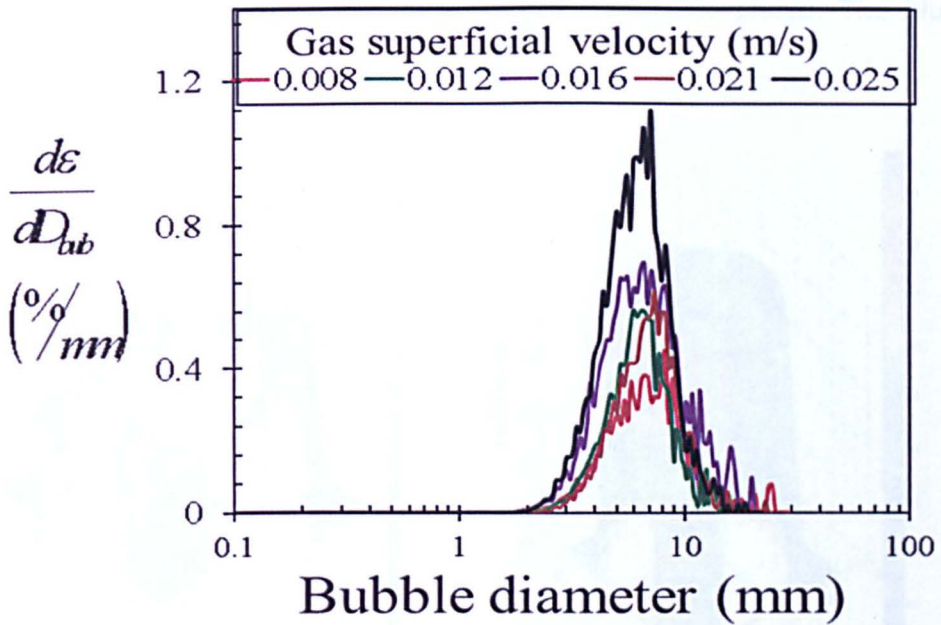
(c)

Figure 6.16: Bubble size distribution at superficial liquid velocity of 0.25m/s for (a) conical cap (b) spherical cap data (c) no cap at 0.52m/s superficial liquid velocity

Aside from bubble size distribution measurements, another feature of the Wire Mesh Sensor is the capability to provide the bubbles radial distributions across the pipe conduit. These are illustrated in Figure 6.17. The Figures were constructed through a MATLAB reconstruction programme by loading the diametric data obtained from wire mesh sensor. They show/tell us how the gas-liquid flows were distributed around the instrument. The section which captures the stationary bubble can clearly be observed in Figures 6.17 a(ii), b(ii) and c(ii) which identify the liquid falling by the pipe wall while Figures 6.17a(i), b(i) and c(i) show the interphase of the two phase flow at the bubble wake with void distribution. The roughness of this section is as a result of the wavy nature of the bubble wake. Regions with red colour indicate those occupied by air while

those with yellow or light green indicate gas liquid interphase. The blue regions show the section occupied by water.

(i)   (ii)
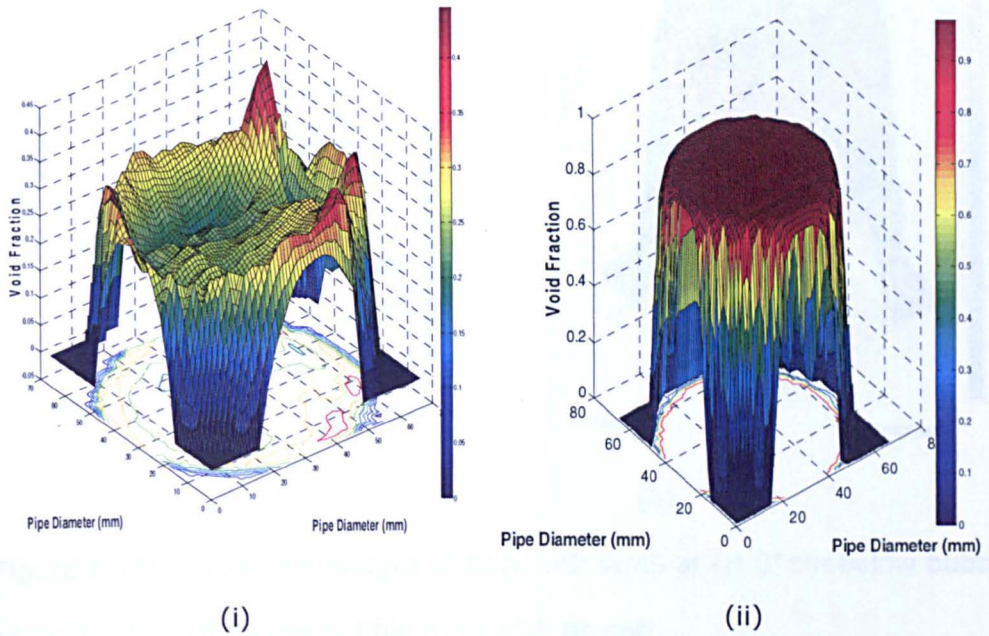
Figure 6.17(a): Contour images of flow with WMS at (i) 81cm below bubble nose (ii) 35.5 cm below bubble nose with conical cap geometry

(i)   (ii)
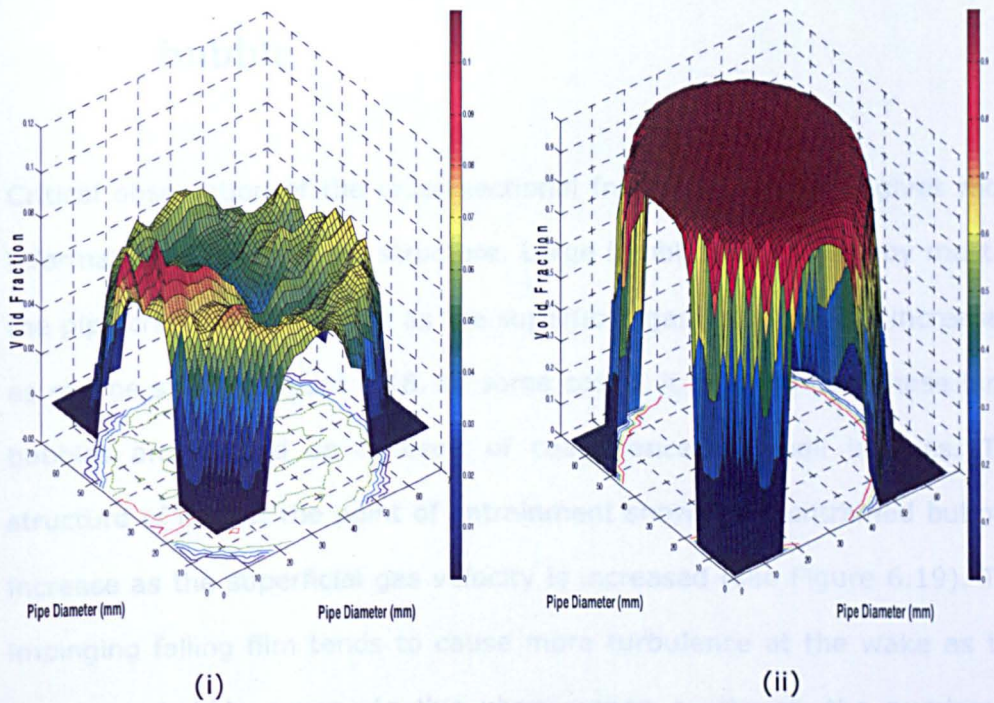
Figure 6.17(b): Contour images of flow with WMS at (i) 81cm below bubble nose (ii) 35.5 cm below bubble nose with spherical cap geometry

Abolore Abdulahi

(i)   (ii)
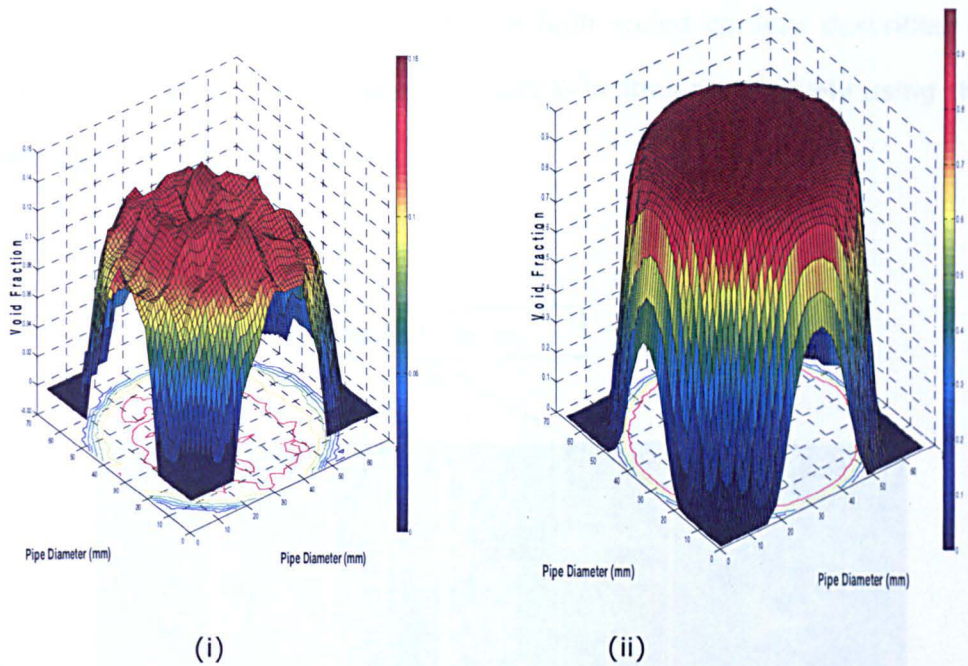
Figure 6.17(c): Contour images of flow with WMS at (i) 81cm below bubble nose (ii) 35.5 cm below bubble nose with no cap

6.5   Structure of flow below the stationary bubble

Critical observation of the cross-sectional frames of the WMS gives more information about the flow structure. Large bubbles, which occupy most of the pipe cross section, occur as the superficial gas velocities are increased, as can be seen in Figure 6.18. In some cases, it appears that these large bubbles are formed as a result of coalescence of small bubbles. The structure of flow at the point of entrainment shows that entrained bubbles increase as the superficial gas velocity is increased (see Figure 6.19). The impinging falling film tends to cause more turbulence at the wake as the stationary bubble grows. As this phenomenon continues, the number of entrained bubbles increases, as can be seen in Figure 6.19. More entrained bubbles were observed when the gas velocity was increased. The images

Abolore Abdulahi

in Figure 6.19 were captured using the high speed camera described in Chapter 5 at low and high superficial gas velocities respectively using the same liquid superficial velocity.

(a)   (b)   (c)   (d)   (e)   (f)   (g)   (h)
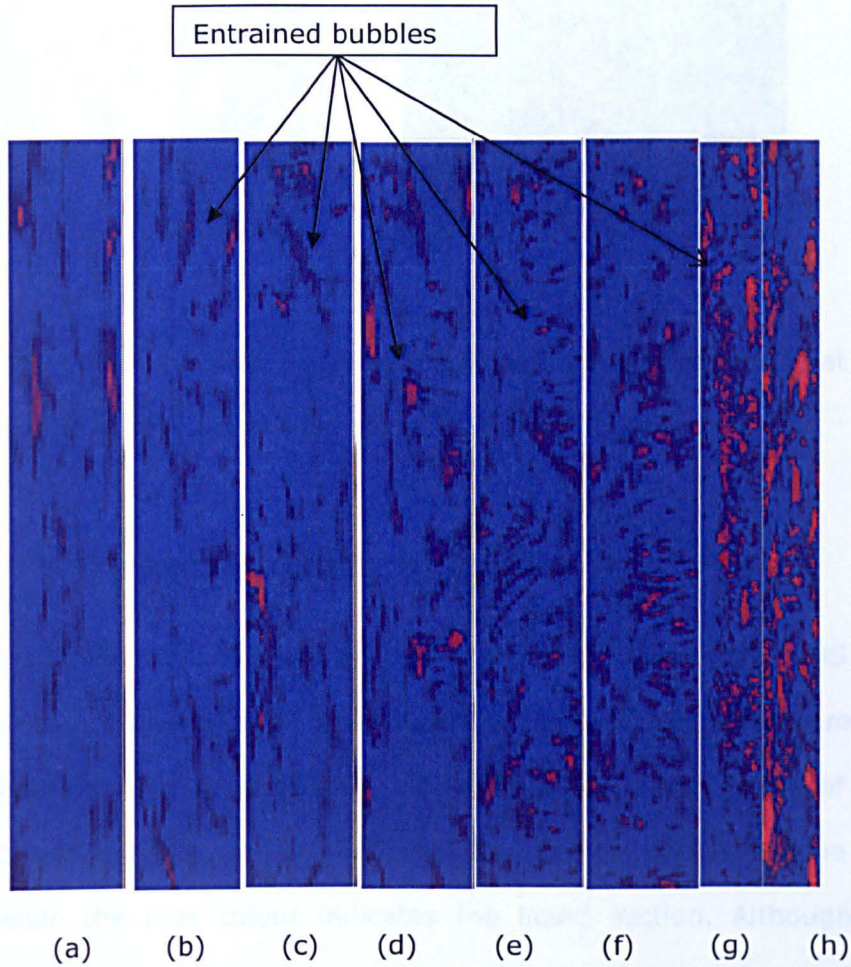
Figure 6.18: Flow structure from WMS display at Usl=0.29m/s and Usg (m/s) at (a) 0.008, (b) 0.016 (c) 0.024 (d) 0.033 (e) 0.041 (f) 0.049 (g) 0.057 (h) 0.065

Abolore Abdulahi

(a)	(b)
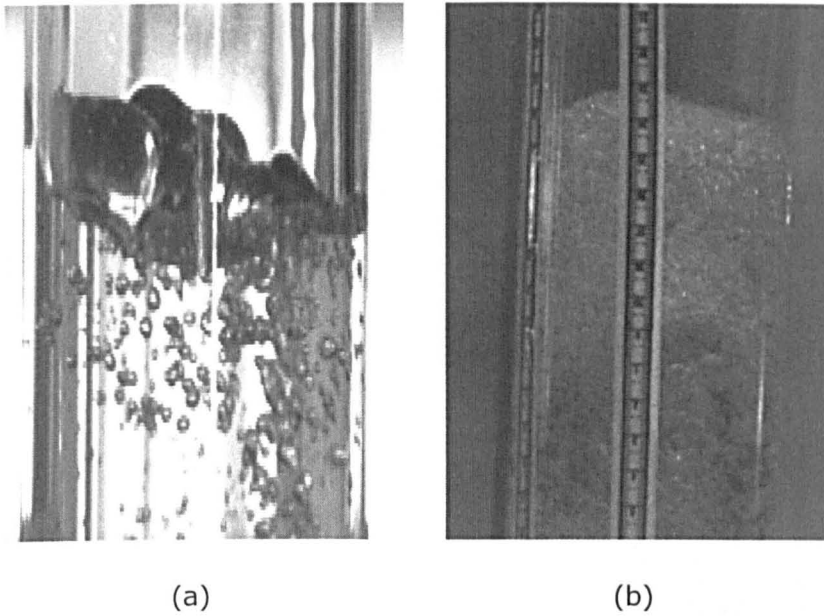
Figure 6.19: Entrained bubbles below the Stationary bubble tail (a) at low superficial gas velocity (b) at high superficial gas velocity

6.6   Wire Mesh sensor images

The images in Figure 6.20 illustrate how the acquired data from WMS are viewed when a special display programme is used. These images are for the stationary bubble section (i.e. 35.5cm from the bubble nose) of the three geometries discussed in Chapter 5. The red colour indicates the gas section while the blue colour indicates the liquid section. Although no distinct changes may be noticed, the blue section can be seen to be thinner as the superficial gas velocity (Ugs) is increased, especially in Figures 6.20 (a-c). This is true when compared with the plots of the void fraction which shows that the void fraction increases with an increase in the gas superficial velocity at a constant liquid superficial velocity
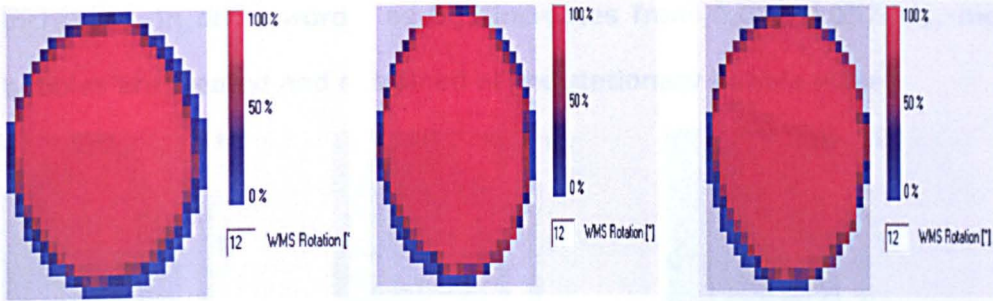
(a) Ugs= 0.041m/s   (b) Ugs=0.049m/s   (c) Ugs=0.073m/s
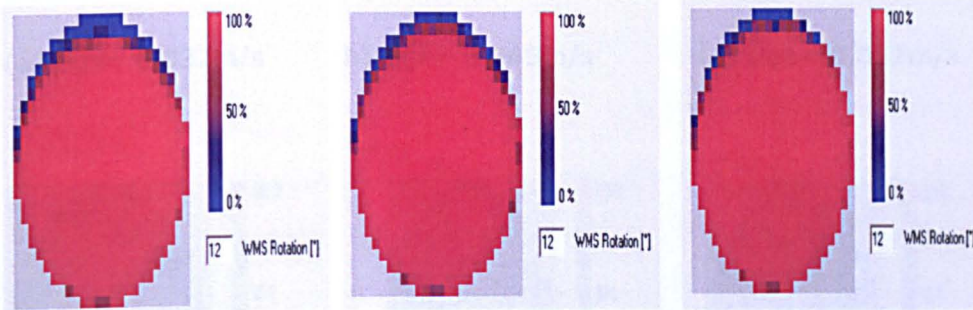
(d) Ugs= 0.041m/s   (e) Ugs=0.049m/s   (f) Ugs=0.073m/s
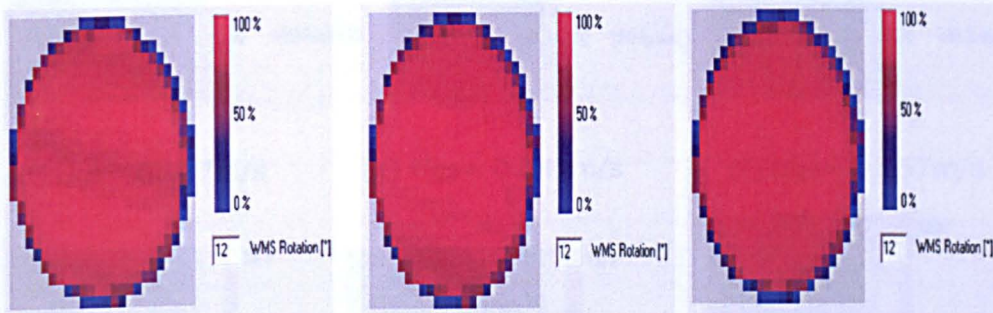
(g) Ugs= 0.041m/s   (h) Ugs=0.049m/s   (i) Ugs=0.073m/s

Figure 6.20: Display by WMS showing the bubble section with no cap (a-c), with conical cap (d-f) and with spherical cap (g-i).

The images in Figure 6.21(a-i) show the entrained gas bubbles for all the three cap geometry used when WMS was placed at the wake section of the stationary bubble. The blue colour shows the predominant liquid section while the red colour shows the gas (air). The images reveal that as the gas superficial velocity is increased, the entrained gas bubbles in the wake also

increased. In other words, as Ugs increases from 0.037-0.057m/s, more

bubbles are created and entrained at the stationary bubble wake.
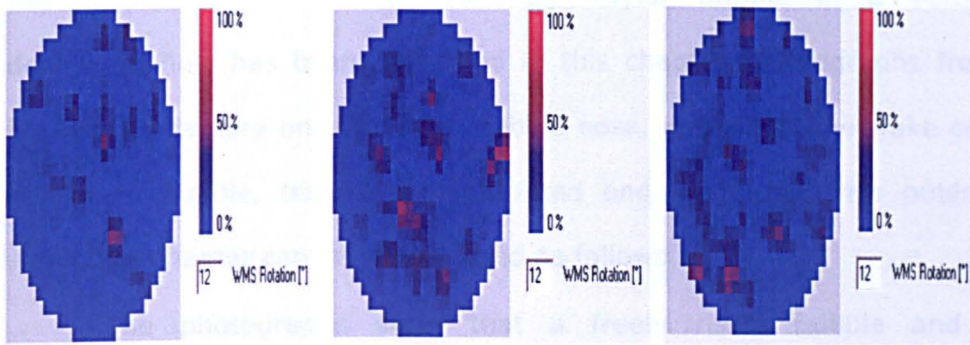
(a) Ugs= 0.037m/s   (b) Ugs= 0.045m/s   (c) Ugs= 0.057m/s
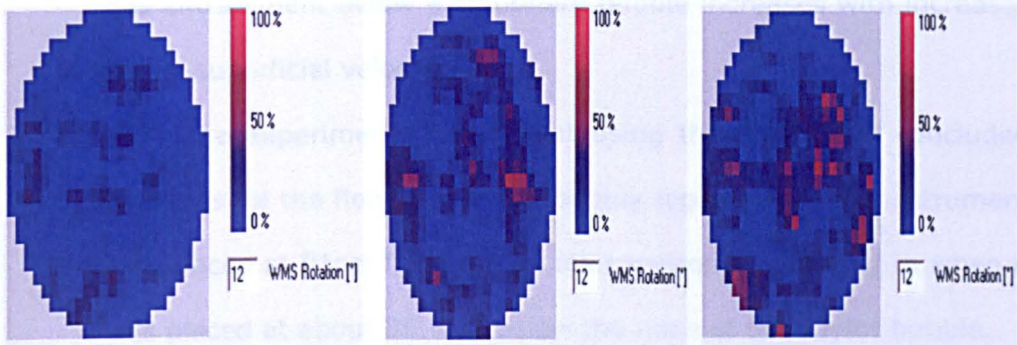
(d) Ugs= 0.037m/s   (e) Ugs= 0.045m/s   (f) Ugs= 0.057m/s
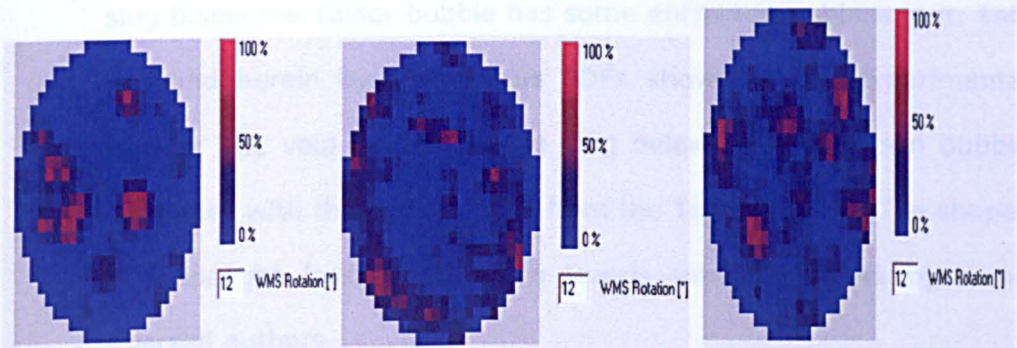
(g) Ugs= 0.037m/s   (h) Ugs= 0.045m/s   (i) Ugs= 0.057m/s

Figure 6.21: Display by WMS showing the wake section with no cap (a-c),

with conical cap (d-f) and with spherical cap (g-i).

6.7   Summary

Experimental data from a stationary Taylor bubble in a vertically downward flow has been presented in this chapter. Photographs from a high speed camera on the Taylor bubble nose, as well as the wake of the stationary bubble, have been presented and compared with published work. The chapter can be summarised as follows:

- The photographs show that a freely rising bubble and the theoretical shape resemble the nose of the simulated stationary Taylor bubble. The photographs, as well as the PDFs, illustrate that gas entrainment below a stationary bubble increases with increases in gas superficial velocity.

- From the experiments carried out using the WMS, it is concluded that most of the flows are in the bubbly region when the instrument was placed at 81cm from the air inlet section as opposed to when it was placed at about 35.5cm below the nose of the Taylor bubble.

- Previous work carried by various authors, has shown that the liquid slug below the Taylor bubble has some entrained bubbles in it. This is found herein by the various PDFs shown in the experimental results. The void fraction in the slug below the held down bubble correlates with the gas loss rate from the Taylor bubble. The shapes of these gas loss curves show trends similar to work by some selected authors.

- The wake lengths measured for stationary bubbles were compared with previous work by some authors. This showed that the wake length depends on the class of flow and the pipe diameter. However, maximum and minimum values obtained from the video capture show some agreement with the work by van Hout et al (1992) and are generally close to the results of other authors.

- Bubble sizes increase with increase in gas superficial velocity at constant liquid superficial velocity. This may be as a result of continuous coalescence of entrained bubbles of small diameters to form bigger bubbles until these bubbles become unstable and then deform.

Abolore Abdulahi

Chapter Seven
Film Thickness Measurement on a standing bubble using a Laser Instrument

7.1   Introduction

This chapter reports on measurements carried out on the film thickness of a stationary bubble in a two-phase downward flow. This is needed in the design calculations for the hydrodynamics and heat and mass transfer. The entrainment characteristics discussed in Chapter 6 are not complete without studying the root cause of such entrainment. This has been established in Chapter 6 as being the result of falling liquid films impinging on the tail of a Taylor bubble in slug flows. Also, in chapter two, importance of these falling films were reported.

There is little information concerning mean film thickness for downward co-current flow, especially in the region of strong phase interaction. Kulov et al. (1979) simultaneously measured the mean film thickness, pressure drop and entrainment in a 2m long, 25mm diameter pipe. However, these measurements were based on falling films in upward flows only. A study of the inception and growth of waves on falling liquid films has been reported by Portalski and Clegg (1972). The authors used two experimental techniques, the instantaneous sampling of the varying film thickness at fixed points of the wetted wall using a light absorption method and, 'freezing' of the incipient wave motion on dyed liquid films using photographic means, and using micro-densitometry to produce profiles of the developing waves. They showed that the mean film thickness increased slightly after the inception of waves. Takamasa and Kobayashi

         Abolore Abdulahi

(2000) tried to elucidate details of nonlinear phenomena of waves on a film through spatial temporal knowledge of the interfacial waves. They used a method for measuring waves on a film flowing down the inner wall of a vertical tube, using. The purpose of their study was to clarify the effectiveness of the new method for obtaining detailed information on film thickness or wave characteristics, and to investigate the effect of film entry length on the phenomena. Other reported works by various authors have been described in details in Chapter 2.

Common measurement techniques for film measurements are needle point, pressure probes, pitot tubes and hot-wire anenometers. The main disadvantage of these instruments is the disruption to the flow by the probes because they are intrusive. In some cases, there is the effect of limited spatial resolutions; hence the disturbance of the film flow should be avoided as it can change the characteristics of the film. In addition to the Laser Focus displacement meter used in this chapter, the results from the Wire Mesh Sensor reported in chapter 6 are also compared. The comparison show that Wire Mesh sensor film thickness results are much higher than those obtained locally from LFDM for the superficial velocities considered. This is understandable as the WMS results are generated from the methods explained in Chapter 2. However, the small gaps in the crossing wires are unaccounted for in WMS, hence the difference in results. This will be discussed in details in section 7.3.4.2. of this Chapter. Another reason, as noted by Zangana (2011), is that two instrumentations usually differ in film thickness measurement when the liquid superficial velocities are increased.

7.2   Experimentation

7.2.1   Principle of Laser Focus Displacement Meter

The Laser focus displacement meter utilizes the confocal principle with laser light to determine the location of an interface between two media. When the focal point of a converging beam is moved, the peaks in the reflected light intensity when the laser's focal point is at the two media interface are located by the instrument. Within the LFDM unit, a semiconductor laser source produces a diverging beam of light. This diverging beam of light is reflected by the collimating lens onto the objective lens which makes the beam converge to a point on the test section. The objective lens is moved in an oscillating manner in order to allow up and down movement of the focal point. This is achievable when the collimating lens is constrained to a known location on the test section and securing the objective lens on one of the vibrating prongs of a tuning fork. The tuning fork is then subject to a known frequency from a vibration source and in turn, the objective lens oscillates at a known frequency and amplitude. The focal point of the beam scans up and down at the same frequency and amplitude as the objective lens. When the focal point is located on the target surface, then the light will be reflected back into the LFD measuring unit with greatest intensity. When light passes through the pinhole of the LFDM, the light receiving element senses a light intensity peak. With a known location of the oscillating objective lens measured by a position detection sensor, the LFD can match the light intensity peak with a focal point location. Thus, the target surface location can be determined. In these experiments, the location of the target is within the Perspex pipe (the liquid film). Continuous tuning to set surfaces will ensure identification of the surfaces being penetrated by the laser beam. These are the pipe wall and the liquid inner as well as outer surfaces. Hence, the film

thickness can be measured through measuring of the difference in height between the inner and outer surface of the liquid film which is displayed on the Instrument monitor. The instrument is shown in 7.1.
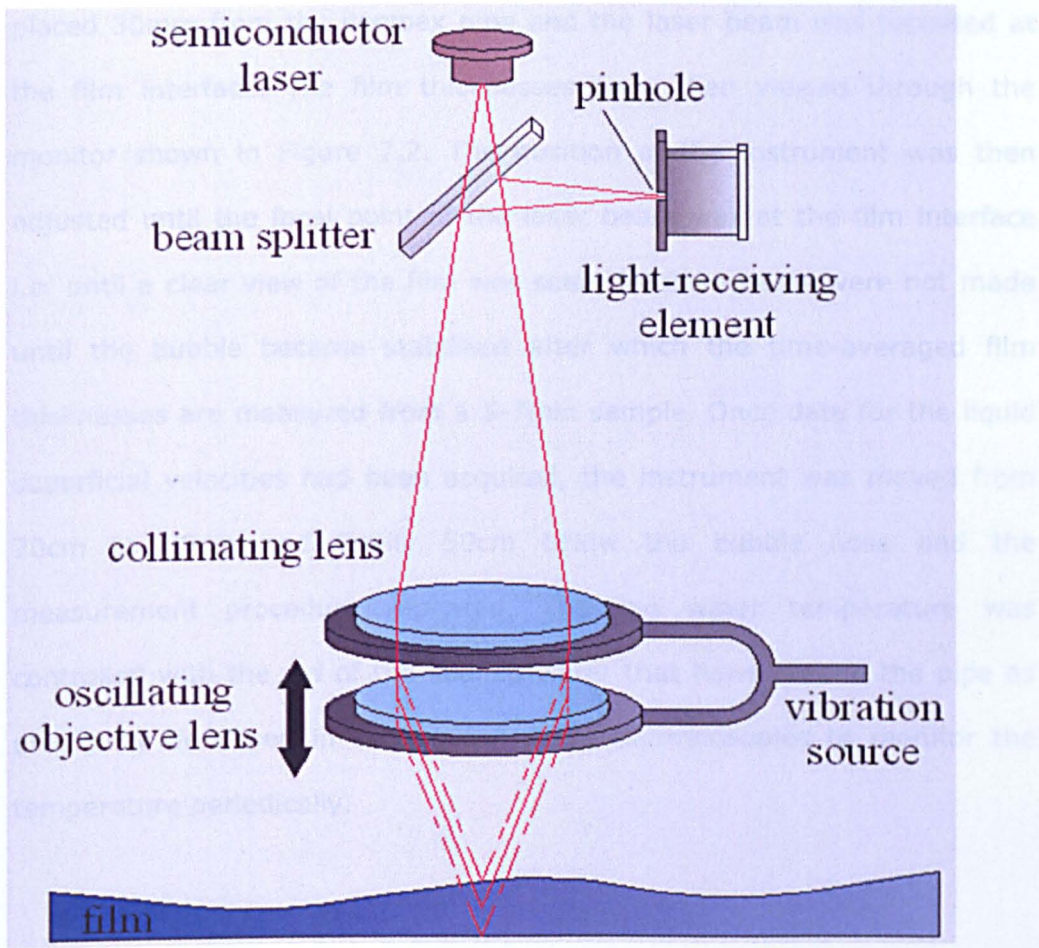
Figure 7.1: Diagram for laser focus displacement meter by Wegener and Drallmeier (2010)

7.2.2   Application of Laser Focal Displacement Meter

The test facility is shown in Figure 7.1. The facility has a closed liquid circuit with a working section 67mm in internal diameter and with a length of 3m and an open gas circuit. The experimental system allowed investigations of liquid superficial velocities ranging from 0.25-0.33 m/s and gas superficial velocities of 0.008-0.08 m/s. Tap water, maintained at 20±0.5°C, was used as the liquid phase, while air taken from the

laboratory compressed air supply was used as the gas phase. The LFDM used has an uncertainty of ±1.5%.

With the initial condition set as that described in Chapter 5, the LFDM was placed 30mm from the Perspex pipe and the laser beam was focussed at the film interface. The film thicknesses were then viewed through the monitor shown in Figure 7.2. The position of the instrument was then adjusted until the focal point of the laser beam was at the film interface i.e. until a clear view of the film was seen. Measurements were not made until the bubble became stabilised after which the time-averaged film thicknesses are measured from a 5-7min sample. Once data for the liquid superficial velocities had been acquired, the instrument was moved from 20cm to 30cm and finally 50cm below the bubble nose and the measurement procedure repeated. The tap water temperature was controlled with the aid of the cooling water that flows around the pipe as previously described in section 5.2 using thermocouples to monitor the temperature periodically.
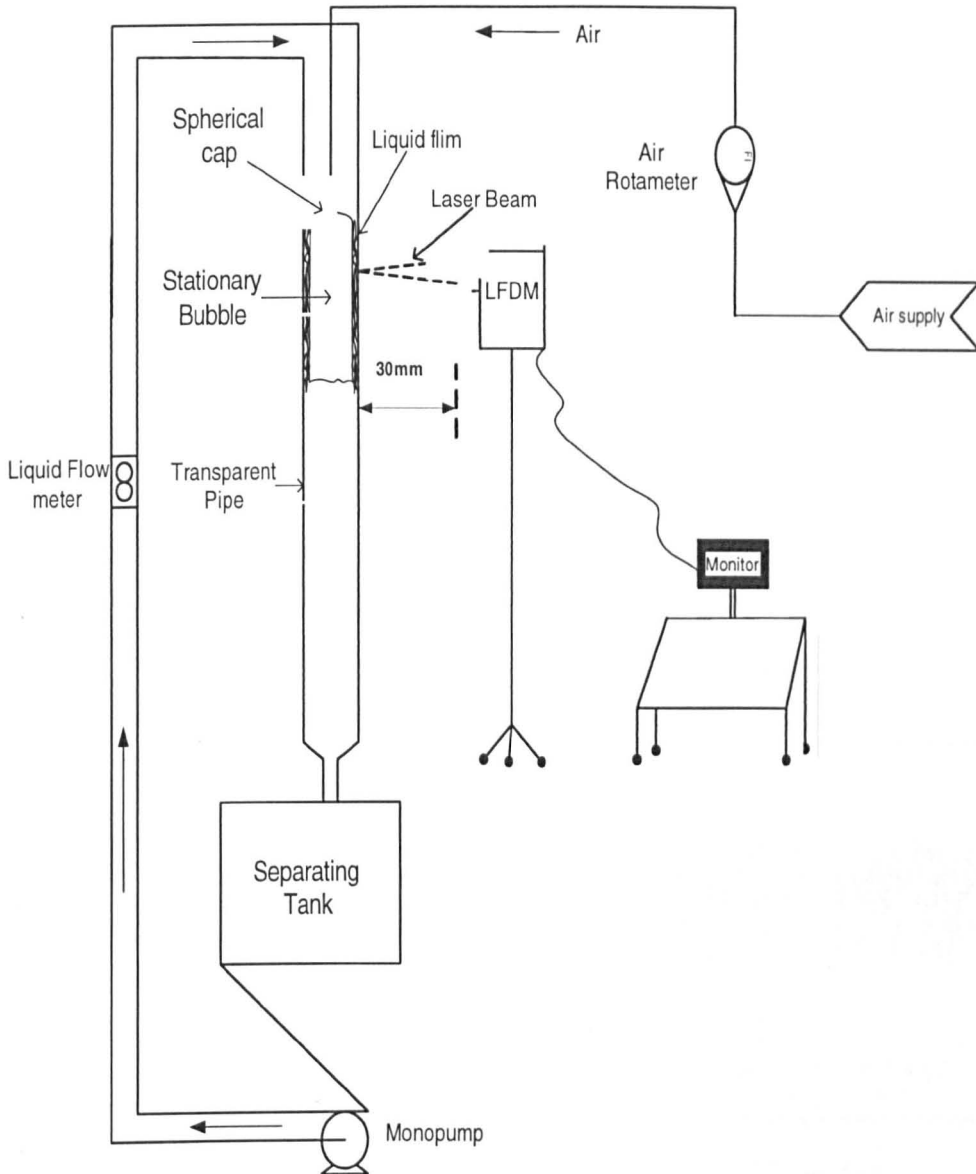
Figure 7.2: Schematic of experimental work using LFDM

7.3 Experimental Results

7.3.1   Time series of film thickness and Mean of film thickness

A different approach to Probability Distribution is to use the time series of

the film thickness. At the lowest focal position of the LFDM lens, 20cm

Abolore Abdulahi

below bubble nose, the film thicknesses for a liquid superficial velocity of 0.29m/s are shown in Figure 7.3:

(a)

(b)

(c)

(d)
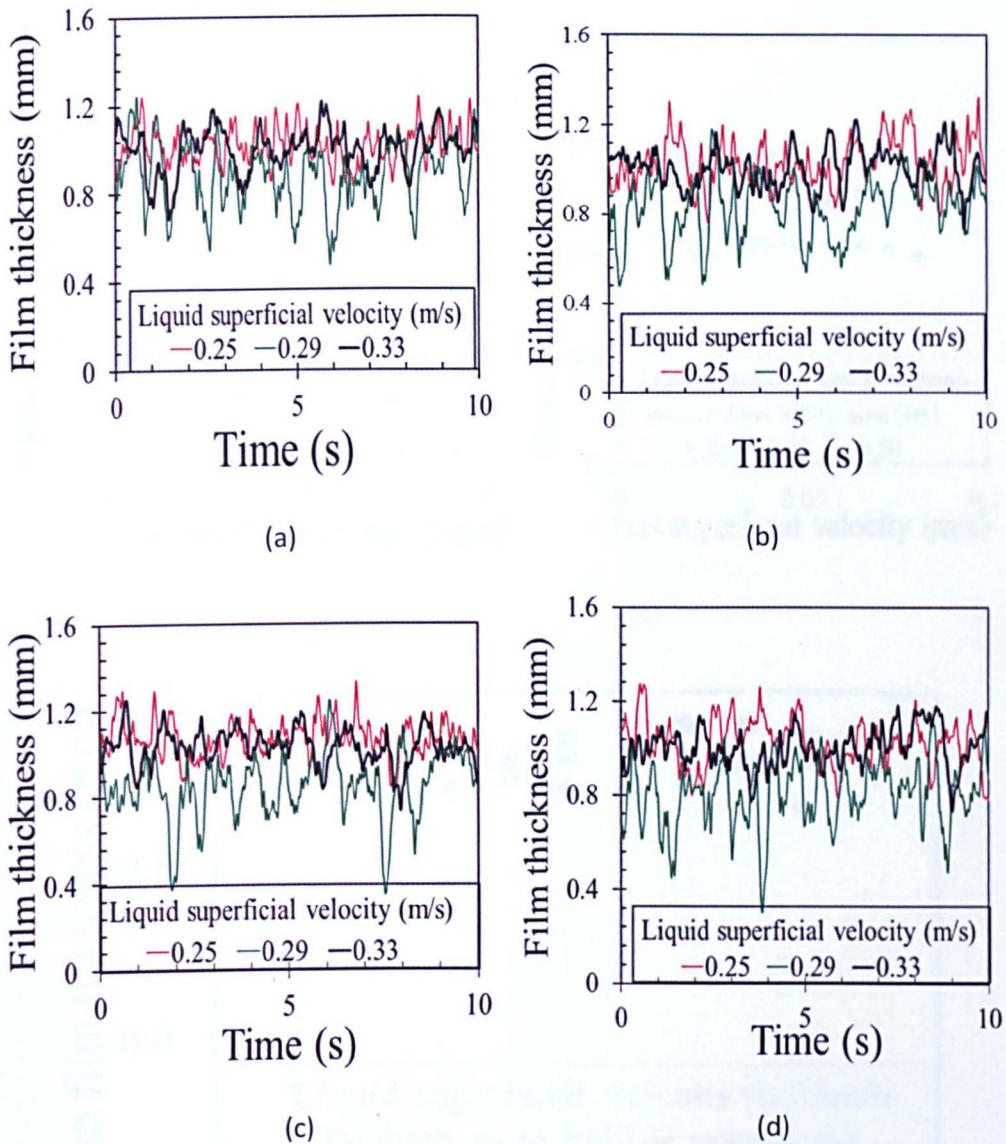
Figure 7.3: Plot of Time series of film thickness at gas superficial velocities of (m/s): (a) 0.008, (b) 0.012, (c) 0.016 and (d) 0.020 with LFDM at 20cm below bubble nose

The mean film thickness for all the data obtained at the three measurement points are shown in Figure 7.4. Interestingly, in the case of mean film thickness, the lowest values were obtained at 20cm below the bubble nose at a liquid superficial velocity of 0.29m/s, which was

equivalent to the rise velocity of the liquid if the gas was assumed to be stationary.

(a)　　　　　　　　　　　　　(b)

(c)
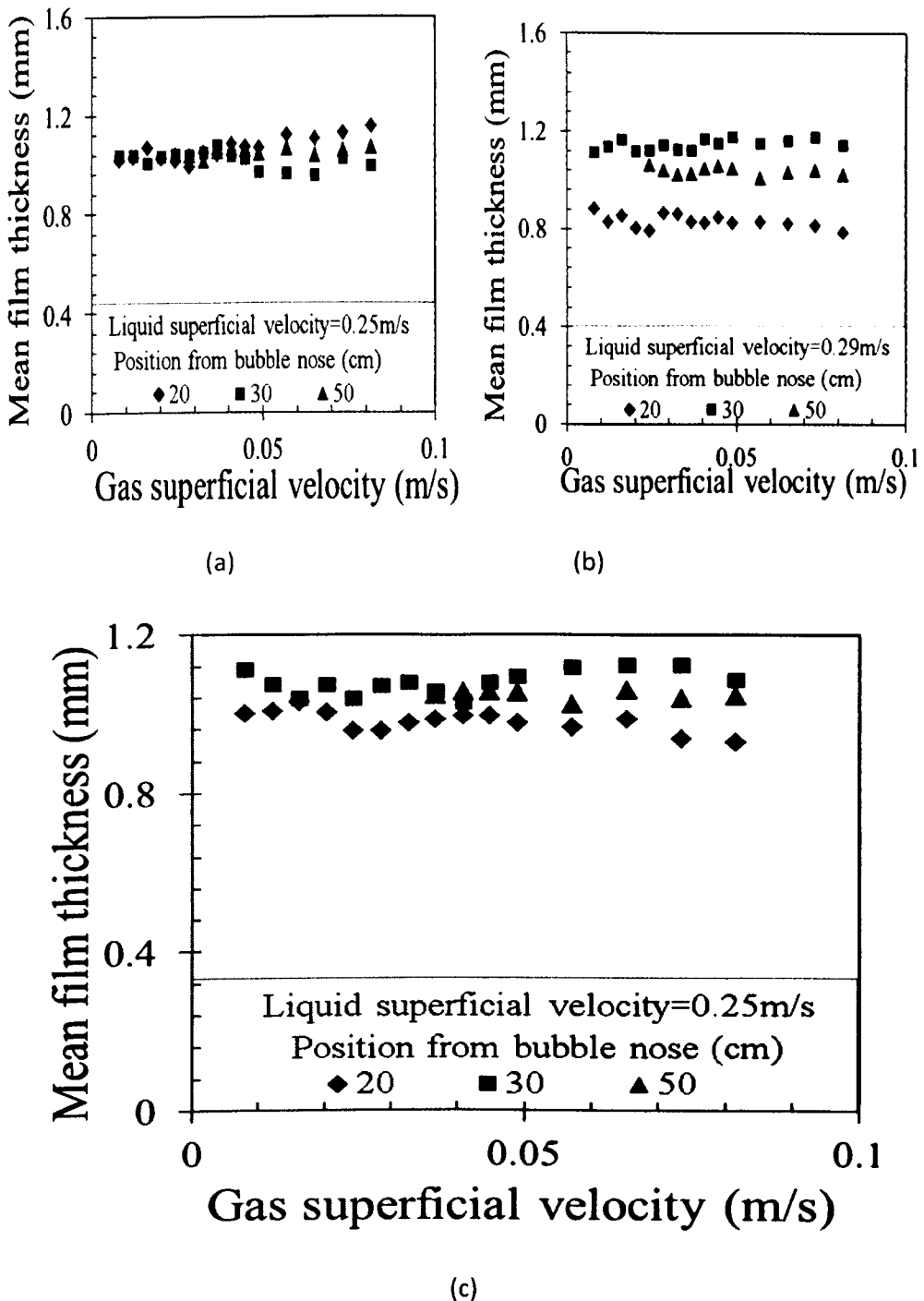
Figure 7.4: Plots of Mean film thickness at liquid superficial velocities of (m/s): (a) 0.25, (b) 0.29, and (c) 0.33 with the LFDM at different positions below the bubble nose as indicated

The percentage standard deviation per mean film thickness shows a peak of 10% in Figure 7.5. This, in a way, shows that the film thickness values are very close, depending on the position of the instrument

(a)

(b)

(c)

(d)
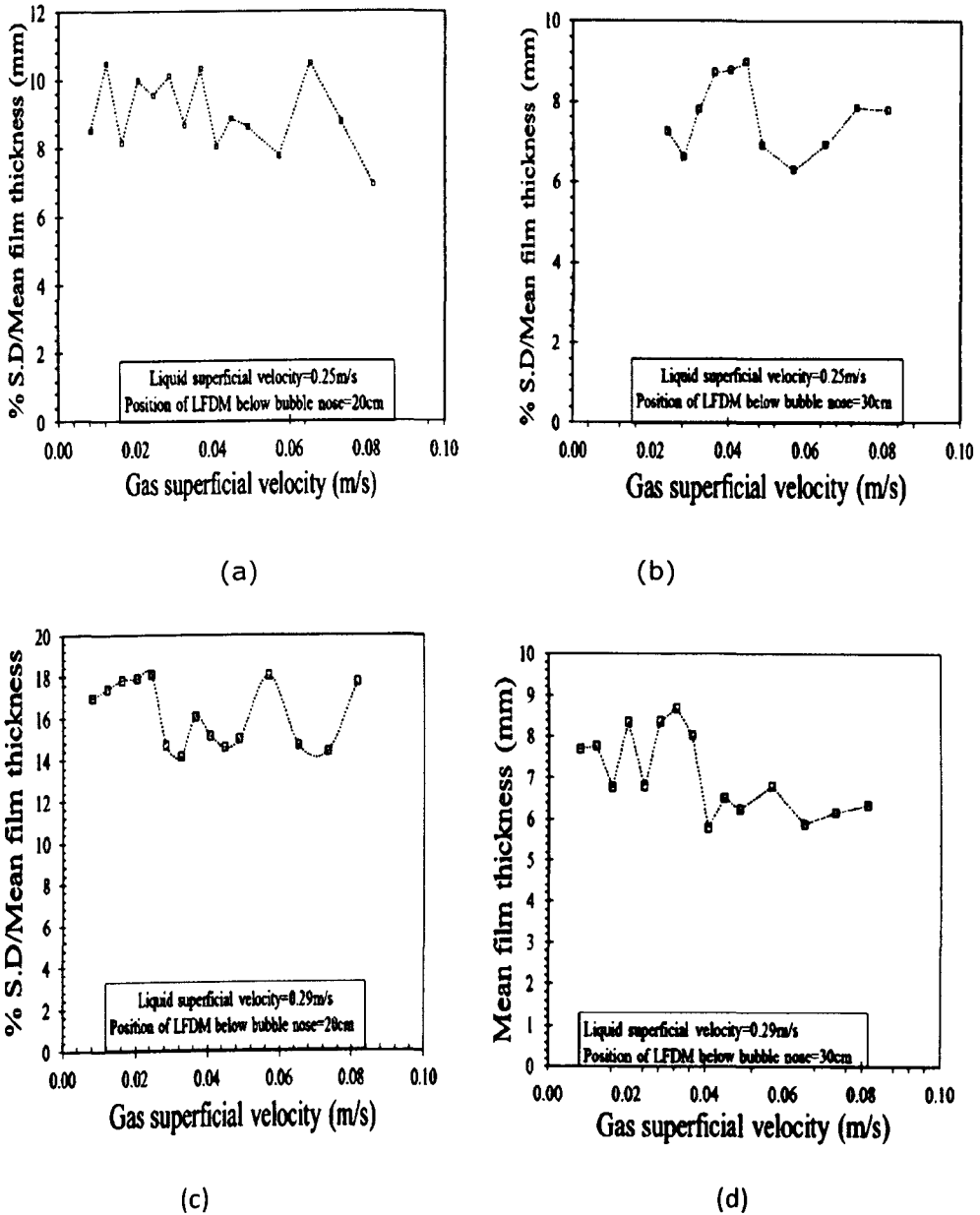
Figure 7.5: Plots of % Standard deviation per mean film thickness at liquid superficial velocities of (m/s): (a) 0.25 and (b) 0.29 with LFDM at 20cm and 30cm below bubble nose

Abolore Abdulahi

7.3.2   Probability Density Function of LFDM

The film thickness PDF is shown in Figure 7.5 (a)-(f).

(a)

(b)

(c)

(d)

(e)   (f)
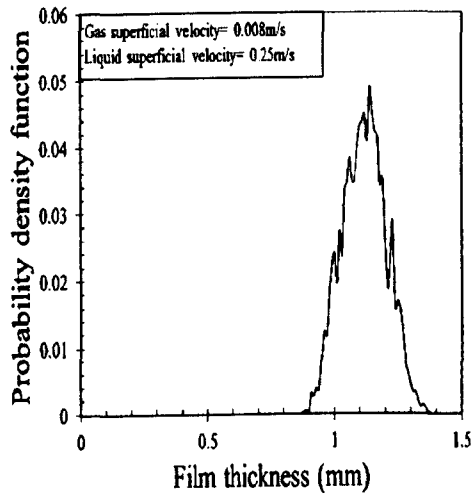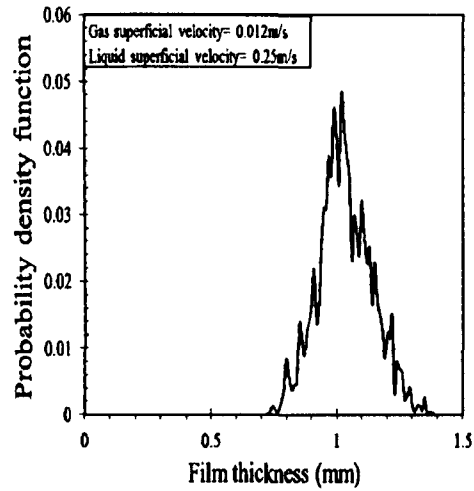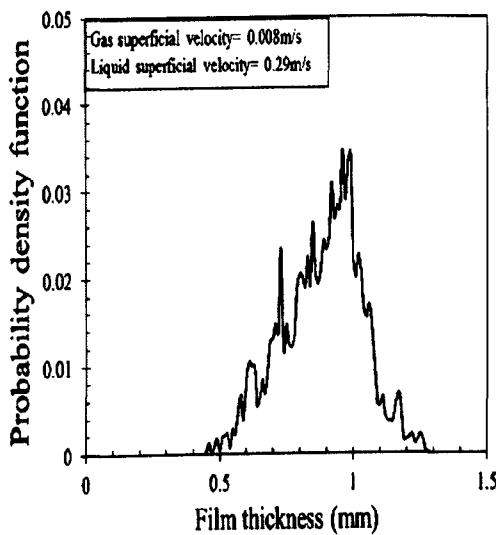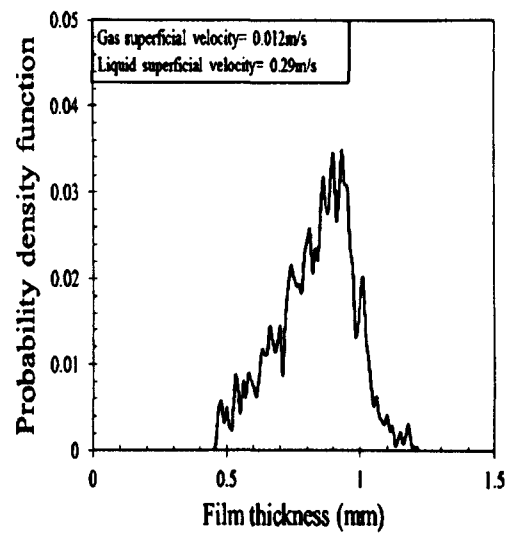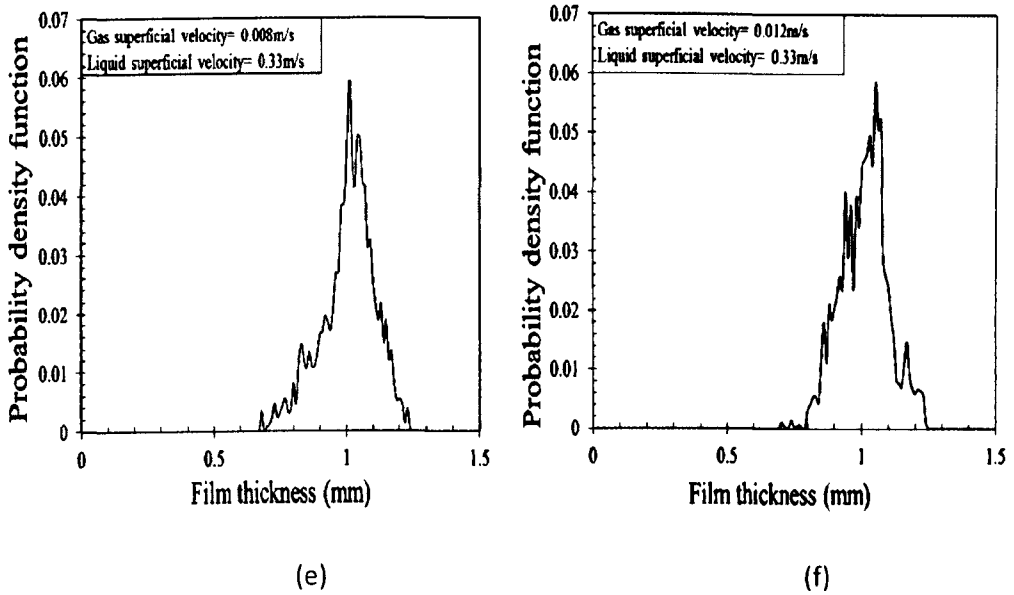
Figure 7.6: Plot of PDF of film thickness with liquid superficial velocities of 0.25, 0.29 and 0.33m/s LFDM at 20cm below bubble nose

They show the film thickness distribution at different superficial gas velocities. Interestingly, the distributions show that film thicknesses obtained for a liquid superficial velocity of 0.29m/s are lower than those obtained at other liquid superficial velocities. This velocity has been described as the drift velocity in Chapter 2. This is further illustrated in Figure 7.7.

(a)   (b)
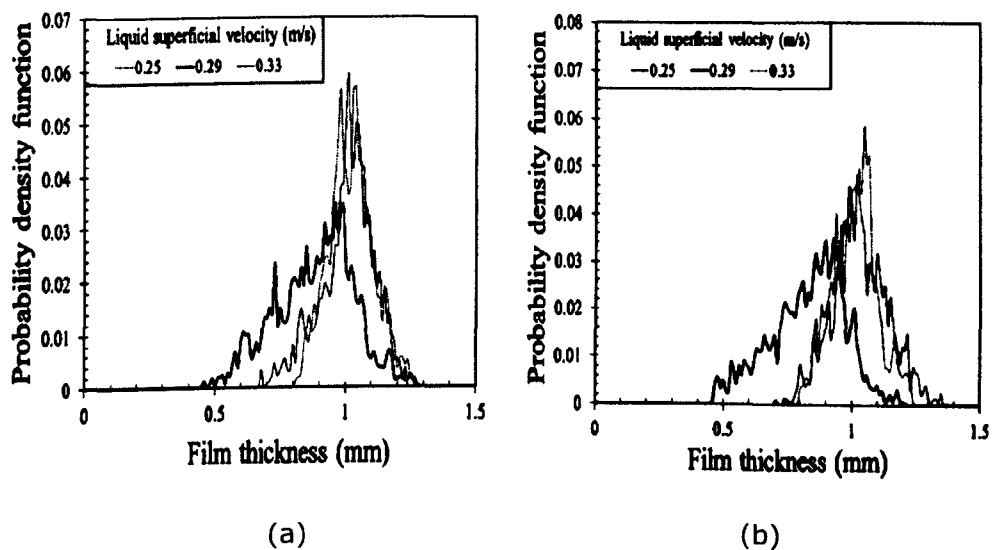
Figure 7.7: Plot of PDF of film thickness at gas superficial velocities of (a) 0.008 and (b) 0.012 with LFDM at 20cm below bubble nose

Abolore Abdulahi

However, as the position of the focus of the LFDM is increased downstream, there is shift in the position of the film thickness distribution and the lower liquid superficial velocity now shows the lowest average film distribution, as illustrated in Figure 7.8.

(a)   (b)
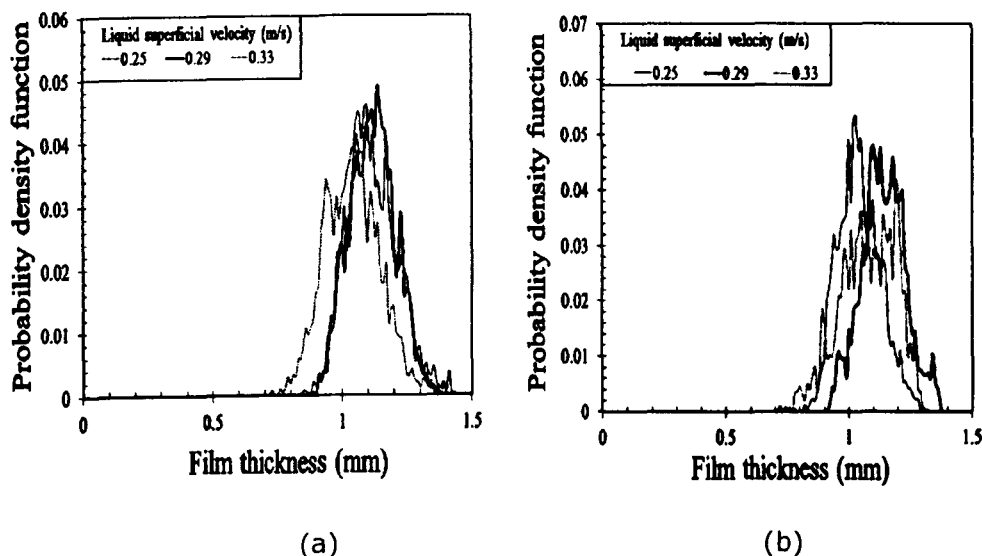
Figure 7.8: Plot of PDF of film thickness at gas superficial velocities (m/s) of (a) 0.008 and (b) 0.012 with LFDM at 30cm below bubble nose.

7.3.3   Power spectral density (PSD) of film thickness

Frequencies were obtained using autocorrelation of Fourier series for the film thicknesses measured. Power spectral densities against frequency are shown in Figures 7.9 (a)-(f). These plots are for the film thickness measurements at positions 20, 30 and 50cm below the nose of the stationary bubble. It is shown that, as the position of the LFDM is f moved downstream, the perturbations by the film waves increases. Hence, the amplitude for waves are generally smoother upstream than downstream. In this case, the plots are not able to be used for flow regime delineation because the experiments are within a single regime of simulated slug flow, unlike in Chapter 4 where PSD plots were used to identify transitions from one regime to another.
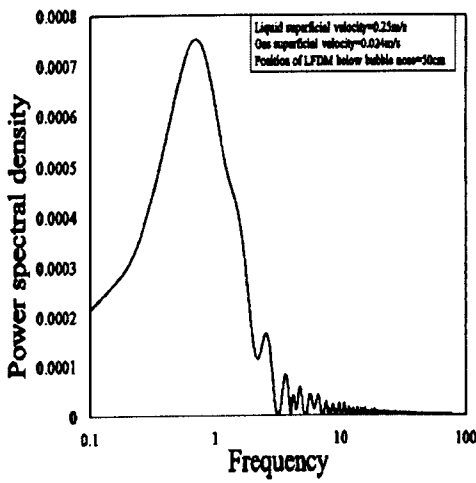
(a)
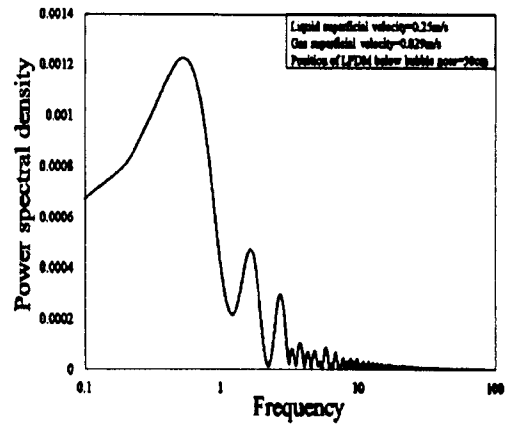
(b)
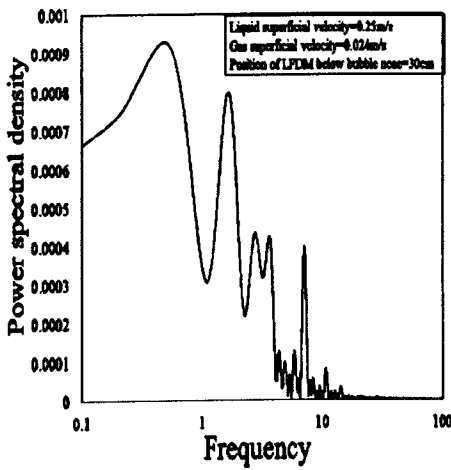
(c)
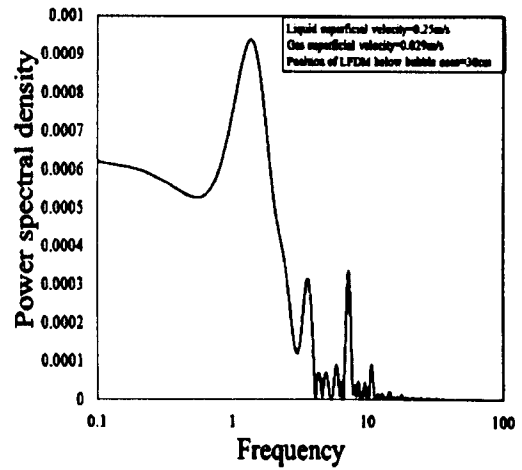
(d)
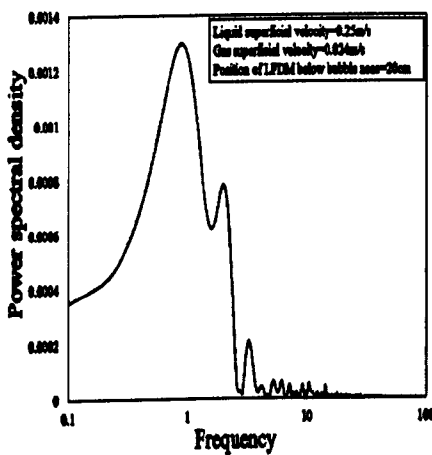
(e)
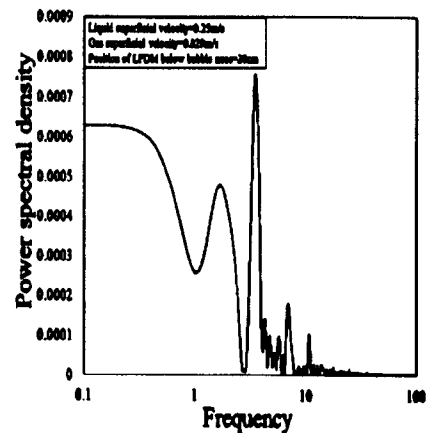
(f)

Figure 7.9: Plots of Power spectral density with LFDM at 20, 30 and 50cm below bubble nose.

Abolore Abdulahi

In a similar way to those shown in Figure 7.9, the dominant frequency generated using the method expressed in Kaji (2008) generally vary sinusoidally with gas superficial velocity, as can be seen in Figure 7.10. The method described in Kaji (2008) involved using the Auto-covariance of the void fraction data in Fourier Transform to obtain the dominant frequency. The nature of the plots is attributed to the perturbations in the film waves as the film falls and the instrument positions are varied downstream.

(a)   (b)

(c)   (d)
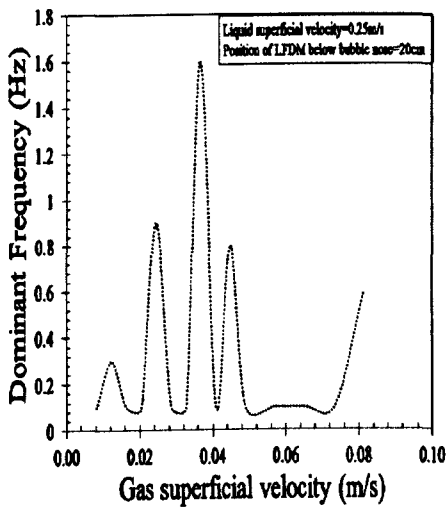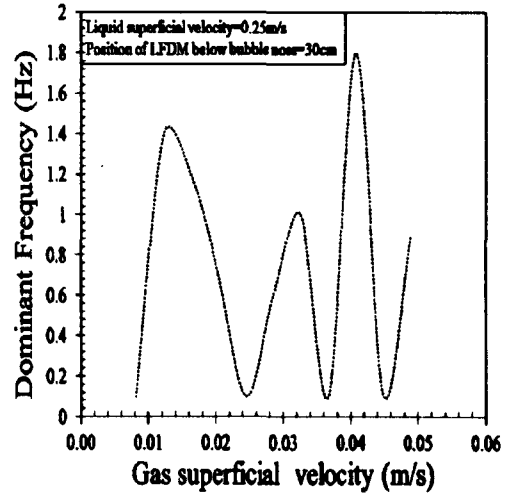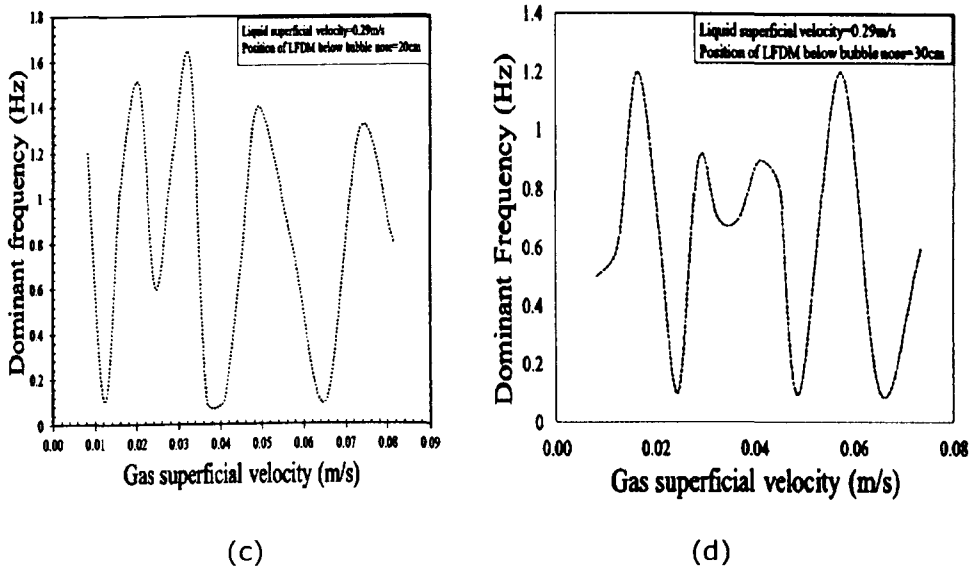
Figure 7.10: Plots of dominant frequency versus gas superficial velocity showing how wave perturbations affect frequency

7.3.4   Comparison with results by other workers

As previously discussed, few authors have reported film thickness measurement of held down bubbles using a laser instruments. Kockx et al. (2005) measured film thickness using Laser Induced Florescence (LIF) as part of the experiments carried out to study gas entrainments in a stationary bubble. However, the pipe diameter in that work was higher (100mm) than in the present study.

7.3.4.1   Comparison with published models and experimental data

The description of Nusselt equation is given in Chapter 2. This equation is the basis of most film thickness model propositions. A summary equation that can fit all previous work by various authors has been proposed by Spedding (2010), which shows the relationship between film thickness and other physical fluid properties as:

$$\delta = a \; (v^2/g)^{\frac{1}{3}} . \; (4\Gamma\rho/\mu)^b \qquad\qquad (7.1)$$

where a and b are constants given in Table 7.1,

v=kinematic viscosity, (m^2/s)

Abolore Abdulahi

$g = acceleration\ due\ to\ gravity\ (m/s)$

Γ= volumetric flow rate per unit circumference, (m^2/s)

ρ= density (kg/m^3)

μ= viscosity (kg/m.s)

This equation was used to predict the film thickness as the author's experimental conditions are altered to represent current study in order to make good analogy. The results are presented in Table 7.1. Nusselt's equation, as well as that proposed by Kapitza, predicted the film thickness accurately, in contrast to the predictions using the model equations by Takahama and Kato (1980) and other authors, as shown in Figure 7.11. They over-predict the film thickness. It is worth noting that work by these authors have been described in Chapter 2.
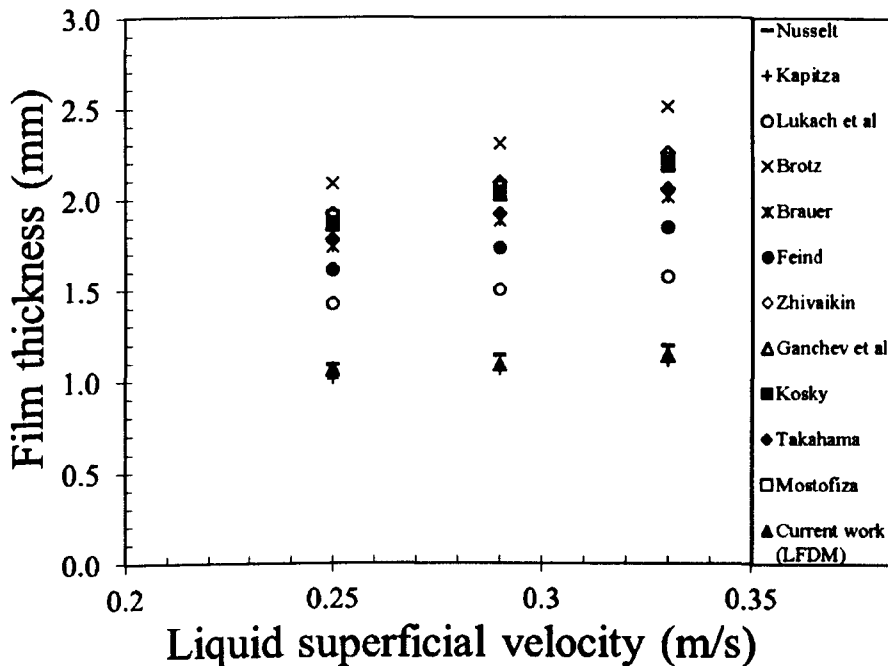
Figure 7.11: Film thickness plot using published models

Table 7.1: Comparison of film thickness results with published data

					Usl=0.25m/s	Usl=0.29m/s	Usl=0.33m/s
Author	Region	a	b	Basis	δ(mm)	δ(mm)	δ(mm)
Nusselt	Laminar	0.91	0.33	Theory	1.09	1.14	1.19
Kapitza	Wavy laminar	0.8434	0.33	Theory	1.01	1.06	1.11
Luka etal	Wavy laminar	0.85	0.37	Experiment	1.42	1.50	1.58
Brotz	Turbulent	0.0682	0.67	Experiment	2.09	2.30	2.51
Brauer	Turbulent	0.2077	0.53	Experiment	1.74	1.88	2.00
Feind	Turbulent	0.266	0.50	Experiment	1.61	1.73	1.85
Zhivaikin	Turbulent	0.141	0.58	Experiment	1.92	2.09	2.25
Ganchev etal	Turbulent	0.1373	0.58	Theory	1.87	2.04	2.20
Kosky	Turbulent	0.1364	0.58	Experiment	1.85	2.02	2.18
Takahama and Kato	Turbulent	0.2281	0.53	Experiment	1.78	1.92	2.06
Mostofizadeh	Turbulent	0.1721	0.56	Theory	1.90	2.07	2.22
current work	Wavy Turbulent			Experiment	1.06	1.09	1.14

7.3.4.2   Comparison with Wire Mesh Sensor results

The void fraction measurements from the WMS, reported in chapter Six, are used in the film thickness equation, expressed in Chapter Two as

$$\left(\frac{D}{2}\left(1-\varepsilon^{0.5}\right)\right).$$ These are compared to the LFDM measurements in Figure

7.11. The difference is explained as follows: The Wire Mesh Sensor based on a two point calibration. Extra calibration with all points of contact with the liquid film would be necessary to achieve the same result as the laser instrument. In addition, it is impossible to avoid the intrusiveness with the film although, it has been shown not to have an effect on the results by Richter et al. (2002) and Prasser et al. (2005a). This is mainly true for two-phase flow measurements where the film thicknesses are unimportant. Lastly, the void fraction results from wire mesh sensor at the crossing points of wires are time-averages. This may affect the accuracy of the film measurement when these are solely used to report film thickness.
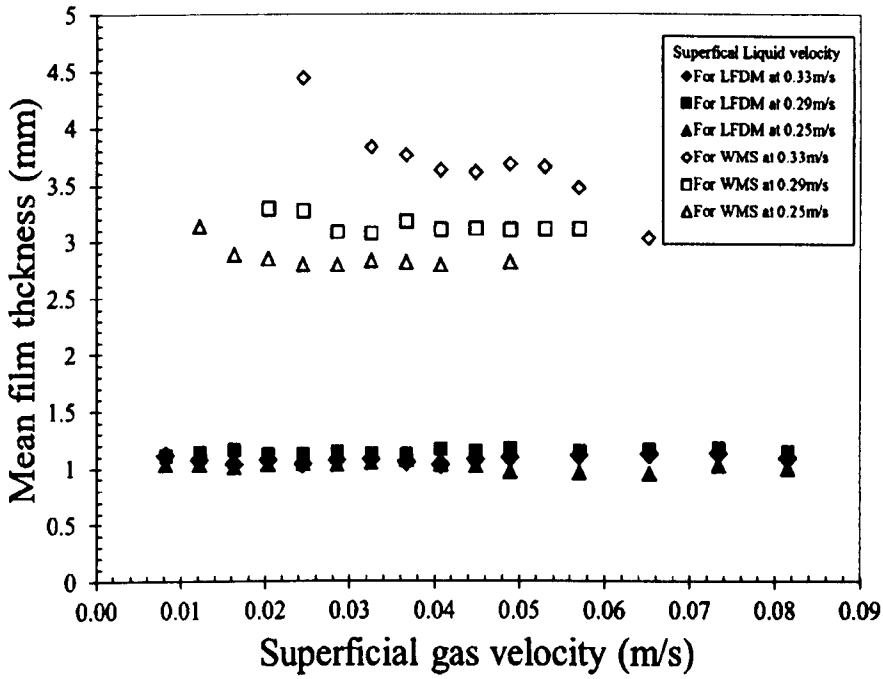
Figure 7.12: Comparison of WMS film thickness with LFDM results

In accounting for the disparity between the data from the LFDM film thickness and the local film thickness calculated from the WMS local void fraction, the schematic diagrams in Fig 7.13-7.15 are used, a sample can be found in Da Silva et al. (2010). The local void fraction is generated based on the signal from each crossing points of the wires in the sensor. However, the distance between the last crossing wires (in Figure 7.14) and the pipe wall is unaccounted for by the crossing wires and hence, this creates a difference in the values (in millimetres) when used to determine film thickness.
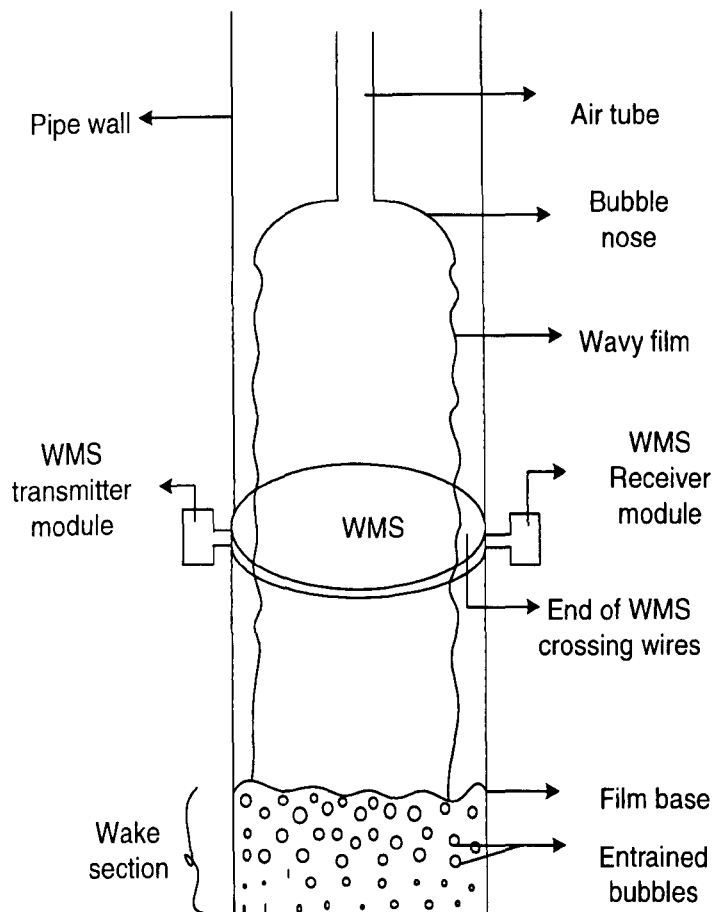
Figure 7.13: Schematic drawing for pipe section showing the film as it crosses the WMS
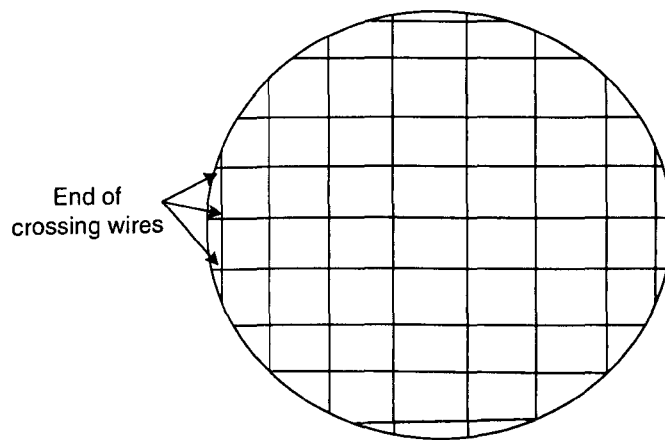
Figure 7.14: Schematic drawing for crossing wires of the WMS with the end of the crossing wires highlighted

The open end of the crossing wires have distances, Δ_1, Δ_2, ... in the range

1.2-1.8mm from the preceding crossing wires, as can be seen in Figure

7.15. If this distance (for instance 1.8mm) is added to the results from

LFDM film thickness, the resulting values will give rise to data almost equal

to film thickness calculated from WMS. For instance: 1.4mm (from LFDM)

+ 1.8mm (from distance between last crossing wire and the wall) =

3.2mm (from the calculated WMS film thickness)
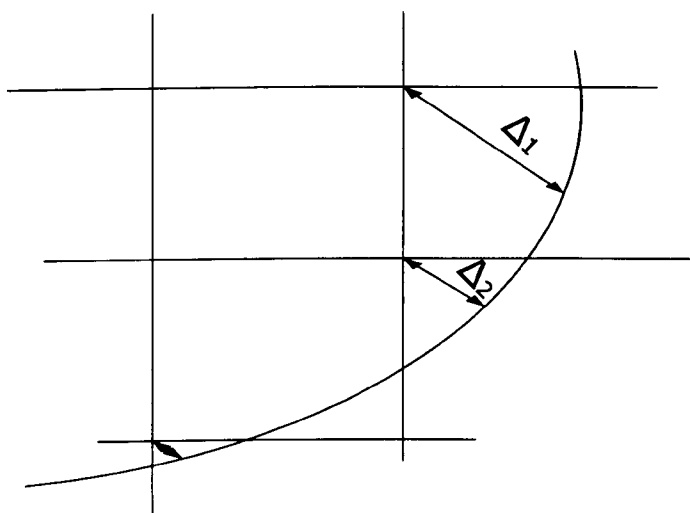
Figure 7.15: Some ends of the crossing wires of the WMS

7.3.5 Qualitative analysis of the films

It is important to analyse the video images captured during

experimentation qualitatively. This will enable thorough understanding of

the nature of the film. As initially identified in Table 7.1, the films in the

current study are turbulent wavy. The images provide the gas-liquid

interface of the flow structure. At a low gas superficial velocity of 0.012m/s

and a superficial liquid velocity of 0.28m/s, the gas-liquid interface was

observed to be smooth, as can be seen in Figure 7.16. The waviness of the

film surface is more obvious as the gas superficial velocities are increased.

At some point, bubbles also began to appear on the film surface at these

higher superficial gas velocities, as shown in Figures 7.17 and 7.18, which

represent a key feature of a falling annular film. These bubbles complement those already created by falling films at the base of the standing bubble and are a source of gas entrainment.
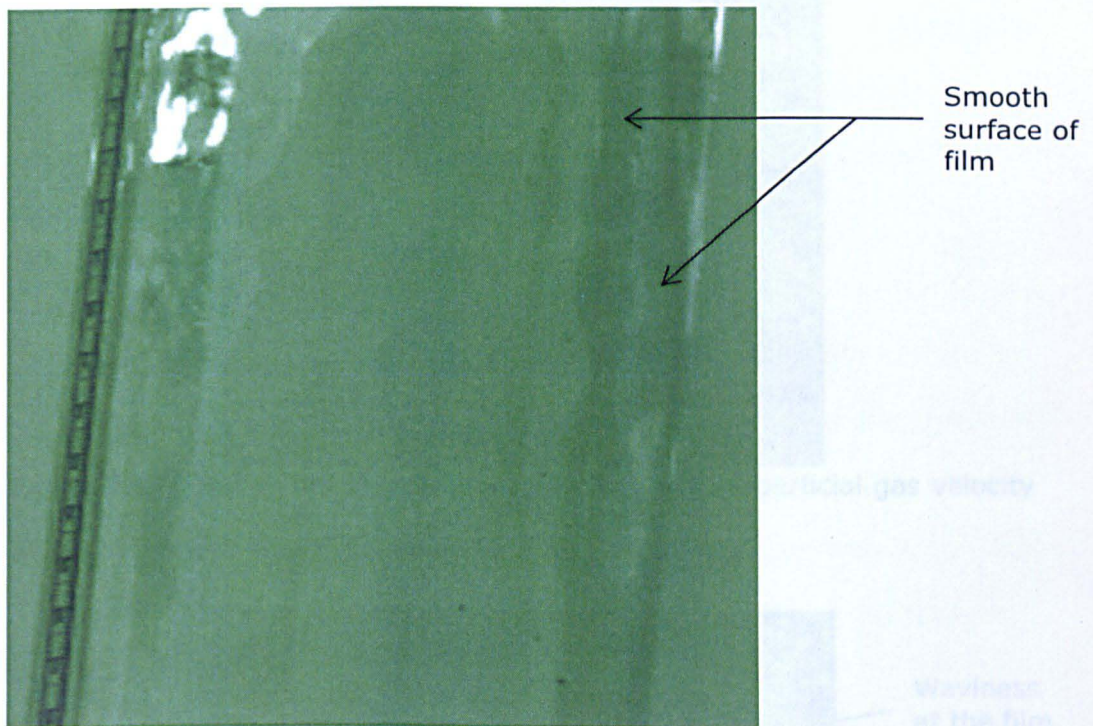
Figure 7.16: Smooth films at with superficial gas velocity at 0.012m/s and superficial liquid velocity at 0.28m/s

The bubble cap allows air to flow and grow into a big bubble, which are shown to grow bigger with increasing the gas superficial gas velocity. In this way, a single bubble is formed with smaller bubbles formed below the stationary bubble with a film flowing around the pipe wall. Liquid was not found to be entrained in the gas core. Dukler and Bergelin (1952) have also shown wave types similar to those in Figure 7.16

Figure 7.17: Wavy Film at gas-liquid interface with superficial gas velocity at 0.020m/s and superficial liquid velocity at 0.28m/s
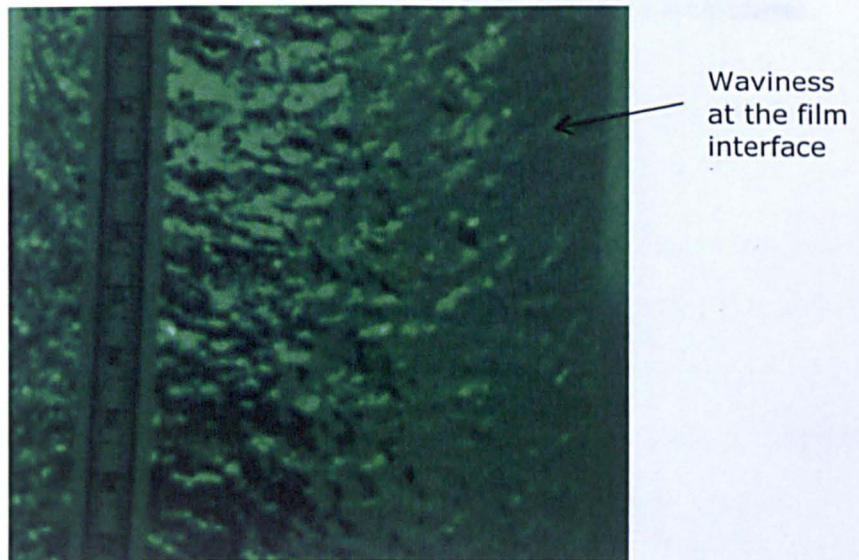
Figure 7.18: Wavy Film at gas-liquid interface with superficial gas velocity at 0.024m/s and superficial liquid velocity at 0.28m/s

7.4 Summary

Film thicknesses of a stationary bubble have been investigated in this chapter and the following summary is made:

- The PDF of film thickness show that their average is 1mm.

- Power spectral densities of the film thickness show that the films straighten out as you move downstream with decreasing superficial gas velocity.

- The film thickness measured by LFDM shows a very good agreement with Nusselt equation and the Kapitza model.

- The LFDM results show a large deviation from those obtained using the models of Takahama and Kato (1980) and others.

- The Wire Mesh Sensor shows a large difference with the results from the LFDM. This is understandable as the WMS results are derived from average values of void fraction at crossing points of the wires. This can be accounted for if the distance from the last crossing wires to the pipe wall are taken into consideration. This will ensure that the results from both instruments are much closer.

Chapter Eight
Effect of viscosity on a two-phase flow in a stationary bubble

8.1   Introduction

In Chapters 5, 6 and 7, water and air were used as the working fluid to study characteristics of gas-liquid flows of a stationary bubble. The same methodology has been used here with the range of conditions shown in Table 8.1. The range undertaken is the same as those used in Chapters 5, 6 and 7. However, unlike the previous chapters where three different caps were used to inject air into the stationary bubble, only the spherical cap has been used in this Chapter. This Chapter introduces the results of flows using two different viscous liquids, thus allowing the study of the effect of viscosity. Only Su and Metcalfe (1997) have reported the effect of viscosity on a fixed bubble. However, the liquid used by these authors still has a relatively low viscosity (6mPa.s). In this Chapter, the liquid used has viscosities of 42mPa.s and 152mPa.s. For better clarity, oil with viscosity of 42mPa.s will be regarded as low viscosity oil while that with a viscosity of 152mPa.s is regarded as high viscosity oil. A comparison is made with the work of Su and Metcalfe (1997) and the air-water experiment previously described in Chapter Six.

Table 8.1: Different cases considered for high viscosity oils

Gas superficial velocity (m/s)	0.008-0.08
Liquid superficial velocity (m/s)	0.25, 0.29, 0.33
Liquid viscosity (mPa.s)	42, 152

8.2   Experimental Results

The same type of flow structure reported in Chapters six and seven were observed using oil when the same methodology was followed, i.e. a stationary bubble was achieved with some entrained gas bubbles in the wake.

8.2.1   Dimensionless Analysis (for Thought Experiment)

The dearth in quantitative data for gas-liquid flows in vertical pipes using high viscosity liquid has been the major concept behind the current research. For a stationary bubble with liquid flowing around it in form of film, the gas entrainments are formed below the bubble wake as previously discussed. This liquid film has been studied extensively in Chapter 7 using low viscosity liquid, it is quite imperative to understand its relationship with viscosity as this may have an effect on gas entrainment since film impingement cause gas being entrained at the bubble wake. A simple way to begin is through the theoretical background between films and viscosity. This will lead to a better understanding when experimental data on viscosity effect are reported in the later part of this Chapter. Nusselt (1916) proposed a relationship between film velocity and film thickness as follows which was also reported by Spedding (2010),

Abolore Abdulahi

$$u_f \propto \delta^2 \tag{8.1}$$

where u_f is film velocity (m/s) and δ is film thickness (m)

But also from Nusselt (1916),

$$\Gamma \propto \delta^3 \tag{8.2}$$

where Γ is the volumetric flow rate per unit circumference

Combining equations (8.1) and (8.2) shows that:

$$u_f^{\frac{1}{2}} \propto \Gamma^{\frac{1}{3}} \tag{8.3}$$

Hence, $u_f \propto \Gamma^{\frac{2}{3}}$ \hfill (8.4)

But $\quad \Gamma = u_b \dfrac{\pi D^2}{4} \cdot \dfrac{1}{\pi D}$ \hfill (8.5)

where u_b is bubble velocity (m/s) and D is pipe diameter (m). This is by interpreting volumetric flow rate per unit circumference as equation 8.5 i.e. (velocity) x (area) ÷ (circumference of the pipe)

and $\quad R_\varepsilon \propto u_f^3$ \hfill (8.6)

where R_ε is rate of entrainment

From these relationships, it can be deduced that:

$$R_\varepsilon \propto u_f^3 \propto \Gamma^2 \propto D^2 \tag{8.7}$$

Hence total $R_\varepsilon \propto D^3$ (at constant u_b and μ_l)

Net rate of entrainment= Total entrainment-Total recoalescence

At constant tube diameter,

$R_\varepsilon \propto u_b^2$ (Since $R_\varepsilon \propto \Gamma^2$)

But

$$\Gamma \propto \frac{1}{\mu_l} \tag{8.8}$$

and $u_f \propto \mu_l^{\frac{-1}{3}}$ (8.9)

therefore $R_\varepsilon \propto \mu_l^{-1}$ (8.10)

The implication of this is that the higher the viscosity, the less bubbles are created by the impinging film. This means that fewer bubbles are created and entrained in the Taylor bubble wake as the liquid velocity is increased. Hence, the equations by Nusselt (1916) will play a role in the experimental work on gas entrainment. This phenomenon will be later demonstrated in this Chapter.

8.2.2   Time averaged void fraction and Mean void fraction

Time series plots obtained from the WMS, positioned at the same locations used in Chapters 5 and 6, displaying the time-averaged void fraction of the wake section of the stationary bubble are shown in Figure 8.1 (a)-(f). These show high and low viscosity oils at different gas and liquid superficial velocities. At low superficial gas velocities, for both liquid viscosities (Figures 8.1 (a), (c), (e)), the void fractions are seen to fluctuate within a narrow band. As the gas superficial velocity is increased, Figures 8.1 (b), (d), (f), the amplitude increases, as did the void fraction range over which the fluctuations occur. The void fraction for the low viscosity liquid show fluctuations with magnitudes higher than those for high viscosity liquid
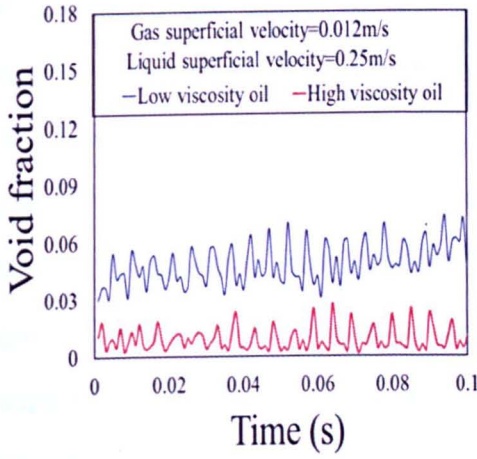
(a)
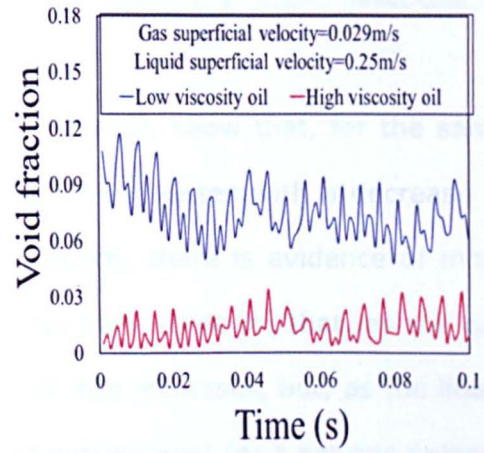
(b)
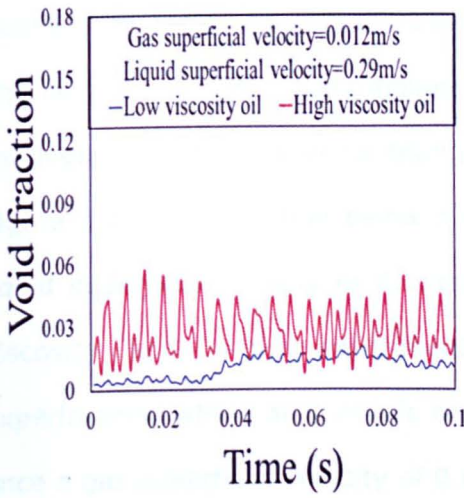
(c)
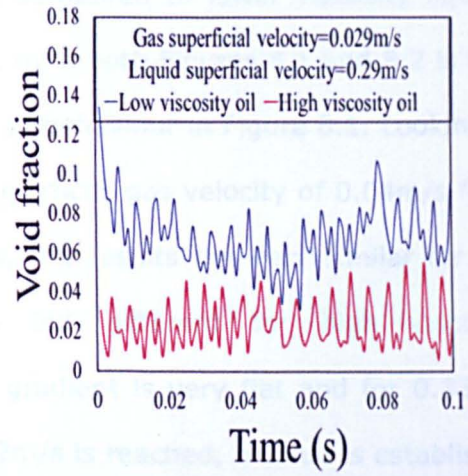
(d)
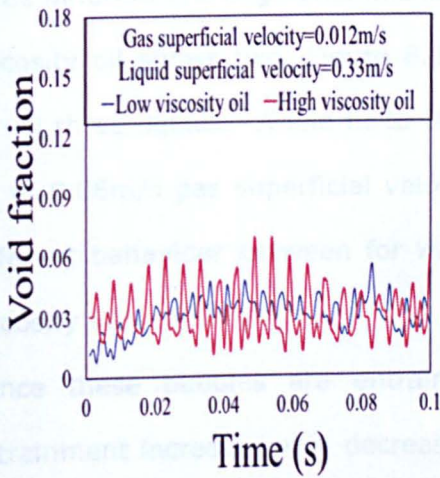
(e)
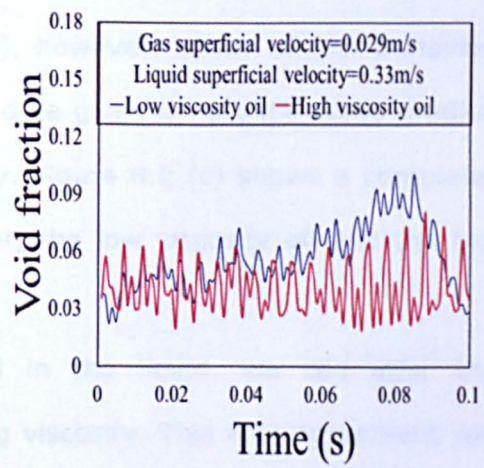
(f)

Figure 8.1: Time series of void fraction at superficial liquid velocities of 0.25m/s, 0.29m/s, and 0.33m/s.

The mean void fraction plots, Figure 8.2 (a)-(c), show that, for the same conditions, the mean void fraction generally increases with a decrease in liquid viscosity. For lower the viscosity liquids, there is evidence of more gas entrainment into the wake region and clear evidence that, as the gas superficial velocity increases, entrainment also increases, but, as the liquid superficial velocity increases the level of entrainment for a set gas velocity decreases. As viscosity is increased, this behaviour remains, but the quantity of entrained gas decreases compared to lower viscosity liquids. The other thing that is very apparent from both Figures 8.1 and 8.2 is that the high viscosity oil sees no change in behaviour in Figure 8.1. Looking at Figure 8.2, it is clear that below a superficial gas velocity of 0.04m/s for a liquid superficial velocity of 0.25m/s, the results are very similar for low viscosity and water experiments but different for high viscosity experiments, whilst at 0.29m/s the gradient is very flat and for 0.33m/s once a gas superficial velocity of 0.02m/s is reached, a value is established which remains. A more critical look at Figure 8.2 (a) shows that there are three different line segments in the high viscosity liquid plot, whilst the low viscosity oil shows two. Figure 8.2(b), however, shows similar behaviour for all three liquids. A line fit to the data gives almost the same gradient up to 0.06m/s gas superficial velocity. Figure 8.2 (c) shows a completely different behaviour between for water, the low viscosity oil and the high viscosity oil.

Since these bubbles are entrained in the liquid, we can infer that entrainment increases with decreasing viscosity. This is in agreement with the thought experiment described earlier in section 8.2.1 of this Chapter.
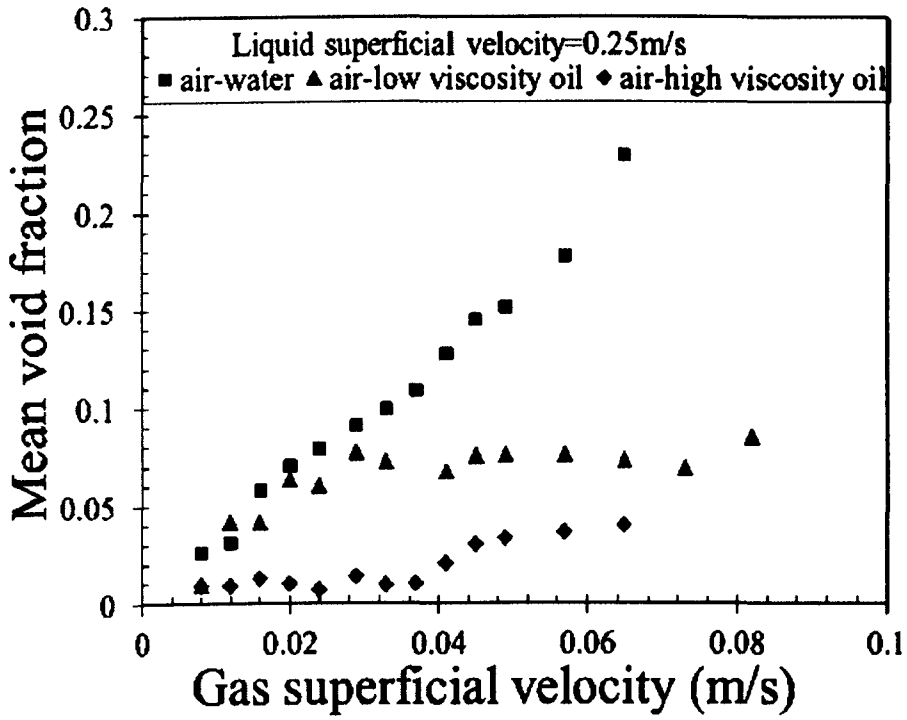
(a)
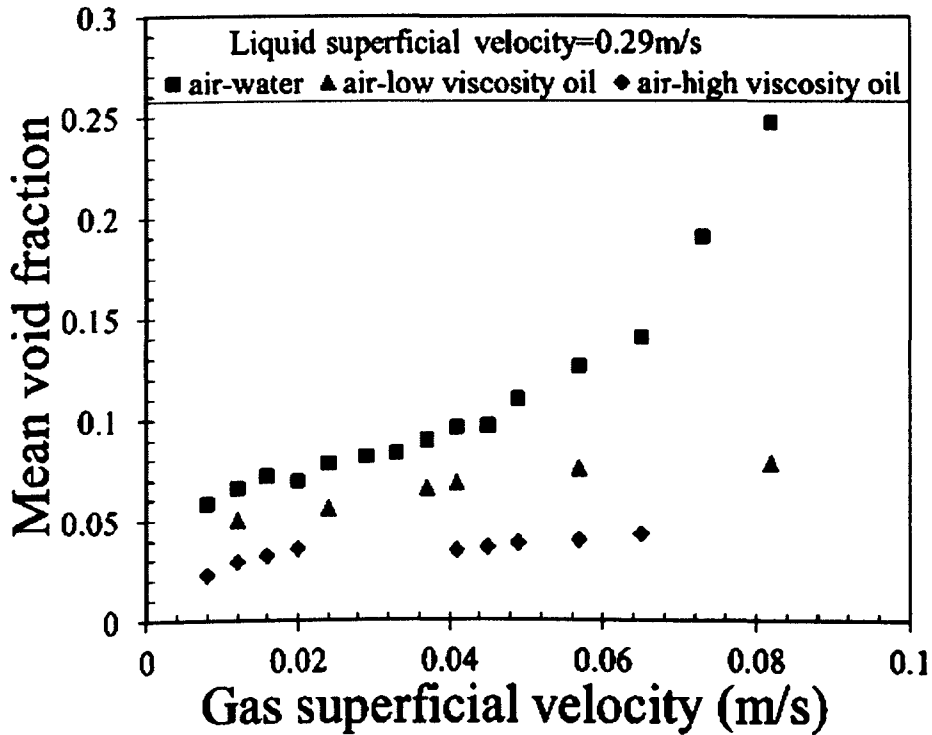
(b)
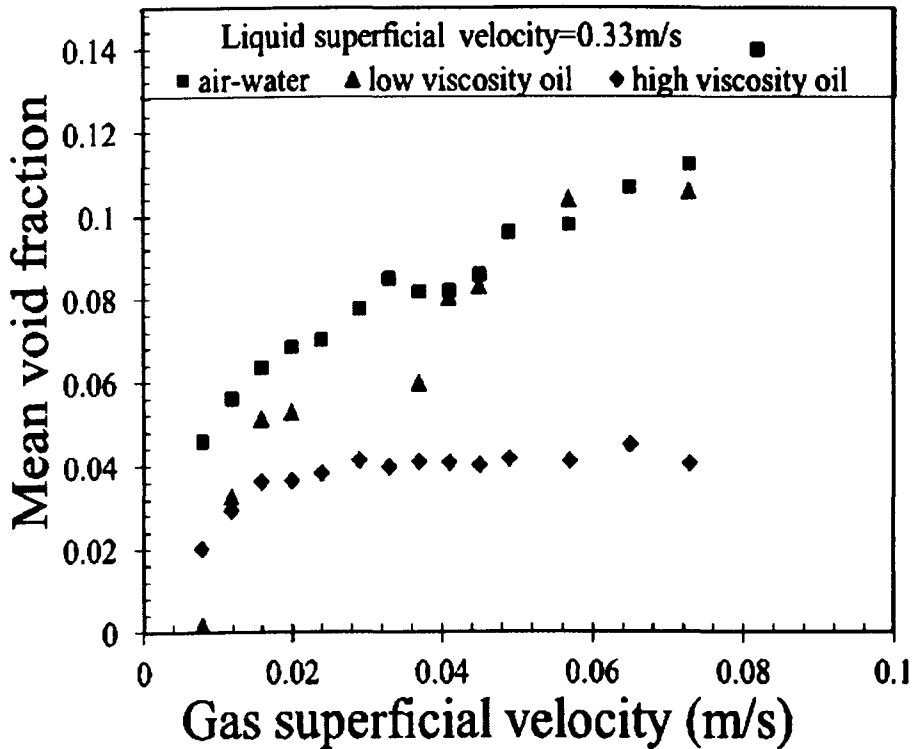
(c)

Figure 8.2: Mean void fraction at superficial liquid velocities of (a) 0.25m/s, (b) 0.29m/s and (c) 0.33m/s

8.2.3   Probability Density Function

The probability distribution of the void fraction in the wake section is shown in Figure 8.3. As the liquid viscosity is increased, the void fraction shifts from right to left, i.e. air present in the wake reduces just like the description in section 8.2.2. The void fraction values at which the peaks for the probability density function (PDF) occur for each liquid are observed to increase as the viscosity of the liquid reduces. These peaks are the void fractions with highest frequency of occurrence for the whole range of void fraction. As can be seen in Figure 8.3 (j), where the peaks for Figure 8.3 (i) are identified, the void fraction, ε, values at which these peaks occur are highlighted and these void fraction values are found to increase with increasing liquid viscosity for the same gas and liquid superficial velocities. They are represented by Peaks A, B, C for decreasing liquid viscosities.
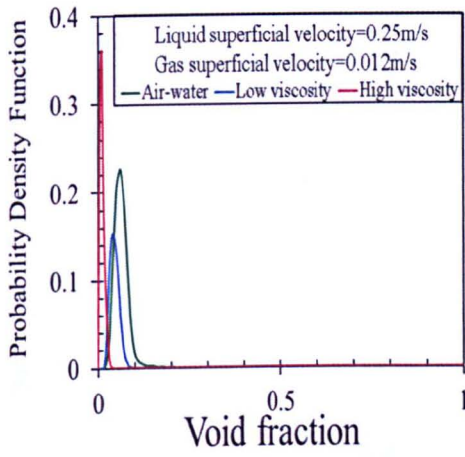
(a)
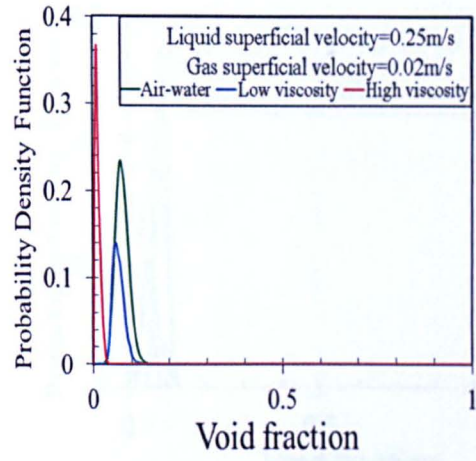
(b)
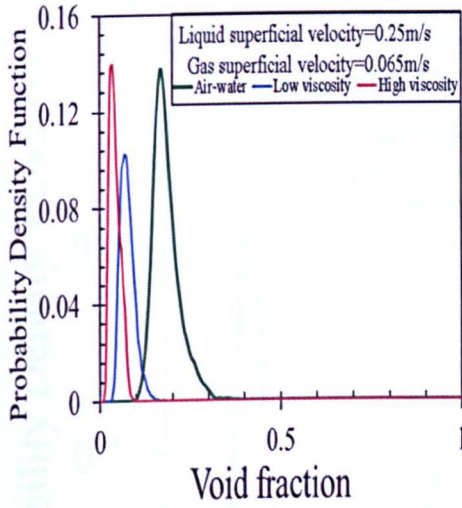
(c)
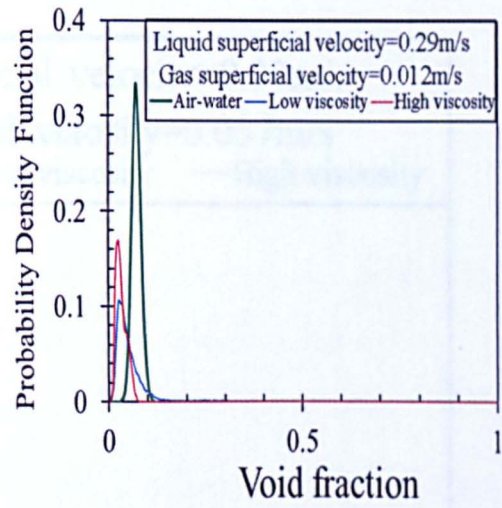
(d)
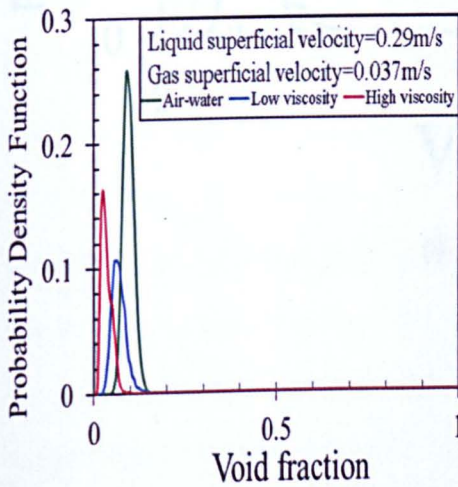
(e)
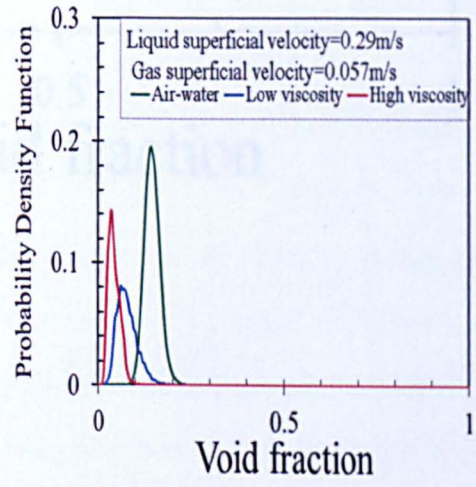
(f)
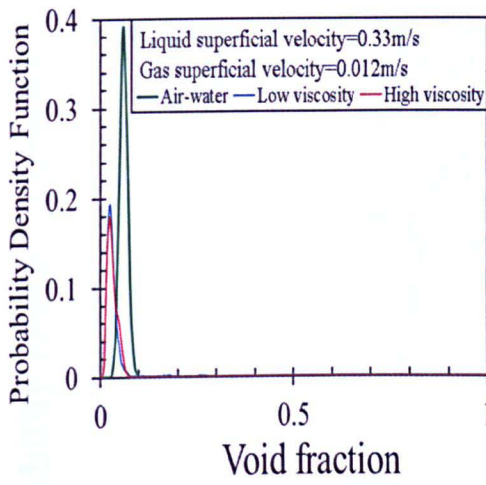
(g)
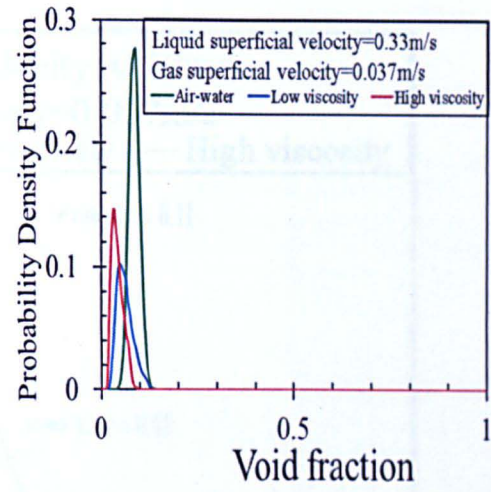
(h)
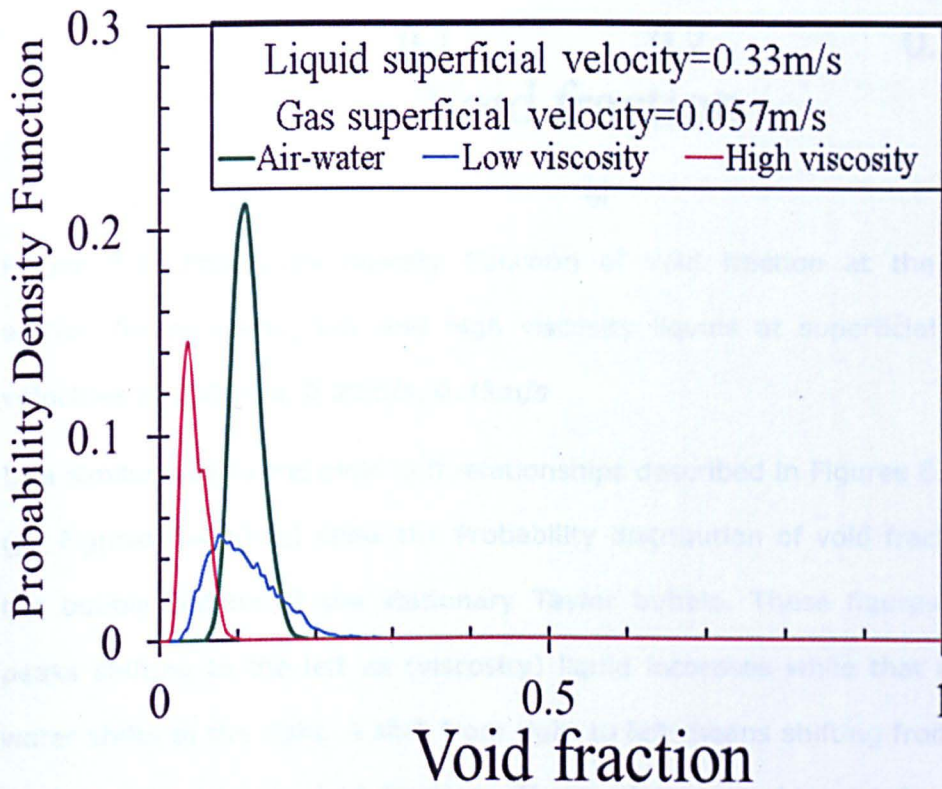
(i)
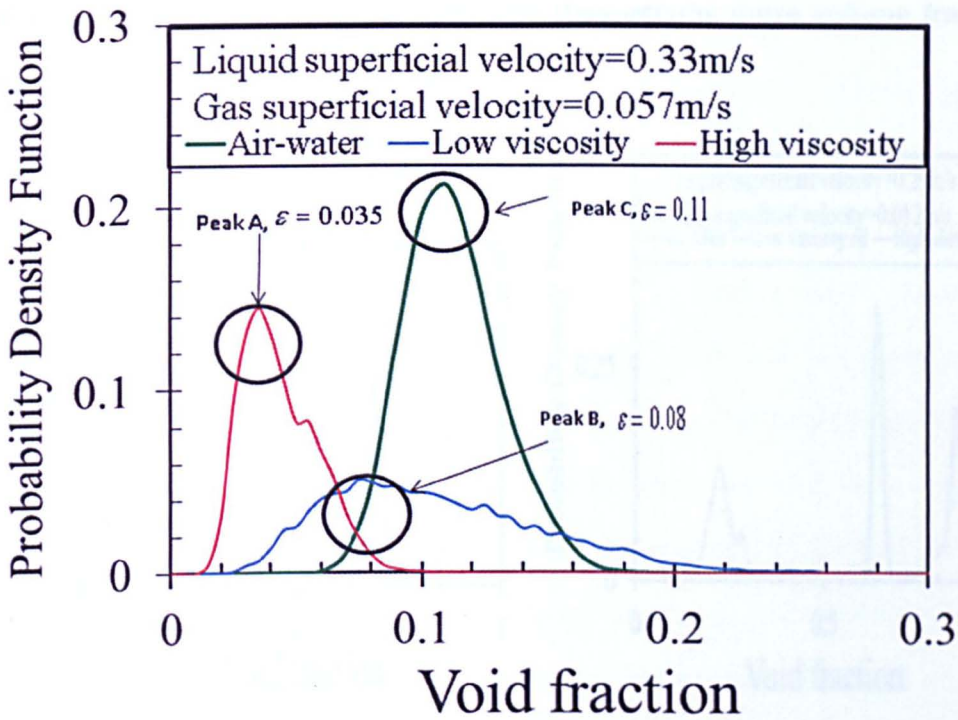
(j)

Figure 8.3: Probability Density Function of void fraction at the wake section for air-water, low and high viscosity liquids at superficial liquid velocities of 0.25m/s, 0.29m/s, 0.33m/s

In a similar way to the plots and relationships described in Figures 8.3 (a)-(j), Figures 8.4(a)-(c) show the Probability distribution of void fraction in the bubble section of the stationary Taylor bubble. These figures show peaks shifting to the left as (viscosity) liquid increases while that of air-water shifts to the right. A shift from right to left means shifting from high void fraction to low void fraction. These plots are obtained from the probability density function of the void fraction in the bubble region of the stationary bubble. The high void fraction in this region is expected as the gas volume in this region is very high compared to the volume in the wake region. From Figures 8.4 (a) – (c), air-water has the highest void fraction in all because the films are thinner and the occupy less volume fraction than gas while air-high viscosity oil has the lowest void fraction because

Abolore Abdulahi

the films in these cases are thicker and they occupy more volume fraction than those in air-water interphases.

(a)

(b)

(c)
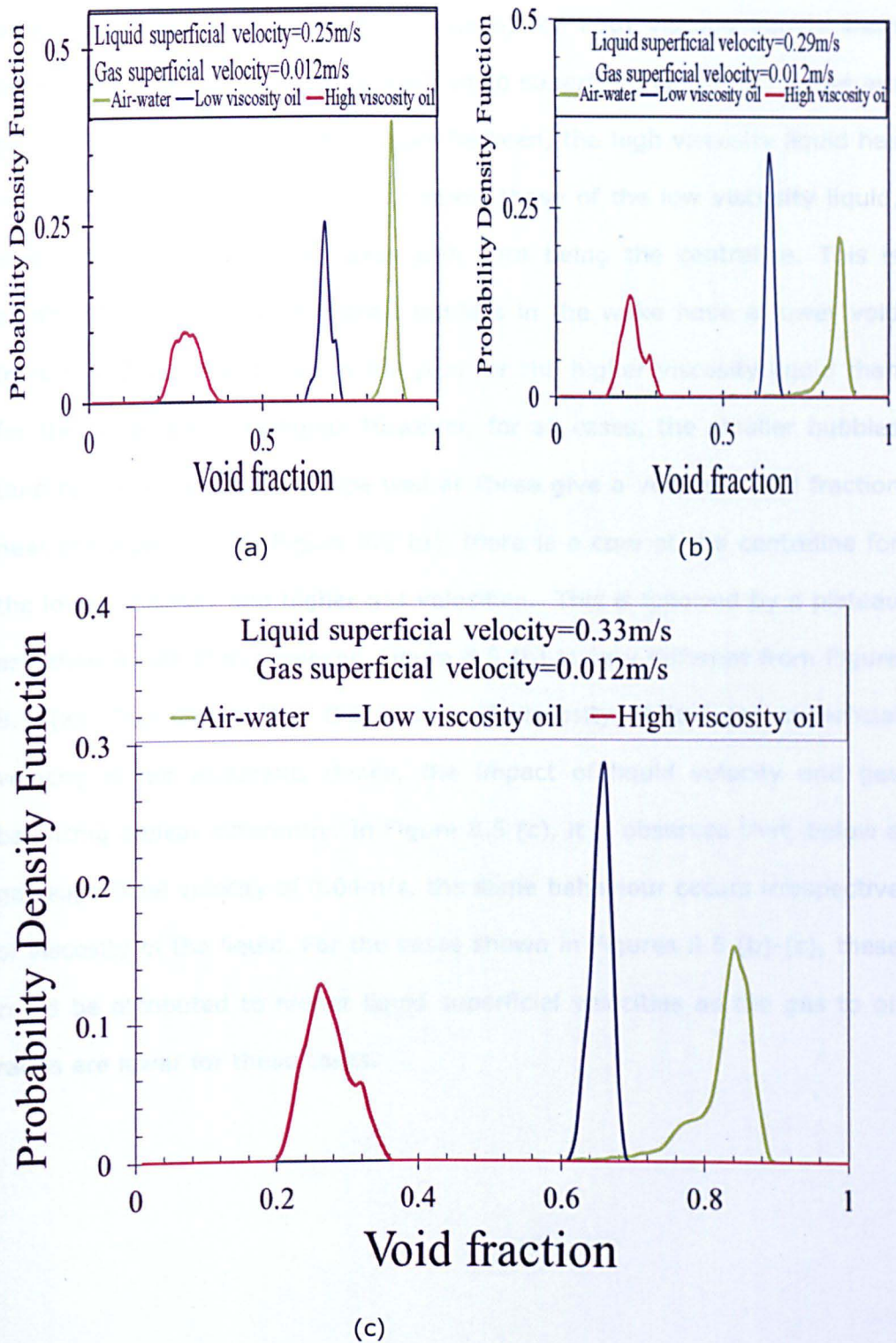
Figure 8.4: Probability Density Function of void fraction at the bubble section for air-water, low and high viscosity liquids at superficial liquid velocities of (a) 0.25m/s, (b) 0.29m/s, (c) 0.33m/s

Abolore Abdulahi

8.2.4   Radial void fraction

The radial distributions of void fraction in the wake section of the standing bubble (or 85cm below the bubble nose) for both viscous liquids were measured and compared at different liquid superficial velocities. These are plotted in Figures 8.5 (a)-(c). As can be seen, the high viscosity liquid has a void fraction radially distributed below those of the low viscosity liquid, when plotted on the same axes with zero being the centreline. This is another indication that entrained bubbles in the wake have a lower void fraction radially distributed in the pipe for the higher viscosity liquid than for the lower viscosity liquid. However, for all cases, the smaller bubbles tend to move towards the pipe wall as these give a very low void fraction near the pipe wall. In Figure 8.5 (a), there is a core at the centreline for the lower viscosity and higher gas velocities. This is followed by a plateau and then a wall film. However, Figure 8.5 (b) is very different from Figure 8.5 (a). This shows that the impact of viscosity at low gas superficial velocity is not apparent. Hence, the impact of liquid velocity and gas balancing appear differently. In Figure 8.5 (c), it is observed that, below a gas superficial velocity of 0.04m/s, the same behaviour occurs irrespective of viscosity of the liquid. For the cases shown in Figures 8.5 (b)-(c), these could be attributed to higher liquid superficial velocities as the gas to oil ratios are lower for these cases.

(a)

(b)

Abolore Abdulahi
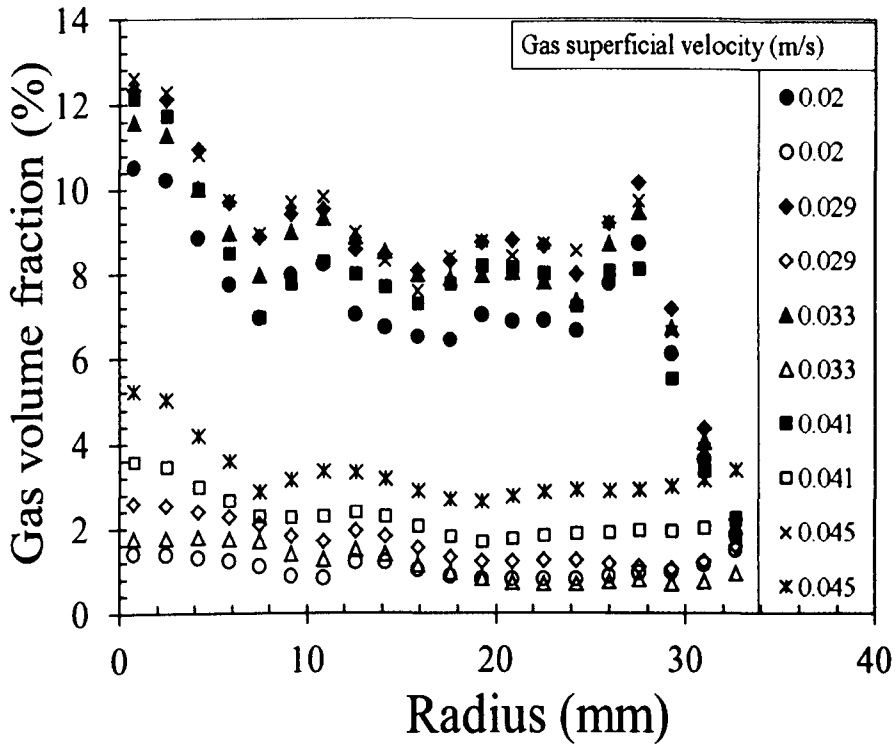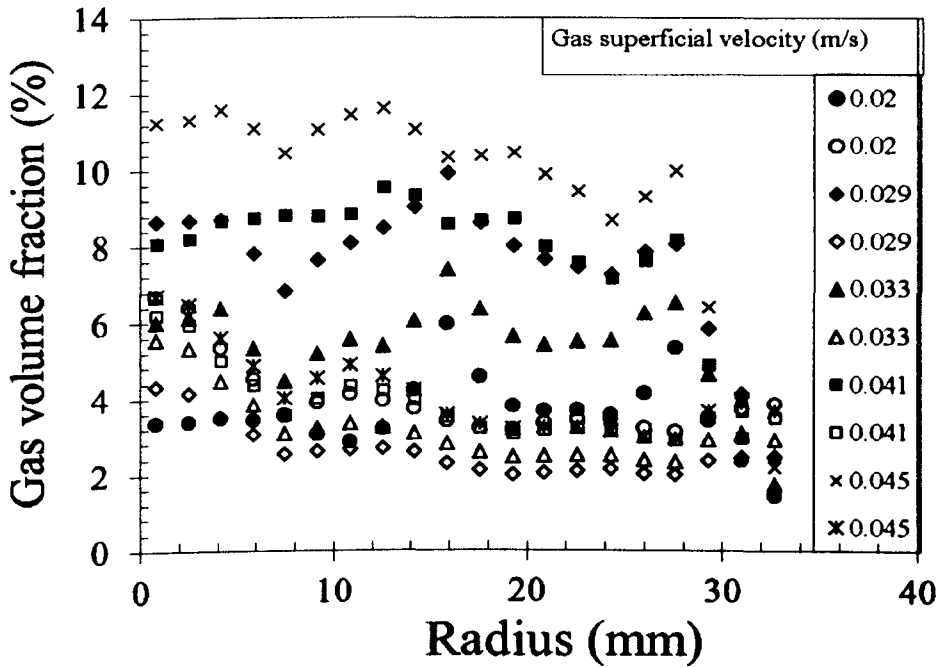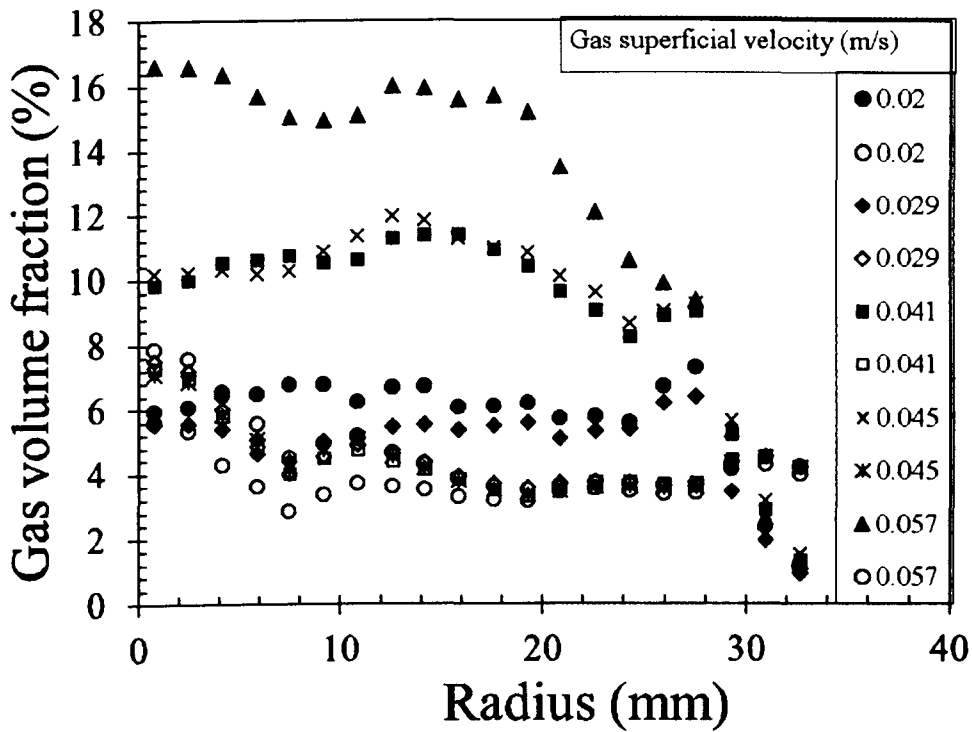
(c)

Figure 8.5: Radial Distribution of void fraction at liquid superficial velocities

(m/s) (a) 0.25, (b) 0.29 and (c) 0.33 (Note: open symbol and ✱ indicate

high viscosity liquid, closed symbol and **x** indicate low viscosity)

8.2.5   Bubble length comparison

Bubble length increases with increasing superficial gas velocity, as

discussed in Chapter Six, and shown in Figure 8.6. However, at low

superficial gas velocity, water has the longest bubble length compared to

higher viscosity liquids. A point is reached where the momentum exerted

by the falling film in higher viscosity liquids is enough to cause bubble

length to increase rapidly. At this point, the highest viscosity liquid show

greatest bubble length while water, with the lowest viscosity, shows the

smallest bubble length. This point of sudden change is assumed to be the

onset of massive entrainment, as gas bubbles are rapidly entrained in the

Abolore Abdulahi

wake section at the lowest viscosity liquid. This assumption is justifiable

through the images shown in Figure 8.8 - 8.10.
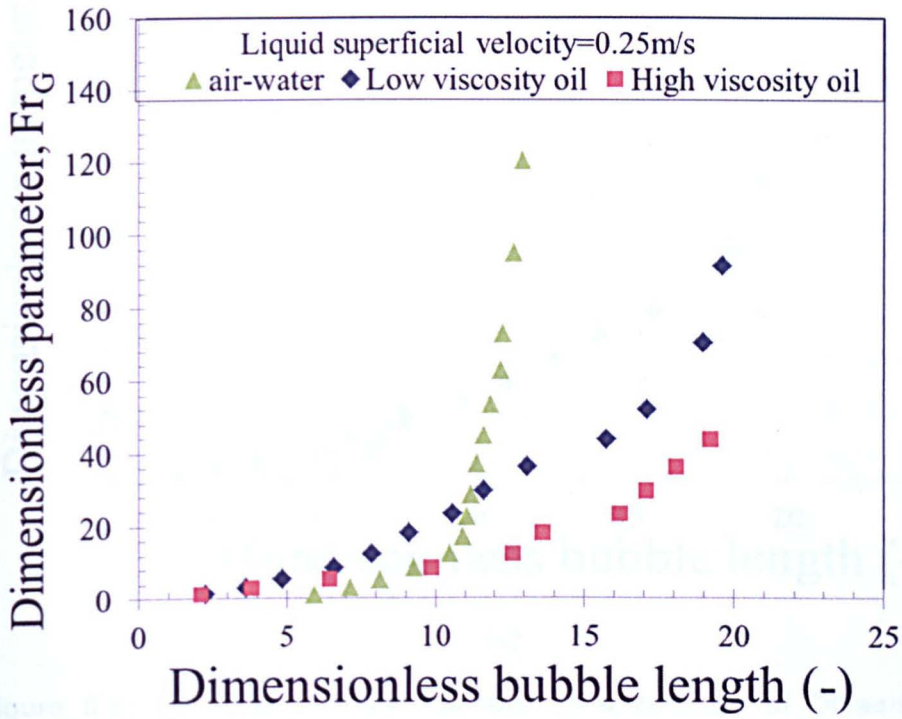
(a)
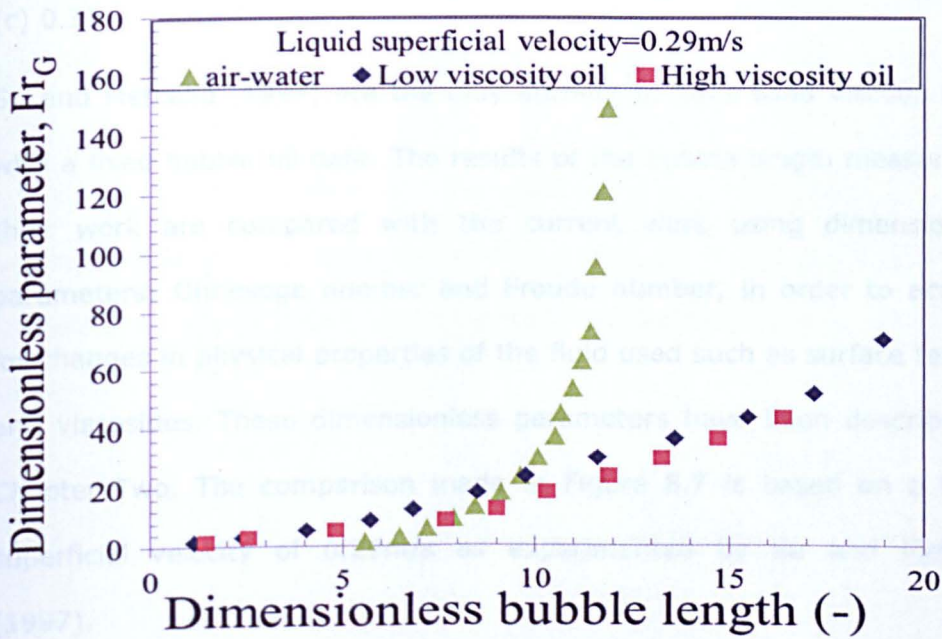
(b)
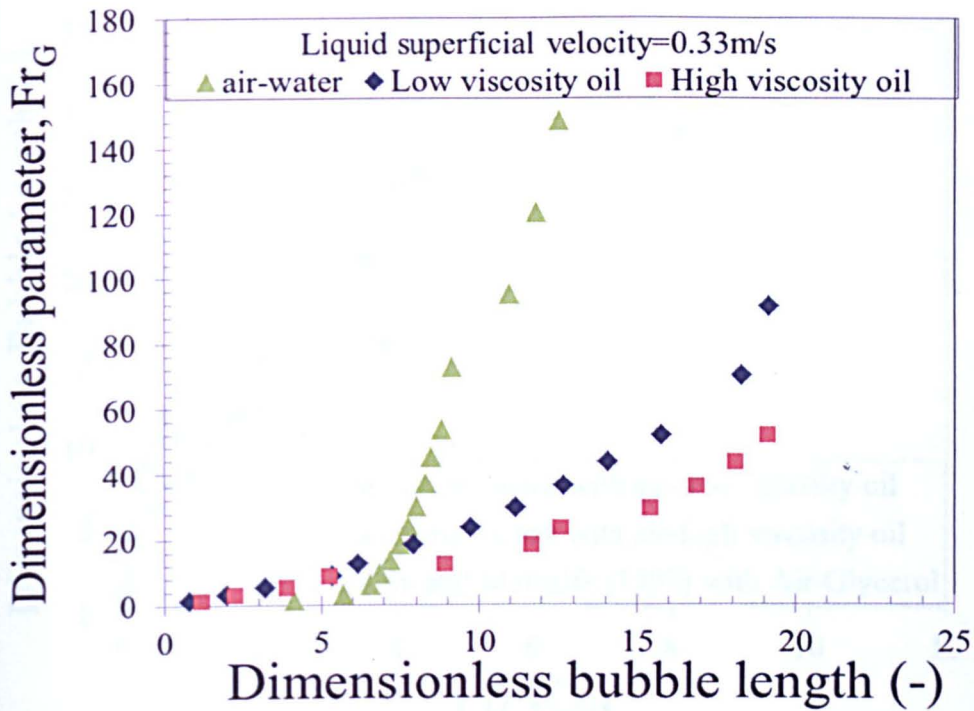
(c)

Figure 8.6: Gas based Froude number as a Function of Dimensionless bubble length at liquid superficial velocities (m/s) (a) 0.25, (b) 0.29 and (c) 0.33

Su and Metcalfe (1997) are the only authors to have used viscous liquid with a fixed bubble till date. The results of the bubble length measured in their work are compared with the current work using dimensionless parameters: Ohnesoge number and Froude number, in order to account for changes in physical properties of the fluid used such as surface tension and viscosities. These dimensionless parameters have been described in Chapter Two. The comparison made in Figure 8.7 is based on a liquid superficial velocity of 0.29m/s as experimented by Su and Metcalfe (1997).
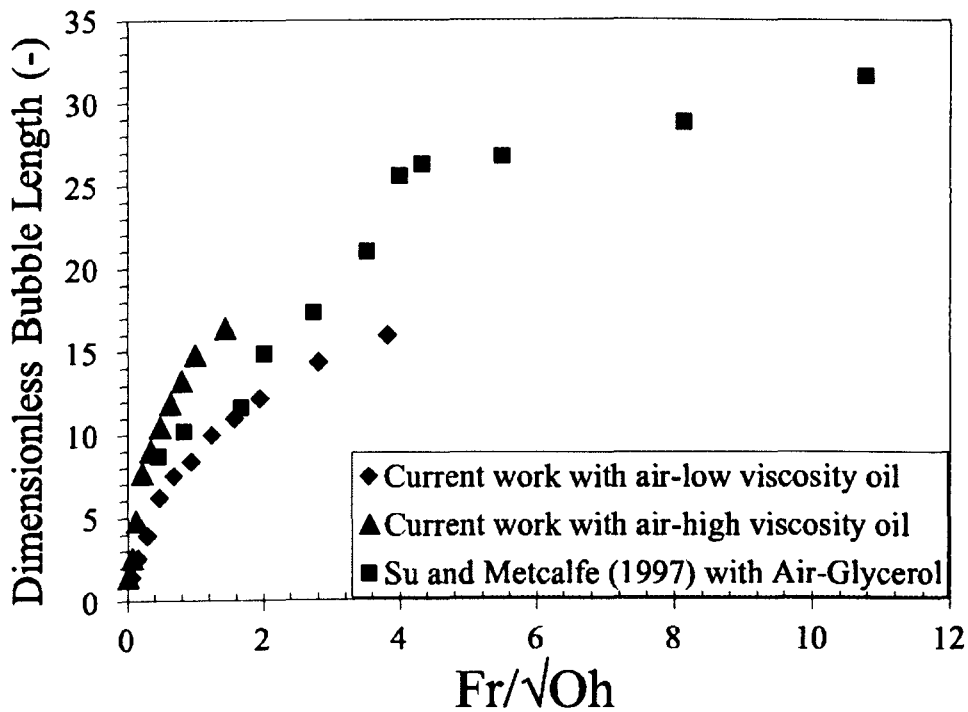
Figure 8.7: Dimensionless bubble length against $\frac{Fr}{\sqrt{Oh}}$ at a superficial liquid velocity of 0.29m/s

A clearer picture of the trend in the experimental data shown in Figure 8.7 can be observed in Figure 8.8. This shows clearly that, despite the differences in viscosity, the data of Su and Metcalfe (1997) show a similar trend with the two viscous oils considered in the current study. It is also worth mentioning that Su and Metcalfe (1997) show that gas entrainment increases with decreasing liquid viscosity as demonstrated n the current work.
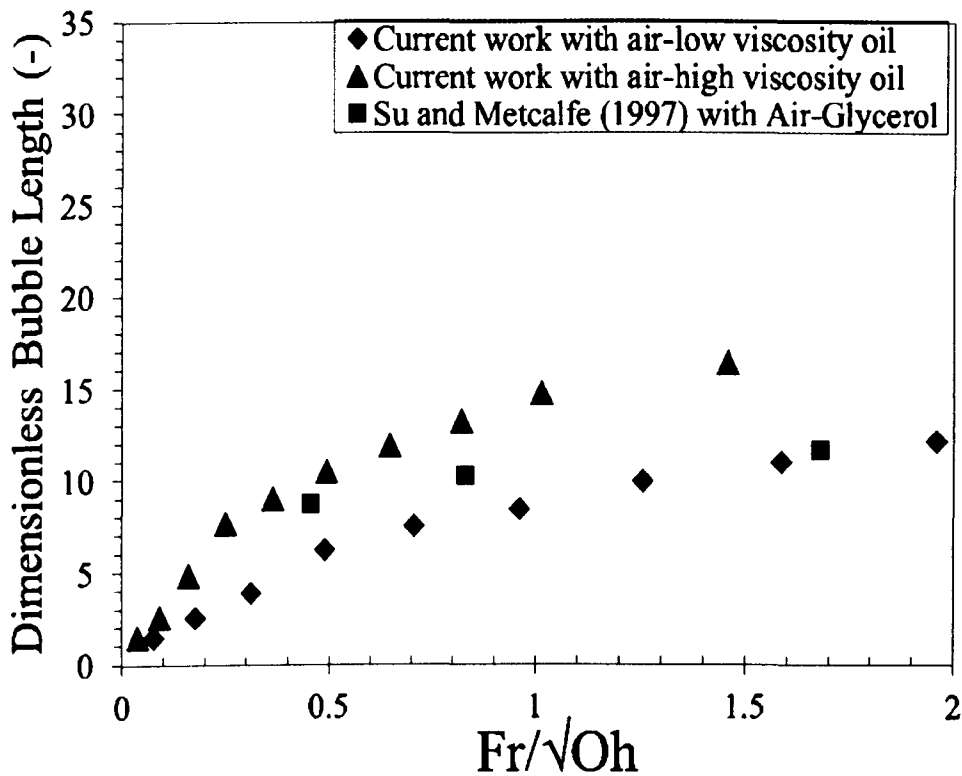
Figure 8.8: A zoomed plot of dimensionless bubble length against $\frac{Fr}{\sqrt{Oh}}$ at a superficial liquid velocity of 0.29m/s

As described in Chapter Two (section 2.8), the Kapitza number (Ka=

$$\frac{\rho_g u_{gs}^2 \sigma^{0.25}}{\left(\left(\rho_l - \rho_g\right)^{0.75} D^{0.75} g \mu_l^{0.5}\right)}$$) is able to account for the physical properties that

may affect fluid flow. Hence the comparisons above have been made using different fluids at different flow conditions.

Of particular interest to the present study is the effect for different viscosities (6cp, 42cp and 152cp). As shown in Figure 8.8, all viscosities follow a similar trend, which is produced by changing Ka through variations in the liquid viscosities. Thus, this change has no other dynamic effect on the free surface, but do have an effect on other physical properties, for instance, changes to surface tension of the liquid. The major point that can be drawn out from this is that balancing of different forces that act on entrained bubbles plays a significant role in maintaining stability to a large

extent. Thus, higher values of *Ka* lead to greater instability. Hence, an increase in *Ka* may result either from lowering the viscosity of liquid or raising the surface tension.

8.2.6   Entrainment qualitative analysis

In the previous sections, the entrainment of gas in the wake section was shown to reduce with increasing liquid viscosity. Here, the still images of the wake section, where gas entrainment occurs, are provided. Figures 8.9-8.11 show the wake section of air-high viscosity liquid, air-low viscosity liquid and air-water experiments respectively. The entrained gas bubbles in the three images are seen to increase in magnitude as the liquid viscosity is reduced. In other words, water, with the lowest viscosity of all the three liquids considered (Figure 8.11), is shown to have the highest number of entrained gas bubbles while high viscosity oil (Figure 8.9) has the lowest number of entrained gas bubbles. Interestingly, air-water has the highest surface tension in all experimental cases (0.08N/m) while air-high viscosity liquid has the lowest (0.027N/m) and is slightly higher than air-low viscosity liquid (0.0275N/m).

Abolore Abdulahi

Figure 8.9: Wake of a standing bubble showing entrained gas at liquid superficial velocities 0.29m/s and gas superficial velocity of 0.02m/s with air-high viscosity oil

Figure 8.10: Wake of a standing bubble showing entrained gas at liquid superficial velocities 0.29m/s and gas superficial velocity of 0.02m/s with air-low viscosity oil

Abolore Abdulahi

Figure 8.11: Wake of a standing bubble showing entrained gas at liquid superficial velocities 0.29m/s and gas superficial velocity of 0.02m/s with air-water

Su and Metcalfe (1997) described the vortices causing gas entrainment as one occurring at the free surface rather than under it when the liquid viscosity increases. This can also be noticed in Figures 8.9-8.11 in the present study. This is primarily responsible for the low gas entrainment in high viscosity liquid which is in good agreement with conclusion by Su and Metcalfe (1997). In a work by Mendoza (2011) using three different liquids to monitor the influence of gas entrainment in a downward flow, it was also concluded that fluid properties (especially surface tension) might play a key role in the difference between the flow patterns and the amount of air entrained and carried under with the liquid.

8.2.7 Flow structures of entrained gas in the wake section

The entrained gas bubbles in the wake section of the stationary bubble can be viewed through a display from a WMS programme which shows the tomography of the two-phase flow structure. These reveal that, at high

liquid viscosity, less gas bubbles are entrained, as previously discussed, but with a decrease in liquid viscosity, more gas bubbles are entrained. In fact, with high liquid viscosity, entrained gas bubbles are hardly visible at an initial stage of gas introduction into the two-phase system. This is more to justify what is shown in Figure 8.2 (a) where the plot for high liquid viscosity show almost flat mean void fraction at the initial gas superficial velocities. A comparison of the tomographic structures for gas-liquid flows in the wake region can be seen in Figure 8.12 which clearly shows the effect of liquid viscosity on gas entrainment.

As can be seen in Figures 8.12 (a)-(d), entrained gas bubbles are not quite visible which is similar to the observation in Figure 8.2 (a) showing the same set of conditions of gas and liquid superficial velocities. As the superficial gas velocity is increased, the entrained bubbles become more visible with the lower viscosity liquid (shown in Figures 8.12 (e) and (f)) than in high viscosity liquid (shown in Figures 8.12 (b) and (c)).

(a) Ugs=0.08m/s   (b) Ugs=0.24m/s   (c) Ugs=0.43m/s

(d) Ugs=0.08m/s   (e) Ugs=0.24m/s   (f) Ugs=0.43m/s
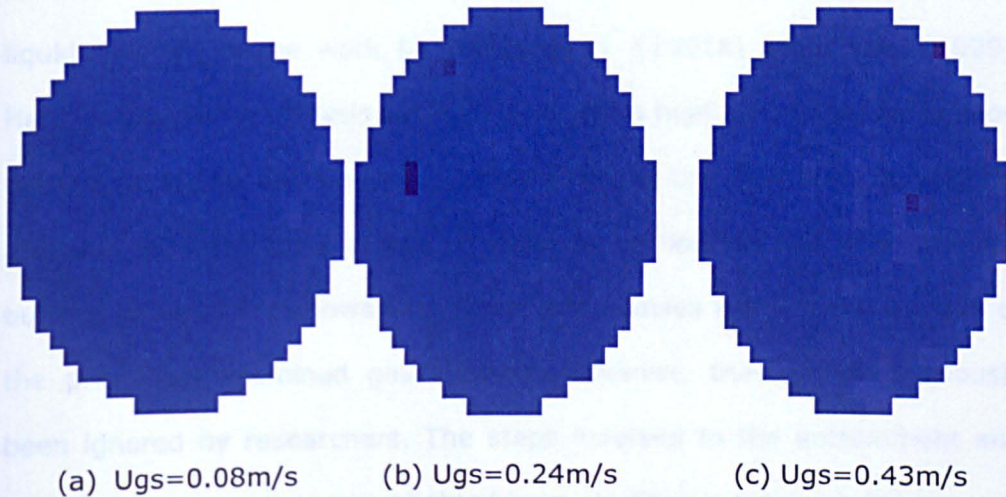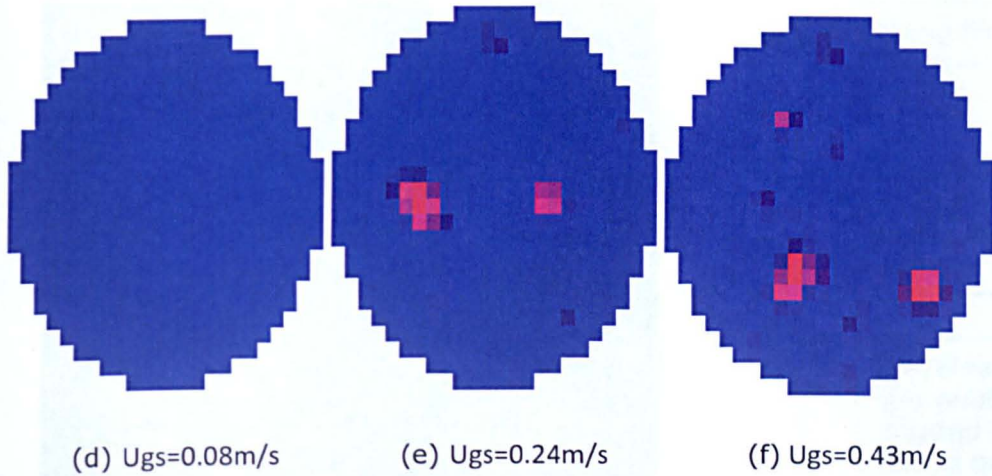
Figure 8.12: Tomography of entrained gas bubbles at the bubble wake at a liquid superficial velocities of 0.25m/s with (a), (b) and (c) being for high viscosity liquid while (d), (e) and (f) are for low viscosity liquid (Note: Blue colour means oil region while red colour means air region)

8.2.8   Recoalescence qualitative analysis

Delfos et al. (2001a) and Kockx (1999) measured the recoalescence of small bubbles back into the fixed bubble. However, water was used as the liquid medium in the work by Delfos et al. (2001a) and Kockx (1999). Here, a qualitative analysis will be made, using high speed videos, to show that some of the entrained gas bubbles below the stationary bubble tail are able to move up the pipe in order to recoalesce with the standing bubble. Observation shows that these gas bubbles are a small fraction of the previously entrained gas bubbles. However, these have previously been ignored by researchers. The steps involved in the entrainment and recoalscence process are highlighted below in Figures 8.13 (a)-(h).

Falling film

Base of stationary bubble

Entrained gas bubbles created by falling film

(a)

Entrained gas bubble begins to move up

(b)

Abolore Abdulahi
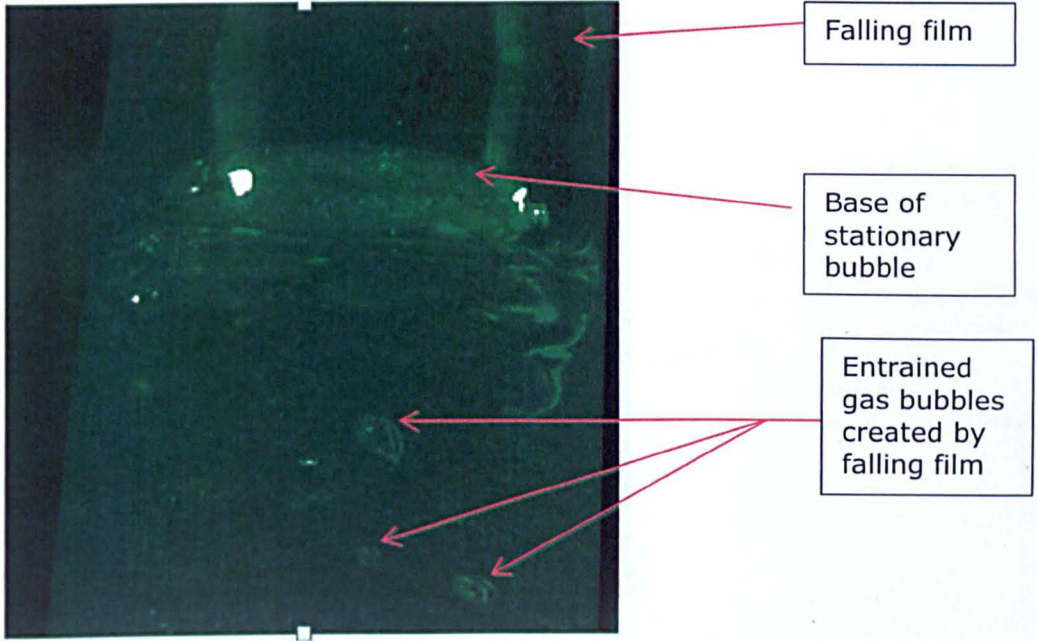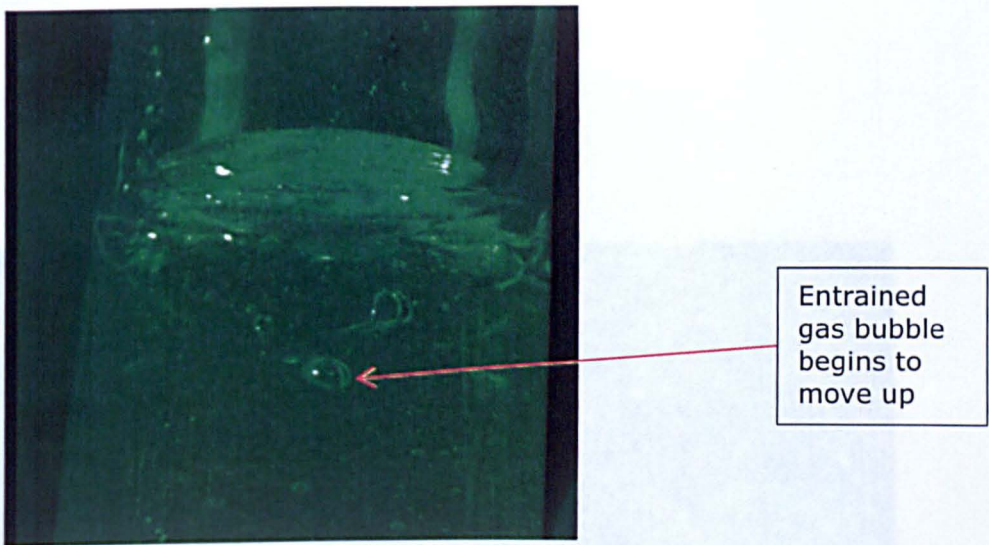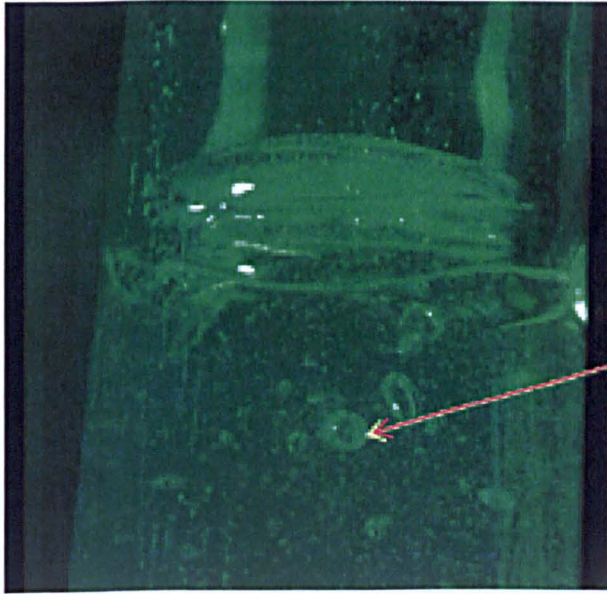
Entrained gas bubble continues moving up while other bubbles are being created

(c)

Continuous upward movement of entrained gas bubble
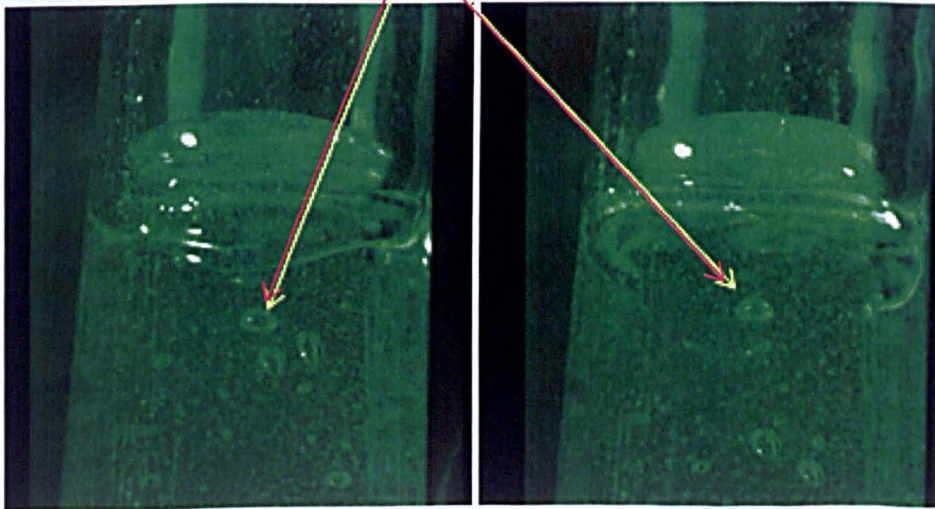
(d)   (e)

Figure 8.13: Wake of a standing bubble showing the steps for recoalescence of entrained gas bubbles at the following time, t (s) (a) 0 (b)3, (c) 5, (d) 7, (e) 9, (f) 12, (g) 14, (h) 18

It is observed in Figure 8.13 that over the time frame considered a gas bubble was able to recoalesce back into the standing bubble out of the numerous gas bubbles that were initially created by the plunging film. The steps involved can be explained further as follow: In Figure 8.13 (a), small bubbles were created as a result of the falling film impinging on the tail of the stationary Taylor bubble (the falling film tears off small gas bubbles from the stationary bubble). These gas bubbles initially remain at the wake of the stationary bubble as they are being created. Some of the bubbles then begin to move downwards with the liquid (slug) while a few start to move upwards as shown in Figure 8.13 (b). In Figure 8.13 (c), more bubbles are created by the falling film while some of the previously entrained bubbles continue to move upwards. This upward movement of entrained gas bubbles continue in Figure 8.13 (d) and (e) until the bubbles find their way to the base of the stationary bubble as can be seen in Figures 8.13 (f) and (g). The bubble finally recoalesces with the stationary bubble from which it was originally created by the film as shown in Figure 8.13 (h).

8.3   Summary

The following is a summary from this Chapter:

> The rate of gas entrainment is inversely proportional to the liquid viscosity for a set condition. In other words, as the liquid viscosity is increased the number of entrained gas bubbles reduces over time. This is in agreement with the proposed thought experiment derived from Nusselt equation described in section 8.2.1.

> Although bubble lengths increase with increasing gas superficial velocities, the lengths are higher for higher viscosity liquid than for

low viscosity liquids. This is in agreement with the work of Su and Metcalfe (1997).

➤ Gas volume fractions for a low viscosity liquid are higher than those for a high viscosity liquid at the same set of gas and liquid superficial velocities.

➤ There is a shift to the left in void fraction for both the bubble and wake section of a stationary bubble as the liquid viscosity is changed from high viscosity to low viscosity. This is further proof that void fraction of gas entrained in a low viscosity liquid is higher than that entrained in a high viscosity liquid when they are subjected to the same conditions (e.g. gas and liquid velocities).

➤ Recoalscence of gas bubbles occurs at the wake of a Taylor bubble. Few of the entrained gas bubbles recoalesces with the stationary bubble.

Chapter Nine
Conclusions and Recommendation for Future work

9.1   Conclusions

Gas-liquid flows using viscous liquids have been studied successfully using Wire Mesh Sensor (WMS) with special attention paid to the effects of viscosity on the characteristics of flow.

A range of experimental data for two-phase flow were obtained and presented for both large (127mm) and small (67mm) diameter pipes. This has been achieved through the change in gas-liquid flow conditions.

Data from the work by other researchers were examined and compared with those from the present study.

For the large (127mm) diameter pipe, which involved high pressure investigations of gas-liquid flows for high viscosity liquid and high density gas, the following summary from Chapters 3 and 4 is drawn:

- The mechanistic flow pattern of Shoham (2006) performed well for the set of experimental conditions under review.

- The time series of void fraction revealed the absence of bridging gas troughs that is characteristic of slug flows.

- The characteristic twin peaked PDFs that indicates the presence of slug flows did not feature in any of the PDFs for the current study which highlights the absence of slug flows in vertical risers using large diameter pipes.

- Radial distributions of void fraction show that, for bubbly flows, the bubbles tend to move away from centre of the pipe towards the pipe

Abolore Abdulahi

wall, while they move towards the centre of the pipe for other flow regimes as a result of bubble coalescence. Hence for bubbly flows, the plot is nearly flat while for other flows the plots are almost parabolic.

- By using the frequencies from power spectral density, the change from one regime of flow to another can be identified as the harmonic signals smoothen out as the flows move from bubbly to intermittent flows.

- Bubble size distribution plots reveal that the bubbles increased in diameter as the superficial gas velocities increased. However, the two characteristic division of bubble layers observed by Prasser et al. (2004) in small diameter pipes was absent, while a similar shape for big diameter pipe in the work by Prasser et al. (2004) has been observed in the current study.

- Pipe diameter, viscosity of the oil and gas density play major roles in shifting the flow regimes, hence, the usual flow pattern maps which have mainly been derived from air-water experiments may not be relevant for handling such fluids. Although some of the flow maps do consider these fluid properties, they are unable to provide a good fit for good flow delineation. The effect of viscosity can be moderated using dimensionless numbers.

- With the flow structures, wisps are easily observed at higher pressure than at lower pressure using the Wire Mesh Sensor.

- Pressure has more effect on mean void fraction at higher liquid superficial velocity than at low liquid velocities.

- As the liquid velocity goes up, the calculated void fraction shows some disparity from measured void fraction.

- Correlations drawn from the literature of CISE/Friedel, homogeneous and Beggs and Brills perform well for void fraction prediction at higher liquid superficial velocities when compared with void fraction measured from experiment. This could be attributed to higher momentum

exhibited by the structure at higher liquid velocity. Better agreement was observed for higher pressure (7.5 bara) than for lower pressure (4.5 bara)

- The changes observed by Owen (1986) in pressure gradient plot was absent in the current study due to non-appearance of slugs in large diameter pipes for plotted pressure gradient.

For the experimental work reported in Chapters 5-8 on a stationary Taylor bubble in a vertically downward flow using both low and high viscosity liquids, the following conclusions are drawn:

- Through images taken on stationary bubbles it was shown that a freely rising bubble and that of the theoretical shape resembles the nose of the simulated stationary Taylor bubble. The images, as well as the PDFs, show that gas entrainment below a stationary bubble increases with increase in gas superficial velocity.

- Most of the flows in the wake of the stationary bubble experiments are in the bubbly region (determined visually and with WMS).

- From previous work carried out by various authors, it was expected that the liquid slug below the Taylor bubble would have entrained bubbles in it. This is hereby demonstrated by the PDFs shown in the experimental results. The void fraction in the liquid slug below the stationary Taylor bubble correlates with the gas loss rate from the Taylor bubble. The shapes of these gas loss curves show trends similar to work by other authors.

- The wake lengths measured for stationary bubbles, whose results were compared with previous work by other authors, showed that the wake length depends on the class of flow and pipe diameter. However, maximum and minimum values obtained from the video capture show

some agreement with the work by Van Hout et al. (1992) and are generally close to the results by other authors.

- Bubble sizes increase with increase in gas superficial velocity at constant liquid superficial velocity. This may be as a result of continuous coalescence of entrained bubbles of small diameters to form bigger bubbles until these bubbles become unstable and then deform.

- The PDF of film thickness show that the measured film thickness averages to about 1mm, while power spectral densities of the film thickness straighten out as you move downstream and with decreasing superficial gas velocity.

- The film thickness based on the use of LFDM has a very good agreement with the Nusselt equation and the Kapitza model.

- The results show a small deviation from those obtained using the models of Takahama and Kato (1980) as well as with the work by other authors.

- Wire Mesh Sensor show a wide difference when compared with the results from LFDM. This is understandable as the WMS results are derived from average values of void fraction at crossing points of the square wires. This can however be accounted for if the distance from the last crossing wires to the pipe wall are taken into consideration

- The rate of gas entrainment is inversely proportional to the liquid viscosity. In order words, as the liquid viscosity is increased the number of entrained gas bubbles reduce. This is in agreement with the proposed theory derived from Nusselt equation described in Chapter Eight.

- Although bubble lengths increase with increasing gas superficial velocities, the lengths are higher for higher viscosity liquid than for low

viscosity liquids. This is in agreement with the work of Su and Metcalfe (1997).

- Gas volume fraction for low viscosity liquid are higher than those for high viscosity liquid

- There is a shift to the left for void fraction at both bubble and wake section of a stationary bubble for high viscosity liquid. This is a further evidence that void fraction of gas entrained in a low viscosity liquid is higher than that entrained in high viscosity liquid when they are subjected to the same conditions (e.g. gas and liquid velocities).

9.2   Contribution to knowledge

There is an effect of pressure on two-phase gas-liquid flows when using highly viscosity liquids and high density gas. This effect becomes significant at high liquid superficial velocity.

Viscosity has an effect on gas entrainment in gas-liquid two-phase flows, with re-coalescence of some of the entrained gas bubbles back to the original Taylor bubble from the bubble wake. The effect become limiting as the liquid viscosity gets higher.

9.3   Recommendation

Although the current study has been undertaken using high viscosity liquid, oil and gas industries may have to handle higher viscosity liquids in larger diameter pipes than those studied here. The following is recommended for future work:

1. Experimental condition for the large diameter pipe should be extended to higher liquid and gas flow rates to test the prediction of the existing models over wider ranges, especially the churn and annular regions.

Such data will provide important information to validate the existing models.

2. Although a pipe with a diameter of 127 mm has been used for the current study, pipes of considerably larger diameter (greater than 200mm) could also be used to examine the effect of pipe diameter on flow patterns maps and transitions using high viscosity liquid.

3. Measurement of film thickness of viscous fluids in order to see how they compare with film thickness of fluids with low viscosities.

4. Stationary bubbles in large pipe diameters could also be explored and the results could be compared with small diameter pipes to see the effect on gas entrainment.

5. Further experimental work on standing bubble to quantify the recoalescence of bubbles back to the stationary bubble could be extended by the introduction of Helium gas into the wake section. This will allow measurement of the concentration of Helium that recoalesces back into the stationary bubble with air.

References

Abdulahi, A., Abdulkareem, L. A., Sharaf, S., Abdulkadir, M., Perez, V. H. and Azzopardi, B. J. Investigating the Effect of Pipe Inclination on Two-Phase Gas-Liquid Flows Using Advanced Instrumentation. ASME/JSME 2011 8th Thermal Engineering Joint Conference, 2011. T30080-T30080-9.

Abduvayt, P., Manabe, R. and Arihara, N. 2003. Effects of Pressure and Pipe Diameter on Gas-Liquid Two-Phase Flow Behavior in Pipelines. *SPE Annual Technical Conference and Exhibition.* Denver, Colorado: Society of Petroleum Engineers.

Ali, S. F. 2009. *Two phase flow in large diameter vertical riser.* PhD Thesis, Cranfield University, UK.

Ali, S. F. and Yeung, H. 2013. Two-phase flow patterns in large diameter vertical pipes. *Asia-Pacific Journal of Chemical Engineering,* n/a-n/a.

Alves, G. E. 1954. Cocurrent liquid–gas flow in a pipeline contractor. *Chem. Eng. Prog.,* 50, 449–456.

Azzopardi, B. J. 1983. Mechanisms of entrainment in annular two-phase flow. *UKAEA Report AERE-R 11068.*

Azzopardi, B. J. 2006. *Gas-liquid flows,* New York, Begell house incorporated.

Azzopardi, B. J., Abdulkareem, L. A., Sharaf, S., Abdulkadir, M. A. and Ijioma, A. 2010a. Using Tomography To Interrogate Gas Liquid Flow. *28th UIT Heat Transfer Congress.* Brescia, Italy

Azzopardi, B. J., Abdulkareem, L. A., Zhao, D., Thiele, S., Da Silva, M. J., Beyer, M. and Hunt, A. 2010b. Comparison between Electrical Capacitance Tomography and Wire Mesh Sensor Output for Air/Silicone Oil Flow in a Vertical Pipe. *Industrial & Engineering Chemistry Research,* 49, 8805-8811.

Azzopardi, B. J., Hernandez Perez, V., Kaji, R., Da Silva, M. J., Beyer, M. and Hampel, U. 2008. Wire Mesh Sensor studies in a vertical pipe. *Fifth International Conference on Transport Phenomena in Multiphase Systems, HEAT 2008.* Bialystok, Poland.

Bacon, R. P., Scott, D. M. and Thorpe, R. B. 1995. Large bubbles attached to spargers in downwards two-phase flow. *International Journal of Multiphase Flow,* 21, 949-959.

Barbosa Jr, J. R., Govan, A. H. and Hewitt, G. F. 2001. Visualisation and modelling studies of churn flow in a vertical pipe. *International Journal of Multiphase Flow,* 27, 2105-2127.

Barnea, D. 1986. Transition from annular flow and from dispersed bubble flow—unified models for the whole range of pipe inclinations. *International Journal of Multiphase Flow,* 12, 733-744.

Barnea, D. and Brauner, N. 1985. Holdup of the liquid slug in two phase intermittent flow. *International Journal of Multiphase Flow,* 11, 43-49.

Barnea, D. and Shémer, L. 1989. Void fraction measurements in vertical slug flow: applications to slug characteristics and transition. *International Journal of Multiphase Flow,* 15, 495-504.

Barnea, D., Shoham, O. and Taitel, Y. 1982. Flow pattern transition for vertical downward two phase flow. *Chemical Engineering Science,* 37, 741-744.

Beggs, D. H. and Brill, J. P. 1973. A Study of Two-Phase Flow in Inclined Pipes   *Journal of Petroleum Technology,* Volume 25, Number 5, 607-617.

Belkin, H. H., Macleod, A. A., Monrad, C. C. and Rothfus, R. R. 1959. Turbulent liquid flow down vertical walls. *AIChE Journal,* 5, 245-248.

Bendiksen, K. H. 1984. An experimental investigation of the motion of long bubbles in inclined tubes. *International Journal of Multiphase Flow,* 10, 467-483.

Benítez-Centeno, O. C., Cazarez-Candia, O. and Moya-Acosta, S. L. 2012. Slug Flow Model Using the Two Fluid Approach. *In:* Klapp, J., Cros, A., Velasco Fuentes, O., Stern, C. and Rodriguez Meza, M. A. (eds.) *Experimental and Theoretical Advances in Fluid Dynamics.* Springer Berlin Heidelberg.

Bennett, B. a. W., Hewitt, G. F., Kearsey, H. A., Keeys, R. K. F. and Lacey, P. M. C. 1965. Paper 5: Flow Visualization Studies of Boiling at High Pressure. *Proceedings of the Institution of Mechanical Engineers, Conference Proceedings,* 180, 260-283.

Biń, A. K. 1993. Gas entrainment by plunging liquid jets. *Chemical Engineering Science,* 48, 3585-3630.

Bonizzi, M. and Issa, R. I. 2003. A model for simulating gas bubble entrainment in two-phase horizontal slug flow. *International Journal of Multiphase Flow,* 29, 1685-1717.

Brauner, N. and Barnea, D. 1986. Slug/Churn transition in upward gas-liquid flow. *Chemical Engineering Science,* 41, 159-163.

Brauner, N. and Ullmann, A. 2004a. Modelling of gas entrainment from Taylor bubbles. Part A: Slug flow. *International Journal of Multiphase Flow,* 30, 239-272.

Brauner, N. and Ullmann, A. 2004b. Modelling of gas entrainment from Taylor bubbles. Part B: A stationary bubble. *International Journal of Multiphase Flow,* 30, 273-290.

Brodkey, R. S. 1967. The Phenomena of Fluid Motion. *Addison-Wesley Press.*

Broz, W. 1954. Uber die vorausberechnung der absorptionsgeschwindigkeit con gasen in stromenden flussigkeitsschichten. *Chemie Ingeniur Technik,* Vol. 26, pp. 470.

Calderbank, P. H. 1958. Physical rate processes in industrial fermentation. Part I: The interfacial area in gas-liquid contacting with mechanical agitation. *Transactions of the Institution of Chemical Engineers,* Vol. 36, pp. 443-46.

Campos, J. B. L. M. and Carvalho, J. R. F. G. D. 1988. An experimental study of the wake of gas slugs rising in liquids. *Journal of Fluid Mechanics Digital Archive,* 196, 27-37.

Chanson, H. and Jaw-Fang, L. 1997. Plunging jet characteristics of plunging breakers. *Coastal Engineering,* 31, 125-141.

Cheng, H., Hills, J. H. and Azzopardi, B. J. 2002. Effects of initial bubble size on flow pattern transition in a 28.9 mm diameter column. *International Journal of Multiphase Flow,* 28, 1047-1062.

Chisholm, D. 1972. An equation for velocity ratio in two-phase flow. *N.E.L. Report No 535.*

Chisholm, D. and Laird, D. K. 1958. Two-phase flow in rough tubes. *Transaction ASME,* Vol. 80, pp. 276-286.

Chu, K. J. and Dukler, A. E. 1974. Statistical characteristics of thin, wavy films: Part II. Studies of the substrate and its wave structure. *AIChE Journal,* 20, 695-706.

Collins, R., Moraes, F. F. D., Davidson, J. F. and Harrison, D. 1978. The motion of a large gas bubble rising through liquid flowing in a tube. *Journal of Fluid Mechanics Digital Archive,* 89, 497-514.

Conte, G. and Azzopardi, B. J. 2003. Film thickness variation about a T-junction. *International Journal of Multiphase Flow,* 29, 305-328.

Costigan, G. and Whalley, P. B. 1997. Slug flow regime identification from dynamic void fraction measurements in vertical air-water flows. *International Journal of Multiphase Flow,* 23, 263-282.

Crowley, C. J., Sam, R. C., Wallis, G. B. and Metha, D. C. 1984. Slug flow in large diameter pipe: I. Effect of fluid properties. *AIChE Annual Meeting.* San Francisco, CA.

Cummings, P. D. and Chanson, H. 1997. Air Entrainment in the Developing Flow Region of Plunging Jets—Part 1: Theoretical Development. *Journal of Fluids Engineering,* 119, 597-602.

Cummings, P. D. and Chanson, H. 1999. An Experimental Study of Individual Air Bubble Entrainment at a Planar Plunging Jet. *Chemical Engineering Research and Design,* 77, 159-164.

Da Silva, M. J., Schleicher, E. and Hampel, U. 2007. Capacitance Wire Mesh Sensor for Fast Measurement of Phase Fraction Distributions. *Measurement Science and Technology,* 18, 2245–2251.

Da Silva, M. J., Thiele, S., Abdulkareem, L., Azzopardi, B. J. and Hampel, U. 2010. High-resolution gas-oil two-phase flow visualization with a capacitance wire-mesh sensor. *Flow measurement and Instrumentation,* 21, 191-197.

Davidson, J. F. and Kirk, F. A. 1969. Holding a bubble fixed by downward flow. *Chemical Engineering Science,* 24, 1529-1530.

Davidson, P. J., Crooks, S. P., Davidson, J. F. and Harrison, D. 1979. Holding two-dimensional bubble fixed by downward flow. *Chemical Engineering Science,* 34, 1168-1170.

Davies, R. M. and Taylor, G. The Mechanism of Large Bubbles Rising through Extended Liquids and through Liquids in Tubes. Proceedings of the Royal Society of London, 1949. The Royal Society, 375-390.

Davoust, L., Achard, J. L. and El Hammoumi, M. 2002. Air entrainment by a plunging jet: the dynamical roughness concept and its estimation by a light absorption technique. *International Journal of Multiphase Flow,* 28, 1541-1564.

De Cachard, F. and Delhaye, J. M. 1996. A slugh-churn flow model for small-diameter airlift pumps. *International Journal of Multiphase Flow,* 22, 627-649.

Delfos, D. R. 1996. *Experiments on air entrainment from a stationary slug bubble in a vertical tube.* PhD Thesis, Delft University of Technology.

Delfos, R., Rops, C. M., Kockx, J. P. and Nieuwstadt, F. T. M. 2001a. Measurement of the recoalescence flux into the rear of a Taylor bubble. *Physics of Fluids,* 13, 1141-1150.

Delfos, R., Wisse, C. J. and Oliemans, R. V. A. 2001b. Measurement of air-entrainment from a stationary Taylor bubble in a vertical tube. *International Journal of Multiphase Flow,* 27, 1769-1787.

Dukler, A. E. and Taitel, Y. 1986. FLOW PATTERN TRANSITIONS IN GAS-LIQUID SYSTEMS: MEASUREMENT AND MODELING. 2, 1-94.

Dumitrescu, D. T. 1943. Flow on a air bubble in the vertical tube. *Zeitschrift Fur Angewandte Mathematik Und Mechanik,* 23, 139-149.

Dziubinski, M., Fidos, H. and Sosno, M. 2004. The flow pattern map of a two-phase non-Newtonian liquid-gas flow in the vertical pipe. *International Journal of Multiphase Flow,* 30, 551-563.

Eskerud Smith, I., Krampa, F. N., Fossen, M., Brekken, C. and Unander, T. E. 2011. Investigation of horizontal two-phase gas-liquid pipe flow using high viscosity oil: Comparison with experiments using low viscosity oil and flow simulations. *15th International Conference on Multiphase production Technology.* Cannes, France: BHR Group.

Fernandes, R. C., Semiat, R. and Dukler, A. E. 1983. Hydrodynamic model for gas-liquid slug flow in vertical tubes. *AIChE Journal,* 29, 981-989.

Fukano, T. and Furukawa, T. 1998. Prediction of the effects of liquid viscosity on interfacial shear stress and frictional pressure drop in vertical upward gas-liquid annular flow. *International Journal of Multiphase Flow,* 24, 587-603.

Fulford, G. D. 1964. The flow of liquid in thin films *Advances in Chemical Engineering,* Vol. 5, pp. 151-236.

Furukawa, T. and Fukano, T. 2001. Effects of liquid viscosity on flow patterns in vertical upward gas-liquid two-phase flow. *International Journal of Multiphase Flow,* 27, 1109-1126.

Geraci, G., Azzopardi, B. J. and Van Maanen, H. R. E. 2007. Effect of inclination on circumferential film thickness variation in annular gas/liquid flow. *Chemical Engineering Science,* 62, 3032-3042.

Gokcal, B., Al-Sarkhi, A. S., Sarica, C. and Al-Safran, E. M. 2009. Prediction of Slug Frequency for High Viscosity Oils in Horizontal Pipes. *SPE Annual Technical Conference and Exhibition.* New Orleans, Louisiana: Society of Petroleum Engineers.

Goldsmith, H. L. and Mason, S. G. 1962. The movement of single large bubbles in closed vertical tubes. *Journal of Fluid Mechanics,* 14, 42-58.

Govan, A. H., Hewitt, G. F., Richter, H. J. and Scott, A. 1991. Flooding and churn flow in vertical pipes. *International Journal of Multiphase Flow,* 17, 27-44.

Griffith, P. and Wallis, G. B. 1961. TWO-PHASE SLUG FLOW. *Journal Name: Journal of Heat Transfer (U.S.); Journal Volume: Vol: 83; Other Information: Orig. Receipt Date: 31-DEC-61,* Medium: X; Size: Pages: 307-20.

Guet, S., Ooms, G. and Oliemans, R. V. A. 2002. Influence of bubble size on the transition from low-Re bubbly flow to slug flow in a vertical pipe. *Experimental Thermal and Fluid Science,* 26, 635-641.

Harmathy, T. Z. 1960. Velocity of large drops and bubbles in media of infinite or restricted extent. *AIChE Journal,* 6, 281-288.

Hawkes, N. J., Lawrence, C. J. and Hewitt, G. F. 2000. Studies of wispy-annular flow using transient pressure gradient and optical measurements. *International Journal of Multiphase Flow,* 26, 1565-1582.

Hernandez Perez, V. 2008. *Gas-liquid two-phase flow in inclined pipes.* PhD, University of Nottingham.

Hernandez Perez, V., Azzopardi, B. J., Kaji, R., Da Silva, M. J., Beyer, M. and Hampel, U. 2010. Wisp-like structures in vertical gas–liquid pipe flow revealed by wire mesh sensor studies. *International Journal of Multiphase Flow,* 36, 908-915.

Hewitt, G. F. 1978. *Measurement of two phase flow parameters,* Pergamon Press.

Abolore Abdulahi

Hewitt, G. F. 2012. Churn and Wispy Annular Flow Regimes in Vertical Gas–Liquid Flows. *Energy & Fuels,* 26, 4067-4077.

Hewitt, G. F. and Hall-Taylor, N. S. 1970. *Annular Two-Phase Flow,* Pergamon Press, Oxford.

Hewitt, G. F. and Jayanti, S. 1993. To churn or not to churn. *International Journal of Multiphase Flow,* 19, 527-529.

Hewitt, G. F. and Roberts, D. N. 1969. Studies of Two-Phase Flow Patterns by Simultaneous X-Ray and Flash Photography *UKAEA Report No. AERE-M2159.* UKAEA.

Hikita, H., Ishimi, -. K., Koroyasu, S. and Nakai, T. 1987. Entrance Region Flow of Falling Liquid Films in Inclined Wetted-Wall Columns with and Overflow-Type Distributor. *Journal of Chemical Engineering of Japan,* 20, 172-176.

Hinze, J. O. 1955. Fundamentals of the hydrodynamic mechanism of splitting in dispersion processes. *AIChE Journal,* 1, 289-295.

Hubbard, M. G. 1965. *An analysis of horizontal gas-liquid slug.* PhD PhD Thesis, University of Houston.

Hubbard, M. G. and Duckler, A. E. The characterization of flow regimes for horizontal two-phase flow: statistical analysis of wall pressure fluctuations. Proceedings of the 1966 Heat Transfer and Fluid Mechanics Institute, 1966. 100-121.

Jayanti, S. and Hewitt, G. F. 1992. Prediction of the slug-to-churn flow transition in vertical two-phase flow. *International Journal of Multiphase Flow,* 18, 847-860.

Kaichiro, M. and Ishii, M. 1984. Flow regime transition criteria for upward two-phase flow in vertical tubes. *International Journal of Heat and Mass Transfer,* 27, 723-737.

Kaji, R. 2008. *Characteristics of Two-phase Flow Structures and Transitions in Vertical Upflow.* PhD Thesis, PhD Thesis, University of Nottingham.

Karapantsios, T. D. and Karabelas, A. J. 1995. Longitudinal characteristics of wavy falling films. *International Journal of Multiphase Flow,* 21, 119-127.

Karapantsios, T. D., Paras, S. V. and Karabelas, A. J. 1989. Statistical characteristics of free falling films at high reynolds numbers. *International Journal of Multiphase Flow,* 15, 1-21.

Karimi, G. and Kawaji, M. 1998. An experimental study of freely falling films in a vertical tube. *Chemical Engineering Science,* 53, 3501-3512.

Karimi, G. and Kawaji, M. 1999. Flow characteristics and circulatory motion in wavy falling films with and without counter-current gas flow. *International Journal of Multiphase Flow,* 25, 1305-1319.

Kockx, J. P. 1999. *Experiments on the gas exchange between a Taylor bubble and its liquid slug in a vertical tube.* PhD, Delft University of Technology.

Kockx, J. P., Delfos, R. and Oliemans, R. V. A. 1998. Measurement of Film Characteristics. *International Symposium on Application of Laser Techniques to Fluid Mechanics.* Lisbon, Portugal.

Kockx, J. P., Nieuwstadt, F. T. M., Oliemans, R. V. A. and Delfos, R. 2005. Gas entrainment by a liquid film falling around a stationary Taylor bubble in a vertical tube. *International Journal of Multiphase Flow,* 31, 1-24.

Kostoglou, M., Samaras, K. and Karapantsios, T. D. 2010. Reconstruction of film thickness time traces for wavy turbulent free falling films. *International Journal of Multiphase Flow,* 36, 184-192.

Kulov, N. N., Maksimov, V. V., Maljusov, V. A. and Zhavoronkov, N. M. 1979. Pressure drop, mean film thickness and entrainment in

Abolore Abdulahi

downward two-phase flow. *The Chemical Engineering Journal,* 18, 183-188.

Kusabiraki, D., Yamagiwa, K., Yasuda, M. and Ohkawa, A. 1992. Gas entrainment behavior of vertical plunging liquid jets in terms of changes in jet surface length. *The Canadian Journal of Chemical Engineering,* 70, 181-184.

Lee, Y. H., Scott, D. M. and Thorpe, R. B. 1999. The scale-up of large bubbles attached to spargers in downward two-phase flow. *Chemical Engineering Science,* 54, 3893-3898.

Legius, H. J. W. M., Van Den Akker, H. E. A. and Narumo, T. 1997. Measurements on wave propagation and bubble and slug velocities in cocurrent upward two-phase flow. *Experimental Thermal and Fluid Science,* 15, 267-278.

Liu, J., Paul, J. D. and Gollub, J. P. 1993. Measurements of the primary instabilities of film flows. *Journal of Fluid Mechanics,* 250, 69-101.

Liu, J., Schneider, J. B. and Gollub, J. P. 1995. Three-dimensional instabilities of film flows. *Physics of Fluids,* 7, 55-67.

Lockhart, R. W. and Martinelli, R. C. 1949. Proposed correlation of data for isothermal two-phase, two-component flow in pipes . *Chem. Eng. Prog,* Vol. 45, No. 1,, pp. 39-48.

Lucas, D., Krepper, E. and Prasser, H. M. 2005. Development of co-current air–water flow in a vertical pipe. *International Journal of Multiphase Flow,* 31, 1304-1328.

Mandal, T. K., Das, G. and K. Das, P. 2007. Prediction of rise velocity of a liquid Taylor bubble in a vertical tube. *Physics of Fluids,* 19, 128109-4.

Mao, Z.-S. and Dukler, A. E. 1985. Rise velocity of a Taylor bubble in a train of such bubbles in a flowing liquid. *Chemical Engineering Science,* 40, 2158-2160.

Mao, Z.-S. and Dukler, A. E. 1990. The motion of Taylor bubbles in vertical tubes. I. A numerical simulation for the shape and rise velocity of Taylor bubbles in stagnant and flowing liquid. *Journal of Computational Physics,* 91, 132-160.

Martin, C. S. 1976. Vertically downward two-phase slug flow. *Journal of Fluids Engineering,* 98, 715-722.

Mckeen, T. and Pugsley, T. 2003. Simulation and experimental validation of a freely bubbling bed of FCC catalyst. *Powder Technology,* 129, 139-152.

Mckeogh, E. J. and Ervine, D. A. 1981. Air entrainment rate and diffusion pattern of plunging liquid jets. *Chemical Engineering Science,* 36, 1161-1172.

Mcneil, D. A. and Stuart, A. D. 2003. The effects of a highly viscous liquid phase on vertically upward two-phase flow in a pipe. *International Journal of Multiphase Flow,* 29, 1523-1549.

Mcneil, D. A. and Stuart, A. D. 2004. Vertically upward two-phase flow with a highly viscous liquid-phase in a nozzle and orifice plate. *International Journal of Heat and Fluid Flow,* 25, 58-73.

Mcquillan, K. W. and Whalley, P. B. 1985. A comparison between flooding correlations and experimental flooding data for gas-liquid flow in vertical circular tubes. *Chemical Engineering Science,* 40, 1425-1439.

Mendoza, J. M. L. 2011. *Falling Film and Gas Entrainment in VerticalL Downward Two-phase Flow.* PhD Thesis, The University of Tulsa.

Modell, M. and Reid, R. C. 1983. *Thermodynamics and its applications,* Prentice-Hall.

Abolore Abdulahi

Moissis, R. and Griffith, P. 1962. Entrance effects in a two-phase slug flow. *Journal of Heat Transfer,* 84.

Mori, K., Kondo, Y., Kaji, M. and Yagishita, T. 1999. Effects of Liquid Viscosity on Characteristics of Waves in Gas-Liquid Two-Phase Flow (Characteristics of Huge Waves and Disturbance Waves). *JSME International Journal Series B,* 42, 658-666.

Mori, K., Yoshida, H., Nakano, K. and Shiomi, Y. 2007. Effects of liquid viscosity on inception of disturbance waves and droplets in gas-liquid annular two-phase flow. *Heat Transfer - Asian Research,* 36, 529-541.

Nicklin, D. J. 1962. Two-phase bubble flow. *Chemical Engineering Science,* 17, 693-702.

Nigmatulin, T. R. and Bonetto, F. J. 1997. Shape of Taylor bubbles in vertical tubes. *International Communications in Heat and Mass Transfer,* 24, 1177-1185.

Nishikawa, K., Sekoguchi, K. and Fukano, T. 1969. On the Pulsation Phenomena in Gas-Liquid Two-Phase Flow : Relationship between Pulsating Pressure and Flow Pattern in Upward Two-Phase Flow. *Bulletin of JSME,* 12, 1410-1416.

Nogueira, S., Riethmuller, M. L., Campos, J. B. L. M. and Pinto, A. M. F. R. 2006. Flow patterns in the wake of a Taylor bubble rising through vertical columns of stagnant and flowing Newtonian liquids: An experimental study. *Chemical Engineering Science,* 61, 7199-7212.

Nusselt, W. 1916. Die Oberfluchenkondensation des Wasserdampfes. *Verein Deutscher Ingenieure, Zeitschirift, ,* Vol. 60, No. 28, pp. 569.

Nydal, O. J. 1991. *An experimental investigation of slug flow* PhD Thesis, PhD Thesis, University of Oslo.

Olerni, C., Jia, J. and Wang, M. 2013. Measurement of air distribution and void fraction of an upwards air–water flow using electrical resistance tomography and a wire-mesh sensor. *Measurement Science and Technology,* 24, 035403.

Omebere-Iyari, N. K. 2006. *The Effect of Pipe Diameter and Pressure of Vertical Two-Phase Flow.* PhD Thesis, University of Nottingham.

Oron, A., Gottlieb, O. and Novbari, E. 2009. Numerical analysis of a weighted-residual integral boundary-layer model for nonlinear dynamics of falling liquid films. *European Journal of Mechanics - B/Fluids,* 28, 1-36.

Owen, D. 1986. *An experimental and theoretical analysis of equilibrium annular flow.* PhD Thesis, University of Birmingham.

Pietruske, H. and Prasser, H. M. 2007. Wire-mesh sensors for high-resolving two-phase flow studies at high pressures and temperatures. *Flow measurement and Instrumentation,* 18, 87-94.

Pinto, A. M. F. R. and Campos, J. B. L. M. 1996. Coalescence of two gas slugs rising in a vertical column of liquid. *Chemical Engineering Science,* 51, 45-54.

Pioli, L., Bonadonna, C., Azzopardi, B. J., Phillips, J. C. and Ripepe, M. 2012. Experimental constraints on the outgassing dynamics of basaltic magmas. *Journal of Geophysical Research: Solid Earth,* 117, B03204.

Polonsky, S., Barnea, D. and Shemer, L. 1999. Averaged and time-dependent characteristics of the motion of an elongated bubble in a vertical pipe. *International Journal of Multiphase Flow,* 25, 795-812.

Abolore Abdulahi

Portalski, S. and Clegg, A. J. 1972. An experimental study of wave inception on falling liquid films. *Chemical Engineering Science,* 27, 1257-1265.

Prasser, H.-M., Beyer, M., Böttger, A., Carl, H., Lucas, D., Schaffrath, A., Schütz, P., Weiss, F.-P. and Zschau, J. 2004. TOPFLOW tests on the structure of the gas-liquid interface in a large vertical pipe. *Annual Meeting on Nuclear Technology.* Germany.

Prasser, H.-M., Krepper, E. and Lucas, D. 2002. Evolution of the two-phase flow in a vertical tube—decomposition of gas fraction profiles according to bubble size classes using wire-mesh sensors. *International Journal of Thermal Sciences,* 41, 17-28.

Prasser, H. M., Böttger, A. and Zschau, J. 1998. A new electrode-mesh tomograph for gas-liquid flows. *Flow measurement and Instrumentation,* 9, 111-119.

Prasser, H. M., Misawa, M. and Tiseanu, I. 2005a. Comparison between wire-mesh sensor and ultra-fast X-ray tomograph for an air-water flow in a vertical pipe. *Flow measurement and Instrumentation,* 16, 73-83.

Prasser, H. M., Misawa, M. and Tiseanu, I. 2005b. Comparison between wire-mesh sensor and ultra-fast X-ray tomograph for an air-water flow in a vertical pipe. *Flow measurement and Instrumentation,* 16, 73-83.

Prasser, H. M., Scholz, D. and Zippe, C. 2001. Bubble size measurement using wire-mesh sensors. *Flow measurement and Instrumentation,* 12, 299-312.

Premoli, A., Francesco, D. and Prina, A. 1970. An empirical correlation for evaluating two-phase mixture density under adiabatic conditions. *European Two-Phase Flow Group Meeting, Milan.*

Radovcich, N. A. and Moissis, R. 1962. The transition from two phase bubble flow to slug flow. *Department of Mechanical Engineering, Massachusetts Institute Of Technology,* Report No. 7-7673-22, pp. 1-47.

Richter, S., Aritomi, M., Prasser, H. M. and Hampel, R. 2002. Approach towards spatial phase reconstruction in transient bubbly flow using a wire-mesh sensor. *International Journal of Heat and Mass Transfer,* 45, 1063-1075.

Riiser, K., Fabre, J. and Suzanne, C. 1992. Gas entrainment at the rear of Taylor-bubble. *29th Meeting of the European Two-phase Flow Group.* Stockholm, Sweden.

Sam, R. G. and Crowley, C. J. 1986. Investigation of two-phase flow processes in coal slurry/hydrogen heaters. Hanover, NH: Creare Inc.

Sarica, C., Wilkens, R. J. and Zhang, H.-Q. 2011. Sensitivity of Slug Flow Mechanistic Models on Slug Length. *Journal of Energy Resources Technology,* 133, 043001-043001.

Schagen, A., Modigell, M., Dietze, G. and Kneer, R. 2006. Simultaneous measurement of local film thickness and temperature distribution in wavy liquid films using a luminescence technique. *International Journal of Heat and Mass Transfer,* 49, 5049-5061.

Sharaf, S. 2011. *Testing and Application of Wire Mesh Sensors in Vertical Gas Liquid Two-Phase Flow.* PhD Thesis, University of Nottingham.

Sharaf, S., Van Der Meulen, G. P. and Azzopardi, B. J. 2013. Reconciliation between two forms of churn flow in large diameter vertical pipes. *8th International Conference of Multiphase Flows.* Jeju, Korea.

Abolore Abdulahi

Shoham, O. 2006. *Mechanistic Modeling of Gas-Liquid Two-Phase Flow in Pipes*, Society of Petroleum Engineers.

Skartlien, R., Julshamn, J. A., Lawrence, C. J. and Liu, L. 2012. A gas entrainment model for hydraulic jumps in near horizontal pipes. *International Journal of Multiphase Flow*, 43, 39-55.

Song, C. H., No, H. C. and Chung, M. K. 1995. Investigation of bubble flow developments and its transition based on the instability of void fraction waves. *International Journal of Multiphase Flow*, 21, 381-404.

Sotiriadis, A. A. and Thorpe, R. B. 2005. Liquid re-circulation in turbulent vertical pipe flow behind a cylindrical bluff body and a ventilated cavity attached to a sparger. *Chemical Engineering Science*, 60, 981-994.

Sotiriadis, A. A., Thorpe, R. B. and Smith, J. M. 2005. Bubble size and mass transfer characteristics of sparged downwards two-phase flow. *Chemical Engineering Science*, 60, 5917-5929.

Spedding, P. L. 2010. Falling Film Flow. *Thermopedia: A-to-Z Guide to Thermodynamics, Heat & Mass Transfer, and Fluids Engineering*.

Su, C. 1995. *Gas Entrainment at the Bottom of a Taylor Bubble in Vertical Gas-Liquid Slug Flows.* PhD PhD Thesis, University of Houston.

Su, C. and Metcalfe, R. W. Influences of liquid properties on gas entrainment at the bottom of a fixed bubble. Proceedings of the ASME Fluids Engineering Division Summer Meeting, 1997 Vancouver. 1–7.

Szalinski, L., Abdulkareem, L. A., Da Silva, M. J., Thiele, S., Beyer, M., Lucas, D., Hernandez Perez, V., Hampel, U. and Azzopardi, B. J. 2010. Comparative study of gas–oil and gas–water two-phase flow in a vertical pipe. *Chemical Engineering Science*, 65, 3836-3848.

Taha, T. and Cui, Z. F. 2006. CFD modelling of slug flow in vertical tubes. *Chemical Engineering Science*, 61, 676-687.

Taitel, Y., Barnea, D. and Dukler, A. E. 1980. Modelling flow pattern transitions for steady upward gas-liquid flow in vertical tubes. *AIChE Journal*, 26, 345-354.

Taitel, Y., Barnea, D., James, P. H. and Thomas F. Irvine, Jr. 1990. Two-Phase Slug Flow. *Advances in Heat Transfer.* Elsevier.

Takahama, H. and Kato, S. 1980. Longitudinal flow characteristics of vertically falling liquid films without concurrent gas flow. *International Journal of Multiphase Flow*, 6, 203-215.

Takamasa, T. and Kobayashi, K. 2000. Measuring interfacial waves on film flowing down tube inner wall using laser focus displacement meter. *International Journal of Multiphase Flow*, 26, 1493-1507.

Talvy, C. A., Shemer, L. and Barnea, D. 2000. On the interaction between two consecutive elongated bubbles in a vertical pipe. *International Journal of Multiphase Flow*, 26, 1905-1923.

Thiele, S., Da Silva, M. J., Hampel, U., Abdulkareem, L. and Azzopardi, B. J. 2008. High-resolution oil-gas two-phase flow measurement with a new capacitance wire-mesh tomography. *5th International Symposium on Process Tomography.* Zakopane, Poland.

Turner, R. G., Hubbard, M. G. and Dukler, A. E. 1969. Analysis and Prediction of Minimum Flow Rate for the Continuous Removal of Liquids from Gas Wells. *Journal of Petroleum Technology*, Volume 21, Number 11, 1475-1482.

Abolore Abdulahi

Van De Sande, E. and Smith, J. M. 1976. Jet break-up and air entrainment by low velocity turbulent water jets. *Chemical Engineering Science,* 31, 219-224.

Van Der Meulen, G. P. 2012. *Churn-Annular Gas-Liquid Flows In Large Diameter Vertical Pipes.* PhD Thesis, University of Nottingham.

Van Hout, R., Shemer, L. and Barnea, D. 1992. Spatial distribution of void fraction within a liquid slug and some other related slug parameters. *International Journal of Multiphase Flow,* 18, 831-845.

Wallis, G. B. 1961. Flooding velocities for air and water in vertical tubes. *UKAEA Report AEEW-R123.*

Wangjiraniran, W., Aritomi, M., Kikura, H., Motegi, Y. and Prasser, H. M. 2005. A study of non-symmetric air water flow using wire mesh sensor. *Experimental Thermal and Fluid Science,* 29, 315-322.

Watson, M. J. and Hewitt, G. F. 1999. Pressure effects on the slug to churn transition. *International Journal of Multiphase Flow,* 25, 1225-1241.

Wegener, J. L. and Drallmeier, J. A. 2010. Measurement of Thin Liquid Film Characteristics using Laser Focus Displacement Instruments for Atomization Applications. *22nd Annual Conference on Liquid Atomization and Spray Systems.* Cincinnati, Ohio, USA.

White, E. T. and Beardmore, R. H. 1962. The velocity of rise of single cylindrical air bubbles through liquids contained in vertical tubes. *Chemical Engineering Science,* 17, 351-361.

Xu, Z. F., Khoo, B. C. and Wijeysundera, N. E. 2008. Mass transfer across the falling film: Simulations and experiments. *Chemical Engineering Science,* 63, 2559-2575.

Zangana, M. H. S. 2011. *Film Behaviour of Vertical Gas-Liquid Flow in a Large Diameter Pipe.* PhD Thesis, University of Nottingham.

Zhou, D. W., Gambaryan-Roisman, T. and Stephan, P. 2009. Measurement of water falling film thickness to flat plate using confocal chromatic sensing technique. *Experimental Thermal and Fluid Science,* 33, 273-283.

Zuber, N. and Findlay, J. A. 1965. Average Volumetric Concentration in Two-Phase Flow Systems. *Journal of Heat Transfer,* 87, 453-468.

Zukoski, E. E. 1966. Influence of viscosity, surface tension, and inclination angle on motion of long bubbles in closed tubes. *Journal of Fluid Mechanics,* 25, 821-837.

NOMENCLATURE

Symbol	Meaning	unit
A	Area	(m^2)
C	Constant in equation (2.30)	(-)
C_0	Constant in equation (2.24)	(-)
C_1	Constant in equation (A-3)	(-)
C_2	Constant in equation (A-4)	(-)
C_{B1}	Constant in Table 2.1	(-)
C_{B2}	Constant in Table 2.1	(-)
C_{B3}	Constant in Table 2.1	(-)
C_{B4}	Constant in Table 2.1	(-)
C_D	Drag coefficient	(-)
C_E	Concentration of entrained droplets	(k)
C'	Constant in equation (A-18)	(-)
c	Wave velocity	(m/s)
D_b	Bubble diameter	(m)
D_p	Pipe diameter	(m)
D_t	Tube diameter	(m)
d	Diameter	(m)
E	Entrainment rate	$(kg/m^2 s)$
E_1	Parameter defined by equation (2.13)	(-)
E_2	Parameter defined by equation (2.14)	(-)
f	Friction factor	(-)
f	Frequency	(Hz)
Fr	Froude number	(-)
Fr_g	Modified Froude number (gas based)	(-)
g	Acceleration due to gravity	(m/s^2)
j	Parameter defined by equation (2.11)	(-)
Ku	Kutataledze number	(-)
L	Length	(m)
L_w	Wake length	(m)
$\dot{m}$	Mass flux	$(kg/m^2 s)$
N_f	Dimensionless parameter defined Chapter 6	(-)
P	Pressure	(Pa)
Q	Volumetric flow rate	(m^3/s)
Q_{ge}	Volumetric flow rate of bubble entrainment	(m^3/s)
Q_{gb}	Volumetric flow rate of bubble re-coalescence	(m^3/s)
Q_{gs}	Volumetric flow rate released from TB unit	(m^3/s)
Rn	Radius of curvature	(m)
Re	Reynolds number	(-)
St_g	Strouhal number (Gas based)	(-)
T	Time or Sample duration	(s)

Abolore Abdulahi

U	Velocity	(m/s)
U_R	Slip ratio	(-)
U_0	Terminal velocity of bubbles	(m/s)
U_{GS}, U_{SG}	Gas superficial velocity	(m/s)
U_{LS}, U_{SL}	Liquid superficial velocity	(m/s)
U_{TB}	Rise velocity of elongated bubbles	(m/s)
u	Velocity	(m/s)
u_0	Rise velocity of bubble	(m/s)
u_m	Mixture velocity	(m/s)
We	Weber Number	(-)
x_g	Quality	(-)
X_b	Parameter defined by equation (2.26)	(-)
X	Lockhart Martinelli parameter	(-)
V	Velocity	(m/s)
V_{gd}	Drift velocity	(m/s)
v'	Fluctuating velocity for y component	(m/s)
w'	Fluctuating velocity for z component	(m/s)
z	Axial distance	(m)
λ	Wavelength	(m)

Greek symbols

β	Inclination angle from horizontal	(deg)
γ	Electrical conductivity	$(1/\Omega m)$
Γ	Volumetric film flow rate per unit circumference	(m^2/s)
δ	Film thickness	(m)
δ_m	Mean film thickness	(m)
ε	Void fraction	(-)
ε_g	Void fraction	(-)
ε_{gc}	Critical void fraction	(-)
φ	Two phase multiplier	(-)
η	Dynamic Viscosity	(kg/ms)
v	Kinematic Viscosity	(m^2/s)
ρ	Density	(kg/m^3)
σ	Surface tension	(N/m)
τ	Shear stress	(N/m^2)

Subscripts

b	bubble, base film
c	critical
e	entrained
l	liquid
ls	liquid superficial
l_f	liquid film
m	mixture
g	gas
gs	gas superficial
H	homogeneous
tb	Taylor bubble

Abolore Abdulahi

w   wall
max   maximum
min   minimum

Superscripts

w   wake region
s   far wake region

Abbreviations

LFDM   Laser focal displacement meter

PDF   Probability density function
PSD   Power Spectrum Density
TB   Taylor Bubble
WMS   Wire Mesh Sensor

Appendix A

A1   Slug to churn flow transition

For flooding conditions, Wallis (1961) proposed the following equation,

$$\sqrt{u_g^*} + \sqrt{u_l^*} = C,$$ (A-1)

where u_l^* and u_g^* are respectively dimensionless liquid and gas superficial velocities given by

$$u_l^* = \frac{u_{ls}\sqrt{\rho_l}}{\sqrt{gD(\rho_l - \rho_g)}} \quad \text{and} \quad u_g^* = \frac{u_{gs}\sqrt{\rho_g}}{\sqrt{gD(\rho_l - \rho_g)}}$$ (A-2)

In the model developed by Jayanti and Hewitt (1992), the flooding conditions are included to consider the effect of film length:

$$\sqrt{u_{tb}^*} + c_1\sqrt{u_{lf}^*} = c_2,$$ (A-3)

where

$$c1 = 0.1928 + 0.01089(\frac{L_b}{D_t})^{-0.3754} \times 10^{-5}\ (\frac{L_b}{D_t})^2$$ (A-4)

for $\dfrac{L_b}{D_t} \leq 120$, $c_1 = 0.96$

for $\dfrac{L_b}{D_t} > 120$, $c_2 = 1$.

The superficial velocity of the liquid film and the velocity of the Taylor bubble u_{lf} and u_{tb} were respectively obtained from the following equations,

$$u_{lf} = 9.916(1 - \varepsilon_{tb})\sqrt{\frac{gD_t(\rho_l - \rho_g)(1 - \sqrt{\varepsilon_{tb}})}{\rho_l}}$$ (A-5)

$$u_{tb} = \varepsilon_{tb}\left[1.2u_m + 0.35\frac{\sqrt{gD_t(\rho_l - \rho_g)}}{\rho_l}\right]$$ (A-6)

Abolore Abdulahi

The Taylor bubble length, which is given from the mass balance of liquid phase over a slug unit, is expressed as follows:

$$u_{ls} = u_s(1-\varepsilon_s)\left(1 - \frac{L_b}{L_b + L_s}\right) - u_{lfs}\frac{L_b}{L_b + L_s} \qquad (A-7)$$

A2 Bubble-slug-churn to dispersed bubble flow transition

Taitel et al (1980) derived the correlation for transition to dispersed bubble flow as follows

$$d_{max} = k\left(\frac{\sigma}{\rho_l}\right)^{0.6} E^{-0.4} \qquad (A-8)$$

where E is the rate of energy dissipation per unit mass also given by:

$$E = \left|\frac{dp}{dz}\right|\frac{u_m}{\rho_m} = \frac{2f}{D_t}u_m^3 \qquad (A-9)$$

For the constant k in equation (2.12), Taitel et al. (1980) used 1.14 while Barnea et al. (1982) later used $0.725+4.15\varepsilon_g^{0.5}$, which was suggested by Calderbank (1958), as this was meant to include the effect of void fraction on the sizes of bubble.

The bubble size needs to be small enough to prevent bubbles from coalescing. This criteria was suggested by Brodkey (1967)

$$d_{crit} = \left[\frac{0.4\sigma}{(\rho_l - \rho_g)g}\right]^{0.5} \qquad (A-10)$$

Combining equations (2.12) and (2.14) yields the transition boundary which is given as:

$$2\left[\frac{0.4}{(\rho_l - \rho_g)g}\right]^{0.5}\left(\frac{\rho_l}{\sigma}\right)^{0.6}\left(\frac{2f}{D_t}\right)^{0.4}u_m^{1.2} = 4.15\frac{2u_{gs}}{u_m} + 0.725 \qquad (A-11)$$

A3 Entrainment Model

The bubble entrainment rate from the Taylor bubble tail in Brauner and Ullmann (2004a) described in section 2.7.3 is presumed by the energy balance between the rate of turbulent kinetic energy and that of bubble surface energy production, which is given by

$$\frac{1}{2}\rho_l\left(u'^2+v'^2+w'^2\right)Q_{lf}=C_J\frac{6\sigma}{d_{max}}Q_{ge} \tag{A-12}$$

where

$$Q_{lf}=\left(u_{gtb}-u_{lf}^w\right)\left(1-\varepsilon_{tb}^w\right) \tag{A-13}$$

The conservative values below are used for the component of turbulent velocity:

$$u'^2+v'^2+w'^2\approx 0.03\left(u_{lls}^w-u_{lf}^w\right)^2 \tag{A-14}$$

The maximum stable bubble size is given by,

$$\frac{d_{max}}{D}=\left[\frac{0.4\sigma}{\left(\rho_l-\rho_g\right)g\cos\beta'D_t^2}\right]^{0.5} \tag{A-15}$$

Where β' = 0 for vertical flow.

From equation (2.47)-(2.50),

$$\frac{Q_{ge}}{Q_{lf}}=\frac{1}{400C_J}\frac{d_{max}}{D_t}\left(We-We_c\right) \tag{A-16}$$

where

$$We=\frac{\rho_lD_t\left(u_{lls}^w-u_{lf}^w\right)^2}{\sigma} \tag{A-17}$$

$$We_c=\frac{100C'}{\left(d_{max}/D_t\right)} \tag{A-18}$$

For C_J and C', 1 and $\frac{2}{3}$ were suggested, respectively.

Velocities of bubbles and liquid in the Taylor bubble wake regions are given by,

$$u_{gls}^{w} = C_{0}^{w}u_{m} + u_{r}^{w} \tag{A-19}$$

$$u_{lls}^{w} = \frac{u_{m} - \varepsilon_{ls}^{w}u_{gls}^{w}}{\left(1 - \varepsilon_{ls}^{w}\right)} \tag{A-20}$$

where

$$u_{r}^{w} = 1.53\left[\frac{\sigma D_{t}\left(\rho_{l} - \rho_{g}\right)}{\rho_{l}^{2}}\right]^{0.25} \sin\beta\left(1 - \varepsilon_{ls}^{w}\right)^{1.5} \tag{A-21}$$

The same equations are applied to far wake region by replacing 'w' with 's'. The Taylor bubble translational velocity for vertical upflow is expressed by Nicklin correlation:

$$u_{gtb} = C_{0}u_{m} + u_{0} \tag{A-22}$$

where

$$u_{0} = 0.35\sqrt{\frac{\left(\rho_{l} - \rho_{g}\right)gD_{t}}{\rho_{l}}} \tag{A-23}$$

The rate of re-coalescence to Taylor bubble tail is estimated by the difference between the drift velocity of the Taylor bubble and that of bubble in the swarm,

$$Q_{gb} = \left(u_{0}^{w} - u_{0}\right)\varepsilon_{LS}^{w}\varepsilon_{TB}^{w} \qquad \text{for } u_{0}^{w} > u_{0}$$

$$Q_{gb} = 0 \qquad \text{for } u_{0}^{w} \leq u_{0} \tag{A-24}$$

The net average rate of gas loss from the Taylor bubble tail is shed out of the Taylor bubble wake region and absorbed to the successive slug.

$$Q_{gs} = Q_{ge} - Q_{gb} \qquad \text{for } Q_{ge} > Q_{gb}$$

$$Q_{gs} = 0 \qquad \text{for} \tag{A-25}$$

Void fraction in wake and far wake regions are given by

$$\varepsilon_{lv}^{\prime\prime} - \frac{Q_{gs}}{u_{te} - u_{glv}^{\prime\prime}} = 0 \tag{A-26}$$

$$\varepsilon_{lv}^{\prime} - \frac{Q_{gs}}{u_{te} - u_{glv}^{\prime}} = 0 \tag{A-27}$$

Liquid film superficial velocity is given by

$$u_{lfs} = u_{ms} - \varepsilon_{lf} u_{glb} \tag{A-28}$$

Therefore actual liquid film velocity is

$$u_{lf} = \frac{u_{lfs}}{1 - \varepsilon_{lb}} \tag{A-29}$$

Void fraction of liquid film is given by following equation assuming no-slip between the liquid film and bubbles.

$$\varepsilon_{glf} = \frac{Q_{gs} - \left(u_{te} - u_{glb}\right)\varepsilon_{lb}}{\varepsilon_{lf}\left(u_{te} - u_{lf}\right)} \tag{A-30}$$

Holdup around the Taylor bubble, ε_{lf}, is determined by the momentum balance on the film region.

The continuity equation for the liquid in the coordinate moving with u_{te} is given by

$$\frac{\partial}{\partial z}\left\{\rho_l\left(1-\varepsilon_{glf}\right)\varepsilon_{lf}\left(u_{te}-u_{lf}\right)\right\}=0 \tag{A-31}$$

The continuity equation for the gas is given when no-slip between bubbles and film is considered:

$$\frac{\partial}{\partial z}\left\{\rho_g\varepsilon_{glf}\varepsilon_{lf}\left(u_{te}-u_{lf}\right)+\rho_g Q_{gs}\right\}=0 \tag{A-32}$$

where

$$Q_{gs} = \left(u_{te} - u_{glb}\right)\varepsilon_{lb} \tag{A-33}$$

The momentum balance for the film and the gas flow rates respectively are

$$\frac{\partial}{\partial t}\left\{\rho_m \varepsilon_{lf}\left(u_{tc}-u_{lf}\right)^2\right\}+\rho_g \frac{\partial Q_{gy}}{\partial t}u_{lf}=\frac{\tau_m S_m}{A}-\frac{\tau_i S_i}{A}+\rho_j \varepsilon_{lf}g\sin\beta-\rho_j \varepsilon_{lf}g\sin\beta\frac{\partial h}{\partial t}-\varepsilon_{lf}\frac{\partial P_{il}}{\partial t} \quad \text{(A-34)}$$

$$\frac{\partial}{\partial t}\left\{\rho_g \varepsilon_{lb}\left(u_{tc}-u_{glb}\right)^2\right\}+\rho_g \frac{\partial Q_{gy}}{\partial t}u_{lf}=\frac{\tau_g S_g}{A}-\frac{\tau_i S_i}{A}+\rho_g \varepsilon_{lb}g\sin\beta-\rho_g \varepsilon_{lb}g\sin\beta\frac{\partial h}{\partial t}-\varepsilon_{lb}\frac{\partial P_{ig}}{\partial t} \quad \text{(A-35)}$$

where $\rho_m = \rho_l\left(1-\varepsilon_{glf}\right)+\rho_g \varepsilon_{glf}$

$$\rho_m = \rho_l\left(1-\varepsilon_{glf}\right)+\rho_g \varepsilon_{glf} \quad \text{(A-36)}$$

From Equations (2.69) and (2.70), the gradient of film holdup is given by

$$\frac{\partial \varepsilon_{lf}}{\partial z}=-\frac{D\left(\rho_m-\rho_g\right)\sin\beta+\dfrac{4\tau_m}{\varepsilon_{lf}}-4\left(1-2\tilde{\delta}\right)\left(\dfrac{1}{\varepsilon_{lf}}-\dfrac{1}{1-\varepsilon_{lf}}\right)\tau_i}{\left[\dfrac{\rho_m\left(u_{tc}-u_{lf}\right)\left(u_{glb}-u_{lf}\right)}{\varepsilon_{lf}}+\dfrac{\rho_g\left(u_{tc}-u_{glb}\right)\left(u_{glb}-u_{lf}-u_{tc}/\varepsilon_{lf}\right)}{1-\varepsilon_{lf}}\right]} \quad \text{(A-37)}$$

with $\varepsilon_{lf}=1$ at $\tilde{z}=0$

where $\tilde{z}=\dfrac{z}{D_t}$, $\tilde{\delta}=\dfrac{\delta}{D_t}$ and $\varepsilon_{lf}=4\tilde{\delta}\left(1-\tilde{\delta}\right)$

Appendix B

B-1   Calibration of the differential pressure transducers

Apart from being company calibrated, the differential pressure transducers were also calibrated and tested in the laboratory before they were shipped to SINTEF for use during experimentation. Figure B-1 shows the plot of the results from calibration which perfectly matches those provided by the manufacturer. The equation in the plot was programmed into Labview to generate instantaneous pressure gradient which have been discussed in Chapters 3 and 4.

Abolore Abdulahi
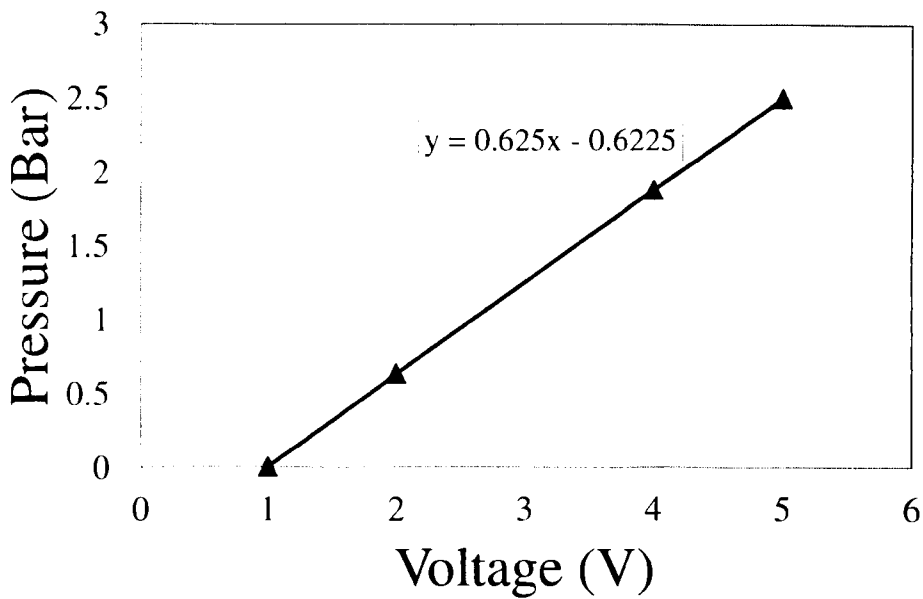
Figure B-1: Calibration of the differential pressure transducers

B-2   Calibration of the Thermocouples

The thermocouples were also calibrated at the University of Nottingham laboratory in order to continuously monitor the temperature of flow since a change in this property affects density, viscosity, surface tension and other physical properties of the fluid. Figure B-2 shows the plot of the temperature versus voltage with a line of best fit. The equation of this line was programmed into Labview to obtain the temperatures of the two-phase flow at the outlet of the riser as well for the liquid inlet at the bottom end of the riser.

Abolore Abdulahi
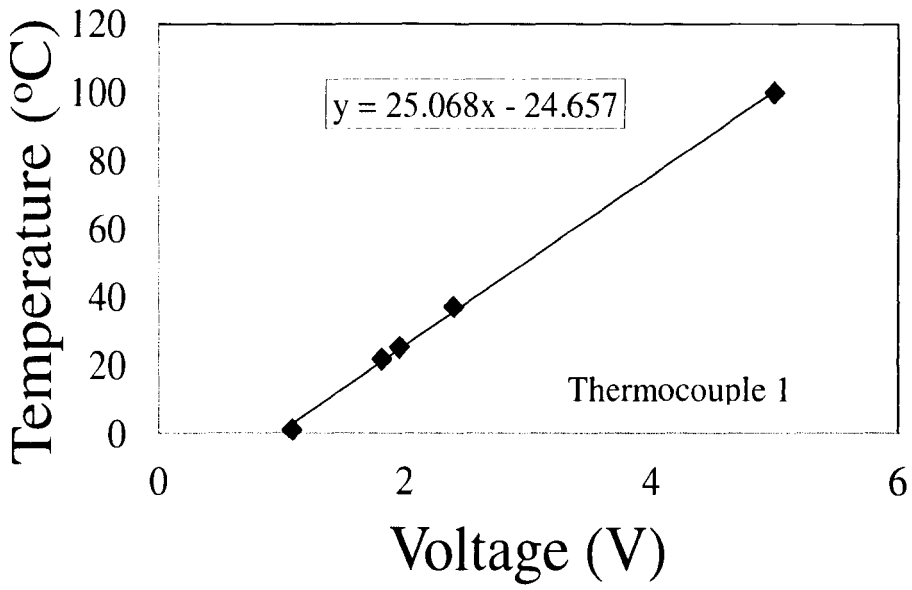
(a)
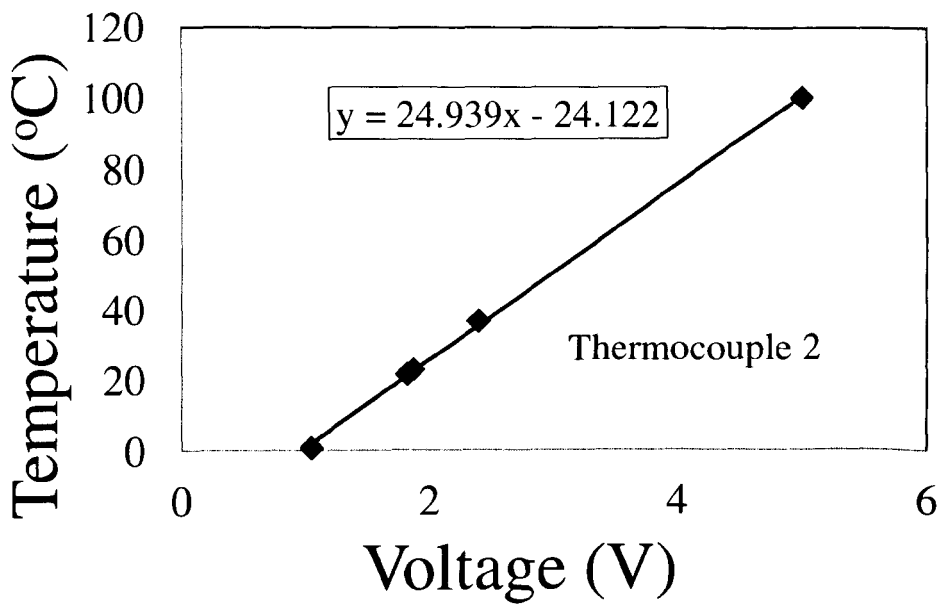
(b)

Figure B-2: Calibration plots for the Thermocouples (a) Thermocouple 1 at

the riser top (b) Thermocouple 2 at the oil inlet

B-3 Experimental conditions

Table B-1: Experimental data sheet of SF6-Oil in the 127mm diameter vertical upflow pipe at 7.5 bars

Superficial liquid velocity (m/s)	Superficial gas velocity (m/s)	Superficial liquid velocity (m/s)	Superficial gas velocity (m/s)
0.07	0.1	0.09	0.4
0.13	0.1	0.19	0.4
0.27	0.1	0.37	0.4
0.40	0.1	0.56	0.4
0.54	0.1	0.75	0.4
0.67	0.1	0.94	0.4
0.81	0.1	0.00	0.0
0.94	0.1	0.00	0.0
1.08	0.1	0.44	0.4
1.22	0.1	1.19	0.4
1.36	0.1	1.38	0.4
1.49	0.1	1.58	0.4
1.63	0.1	1.78	0.4
1.77	0.1	1.98	0.4
1.91	0.1	2.17	0.4
2.04	0.1	2.37	0.4
2.18	0.1	2.57	0.4
2.32	0.1	2.77	0.4
0.07	0.2	2.96	0.4
0.13	0.2	0.10	0.6
0.27	0.2	0.20	0.6
0.40	0.2	0.39	0.6
0.54	0.2	0.59	0.6
0.67	0.2	0.79	0.6
0.81	0.2	0.98	0.6
0.94	0.2	1.18	0.6
1.08	0.2	1.38	0.6
1.21	0.2	1.58	0.6
1.35	0.2	1.77	0.6
1.48	0.2	1.97	0.6
1.89	0.2	2.17	0.6
2.08	0.2	2.37	0.6
2.27	0.2	2.57	0.6
1.70	0.2	2.76	0.6
2.46	0.2	2.96	0.6
2.65	0.2		
2.84	0.2		
3.03	0.2		

Abolore Abdulahi

Superficial liquid velocity (m/s)	Superficial gas velocity (m/s)
0.10	0.8
0.20	0.8
0.39	0.8
0.59	0.8
0.80	0.8
1.00	0.8
1.19	0.8
1.39	0.8
1.59	0.8
1.79	0.8
1.99	0.8
2.19	0.8
2.39	0.8
2.59	0.8
2.79	0.8
2.98	0.8
0.10	1.0
0.20	1.0
0.40	1.0
0.59	1.0
0.79	1.0
0.99	1.0
1.19	1.0
1.39	1.0
1.59	1.0
1.79	1.0
1.98	1.0
2.18	1.0
2.37	1.0
2.57	1.0
2.77	1.0
2.96	1.0

Abolore Abdulahi

Table B-2:   Experimental data sheet of SF6-Oil in the 127mm diameter

vertical upflow pipe at 4.5 bars

Superficial liquid velocity (m/s)	Superficial gas velocity (m/s)	Superficial liquid velocity (m/s)	Superficial gas velocity (m/s)
0.16	0.2		
0.19	0.2	0.10	0.6
0.10	0.2	0.19	0.6
0.38	0.2	0.39	0.6
0.58	0.2	0.59	0.6
0.77	0.2	0.79	0.6
0.96	0.2	0.99	0.6
1.16	0.2	1.18	0.6
1.35	0.2	1.38	0.6
1.58	0.2	1.58	0.6
1.78	0.2	1.78	0.6
1.98	0.2	1.98	0.6
2.18	0.2	2.17	0.6
2.38	0.2	2.37	0.6
2.58	0.2	2.57	0.6
2.78	0.2	2.77	0.6
2.98	0.2	2.97	0.6
0.10	0.4	0.10	0.8
0.20	0.4	0.20	0.8
0.39	0.4	0.39	0.8
0.59	0.4	0.59	0.8
0.79	0.4	0.79	0.8
0.99	0.4	0.99	0.8
1.19	0.4	1.18	0.8
1.40	0.4	1.38	0.8
1.59	0.4	1.58	0.8
1.80	0.4	1.80	0.8
2.00	0.4	2.00	0.8
2.20	0.4	2.19	0.8
2.40	0.4	2.40	0.8
2.60	0.4	2.60	0.8
2.81	0.4	2.80	0.8
3.01	0.4	2.99	0.8

Abolore Abdulahi